# Coupling Reactive Transport and Travel Time Modeling at the Watershed Scale

by

Gabriel Bacca-Cortes

A thesis
presented to the University of Waterloo
in fulfillment of the
thesis requirement for the degree of
Doctor of Philosophy
in
Earth Sciences

Waterloo, Ontario, Canada, 2018

## Examining Committee Membership

The following served on the Examining Committee for this thesis. The decision of the Examining Committee is by majority vote.

| | |
|---|---|
| External Examiner | Dr. Jan Fleckenstein<br>Head of Hydrogeology Department at UFZ<br>Helmholtz Centre for Environmental Research,<br>UFZ-Leipzig |
| Supervisor(s) | Dr. Philippe Van Cappellen<br>Ecohydrology Research Group<br>Department of Earth and Environmental<br>Sciences |
| Internal Member | Dr. David Rudolph<br>Department of Earth and Environmental<br>Sciences |
| Internal-external Member | Dr. James Craig, P.Eng.<br>Associate Professor<br>Department of Civil and Environmental<br>Engineering |
| Other Member(s) | Dr. Fereidoun Rezanezhad (Ph.D.)<br>Assistant Professor<br>Department of Earth and Environmental<br>Sciences |

# AUTHOR'S DECLARATION

I hereby declare that I am the sole author of this thesis. This is a true copy of the thesis, including any required final revisions, as accepted by my examiners.

I understand that my thesis may be made electronically available to the public.

# Abstract

Nonpoint source pollution poses the greatest threat to water quality in developed countries. Modeling this type of pollution is a challenge for reactive transport models because of the change in scale: moving from a local field site- to a watershed-size problem. Computational resources and detailed watershed characterization are the major limiting factors in the fully time- and space-resolved modeling of the subsurface fate and transport of pollutants from nonpoint sources. While detailed characterization has been performed on a few well-studied watersheds, the knowledge derived from these watersheds has not led to a better understanding of watershed functioning in ungauged watersheds. Consequently, alternative approaches to modeling subsurface nonpoint source pollution have emerged to inform risk assessment to water resources and watershed management.

This study investigates the development of a methodology that decouples flow and transport with the implementation of an analytical approach for 1-D travel time probability distribution functions (PDFs) to simulate subsurface flow at the watershed scale, that is, a 3-D problem. The first two chapters of my thesis focus on constraining and providing tools for the implementation of this methodology in watersheds. First, the analytical methodology for travel time was tested under varying conditions of heterogeneity, slope, and aquifer depths that were imposed on a virtual watershed, using Alder Creek, Ontario, as a test case. The analytical method parameters for the 28 scenarios considered were calibrated against the travel time PDFs generated with a 3-D numerical model (FEFLOW), which was used as baseline for comparison. The analytical method simulations revealed a negative relationship between the watershed mean travel time (wMTT) and the degree of imposed heterogeneity ($\sigma_Y^2$) of geostatistically defined permeability fields. This relationship was attributed to the effect of preferential flow paths. The effect of increasing aquifer depth (i.e., bedrock topography) on wMTT was similar to that of reducing the slope in surface topography, both resulting in an increase in wMTT.

Given the promising results of the analytical method in the Alder Creek virtual analogs, further testing was conducted in 8 additional virtual watersheds. This inter-watershed comparison study examined the effects of 28 geomorphological indexes on wMTT and their predictive power in estimating analytical model parameters. This study is the first inter-watershed comparison of subsurface models that establishes relationships between watershed features and hydrologic functioning for groundwater storage and discharge. Among the classes of watershed features considered, those related to elevation (e.g. *Relief*), texture topography (e.g. drainage density, *Dd*), and Horton's law (e.g. bifurcation factor, $R_B$) were the most influential geomorphological classes emerging in the developed regression models. These regression models enable the application of the analytical methodology for deriving travel time PDF in other environmental settings. The transferability of these tools was verified for three extra watersheds in which the particle median travel time (pMTT), and their travel time distribution (TTD) performed on par to the upper tier of the original watersheds. Further research is proposed to include subsurface heterogeneity in the analysis to better evaluate its role in regulating wMTT in a subset of these watersheds.

This methodology may constitute in a viable modeling alternative where subsurface information is scarce or scale limitations exist in developing a subsurface numerical model. The analytical methodology can provide a first line of knowledge in subsurface travel time and its distribution in an ungauged basin through the use of readily available tools (i.e., GIS and MATLAB). This knowledge can be later challenged or verified as more information becomes available. Potential directions to explore for the improvement of the methodology are proposed for further research.

The third chapter applies the travel time PDF approach to the allocation of nitrogen (N) fluxes from base flow contributions to stream water chemistry in an existing hydrological model of Carroll Creek (Grand River basin, Ontario). This is a prospective chapter in which an outline for the development of an N isotope model linked to a hydrological model is presented. The N isotope model includes relevant N transformation and $^{15}N$ fractionation processes in the plant-soil system and aims at simulating $N\text{-}NO_3^-$ concentrations and

isotopic compositions ($\delta^{15}N$). A bottom-up, stepwise approach is proposed in order to determine the most essential $^{15}N$ discriminating processes and spatial discretization required by the model to match observations in the watershed.

# Acknowledgements

I first want to thank my advisor Dr. Philippe Van Cappellen for the opportunity to work on this project and for the time and resources spent to see this research through. I will always value your ability to grasp the best out of many confusing ideas that I have conveyed in the past. I also would like to thank my PhD committee members Dr. Hans Durr, Dr. David Rudolph, Dr. Nandita Basu, Dr. Martin Thullner, and Dr. Fereidoun Rezanezhad for your valuable input throughout this process.

I would like to also thank the Ecohydrology Research Group for providing a continued source of inspiration through the breadth and the quality of their work.

I would like to especially thank the financial support from the Canadian Government through their Canada Excellence Research Chairs. Their continued funding made this research possible.

Finally, I would like to thank my family, especially my Mom and Sister for their inmense support, inspiration, and guidance, and my Dad for his scientific mind and support. I love you deeply.

# Table of Contents

# List of Figures

# List of Tables

# Chapter 1
# Introduction

Nonpoint source pollution has been recognized as one of the largest threats to water quality (*USEPA, 2002*; *EEA, 2007*; *EC, 2007*). The focus of watershed management has shifted from significantly reducing point sources to address diffuse contamination from agricultural, industrial, and urban activities, in which groundwater plays an important role. Unlike point source pollution, the contamination of groundwater is a long-term process controlled in part by the characteristic water residence time of the watershed, which ranges from months to millennia (*Maxwell et al., 2016*). It is usually assumed that the residence time of solute compounds is equal to the residence time in the groundwater reservoir of the water that carries the solute. Water and solute residence times are the same only for non-reactive solutes, however (*Kazemi et al., 2006*). For this reason, recent mathematical frameworks aimed at characterizing groundwater age started treating it as an intrinsic property of the water molecule (*Goode, 1996*; *Etcheverry & Perrochet, 2000*; *Cornaton, 2004*; *Kazemi et al., 2006*). However, long before the development of mathematical approaches, groundwater age was quantified in the field with the use of environmental tracers (*Fritz & Fontes, 1980*).

Tracer techniques, both physical and computational, have allowed the evaluation of aquifer systems in terms of: renewability (e.g. recharge rate estimation), performance (e.g. prevention of overexploitation, estimation of groundwater flow velocity), origin (e.g. groundwater flow paths), transport properties estimation, groundwater mixing, and groundwater vulnerability to pollution (*Kazemi et al., 2006*). Environmental tracers can generally provide an average estimate of groundwater age considering the sampling conditions associated with screened wells and in groundwater discharge zones. In reality, groundwater samples taken from an aquifer represent a distribution of ages that can only be properly determined through mathematical modeling (*Kazemi et al., 2006*).

A travel time distribution synthesizes the physical transport of the mass of a conservative tracer through the landscape's geographical heterogeneities. This distribution can be

determined either for a single water particle with the travel time distribution (TTD) representing likelihood of appearance or for the entire watershed as individual water particle distributions are collated to form a unified distribution. The groundwater TTD provides a description of the residence time in the subsurface for rainfall water as it gets mixed with tracer-free groundwater until it leaves the watershed at the outlet (*Darracq et al., 2010*; *Botter et al., 2011*). The determination of groundwater age and its distribution in an aquifer still requires the creation of a subsurface model. Following the implementation of lumped-parameter models for the analysis of environmental tracers (*Maloszewski & Zuber, 1982*) (Figure 1-1), analytical solutions for travel time distributions were also developed for watershed-scale (*Haitjema, 1995*) and one-dimensional systems (*Cornaton, 2012*; *Soltani & Cvetkovic, 2013*). These simple mathematical expressions have not yet been applied to a three-dimensional watershed, nor verified against age distribution estimates from numerical models.

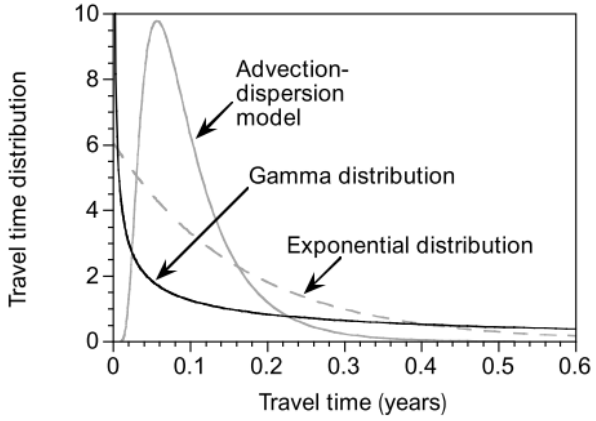


Figure 1-1. Travel time distributions following exponential, gamma, and advection-dispersion models (*Kirchner et al., 2000*).

A comprehensive hydrogeological knowledge of a watershed, as the result of a myriad studies on both hydrology and hydrogeology, if ever really achieved, is a rare occurrence. How much of that knowledge can be transferable to an ungauged basin? This has been the subject of research initiatives in the field of watershed hydrology (*Hrachowitz et al., 2013*) as common practices in hydrology have failed to identify laws of watershed behavior that can

be scaled up to similar or larger watersheds (*Soulsby et al., 2006*). Comparative studies on multiple watersheds have led to the recognition that landscape characteristics, such as topography, and soil type are not only important in predicting watershed response, but also in controlling the mean travel time estimated from isotopic analyses (*Soulsby & Tetzlaff, 2008*; *Tetzlaff et al., 2009*). These studies have also revealed that the insights derived from isotopic analyses are not transferable to all watersheds, which is in turn a confirmation of the concept of uniqueness of watersheds asserted by Beven (*2000, 2001*). This uniqueness concept has not stopped the efforts to find empirical relationships to define hydrologic response dynamics based on landscape characteristics for the purpose of their regionalization (*Hrachowitz et al., 2009*).

The lack of a complete deterministic knowledge of any study site was recognized early in the field of hydrogeology, which motivated the development of stochastic approaches in the 1960's relying on applications of the theory of space random functions (*Rubin, 2003*). Stochastic theory has led to the creation of geostatistical techniques incorporating both airborne geophysical and borehole data for generating conditional geological realizations of three-dimensional permeability fields (*Carle, 1996*; *He et al., 2014*). Conditional and random permeability fields have been incorporated into watershed-scale reactive transport models where accurate flow and transport conditions are necessary for estimating groundwater mixing, as well as reaction times and rates (*Green et al., 2010*). Due to the complexity associated with developing a groundwater model, there is a lack of inter-watershed comparisons to identify the controlling factors that might influence watershed response characteristics, including the travel times of water particles in the subsurface.

## 1.1 On Alternative Reactive Transport Models

Subsurface reactive transport models have continued to evolve since their first inception with the incorporation of equilibrium controlled reactions (*Rubin & James, 1973*). These models initially focused on the fate of organic constituents in local, small scale subsurface settings, typically the result of point source contamination as part of remediation projects (*Zheng & Bennett, 2002*), or in nonpoint source pollution using coarse gridded or two

dimensional domains (*Almasri & Kaluarachchi, 2007*; *Jiang and Somers, 2009*; *Zhang and Hiscock, 2011*; *Aisopou et al., 2015*) for watershed-scale studies. For the case of nonpoint source contamination, the model domain is much larger to characterize, monitor, and simulate (*Corwin et al., 1999*; *Zheng & Bennett, 2002*) than localized groundwater contamination at sites. Numerical simulations can, in principle, simulate the spatio-temporal variability of the distributions of contaminants. However, when applied to diffuse contamination, due to limited computational resources, either the spatial resolution or the complexity of the reaction networks will be compromised, which in turn limits how much predictive understanding on contaminant fate and transport can be gained (*Kourakos et al., 2012*). For this reason, new approaches have been sought to efficiently run simulations of multicomponent reaction systems in a groundwater system, which also helped improve understanding of these systems.

Typically, limited information is available - at the watershed scale - that can be used to condition reactions at the multi-scale reactive interfaces within a watershed. In order to deal with this lack of information for flow and transport, the existing approaches have been adapted either by simplifying a three-dimensional (3-D) computational model for solute transport to a quasi 3-D model (*Lin et al., 2010*), or by coupling a spatially distributed watershed model to a one dimensional leaching model of, say, nitrogen (*Styczen & Storm, 1993*), or recently developed alternative techniques such as the streamline simulation model approach have also been implemented (*Martin & Wegner, 1979*; *Green et al., 2010*) (Figure 1-2).

The travel time methodology presented in this thesis is, similar to the streamline simulation approach. It decouples subsurface flow from solute transport hence offering the possibility to treat each process independently. The basic principle is to approximate subsurface flow through the estimation of particle TTDs spread across the watershed on which solute transformation processes can be built. Details on the two main options that were considered when selecting the 1-D analytical equation for particle TTDs are presented in section 1.3.

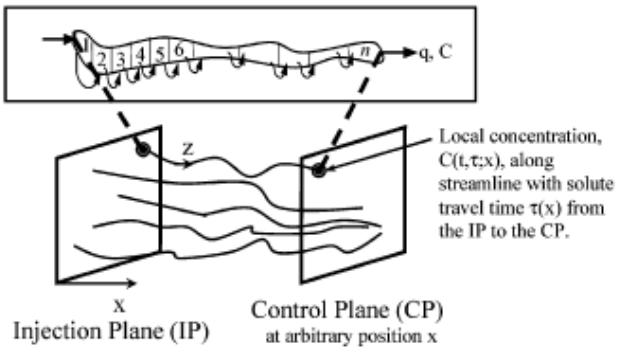


Figure 1-2. Solute transport scheme along flow paths defined for a streamline approach (reproduced from *Malmström et al., 2004*).

## 1.2 The Importance of Travel Time in Watersheds

The diversity of flow paths available to rainfall infiltrating at different locations in the watershed to reach the receiving stream, defines a distribution of travel times (*Kirchner et al., 2000*). A watershed's travel time distribution has become a fundamental watershed metric that can provide information on storage, flow pathways and source of water (*McGuire & McDonnell, 2006*). Hence, the determination of travel time distributions (TTDs) has been the focus of research studies since the mid-1970's (*Przewlocki and Yurtsever, 1974*). Travel time distributions started being developed to provide a quantitative interpretation of environmental radioisotope data in groundwater systems for the transport of water and solutes *(Maloszewski & Zuber, 1982*). In these initial efforts, groundwater age data were fitted to lumped-parameter models following linear, exponential, or gamma distribution functions (*Busenberg & Plummer, 1992*), which were later adopted in stable isotope analysis of surficial hydrology (*Soulsby et al., 2000*).

The application of TTD approaches in the field of surficial hydrology has led to recent advances in the understanding of watershed hydrology, specifically by providing a theoretical basis for i) explaining the power-law behavior of biogeochemical lag times and groundwater mixing patterns (*Kirchner et al., 2000*), ii) the age composition of stream water associated with storm events (*McDonnell et al., 2010*), iii) the conceptualization of hydrological functioning to investigate runoff generation processes by the adequate

description of flow paths and base flow contributions (*Turner et al., 1987*; *Uhlenbrook & Leibundgut, 2002*; *Uhlenbrook et al., 2002*), and iv) the nonlinear (threshold-type) connectivity among landscape reservoirs and their interaction with water age distributions under transient hydrological conditions (*McDonnell, 2003*; *Soulsby et al., 2009*; *McNamara et al., 2011*; *Soulsby et al., 2015*). Calibration and validation of TTDs typically rely on daily and sub-daily isotope databases collected over multiple years to evaluate the fluxes among landscape water storage units that can be used to constrain process-based modeling (*Soulsby et al., 2015*). Several modeling approaches can be conditioned with this information. Predictive subsurface TTD models range from lumped to semi-distributed (with hydrologic response units) to fully distributed spatial representations of the hydrological system (*Birkel & Soulsby, 2015*). Tracer-aided conceptual modeling, in surficial hydrology, also benefited from the use of isotope analyses, in explaining the distinction between the celerity of pressure waves and the pore velocity of water, initially derived by Beven (*1982*), which affect the hydraulic response and the transit time, respectively (*Birkel & Soulsby, 2015*).

Travel time distributions can also yield important information on how contaminant solutes are stored and released from a watershed (*McGuire & McDonnell, 2006*). They have also been used to characterize transport processes at contaminated sites (*Dagan & Nguyen, 1989*; *Cvetkovic and Dagan, 1994*; *Malmström et al., 2004*) applying a Lagrangian approach, and at the watershed scale (*Rinaldo & Marani, 1987*; *Haitjema, 1995*; *McDonnell et al., 2010*; *Botter et al., 2011*) as part of framework methods that include water balance, stochastic, and mass transfer functions. The transit time of a pollutant in a watershed is linked to the extent that it is retained, removed, and/or transformed in the subsurface as a result of geochemical and biogeochemical processes (*Haitjema, 1995*). The temporal and spatial variations of these transformations can also affect the stochastic solute response imprinted in a watershed TTD. The effect of these pollutant transformations is relevant when analyzing watershed TTDs.

The physical or biogeochemical processes that affect a given pollutant may be either ubiquitous or spatially distributed. The outcome of transformations that require specific conditions to occur in the watershed will be the subject of damping as a result of mixing

with solute contributions from areas where those transformations do not occur. The proximity of a point source contamination to a waterbody controls both its attenuation by biogeochemical processes and its contribution to the overall hydrochemical signature of the watershed, because long travel times imply greater contact times for these transformation processes to occur. For nonpoint contamination, on the other hand, the spatial distribution of favorable conditions within the different landscape units controls contaminant attenuation and the overall hydrochemical signature of the watershed. The solute residence distribution in the watershed, then, is controlled by the input function describing the supply of the solutes to the groundwater flow system, the prior concentrations in the landscape reservoirs, and the water residence time distribution of the watershed (*Botter et al., 2005*). The retention of solutes in watersheds has been evidenced in several studies (*Boyer et al., 2002*; *van Breemen, 2002*) leading to the development of the concepts of biogeochemical lag time and solute legacy (*Hamilton, 2012*; *Van Meter & Basu, 2015*; *Van Meter et al., 2016*). These concepts are gaining in recognition because of persistent water quality problems even after pollutant reduction strategies have been put in place.

## 1.3 Existing Analytical TTDs

Several approaches have been developed to derive formulations for analytical travel time PDFs. A Lagrangian approach has frequently been combined with either the 1-D mass balance transport equation (*Soltani & Cvetkovic, 2013*), the 1-D transient groundwater flow equation (*Cornaton, 2012*), or a watershed-scale, flow mass balance (*Botter et al., 2011*). For the Lagrangian approach, the development of a travel time theory for solute transport was initiated for spatially stationary and temporally steady conditions (*Shapiro & Cvetkovic, 1988*; *Dagan and Nguyen, 1989*; *Neuman, 1993*). It was not until the work of Indelman and Rubin (*1996*) that, a nonstationary velocity field defined by a linear trend in the mean logarithmic conductivity field was incorporated into a Lagrangian theory for nonreactive solutes. An analytical solution for the case of quasi-unidirectional mean flows was also provided by Indelman and Rubin (*1996*). Their theory is based on resident concentrations in terms of particle displacement moments. Zhang et al. (*2000*) developed, instead, a solute flux

approach in terms of statistic moments of travel time and transverse displacement, which corresponds to a more general case of nonstationary flow. However, no analytical solution was incorporated as part of their work. A brief description is presented in the next sections, for those options that were considered most pertinent to this study.

### 1.3.1 Haitjema's Analytical Expression

A method for the analytical estimate of the watershed TTD was developed by Haitjema (*1995*), for a steady-state, two-dimensional groundwater. This analytical expression was derived by assuming: i) a Dupuit-Forchheimer groundwater flow condition (i.e., constant hydraulic gradient along the vertical dimension), and ii) the ratio (porosity*saturated aquifer thickness)/(aquifer recharge rate) (θH/r) is constant over the entire groundwater system (*Haitjema, 1995*). The resulting equation indicates that the advection process and discharge conditions follow an exponential function as the basis of the residence time distribution, rather than mixing in the groundwater system (*Leray et al., 2016*). The equation is given by:

$$F(t) = 1 - exp\left(-\frac{tr}{\theta H}\right) \qquad \text{Eq. 1.1}$$

Note that the resulting cumulative distribution function F(t) of travel times does not depend on the following watershed characteristics: size, shape, drainage network, or hydraulic conductivity. Equation (1.1) was derived by applying a water balance around the isochrone area, delineated by a water residence time T, of a completely homogeneous groundwatershed, in which the groundwater flow velocity remains constant, as long as the other variables of the θH/r ratio are constant. In a further evaluation of this expression, Leray et al. (*2016*) found that it can be applied to any type of fully or partially-penetrating outlet: discharge to a stream or to a pumping well, as long as these outlets capture all the flow lines (*Luther & Haitjema, 1998*).

In the above expression, the effect of dispersion is neglected and recharged water is conveyed, and eventually discharged following an exponential TTD. The recharged water is stored at every time step assigning an inception time (i.e., age) to each mass of recharged

water, which is then sampled uniformly by the outlet representing the age distribution of the aquifer (*Harman, 2015*).

### 1.3.2 Cornaton's Analytical Expression

Similar to Haitjema (*1995*), the expression derived by Cornaton (*2012*), who built on the work of Ginn (*1999*) on exposure time in the subsurface and of Delhez and Deleersnijder (*2002*) on oceanic circulations and surface water bodies, is based on a Gaussian-type initial age (τ) distribution ($g(x,\tau)$) in a uniform velocity field. This age distribution is assumed to be the solution to the one-dimensional advection-dispersion equation, where the concentration of non-reactive solutes is approximated by the age distribution resulting in the expression:

$$\frac{\partial g}{\partial t} = -v\frac{\partial g}{\partial x} + D\frac{\partial^2 g}{\partial x^2} - \frac{\partial g}{\partial \tau} \qquad \text{Eq. 1.2}$$

For the solution to this equation and its initial and boundary conditions, Cornaton (*2012*) first applied a Laplace transform using the age ($\tau$) dimension, and a second Laplace transform using the chronological time ($t$) dimension. The resulting expression includes $s$ and $r$ as the complex Laplace variables, for which the system is resolved by Cornaton (*2012*) in the Laplace domain ($\tilde{g}(x,r,s)$). The final expression for the age distribution ($\tau$) recovers the chronological time ($t$) term by applying the inverse Laplace transform to $\tilde{g}(x,r,s)$, obtaining $\hat{g}(x,t,s)$ (see equations A10 and A11 in Cornaton, (*2012*)).

The approach used in this thesis follows that of Soltani & Cvetkovic (*2013*) (see section 2.2.1). In contrast to Cornaton (*2012*) who derived an analytical solution directly from Eq. 1.2, Soltani & Cvetkovic (*2013*) applied the analytical solution of the 1-D advection-dispersion equation for the resident concentration ($C$ for $g$) derived by Bischoff (*1964*). Another difference is that Soltani & Cvetkovic (*2013*) departed from a Lagrangian framework where for conservative solutes $C$ is approximated by the PDF of particle position $p(x;t)$ instead of using $g(x,\tau)$. Later in their derivation, Soltani & Cvetkovic (*2013*) obtained the water age distribution (that is, the sought-after state variable), from $p(x;t)$.

In order to test the performance of his analytical solution, Cornaton (*2012*) applied it to a reference problem consisting of a finite domain length L = 200 m, with a longitudinal dispersivity $\alpha_L$ = 2 m, and an initial, steady-state age distribution $g(x,t,\tau)$. This steady-state age distribution is the result of maintaining a uniform and constant velocity $Uo$ = 1 m/d in the 1-D groundwater flow model. These steady state conditions are then modified by imposing, at $t$ >=0, a constant flow velocity two times lower, i.e., $Uo$ = 0.5 m/d. For the purpose of comparing the Soltani & Cvetkovic (*2013*) expression with Cornaton (*2012*)'s, this reference problem, which shares great similarities with the conditions used in this thesis, was reproduced with the Soltani & Cvetkovic (*2013*) expression (Figure 1-3). In this figure, the breakthrough curve of the age distribution after 50 days of the change in flow velocity is the last one that remains unaltered (dashed blue line). At time t=350 days, the new velocity condition completely flushes out the former age distribution, and replaces it with an older mean age. The Soltani & Cvetkovic (*2013*) estimates of travel time exhibit a short delay with respect to those from the Cornaton (*2012*)'s expression, but an overall good match. This delay may reflect the mathematical approximation used in MATLAB to compute the complementary error function required by the expression.

Considering the complexity of the Cornaton (*2012*)'s expression in the Laplace transform and the good match achieved in the reference problem (Figure 1-3), the Soltani & Cvetkovic (*2013*) expression was selected to be used in this thesis.

## 1.4 The Influence of Landscape in MTT

The relationship between landscape characteristics and watershed's mean travel time (MTT) has been explored for the past 30 years (*Pearce et al., 1986*; *Stewart & McDonnell, 1991*, *Wolock et al., 1997*). This quest has been recently motivated by resetting research goals towards obtaining a better understanding of hydrological functioning in watersheds with the use of less deterministic approaches (*Dooge, 1986*; *McDonnell et al., 2007*; *Soulsby & Tetzlaff, 2008*). In addition to this quest, the initiative of developing generalizable hydrological theories and more flexible model approaches to be applied in ungauged basins (Prediction in Ungauged Basins, PUB; *Sivapalan, 2003*a) has also contributed to recent research efforts (see *Hrachowitz*

*et al., 2013*). These studies have investigated the influence of terrain slope (*McGuire et al., 2005*; *Tetzlaff et al., 2009a, 2009b*), soil type (*Tetzlaff et al., 2009a, 2009b*), watershed size

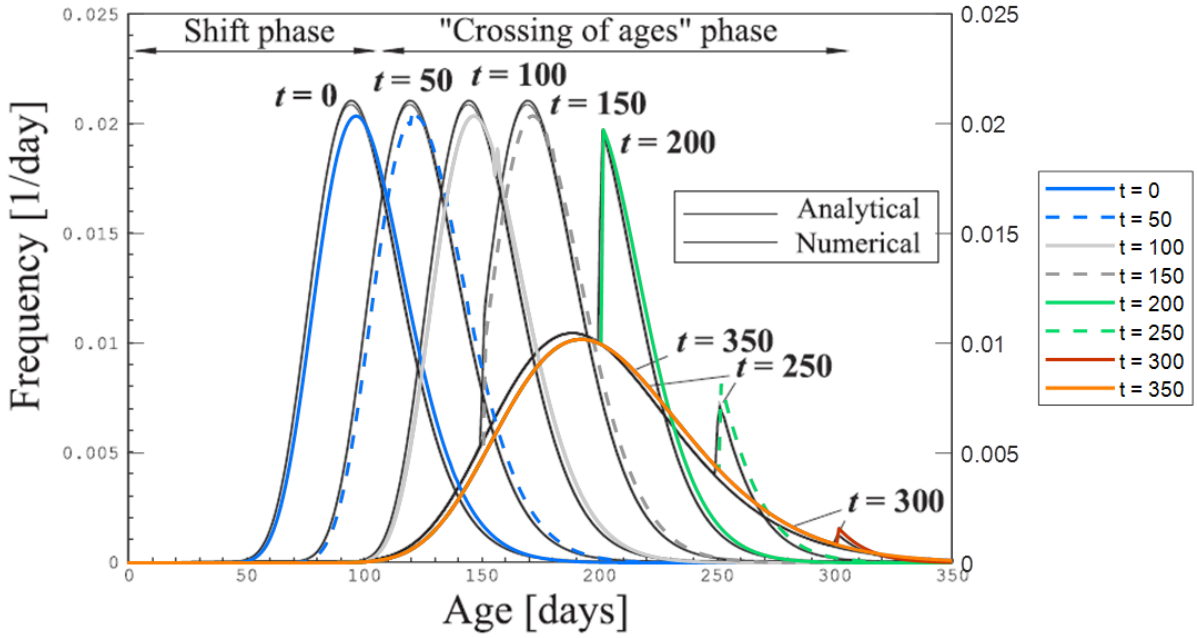


Figure 1-3. Reference problem used by Cornaton (2012) is reproduced using the Soltani & Cvetkovic (*2013*) TTD expression for a 1-D, 200 m model domain with uniform and constant velocity *Uo* = 1 m/d being flushed with a slower velocity *Uo* = 0.5 m/d starting at t=0. Compared with Figure 3a in Cornaton (*2012*) copied here as background.

(*McGlynn et al., 2003*; *Hrachowitz et al., 2010*), and aspect (*Broxton et al., 2009*) on water transit times in watersheds. A summary of these findings is presented in section 3.1. One characteristic common to these findings is that they were obtained primarily for montane watersheds, with shallow aquifers and bedrock surfaces yielding MTT values ranging from months to a few years (<4 years). These MTT estimates were mostly validated with tracer-aided (e.g. chloride, stable isotopes) models and in some cases from inter-watershed comparison studies (*Tetzlaff et al., 2009a, 2009b*; *Hrachowitz et al., 2009*). The study by Tetzlaff et al. (*2009a*) focused on finding these relationships in watersheds from different geomorphic regions, whereas the studies by Tetzlaff et al. (*2009b*) and Hrachowitz et al.

(*2009*) used watersheds located in the same geomorphic regions in Scotland. Hrachowitz et al. (*2009*) provided more regional variability within the same province and developed a regression model for the prediction of MTT (days) based on landscape characteristics:

$$\log(\mathrm{MTT}) = -0.72\,\mathrm{RSC} - 1.04\log(\mathrm{DD}) - 0.09\,\mathrm{PI} - 0.22\,\mathrm{TWImed} + 5.37 \qquad \text{Eq. 1.3}$$

where RSC is the proportion of responsive soil cover (i.e., poorly drained soils), DD is the drainage density, PI is the mean annual precipitation intensity (mm/day), and $\mathrm{TWI}_{\mathrm{med}}$ is the median topographic wetness index. This expression was the result of analyzing 20 study watersheds with a drainage area ranging from 0.3 to 35 km², in mostly steep, montane settings. A similar analysis is presented in this thesis but for watersheds with both steep and more subdued topography, and most importantly, with both deeper aquifers and larger watersheds that could potentially yield MTT values in the tens to hundreds of years.

## 1.5 Nitrogen Isotope Models

The simulation of nonpoint nutrient pollution at watershed scale has been performed using different approaches, including lumped conceptual type models such as GLEAMS (*Leonard et al., 1987*) or CREAMS (*Knisel & Williams, 1995*) to 1-D physically based models such as RZWQM (*DeCoursey et al., 1992*), and DAISY (*Hansen et al., 1991*). When considering hydrological partitioning in the determination of nitrogen (N) fluxes, the numerical process-based model DAYCENT estimates these fluxes in a daily time-step for 1-D modeling (*Del Grosso et al., 2001*). In order to extend the 1-D simulation of DAISY and DAYCENT of N export for the entire watershed, these models have been linked to watershed models like MIKE-SHE (*Styczen & Storm, 1993*; *Refsgaard et al., 1999*; *Boegh et al., 2004*) and SWAT (*Li et al., 2004*), respectively.

The discrimination of the $^{15}$N isotope in various steps of the N cycle in natural systems provides the means to identify the mechanisms that control the transformation and losses of N both in the soils and in the subsurface. However, there have been relatively few attempts to develop models for N isotopes in these environments. One of these N isotope models consisted of adapting DAYCENT with natural N isotope mass balance principles to quantify

the flux of gaseous N emissions from tropical rain forests (*Bai & Houlton, 2009*). Bai & Houlton (*2009*) applied their model to 6 different locations in Hawaii following an annual precipitation gradient. Mary et al. (*1998*) developed the compartmental model FLUAZ to calculate gross N transformation rates in the soil-plant system for experiments using the $^{15}N$ tracing technique, and applying a nonlinear least square algorithm to estimate reaction rates. However, FLUAZ is not driven by the hydrological partitioning occurring in the soil-plant system but only by concentration gradients and has been exclusively implemented to $^{15}N$ tracing experiment data. This model was later updated by Müller et al. (*2004, 2007*) with more reactions and with a Monte Carlo simulation approach to deal with the estimation of a greater number of transformation rates.

## 1.6 Thesis Objectives and Structure

The main goal of this thesis is the development and testing of a methodology for the determination of the age distribution of groundwater particles and the corresponding mean travel time using a 1-D analytical expression applied at the watershed scale. This methodology provides the necessary tools for the implementation the analytical methodology across watersheds based on landscape characteristics. These tools include: selection criteria to predict the quality of performance of the analytical method in a given watershed, estimation of analytical method parameters for future analytical model development for the estimation of particle TTDs and watershed's MTT (wMTT), and a direct estimation of the wMTT based on geomorphological features. This methodology was applied to three watersheds for method verification. A hydrologically linked N isotope model is further developed to couple transformation processes with the groundwater TTD.

To accomplish the above, the 1-D analytical expression developed by Soltani and Cvetkovic (*2013*) for travel time PDF was tested by comparing it against the output from the numerical model FEFLOW (DHI-WASY GmbH) in the form of a breakthrough curve created by the probability of exit field at observation points distributed across the watershed. This comparison entailed a suite of 28 scenarios where different conditions of topography (reduced and actual), subsurface heterogeneity (FGEN generated random

permeability fields), and aquifer depth (actual, deep, shallow) were tested (Chapter 2). These scenarios were simulated using a virtual watershed approach for a watershed that resembles that of Alder Creek (Ontario, Canada). The predictive tools for the analytical model implementation were developed after applying the methodology to another eight watersheds in North America. The geomorphological features of these watersheds were used as predictors in the regression tools to be used for the future implementation of the methodology in other watersheds (Chapter 3). The analytical model is linked to an existing hydrological model (RAVEN) developed for one of these watersheds (Carroll Creek) to ultimately obtain a watershed scale N isotope model that will be able to reproduce observed N concentrations and isotopic compositions (Chapter 4).

The methodology introduced in this thesis is meant to be applied as a first approach to constrain subsurface travel times in ungauged watersheds. These initial estimations can then be later challenged or verified as new hydro(geo)logical information and data become available. The implementation of our analytical methodology may also become advantageous in situations where, in addition to the lack of subsurface information, deterministic models face a problem of scale.

In Chapter 5, the major conclusions from the overall research work are presented, together with the future work that is needed to constrain and complement the methodology outlined here. A brief discussion on how the methodology and the empirical relationships developed in this study can be both transferred and scaled-up to other watersheds, but also they can be further enriched with future implementations. Most importantly, the proposed analytical method relies on readily available tools (i.e., GIS and MATLAB) and is therefore easily implemented when limited observational data on the subsurface hydrology are available.

# Chapter 2

# Analytical Method to Estimate MTT and TTD for Groundwater at a Watershed Scale


## Summary

Modeling of groundwater transport at the watershed scale often focuses on fully addressing water fluxes leaving chemical reactions to a secondary role due to compromises related to computational efficiency. Mean travel time (MTT) and travel time distributions (TTDs) have become parameters commonly used to quantify watershed solute transport response in surface hydrology, but their use in subsurface hydrology is rather limited. The uniqueness concept of a watershed, typically referring to its landscape heterogeneity, fails to recognize the macroscale landscape components that control the distribution of travel times. Here, we develop a method using a one-dimensional analytical equation that provides single particle median travel time (pMTT, and its distribution), and the entire-watershed MTT (wMTT), through the use of simple and ubiquitous tools (e.g. GIS and MATLAB). Results are compared against a three-dimensional subsurface numerical model of a virtual watershed for multiple scenarios (n=28) that include changes in surface topography, subsurface geostatistical heterogeneity, and aquifer depth. When comparing results for pMTT, the goodness of fit between the numerical and analytical methods yields, on average, $r^2$=0.50 ± 0.07, with the lowest value of 0.34 for the deep aquifer scenario (DH) and the highest at 0.58 for one of the reduced topography scenarios. For subsets of scenarios defined by the size of imposed heterogeneity and topography, the analytical wMTT explains the variability of the numerical wMTT estimates from 71% to as high as 94%. A detailed flow path analysis showed that the method employed for the delineation of the flow paths in the analytical method, in some locations, fails to intercept adjacent streams, resulting in longer travel times. This modifies the TTD of the watershed by reducing its skewness to the right. The calibrated velocities ($U_o$) used for the analytical method were positively correlated to the imposed heterogeneity and surface topography, and negatively correlated to aquifer depth.

Some observations indicate that surface topography may exert similar effects on wMTT as the depth to bedrock. Even though our findings on topography and aquifer depth are limited to few settings, the application of this methodology to a wider range of watersheds can help establishing these relationships. The transferability of these relationships to similar ungauged watersheds is important to better understand watershed functioning. The analytical method can be a promising alternative to a numerical method in situations where quick analyses are needed, limited background information is available, and computational efficiency is a constraint.

## 2.1 Introduction

The dispersion of pollutant-bearing groundwater in aquifers and its manifestation in stream chemistry has been quantified using groundwater age as a measure of watershed response by applying field techniques (*Böhlke and Denver, 1995*; *Böhlke et al., 2007*) and numerical models (*Green et al., 2010*). Travel time distributions (TTD) have been proposed as a tool to understand the major hydrological controls at a watershed scale and identify patterns in stream chemistry from both anthropogenic pressures in managed watershed and geomorphological features in ungauged watersheds (*McGuire et al., 2005*; *McDonnell et al., 2007*). Mean travel times (MTTs) can be controlled by many aspects of the landscape structure (*Hrachowitz et al., 2010*).

The concept of a watershed mean travel time (wMTT) has been recognized as an important indicator of the water cycling processes that are taking place in relatively shallow subsurface layers of hillslope environments with respect to water resources renewability, degree of mixing, storage, connectivity (of the different units in the landscape), and discharge (*Soulsby and Tetzlaff, 2008*; *Hrachowitz et al., 2010*; *Soulsby et al., 2011*). In these hillslope studies, soil horizons are included as part of the contributing drainage area to stream flows, but they are shallow compared to watersheds with aquifers of tens of meters deep. Experimental techniques have been used to estimate travel times at different scales. At the watershed scale, MTTs have been estimated experimentally by using stable isotope techniques of the water molecule based on differences in rain and stream signatures, mostly

in upland watershed studies *(Kendall, 1998*; *McGuire et al., 2005*; *Rodgers et al., 2005*). These study areas are characterized by shallow soils and underlying bedrock. Resulting wMTTs ranged from months to few years, as typically the bedrock contribution is neglected. In these environmental settings, tracer analysis including isotopic signatures has allowed assessing potential flow paths and sources in hillslope hydrology (*Uhlenbrook & Leibundgut, 2002*; *Soulsby et al., 2004*; *Rodgers et al., 2005*; *Soulsby et al., 2011*).

The attenuation of rainfall signatures observed in streams, which is characteristic of stable isotopes, is also exhibited by chloride concentrations (*Kirchner et al., 2000*; *Soulsby and Tetzlaff, 2008*). This frequently monitored parameter (Cl) allowed extending the chemical damping analysis to very long rain and stream chemistry databases, resulting in travel time distributions characterized by a long-tail and a power-law shape (*Kirchner et al., 2000*). This behavior indicates that the watershed is acting as a fractal filter with respect to the input signal, by smoothing it into the observed stream chemistry at timescales from days to a few months. However, for streams located at Plynlimon, Wales, at the multi-annual timescale their spectral power coincides, thus reducing their spectral differences, suggesting that upland watersheds store the rainwater chemical pattern at this timescale (*Kirchner et al., 2001*; *Lindgren et al., 2004*). The reasons behind this fractal behavior were attributed to aquifer heterogeneity (*Kirchner et al., 2001*; *Lindgren et al., 2004*).

Kirchner et al. (*2001*) applied a 1-D advection dispersion model to yield a travel time distribution for a hillslope. They fitted it to match the power spectrum of observed $Cl^-$ concentration spectra and that of a gamma distribution that best matched it in their previous work (*Kirchner et al., 2000*). The result was a model that required high values of macrodispersion, of about half that of the flow path length, so that the Peclet numbers, estimated as $vL/2D$ ($v$, flow path mean velocity; $L$: flow path length, and $D$: macrodispersion coefficient), vary between 0.1 and 1.0. The high values of macrodispersion are related to the long-tailed behavior in travel time distributions. The fractal nature of watersheds was subsequently verified by incorporating more subsurface hydrology components with a numerical modeling approach (*Lindgren et al., 2004*; *Kollet and Maxwell, 2008*). Kollet and

Maxwell (*2008*) used a fully integrated subsurface model to test the fractal scaling behavior in base flow travel time distributions. Land surface and variably unsaturated flow processes were included in the vadose zone in a 3-D numerical model for the Little Washita watershed (Oklahoma, USA). Travel time distributions were generated from backward-in-time particle tracking using a Lagrangian scheme for water particles departing from the riverbed back to their points of origin in the watershed. They confirmed both the fractal behavior and the power law shape of the base flow travel time distributions. With the estimated travel times of the particles at both the water table and land surface, the respective distributions were compared revealing the influence in travel time distributions and power spectra due to the processes occurring in the unsaturated zone. This influence was deemed significant but limited to approximately 1 year of arrival time to the river bed, indicating that the vadose zones of areas closer the river are the most influential.

The fractal nature of watersheds has transcended spatial scales (*Kirchner and Neal, 2013*) and its applicability has extended to the interaction with other hydrologic components in the watershed (*Kollet and Maxwell, 2008*; *Wörman et al., 2007*; *Schilling and Zhang, 2012*). Similarly, the identification of the major controls on travel time distribution at the watershed scale focuses on the components of the landscape that are common to any watershed, in order to assess their transferability (*McDonnell, 2003*; *McDonnell et al., 2007*; *Tetzlaff et al., 2009a*). Studies have evaluated the effects of surface topography (*McGuire et al., 2005*; *Cardenas, 2007*; *Tetzlaff et al., 2009b*), watershed size (*Wolock et al., 1997*; *Wörman et al., 2007*; *McGlynn et al., 2004*; *Tetzlaff et al., 2009b*; *Darracq et al., 2010*; *Hrachowitz et al., 2010*), bedrock topography (*Freer et al., 2002*; *Wörman et al., 2007*), and soil cover (*Tetzlaff et al., 2009b*; *Rodgers et al., 2005*) on predicting wMTTs. Most of these studies use tracer approaches in upland watersheds, and numerical modeling in a few of them (*Worman et al., 2007*; *Kollet & Maxwell, 2008*). In general, it has been found that mean slope and percent of responsive soils (low permeability) controls the watershed response to transport regarding travel times. The size of the watershed is not a major controlling factor; whereas the stream density tends to correlate with wMTTs. Worman et al. (*2007*) indicates that subsurface flow is controlled to some extent, at any point in the watershed and at any watershed scale, by small-scale

topographic features. This effect is proportional to the size of these surface features and decays rapidly with depth. With the exception of Worman et al. (*2007*), and contrary to surface hydrology studies, the effects of topography, soil type, and watershed size have not been established in subsurface hydrology.

The travel time distributions for single water particles in a watershed can be defined based on either their point of entry or their point of discharge into a stream (*Botter et al., 2011*). The first distribution keeps track of the particle's original chemical characteristics to deliver the solute into the stream chemistry at a point and travel time, dictated by its own flow path. The second distribution is defined by looking at the stream chemistry and its connection with the watershed's past chemical inputs. It corresponds to the travel times provided by tracer analysis and the backward-in-time particle approach (*Botter et al., 2011*) used by Kollet and Maxwell (*2008*), in which convection and dispersion effects are included. When steady state conditions apply, both types of travel time distributions coincide. There are several methods to identify travel time distributions for single particles or for the entire watershed that incorporate the flow partitioning at the ground surface (*Fiori and Russo, 2008*; *Rinaldo et al., 2011*; *Botter et al., 2011*). However, their application to real watersheds has been limited (*van der Velde et al., 2010*).

The determination of groundwater age has been resolved numerically and has been implemented in several numerical models (HGS, *Therrien and Sudicky, 1996;* ParFlow, *Ashby and Falgout, 1996;* and FEFLOW, DHI-WASY, GmbH). Analytical methods have also been developed for the mean travel time cumulative distribution function for two dimensional groundwater flow (*Haitjema, 1995*), and the one-dimensional particle travel time problem (*Cornaton, 2012*; *Soltani & Cvetkovic, 2013*). Haitjema (*1995*) derived an analytical equation that depends on porosity, saturated aquifer thickness, and recharge rate, and relies on the assumption of Dupuit-Forchheimer flow. Haitjema's analysis is based on establishing a water balance around areal isochrones within the groundwatershed, thereby yielding an equation that is independent of the hydraulic conductivity, groundwater size and shape, and stream network structure (*Haitjema, 1995*). The one-dimensional analytical methods

offer the possibility to decouple flow from transport so that the complexities associated with the steady and unsteady transit of water particles through the watershed can be simplified, and more focus can be given to the biogeochemical transformations. These analytical equations, however, have not been tested and compared for a variety of subsurface conditions.

Here, we use the 1-D analytical equation developed by Soltani and Cvetkovic (*2013*) to obtain travel time distributions for particles departing from the potentiometric surface and moving towards their point of discharge, and calculate their wMTT and TTD for the entire watershed. The wMTT and TTDs estimated by the analytical method are compared to results of a numerical model that uses a backward adjoint model to define the breakthrough curve for travel time. A virtual watershed is used that resembles the Alder Creek watershed in Ontario (Canada), which has been the topic of many studies (summarized in *Frind et al., 2014*). Multiple scenarios (n=28) were simulated in this virtual watershed including changes in topography (two types: reduced and actual topography), geostatistically modelled heterogeneity (included in 24 scenarios), and aquifer depth (in 4 homogeneous scenarios). The layout of scenarios was designed to gain understanding of the relative effects subsurface heterogeneity, topography, and subsurface geometry may exert on subsurface wMTT and TTD at the watershed scale. This study is the first step in applying a 1-D travel time analytical equation to a 3-D watershed scale problem in order to provide a quick tool for the estimation of wMTT and its distribution in ungauged watersheds.

## 2.2 Analytical Equation for Travel Time

### 2.2.1 Soltani and Cvetkovic Equation

In this study, the analytical approach developed by Soltani and Cvetkovic (*2013*) is used to generate travel time probability density functions (PDFs) along 1-D flow paths distributed across the watershed. Some generalities of their equation are discussed here but for more details on its development and verification we refer to the original publication. The equation was derived from the solution of the 1-D ADE equation that incorporates a Fickian

macrodispersivity term ($\lambda_L$) and a convective term defined by $U(t)$, which corresponds to the flow field velocity assumed to be relatively uniform in space ($x$):

$$\frac{\partial C}{\partial t} + U(t)\frac{\partial C}{\partial x} = \lambda_L U(t)\frac{\partial^2 C}{\partial x^2} \qquad \text{Eq. 2.1}$$

where $C$ is the concentration of a conservative solute; and $x$, is the distance along the flow path running parallel to the velocity field ($U$). A Lagrangian framework is applied to the solution of this equation by making the behavior of a non-reactive solute concentration (C) equivalent to the particle position ($x$)'s PDF at any time $t$, $p(x,t)$. The final solution is then obtained for the forward model in the form of a cumulative density function (CDF), according to:

$$F_f(t;x) = \frac{1}{2} erfc\left(\frac{x - U_0\varphi(t)}{\sqrt{4\lambda_L U_0 \varphi(t)}}\right) \qquad \text{Eq. 2.2}$$

where $U_0$ is the mean velocity field; $\varphi(t)$ is a dimensionless function that depends on time and applied to $U_0$ make the analytical equation suitable to transient flow applications: $U(t) = U_o\varphi(t)$. For this study, a stationary flow field is used, i.e., $\varphi(t)$=1.

Soltani and Cvetkovic (*2013*) tested the results of the above equation against another analytical equation developed by Cornaton (*2012*) derived from a water age density that is a more general approach. The validation was satisfactory against Monte Carlo trajectory simulations, which were generated by randomizing the spatial component of intrinsic permeability, $\kappa(x)$, of the spatio – temporal velocity term, $v(x,t) = U_o\kappa(x)\varphi(t)$, with a normally distributed function ($Y(x)$) of heterogeneity and a negative-exponential structure, $\kappa(x) = exp[Y(x)]$ for $\sigma_Y^2 = Var(Ln\ K) = 0.8$ and correlation length ($I_Y$) of 50 m. Fixed values of macrodispersion ($\lambda_L \sim \sigma_Y^2 I_Y$) and uniform velocity ($= U_O \exp(-\sigma_Y^2/2)$ were applied to the analytical equation to match those used in the trajectory simulations. A similar approach is adopted in the present study by using the one-dimensional analytical formulation but applying it to a three-dimensional virtual watershed in which the subsurface has been modified to create hydraulic conductivity fields with known degrees of heterogeneity. The

challenge of the analytical methodology presented here is to identify the most suitable uniform velocity and changes in macrodispersion with flow path distance.

### 2.2.2 Travel Time PDFs from Analytical Approach

The forward (or backward) model version of the analytical equation developed by Soltani and Cvetkovic (*2013*) is applied to water particles across the watershed at locations that coincide with the observation points used in the numerical modeling, in order to allow for comparisons of the results. The analytical equation relies on three main parameters for each water particle flow path: a constant mean flow velocity (*Uo [L/T]*), a characteristic flow path distance (*x [L]*) and a constant macrodispersion ($\lambda_L$ *[L]*). An evenly spaced-grid of 200 meters by 200 meters was used to distribute the water particles across the watershed. ArcNLET, a GIS application developed by Rios et al. (*2013*), incorporates a particle tracking protocol based on groundwater flow direction and magnitude vectors. These vectors are estimated using a two-dimensional Dupuit-Forchheimer assumption, which uses the ground surface elevation as proxy to delineate the water table elevation map, and maps of vertically homogeneous hydraulic conductivity and porosity. These maps ultimately allow the estimation of direction and the magnitude of flow, in the form of informal-gridded raster data. The method provides the means to control how similar the water table elevation is to the overlying topography, via a smoothness factor (*SF*). The higher this value is the more independent the water table is from topography. This parameter dictates where locally recharged groundwater will discharge, either into an adjacent river or into a farther surface water feature through a deeper and longer flow path. A digital elevation model of 100-m cell-size was used for the tracking as it smoothed out even more the surface features. A horizontally homogeneous map of hydraulic conductivity and porosity ($\eta$), with the values of 6.5 x $10^{-5}$ m/s and 0.33, respectively, were used in the particle tracking. The GIS application yields the flow path distance ($x$) for each observation point.

The bulk velocity of each water particle was initially calculated as the bulk Darcy velocity $K \cdot dh/x$ using the flow paths from ArcNLET's particle tracking ($x$) and the digital elevation map (DEM) for the actual topography. The macrodispersion was initially assumed to be

10% of the total flow path distance ($x$): $\lambda_L = 0.10 \cdot x$. With these three parameters an ensemble of travel time CDF curves was initially obtained one for each distributed water particle, and after applying the derivative to these curves, a uncalibrated set of travel time PDFs were generated. As suggested by Soltani and Cvetkovic (*2013*), in developing the analytical equation, a uniform velocity field was applied to the ensemble of streamlines. Even though a transient velocity field in time could be applied to the formulation, the velocity does not vary spatially from streamline to streamline to match the limitation of the numerical model of travel time estimation under stationary conditions.

The median of the travel time CDF was chosen as the statistic of comparison of travel time as this variable is skewed towards the longer travel times. Generally in this type of distributions, the statistics are located from left to right in the order: mode (at peak), median (at 50% of CDF), and mean. Median and mean tend to be close to each other in a PDF with normal macrodispersion; whereas, in a PDF with a long tail, associated with greater macrodispersion, the gap between the median and the mean also increases. For this study, the median of the distribution was chosen to be the most appropriate mean travel time variable.

## 2.3 Travel Time Distribution using the Numerical Model

A number of approaches and conceptualizations have been developed to mathematically characterize groundwater age. One of these relies on treating groundwater age as a random variable that is probabilistically distributed as if it were the concentration of a conservative tracer, using the advection-dispersion-equation (ADE) commonly applied in pollutant transport problems. The approach developed by Cornaton (*2004*) and Cornaton and Perrochet (*2006*), and recently updated in Cornaton (*2014*), has been implemented in subsurface models such as Hydrogeosphere (HGS) and FEFLOW (DHI-WASY GmbH). The equations for life expectancy (E), defined as the time left for a particle before leaving the domain, were derived from the backward adjoint model (*Cornaton, 2004*) and are presented in Appendix A. In the backward-in-time model, used to determine the life expectancy CDF ($g_E$), the boundary conditions (BCs) dictate that only outlets can be assigned a non-zero

mass-transport condition. This Cauchy-type BC is kept constant throughout the simulation, but the zero condition applied elsewhere in the domain will evolve from an initial value of zero yielding $g_E$. However, this $g_E$ does not provide any information regarding whether a given position $x$ in the aquifer does actually make part of the natural drainage basin of a particular outlet. Thereby, an adapted version of the backward-in-time model (*Cornaton, 2014*) that transports the probability of exit ($p_E$) as random variable can be used to identify both the time expected for a water particle anywhere in the domain to exit through one and/or several specified outlets, and the probability value ($0 \leq p_E \leq 1$) of a water particle to exit the domain through one over other outlets. Here $p_E(x, t, \Gamma_{out})$, is the lifetime-expectancy-to-outlet CDF, which defines, for a particular transit time $t$, the probabilistic drainage basin associated with a specific outlet $\Gamma_{out}$ (*Cornaton, 2014*). This problem is similar to that of defining wellfield capture zones where the outlet is the well screen. Here, however, the outlet corresponds to thousands of points spread around the streambed at subsurface-surface water exchange elements identified by a steady state model.

The modified version of the backward-in-time model and its boundary conditions for the probability of exit are:

$$\frac{\partial \theta p_E}{\partial t} = \nabla \cdot \mathbf{q} p_E + \nabla \cdot \theta \mathbf{D} \nabla p_E - q_I p_E \quad in\ \Omega,$$

$$p_E(\boldsymbol{x}, 0) = 0 \quad in \quad \Omega,$$

$$-\theta \mathbf{D} \nabla p_E \cdot \boldsymbol{n} = 0 \quad on \quad \Gamma_0, \qquad \text{Eq. 2-3.}$$

$$[-\mathbf{q} p_E - \theta \mathbf{D} \nabla p_E] \cdot \boldsymbol{n} = -\mathbf{q} \cdot \boldsymbol{n} \quad on \quad \Gamma_{out},$$

$$[-\mathbf{q} p_E - \theta \mathbf{D} \nabla p_E] \cdot \boldsymbol{n} = 0 \quad on \ \Gamma_+ \setminus \Gamma_{out},$$

where $\Omega$, $\Gamma_o$, $\Gamma_+$, $\Gamma_{out}$ represent the entire domain, the domain's impervious boundary, the watershed's subsurface outlet, and the internal outlet system, respectively; $\nabla$ denotes the Nabla operator; $\theta$ is porosity or mobile water content; q is the Darcy flux vector; D is the tensor of macro-dispersion; $n$ is a normal outward unit vector; and $q_I p_E$ is a source term to represent recharge. These equations are similar to the $g_E$ equations (Appendix A), except for

a couple of differences. First, the probability of exit $p_E(x,t)$ converges to unity, as $t$ increases to infinity, matching its maximum value at the outlet $\Gamma_{out}$. Second, it allows creating multiple Cauchy-type BCs to target a specific outlet from all potential outlets of the groundwater system, including wells, springs, surface waterbodies, and interconnection zones between aquifers. It does so by simply assigning $[-\mathbf{q}p_E - \theta\mathbf{D}\nabla p_E]\cdot\boldsymbol{n} = 1$ to the sought outlet(s), which in our case are the exchange flux river bed elements. For those water particles that will not be intercepted by the sought outlet $\Gamma_{out}$, a value of $p_E(\boldsymbol{x},t)$ less than one will be achieved in the CDF's plateau (*Cornaton, 2014*). These equations are valid only when simulating groundwater flow at steady state and running a mass transport problem under transient conditions, where the mass transported, in this case, is $p_E(x,t)$.

### 2.3.1 Setup of the Numerical Model

A virtual watershed approach is used for this study allowing for the evaluation of a specific parameter under multiple imposed conditions. The model domain is based upon that of Alder Creek in Ontario, Canada. Alder Creek is part of the Grand River watershed. It has a total area of 81.2 km$^2$ and comprises mostly agricultural lands, some undisturbed natural vegetation, and urban and rural development. The local aquifer is part of the Waterloo Moraine, a multi-layer aquifer characterized by three till confining units, lying in between glaciofluvial sand, fine sands, and gravel units (*Martin & Frind, 1998*; *Frind et al., 2014*). The footprint outlined by the model boundary (Figure 2-1), is greater in some areas, as dictated by topography to evaluate the analytical approach in adjacent areas to the boundary. In doing so, parts of other watersheds were included in the north and southwest boundary as it was suspected based on topography that they contribute groundwater to the Alder Creek watershed. Additionally, the model domain differs from the real watershed in its elevation as it was shrunk by approximately 60 meters in order to favor conditions for exchange between subsurface and surface water. The shrinking was made by keeping the lowest elevation by the outlet constant as the remaining elevation points in a raster were altered by a reduction factor. The resulting topographic relief was modified to 348.1 meters above sea level (masl) at its highest point and 289.3 masl at its lowest point from 410.5 masl and 289.3

masl, respectively. The reduced topography model increased the exchange flux points by 21% with respect to the actual topography model.

The mesh for the numerical model was created with GridBuilder (*McLaren, 2011*) using an approximated element size of 200 meters. For the first six slices, a vertical separation of 0.25 meters was kept along the entire domain to emulate the pseudo-unsaturated approach selected in FEFLOW version 6.2 (DHI-WASY GmbH, 2015) to model the potentiometric surface and saturated flow at a watershed scale. This approach vertically linearizes unsaturated flow using pressure head and saturation, which compares well with the fully applied Richards' equation if only saturated groundwater flow is sought (*Diersch, 2014*). These linear relationships are determined from relating the actual geometric condition of the element in order to scale balance terms of saturation and pressure head between adjacent element nodes for partially saturated conditions within the element.

The subsurface model was implemented in FEFLOW as an unconfined aquifer with the top slice acting as a phreatic boundary condition. Two different model configurations were created for the simulation scenarios considered in the study: reduced topography and actual topography. The reduced topography model follows the description provided in the previous paragraphs; the actual topography model corresponds to the unmodified topography of the watershed. Three versions of the actual topography model were used, one with the unmodified aquifer geometry (AH), one with a deeper (DH) and one with a shallower (SH) aquifer. The latter two were created by increasing aquifer thickness by 50 m and by reducing aquifer thickness approximately by half that of the actual topography model, respectively. These three model configurations used the actual topography and intend to shed light on the effects of aquifer geometry, further assuming a fully completely homogeneous porous media. These models were built in the same manner as the reduced topography model, with the same number of slices and their vertical separation for the top 1.5 meters of unsaturated soil. For the DH model, the additional 50-meter aquifer thickness was achieved by separating the 6 bottom slices, out of the 32, by 10-meter intervals. The base of the aquifer (bottom slice) for the reduced topography model was created by smoothing

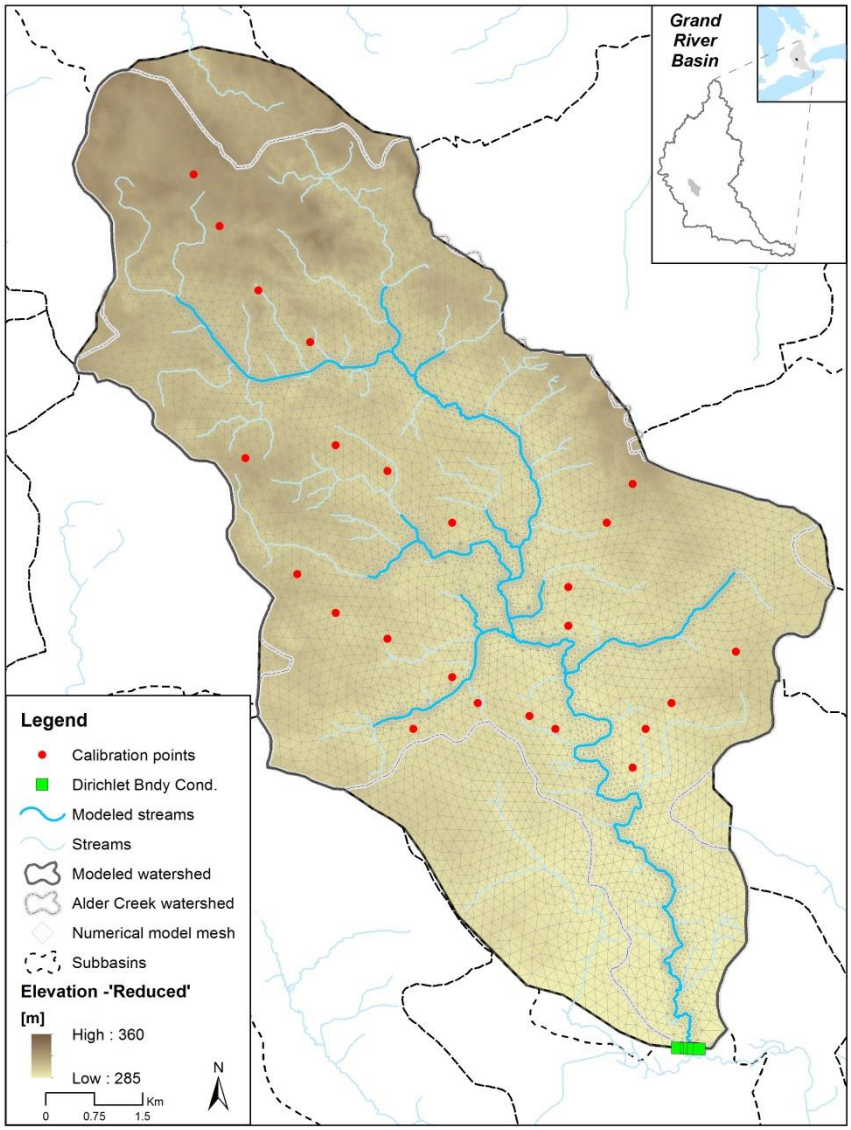


Figure 2-1. Alder Creek watershed map showing the 2D mesh and streams used in the numerical model, along with the reduced topography and the location of calibration points used for the analytical approach. The triangular element grid was created using the GridBuilder (*McLaren, 2011*) code by limiting the size of elements to 200 meters. The elements of the grid around the rivers were then selected for further refinement making a total of 16,371 triangular elements per slice, which were replicated in 32 slices for a grand total of 523,872 elements for the entire model domain. The slices were vertically separated with a maximum of 3.0 meters, and a minimum vertical interval of 0.25 meters applied to the entire domain wherever the dynamic distribution of intervals between slices is constrained by the underlying bedrock.

out its topography after converting a 25-meter cell size DEM to a 600-meter cell size. This conversion was made by resampling the original raster using a bilinear function in ArcGIS. For the aquifer geometry models (i.e., AH, SH, DH), the base of the aquifer was made equivalent to the bedrock surface elevation model available from the Grand River Conservation Authority (GRCA)'s GIS database. The main subsurface model properties for each topographic/domain condition are listed in Table 2-1. Local studies have identified a wide range of groundwater recharge rate estimates from as low as 100 mm/year (*Rudolph, 1985*) to as high as 310 mm/year (*Martin and Frind, 1998*). For this hypothetical study, a value of 237 mm/year ($6.5 \times 10^{-4}$ m/d) was chosen similar to that of Radcliffe (*2000*), who studied in detail the local physical hydrogeology to evaluate the impact of urbanization. For the purpose of this study the material associated with the aquifer properties listed in Table 2-1 correspond to that of clayey sand, and the values of the properties were taken from local studies that included this lithologic category as a result of their modeling calibration effort (*Martin & Frind, 1998*; *Radcliffe, 2000*). Aquifer properties were kept the same for both topographic models, except for the hydraulic conductivity which varied accordingly to the degree of heterogeneity defined for each scenario. Table 2-2 provides a list of the 28 scenarios evaluated in this study and their IDs classified by topography, heterogeneity, and aquifer thickness. This latter set is to get some insight on potential changes in flow path distance with respect to aquifer geometry.

### 2.3.2 Heterogeneity (Numerical Modeling)

The assignment of different levels of heterogeneity to the model domain was performed by generating statistically anisotropic permeability fields on a uniformly distributed grid. This grid is later transposed to the geometry used by the model domain comprised of triangular elements of various planar dimensions and heights. The permeability realizations were generated using the algorithm called FGEN developed by Robin et al. (*1993*). The parameters used in these realizations are presented in Table 2-3.

Table 2-1. Model properties used in simulations and other watershed parameters.

| Property | Value | Unit |
|---|---|---|
| Annual recharge | 237 | mm |
| Hydraulic conductivity ($K_{avg}$) | $6.5 \times 10^{-5}$ | m $s^{-1}$ |
| Specific storage ($S_s$) | $1.3 \times 10^{-4}$ | $m^{-1}$ |
| Porosity (θ) | 0.33 | -- |
| Hydraulic head (Dirichlet BC) | 282.0 | masl[1] |
| Slices | 32 | 32 |
| *Reduced Topography* [2] | | |
| Elevation range (top slice) | 289.3 - 348.1 | masl |
| Elevation range (bottom slice) | 236.7 - 263.5 | masl |
| Aquifer thickness (min - max) | 51.3 - 86.6 | m |
| Vertical separation (slices) | 3.0 | m |
| Mean slope | 1.24 | deg |
| Mean aspect | 173.0 | deg |
| Topographic index | 8.65 | -- |
| *Actual Topography* [2] | | |
| Elevation range (top slice) | 292.2 - 409.1 | masl |
| Elevation range (bottom slice) | 237.1 - 302.1 | masl |
| Aquifer thickness (min - max) | 39.8 - 142.4 | m |
| Vertical separation (slices) | 4.7 | m |
| Mean slope | 2.53 | deg |
| Mean aspect | 172.7 | deg |
| Topographic index | 8.02 | -- |
| *Deep Aquifer (DH)* | | |
| Elevation range (top slice) | 292.2 - 409.1 | masl |
| Elevation range (bottom slice) | 187.1 - 252.1 | masl |
| Aquifer thickness (min - max) | 89.8 - 192.4 | m |
| Vertical separation (slices) | 6.2 (top) - 10.0 (bottom) | m |
| *Shallow Aquifer (SH)* | | |
| Elevation range (top slice) | 292.2 - 409.1 | masl |
| Elevation range (bottom slice) | 264.7 - 331.4 | masl |
| Aquifer thickness (max - min) | 26.1 - 93.2 | m |
| Vertical separation (slices) | 3.3 | m |

[1] meters above sea level

[2] RH and AH correspond to the homogeneous case for the reduced and actual topography models.

Table 2-2. List of scenarios classified by topographic relief, imposed heterogeneity, and aquifer thickness (geometry, G).

| **Topographic Relief** | **Correlation Length, $I_{xy}$[m]** | **VAR [Ln K] = $\sigma_Y^2$ - Scenario ID** | | | | | |
|---|---|---|---|---|---|---|---|
| | | $\sigma_Y^2 =$ **0.3** | $\sigma_Y^2 =$ **0.7** | $\sigma_Y^2 =$ **1.0** | $\sigma_Y^2 =$ **1.25** | $\sigma_Y^2 =$ **1.5** | $\sigma_Y^2 =$ **2.0** |
| Reduced | 150 | 1 | 2 | 3 | 4 | 5 | 6 |
| Reduced | 300 | 7 | 8 | 9 | 10 | 11 | 12 |
| Reduced | 450 | 13 | 14 | 15 | 16 | 17 | 18 |
| Actual | 300 | 19 | 20 | 21 | 22 | 23 | 24 |
| Reduced | Homogeneous (RH) | | | | | | |
| Actual | Homogeneous (AH) | | | | | | |
| Actual(G1) | Deep Aquifer - Homogeneous (DH) | | | | | | |
| Actual(G2) | Shallow Aquifer - Homogeneous (SH) | | | | | | |

Table 2-3. Parameters used for permeability realizations in FGEN.

| **Parameters** | **Value** | **Units** |
|---|---|---|
| Mean hydraulic conductivity ($K_{avg}$) | $6.5 \times 10^{-5}$ | m $s^{-1}$ |
| Variance (Ln K), $\sigma_Y^2$ | 0.3, 0.7, 1.0, 1.25, 1.5, 2.0 | m $s^{-1}$ |
| Correlation lengths ($I_x$, $I_y$, $I_z$) | 150, 150, 2.7 | m |
| Correlation lengths ($I_x$, $I_y$, $I_z$) | 300, 300, 2.7 | m |
| Correlation lengths ($I_x$, $I_y$, $I_z$) | 450, 450, 2.7 | m |
| Power spectrum model | exponential covariance | -- |
| Spatial step size: Xu, Yu, Zu | 150, 150, 2.7 | m |
| Number of nodes (full) x, y, z | 256, 256, 128 | -- |
| Number of nodes (truncated) | 110, 110, 70 | -- |
| Number of realizations | 10 | -- |

Transposing the generated permeability field to the model domain geometry was performed in MATLAB by using only the truncated field and matching the nearest centroid of the elements from both grids. The maps with $I_{xy}$ = 150 m (Figure A1 in Appendix A) show a higher density of clusters of porous media with similar hydraulic conductivity, which is directly dependent on the number of seeds used in the simulation. As the correlation length increases, so does the connectivity of areas creating larger extensions of area with similar property materials. This behavior is also observed in the cross sections where interbedded areas seem partially connected at different depths of both high (red) and low (blue) conductivity zones.

The permeability fields for each scenario were generated for a single realization. The ergodicity hypothesis verifies that this realization is a true reflection of the ensemble statistics of permeability ($k$) that were applied to create it (*Rubin, 2003*), and it constitutes, according to Zhan (*1999*) in a '*bridge connecting the single realization to the ensemble*'. The ergodicity hypothesis of the generated permeability fields was tested estimating the relative variances of the spatial average of the hydraulic conductivity, defined by $R$, using the closed-form equation for $R$ developed by Zhan (*1999*) for the three-dimensional problem. The ergodicity hypothesis depends not only on the ratio of the scale of the watershed over the horizontal correlation length ($I_{xy}$) but it is also affected by its vertical component ($I_z$=2.7m), the degree of heterogeneity ($\sigma_Y^2$), the geometry of the model domain (i.e., L·W·H), and the autocorrelation method used to generate the field (i.e., linear or exponential). The values of $R$ for all scenarios with the same imposed heterogeneity ($\sigma_Y^2$, $I_{xy}$, $I_z$) and with different subsurface geometry (i.e., RH, AH, DH, SH) fell within a narrow range. The highest $R$ value (~$3.2 \times 10^{-4}$) corresponded to the scenarios with the largest correlation length ($I_{xy}$=450m) and degree of heterogeneity ($\sigma_Y^2$ =2.0). Its associated error index ($\sqrt{R}$) of using the ergodicity hypothesis should be kept lower than 10% (*Zhan, 1999*), which in our case was less than 2% for all scenarios.

### 2.3.3 Travel Time PDFs from Numerical Model

FEFLOW (DHI-WASY GmbH) is used to generate the travel time PDFs for observation points distributed across the watershed in order to evaluate the performance of applying the 1-D analytical travel time equation. The numerical approach by Cornaton (*2014*) presented previously for determining the probability of exit CDF, $p_E(x,t)$, is applied to the study area to obtain both:

- the probability of exit of a water particle (added as an observation point in FEFLOW at the water table elevation) through exchange flux points (identified through a steady state model analysis), and,
- the travel time CDF defined as the evolution of the probability of exit field as it moves backward-in-time from the exchange flux plane up until it reaches the observation points, depicting, as it transports $p_E(x,t)$ through the model domain, a breakthrough curve of probability of exit.

The maximum value of the CDF, $p_E(x,t)$, corresponds to the probability of exit, which could be one (1.0) for those water particles exiting the domain through the exchange flux plane, or less than one for those that exit the domain through other outlet(s). In order to identify which water particles (i.e., observation points) should be included in the analysis to eventually compare them to their analytical counterparts, a value of 0.5 was chosen as threshold of probability of exit, that is, that only water particles with a probability of exit equal or greater than 50% were considered for further analysis. A similar probability value is typically used when delineating well capture zones (*Souza et al. 2013*). By doing so, the selected area of the model domain is that which has a probability >50% to truly contribute to the river flow (i.e., groundwatershed), and in FEFLOW defines an effective drainage area to the river. Because in the case considered there are no other surface outlets (e.g. wellfields), the non-selected area is thought to be part of a deeper (regional) groundwater flow system that exits the watershed through the Dirichlet boundary condition located along the outlet. Once the travel time CDF is defined for each observation point, it is converted to a PDF by applying a derivative.

For each simulation scenario a new steady state is obtained together with a new set of exchange flux locations along the streambed to be used as the source of the probability of exit by imposing a non-zero BC on them. Simulations are run for a period of 165,000 days (~452 years) assuring that most of water particles have exited the model domain. The transport component of probability of exit $p_E(x,t)$ in the model is simulated in transient state as it moved through the stationary velocity field. The transport of the variable $p_E(x,t)$ through the porous media entails the use of parameters that control its macro-dispersion (**D**), i.e., the longitudinal ($\alpha_L$) and transverse ($\alpha_T$) dispersivity coefficients, which proved to be very sensitive to recovering all the mass in the shape of the CDF. A range of $\alpha_L$ values between 35 m to 45 m was obtained in order to recover the observation points' mass through the travel time breakthrough curve, whereas the $a_T$ value resulted in values close to 10% that of $\alpha_L$.

## 2.4 Calibration

The shapes of the resulting travel time PDFs for individual observation points and for different scenarios that were generated by the numerical model are not uniquely skewed to the right and high kurtosis values, even though this is the dominating shape. There are several PDFs that tend to delineate another milder, wider peak, making the overall shape of the travel time PDF almost bi-modal in these cases. These PDFs are likely the result of the interactions of topography and/or variability of the hydraulic conductivity along the flow paths. In some cases, these PDFs correspond to water particles released at short distances from the point of discharge, along rising slopes. It is likely that their peak value is attenuated by the interference of a longer, upstream flow path that originates from a zone with higher hydraulic head; or due to the mixing of flow paths as a result of the resistance to flow generated by the presence of a less conductive zone. The former case describes areas next to the streams where discharge creates zones of enhanced mixing of incoming flow paths, mixing waters of different ages and solute concentrations. The latter case is the result of landscape heterogeneity units including surface and bedrock topography, porous media, and stream density. It is difficult to discern between these two potential explanations.

Regardless of the actual reason behind the shape of these deviating distributions, the resulting PDF are indicative of extensive mixing experienced along the flow path where the transport mechanism is switching from an advective-dominated to a more dispersion-dominated flow field. This is the case especially for longer-tailed distributions, which are characterized by low Peclet numbers (estimated as $vL/2D$). Nonetheless, the most dominant shape is skewed to the right, for which both mode and median of the travel time PDF tend to be close from each other, and Peclet numbers are typically greater than 1.0, due to lower macrodispersion. In summary, it is important to note that not all PDFs generated look alike and that the shapes of some cannot be replicated by the analytical solution regardless of the parameters values chosen for calibration.

Two types of calibration were attempted to match not only the shape of a particular travel time PDF but also the overall distribution of the median travel time variable obtained from the half-mass point of the travel time CDF. A first calibration approach entails matching the shape of the analytical travel time PDFs for a total of twenty four (24) points in the watershed with variable flow path distances, with that from the numerically generated PDFs. The locations of these 24 calibration points are shown in Figure 2-1. The shape of a given PDFs is matched by iteratively (manually) varying the calibration parameters in the analytical equation: mean flow path velocity ($U_0$) and macrodispersion ($\lambda_L$). The former allows matching the location of the travel time mode (peak), and the latter helps matching the arrival frequency and also in refining the location of the mode. A summary of this calibration process is depicted in a flow chart included in Appendix A (Figure A2). For each scenario, this calibration was conducted and values for the calibration parameters were obtained for each of the 24 calibration points. As these points are spread across the entire watershed, they are believed to represent most of the expected flow paths being affected by both topography and heterogeneity of the porous media. Out of the 24 calibration points, two showed evidence of either having a bi-modal behavior or having a milder or not a clearly defined peak. In these special cases, the location of the center of mass of the distribution was targeted rather than the location of its peak.

The values of the calibration parameters are related to flow path distance to evaluate a potential pattern with the distance to discharge. The mean flow path velocity is poorly related to distance in all the reduced topography scenarios, averaging $r^2$=0.06; whereas, it was mildly related in all the actual topography scenarios, averaging $r^2$=0.30 with values as high as 0.49 and as low as 0.08. In the case where a relation exists, it takes the form of a negative power function exhibiting higher values of velocity at shorter distances, and lower ones as the distance to the point of discharge increases. Conversely, the macrodispersion values generally followed a distinctive relation with distance, taking the form of a positive power function assigning values of macrodispersion of 75 m for a flow path 1000-m long, and ranging from 130 m to 160 m for flow paths approximately 5000 -m long (Figure 2-2). This relationship is not only evident in all scenarios but it also exhibits a trend in heterogeneous scenarios of the reduced topography model where the macrodispersion decreases with distance as the degree of modeled heterogeneity increased, while the opposite tendency is observed for the actual topography model ($I_{xy}$= 300 m), that is, increasing macrodispersion with degree of heterogeneity at longer flow paths. Even though these relationships are generally weaker for the reduced topography cases (lower $r^2$ values), the trend is still verified by the scenarios in which this relationship holds stronger: $\sigma_Y^2 = 1.0$ and $\sigma_Y^2$ =2.0, both with $r^2$~0.76. For both reduced and actual topography, the macrodispersion relates, in general, to both flow path distance and degree of heterogeneity by exhibiting lower variability at short and mid-distances and higher variability at distances far from the point of discharge. This characteristic becomes more evident in the actual topography model where the variability of macrodispersion is narrower suggesting that a specific value satisfies all degrees of heterogeneities evaluated for a given flow path distance. The positive power function for each scenario, in addition to the average calibrated flow path velocity from 24 points, constitute the first approach to calibration against the travel time PDFs (Table A1 in Appendix A) from the numerical model using the probability of exit ($P_{exit}$ *or* $p_E$).

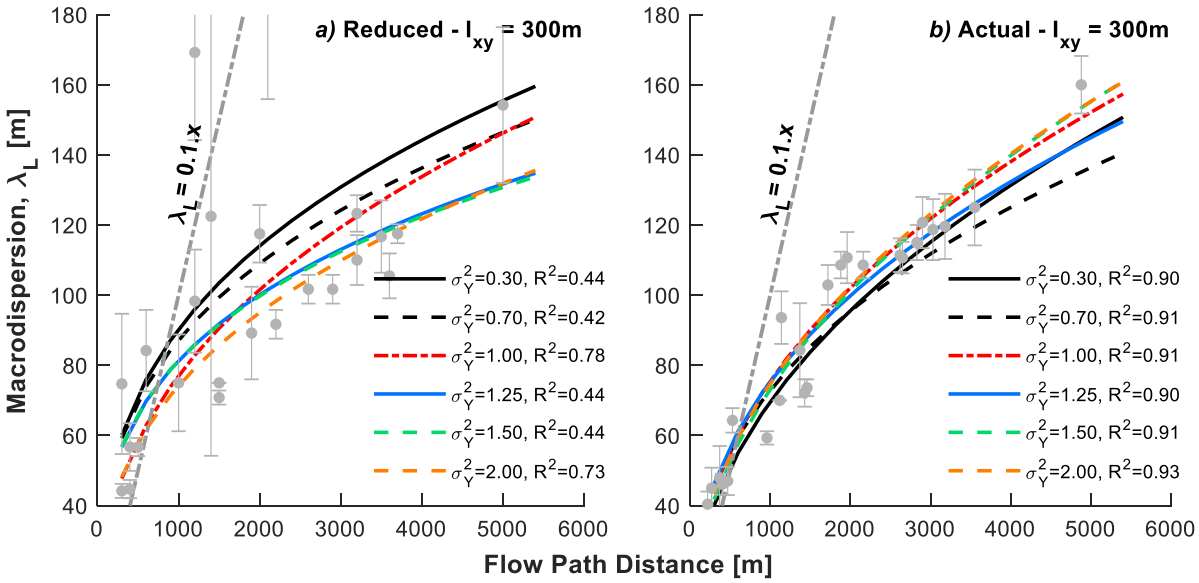


Figure 2-2. Calibrated macrodispersion and its relationship to flow path distance ($x$) for reduced and actual topography scenarios with $I_{xy}$=300 m and $I_z$=2.7m. Raw $\lambda_L$ and $x$ data for the relationship is also shown as average (grey circle) and standard deviation (brackets) of all scenarios with $I_{xy}$=300 m, along with the widely used reference ratio for $\lambda_L$ of 10 percent of $x$. Expressions for power functions are listed in Table A1 (Appendix A).

The second calibration procedure consisted of identifying the mean flow path velocity for each scenario so that a fitted line for the median travel time estimated by $p_E(x,t)$ and the analytical equation intercepts the origin at a 45 degree angle (i.e., the 1:1 relationship). By doing so, the overall response of the analytical methodology moved downward (with high $U_0$ values) and upward (with low $U_0$ values) defining angles lower and greater than 45, respectively. The velocities identified are listed in Table A1 (Appendix A). For this calibration effort, the macrodispersion values obtained from their positive power relation to flow path distance are used, although, their effect on the resulting velocity is secondary, it does help in reaching targeted arrival frequencies. For each scenario, the second calibration velocities are systematically lower than those estimated from the calibration of the 24 flow paths described earlier. Results discussed in the following sections relate to the first calibration approach as it provides better agreement with the numerical model. A brief

commentary is presented later in relation to the use of the second calibration method and the resulting comparison with the numerical model.

## 2.5 Analysis of Calibration Results

### 2.5.1 pMTT Comparison for the Reduced Topography Scenarios

The first calibration approach assigns an average velocity ($Uo$) to the entire flow path ensemble for each scenario. The $Uo$ value is estimated from the calibrated velocities of 24 water particles (i.e., 24 observation points) spread across the watershed. For the analytical method, a smoothing factor of 20 is applied in all the scenarios, thus, only one set of flow paths is generated (i.e., $x$ is constant for all scenarios) leaving only $U_o$ and $\lambda_L$ to be adjusted for calibration. The adjusted velocities and the resulting $r^2$ used as a measure of fit of a line intercepting the origin varies from as low as 0.34 for the Deep Aquifer (DA) scenario to as high as 0.58 for scenarios 5 ($I_{xy}$=150 m, $\sigma_Y^2$=1.5) and 10 ($I_{xy}$ =300 m, $\sigma_Y^2$=1.25) (Table A1). On average, the $r^2$ in the reduced topography model for scenarios with $I_{xy}$ =150 m and $I_{xy}$ =450 m, is 0.53, and with $I_{xy}$ =300 m, 0.54; however, in the actual topography model the scenarios with $I_{xy}$ =300 m have $r^2$=0.43, and when considering the homogeneous scenarios only (AH, DH, SH) the average is $r^2$=0.41 (Table A1).

The estimates of individual travel times were compared for both methods and for a selected group of scenarios: RH, ID 6 ($I_{xy}$= 150 m, $\sigma_Y^2$ = 2.0), ID 12 ($I_{xy}$= 300 m, $\sigma_Y^2$ = 2.0), and ID 18 ($I_{xy}$= 450 m, $\sigma_Y^2$ = 2.0) (Figure 2-3). Other scenarios for the same correlation length were also examined but they did not exhibit much difference from those with the largest imposed heterogeneity ($\sigma_Y^2$ = 2.0). This implies that is not the degree of heterogeneity but its size, controlled by the correlation length, that modulates the variability in the spread of pMTT among scenarios. Considering that in the proposed methodology, a single bulk velocity ($U_0$) is applied to all observation points, it is the flow path lengths that define the spread of pMTTs. In this case, the delineation of the flow paths in the analytical model matches well that of the numerical model for most of the observation points (Figure 2-3). Data points for which the analytical equation is either systematically overestimating or underestimating are

highlighted on Figure 2-3 for further analysis: data points labeled as 'location set 1' and 'location set 3' are selected from panel (a), the homogeneous case for the reduced topography model, and 'location set 2' from panel (d), scenario 18 ($I_{xy}$= 450 m, $\sigma_Y^2$ = 2.0). Each point location represents a set of points with different imposed heterogeneities of varying correlation lengths. The stream traces (i.e., flow paths) from FEFLOW (Figure 2-4), are those generated under steady state flow conditions by placing the starting points of the trace located at the node nearest to the observation grid points. These starting points were set at slice number 7, corresponding to an elevation of 1.5 to 2.0m below ground surface, where a fully saturated water table is expected. These stream traces correspond to the two-dimensional view of a three-dimensional path taken by water particles released at the locations described above.

Note that the overall distribution of observation points does not cover the entire area of the watershed (Figure 2-4). The reason is that the area in which the observation points are located corresponds to the extent of the area draining into the surface water features as determined by the condition $p_E(x,t) > 0.50$ in the numerical model. The areas excluded recharge the aquifer, but exit the model domain via the porous media Dirichlet boundary condition (Figure 2-1). In a regional context, they are likely to discharge into adjacent subbasins.

The set of data points 'location set 1' and 'location set 3' are both starting in the homogeneous scenario with a weak agreement against the numerical model. Their agreement improved in all the heterogeneous scenarios, however. It does so for 'location set 1' by both increasing the mean flow velocity in the analytical equation and by decreasing it in the numerical model, likely due to either the intersection of a less conductive porous media or a change in course in the flow path for one with a longer distance. The data points for 'location set 2', selected from panel (d) of Figure 2-3 for being the most underestimated set of travel times by the analytical equation. Considering that this set showed a better agreement in the homogeneous model, indicates that the increased velocity required by the imposed heterogeneity, combined with the differences in the flow path length from both

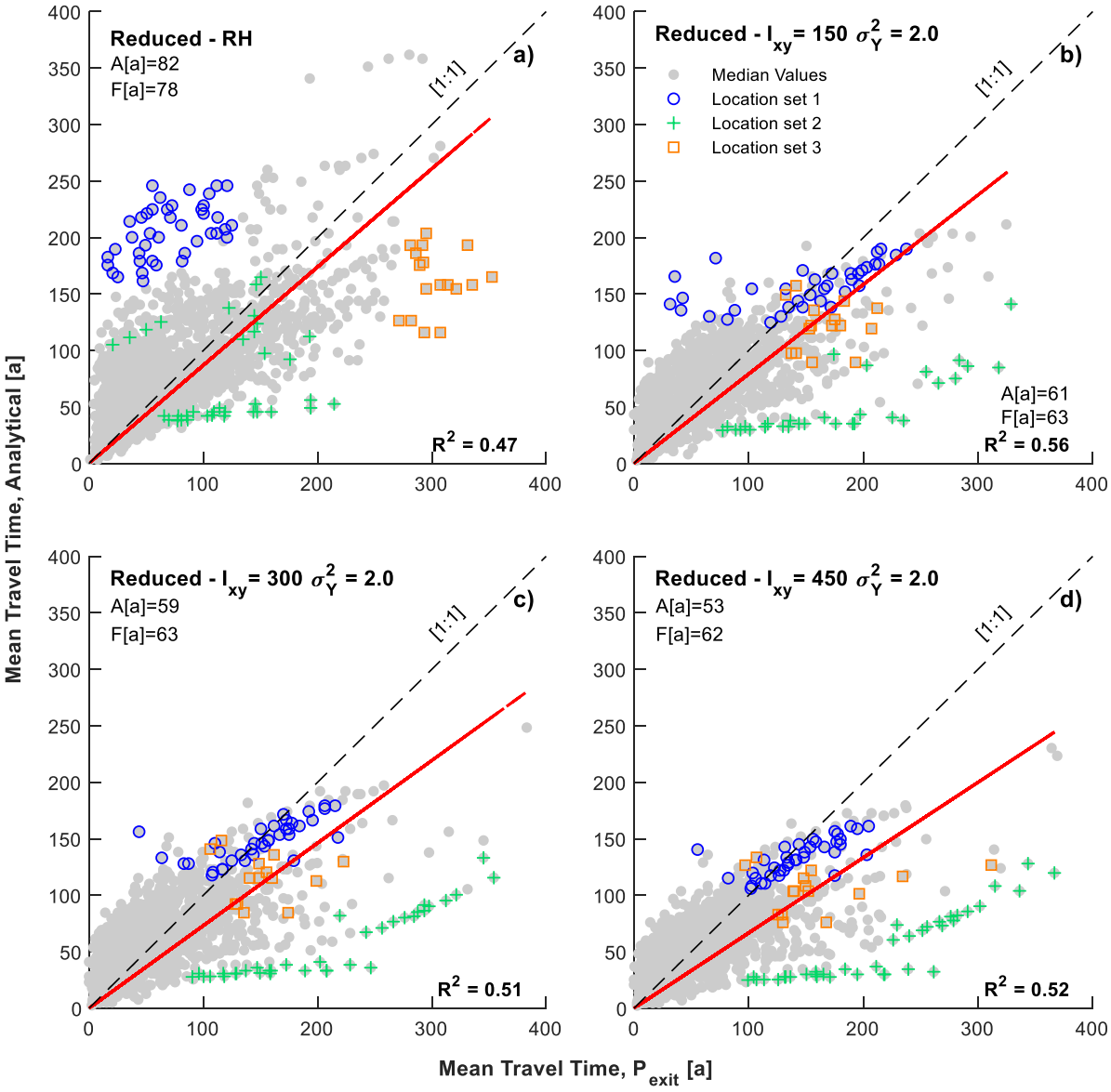


Figure 2-3. Comparison of estimated pMTTs and wMTTs for observation points scattered in a 200-m grid using the proposed analytical approach (A) versus the numerical (F) approach ($P_{exit}$) for: a) scenario RH, b) scenario 6, c) scenario 12, and d) scenario 18. Locations of interest have been highlighted for further analysis in Figure 2-4.

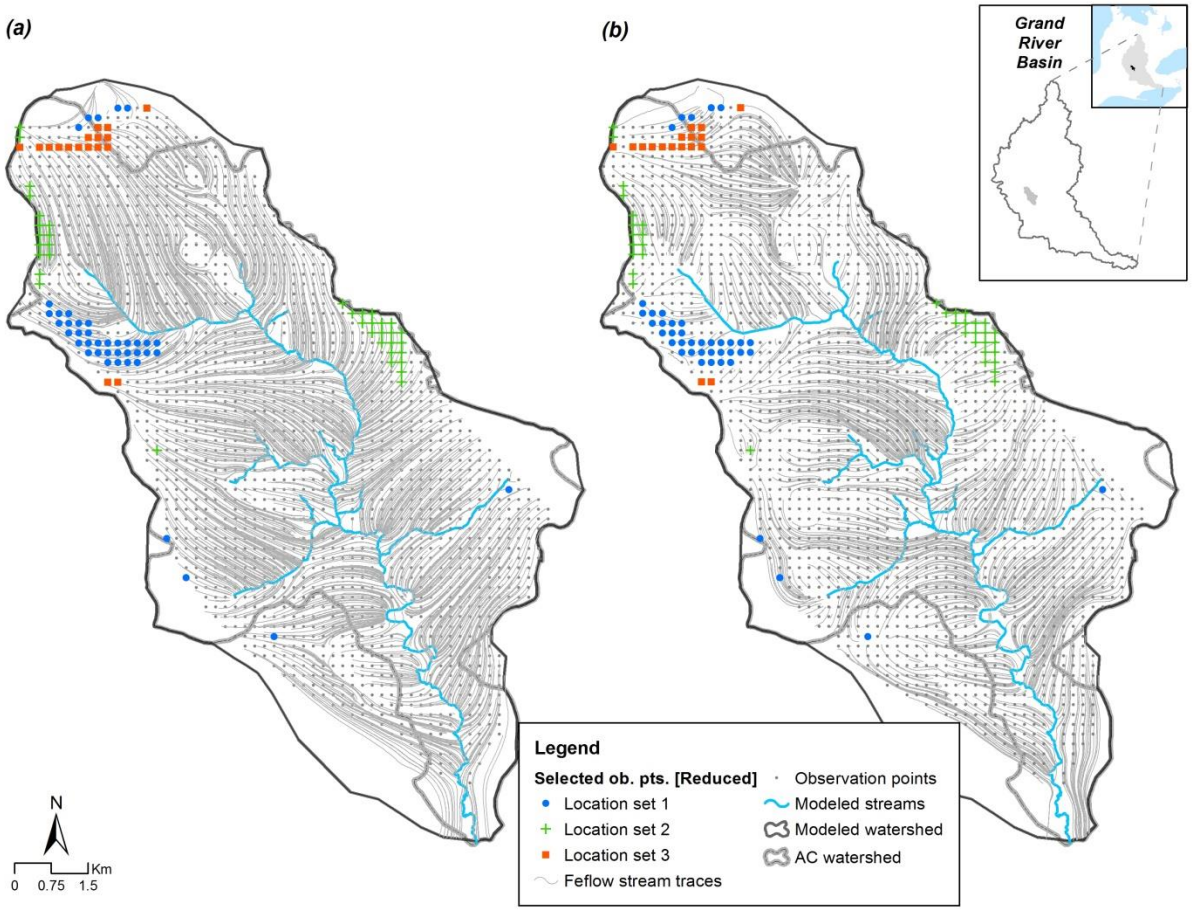


Figure 2-4. Stream trace produced by the numerical model for scenarios a) RH and b) 18 ($I_{xy}$=450m, $\sigma_Y^2$ =2.0) with reduced topography including the highlighted sets of data in Figure 2-3.

methods, generated large discrepancies along a wide range of median travel time estimates from the numerical model (e.g., discrepancies in years of 75 (100, 25) and 250 (375, 125), taken from Figure 2-3d). The stream traces for 'location set 2' (Figure 2-4b) do not reflect in any way the range of travel times, ranging from 100 to 375 years (Figure 2-3d). This disparity can be explained by the fact that in this area the depth to the water table is 8-9 m where the numerical model likely traces these flow paths through low conductivity units that could be disconnected from a fully saturated groundwater table. Similar patterns occur in areas where stream traces are unexpectedly short in upland regions. This constitutes a

limitation of using stream traces from the numerical model as reference of how flow paths should look like, instead, they are used here as tools in providing a general idea of their flow path patterns and distributions in the watershed.

Even though the traces for the 'location set 2' area are discontinued (Figure 2-4b), the aging of the groundwater is not, as reflected by the estimated travel times. For 'location set 3', the flow paths of these observation points intercept the imposed heterogeneity (scenario 18, $I_{xy}$=450m, $\sigma_Y^2$ =2.0) and change their course towards points of discharge located at shorter distances. This reduces the estimated travel times in the numerical model. The calibrated *Uo* is increased accordingly with respect to the homogeneous case making the estimated travel time shorter as well. However, the latter occurs without changing the flow paths predicted by the numerical model, a feature which the analytical method fails to predict. The pMTTs are thus in better agreement with the numerical approach, but not for the right reasons. The only way in which the analytical method incorporates the heterogeneity component is by varying the mean flow path velocity ($U_o$) and macrodispersion ($\lambda_L$).

### 2.5.2 pMTT Comparison for the Actual Topography Scenarios

The pMTT estimates are also compared for the actual topography scenarios (Figure 2-5). For the same degree and type of heterogeneity, these scenarios require a greater calibrated velocity than those from the reduced topography. The level of correlation for the estimated pMTTs from both methods is unchanged to that of the reduced topography (Figure 2-3). The same flow path delineation in the analytical model with a smoothing factor of 20 is used here as in the reduced topography scenarios. A greater topography yields shorter stream traces in the numerical model as streams are more readily intercepted. Therefore, the greater $U_0$ required by the actual topography scenarios in the analytical model is due to both shorter stream traces and greater pore velocities in the numerical model.

Similarly as for the reduced topography, the sets of data points 'location set 1' and 'location set 2' were selected from the AH scenario; whereas, the set for 'location set 3' was selected from the DH scenario. The analytical approach overestimates and underestimates

the data sets 'location set 1' and 'location set 3', respectively. Their distribution does not abruptly differ from one scenario to the next indicating that both subsurface geometry and imposed heterogeneity in the numerical model do not significantly improve or worsen their correlation with the analytical approach. However, the overall agreement of the analytical approach to the numerical model estimates is diminished in the DH scenario. The data set 'location set 2' is selected due to the relatively acceptable agreement between the two methods at long travel times for scenarios AH and 24 ($I_{xy}$=300 m, $\sigma_Y^2$ =2.0). The flow paths delineated by the analytical method for the area comprised by a subset of points from 'location set 1' are in the vicinity to those estimated by the scenario AH in the numerical model for 'location set 2' (Figure 2-6a). However, the data set 'location set 1' is greatly overestimated by the analytical method, as the flow path delineation does not intercept the adjacent stream.

The 'location set 2' data set, in turn, shows stream traces in Figure 2-6b that are not representative of the long travel times estimated by the numerical approach (~225a in Figure 2-5b). This again shows a disparity between the stream traces delineation and the expected distances from those of the longest travel times estimated in the watershed by the numerical model. In the flow path analysis section (section 2.5.6), a further explanation of this disparity is presented (Figure A5b, Appendix A). Figure 2-5b shows the increase in velocity for both approaches as this set of points/traces ('location set 2') yields shorter travel times when compared to the homogeneous case. The set of points for 'location set 3' is found on the east and west side of the watershed. The subset on the east of the watershed is in an area with the deepest water table locations in the numerical model, but with enough head with respect to the river. The travel times for this set in scenario 24 are comparable to those estimated for the homogeneous case (AH), even though their stream trace delineations do not compare well. The reason for this underestimation is twofold, a deep water table elevation and the location of this area with respect to the regional groundwater flow, which both limit flow toward the stream and yield low local velocities. For the subset on the west, a combination of a slight difference in flow paths and a large difference in particle velocities between both methods explains the significant underestimation of the travel times by the

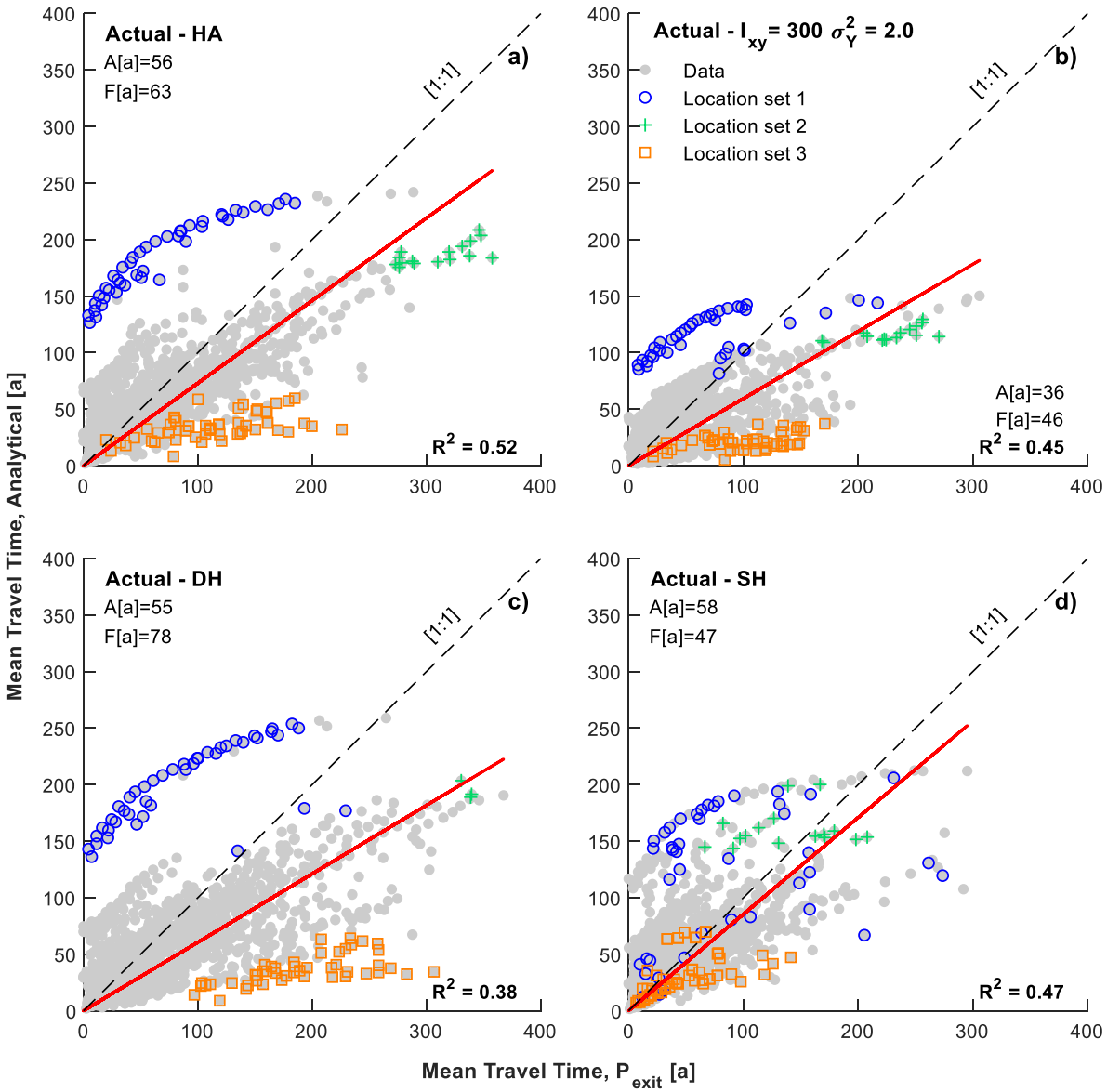


Figure 2-5. Comparison of estimated pMTTs and wMTTs for observation points spread across the 200-m grid using the proposed analytical (A) approach against the numerical (F) approach ($P_{exit}$) for: a) scenario AH, b) scenario 24, c) scenario DH, and d) scenario SH. Locations of interest have been highlighted for further analysis in Figure 2-6.

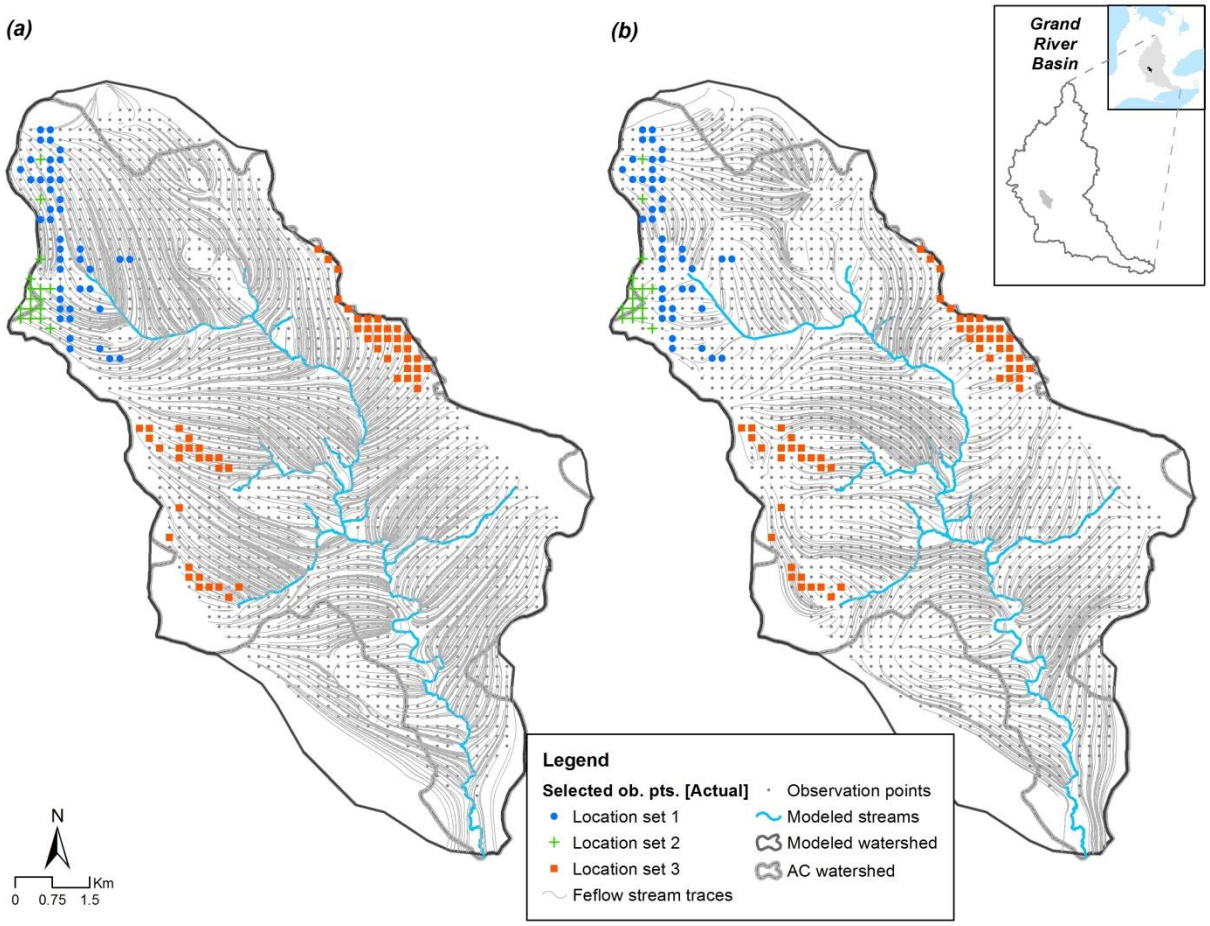


Figure 2-6. Stream trace produced by the numerical model for scenarios a) AH and b) 24 ($I_{xy}$=300 m, $\sigma_Y^2$ =2.0) including also the location of highlighted sets of data in Figure 2-5.

analytical method. The distribution of these data sets is rearranged in scenario SH indicating that under shallow aquifer depths the noted problems of not-intersected streams and the effects of deep water table and watershed geometry do play a less important role.

### 2.5.3 Spatially Bound pMTT Comparison

The analytical method pMTT estimates were spatially compared to the pMTT values from the numerical model for both the RH and AH homogeneous scenarios (Figure 2-7). The

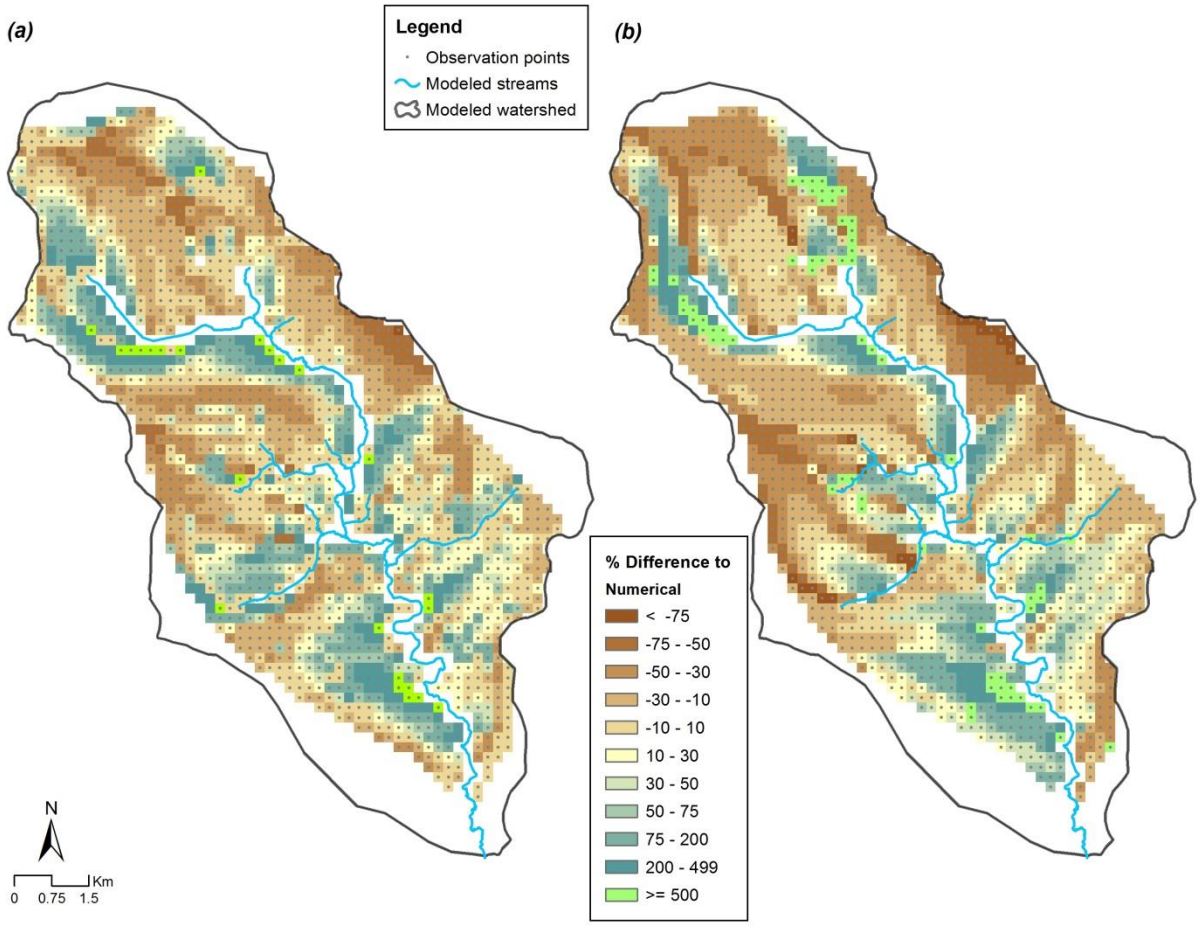


Figure 2-7. Distribution of percent differences in the estimates of pMTTs between the analytical (calibrated) and numerical approaches, for the homogeneous scenarios of both a) reduced and b) actual topographic models.

largest discrepancies are present in the AH scenario, where the number of observation points with differences exceeding 500% (identified by points with a white background) is almost twice as high as in the RH scenario. This figure highlights areas exhibiting the greatest analytical-numerical discrepancies in the watershed that have been previously discussed such as those in the east (underestimated, dark brown) and in the northwest (overestimated, turquoise), as well as new areas that are located at or immediately adjacent to streams (overestimated, bright green). The data points with discrepancy values of 500

percent or larger for the homogeneous model that were highlighted in Figure 2-7 are also highlighted in Figure A3 (Appendix A) using the estimated pMTTs from both methods. Identified points from scenario RH (Figure 2-7a) were also plotted in the scenario AH panel (Figure A3b) and vice versa. The conditions that made these extreme discrepancies in observation points (>500%) in the RH (or AH) scenario are seemingly damped for some of those locations when tracking them into the AH (or RH) scenario (Figure A3). For all of these points, their proximity to a stream yields relatively short travel times in the numerical model. Considering the problem areas discussed previously plus the latter areas adjacent to streams, the results suggest that the analytical approach tends to be in better agreement with the numerical model at mid- to long-distance flow paths. The further away from streams an observation point is, the better its travel time is predicted as it is less likely for the analytical method to fail intercepting streams and overestimating their time before discharge.

### 2.5.4 Mean Watershed Travel Times (wMTT)

The distribution of travel times of water particles released across the watershed provides some insight into the response of the watershed to external forcings, be they purely hydrological such as recharge variability, or the spread of contaminant inputs in terms of rates and locations throughout the watershed. The influence of topography, subsurface heterogeneity and geometry in the wMTT response are examined in this section by using the average of the ensemble of the median travel time PDFs (pMTTs) generated with both methods.

When averaging the individual travel time distributions from the individual observation points in the watershed, a mean travel time PDF is obtained for each numerical modeling scenario. The resulting PDFs can be compared against those generated with the analytical approach (Figure 2-8). The mean numerical model PDFs are more strongly skewed to the right than those from the analytical method, in all scenarios. A common pattern of exhibiting a higher peak of arrival frequency with increasing heterogeneity is present in both methods. This suggests that the mode and, most likely, the median of the travel time

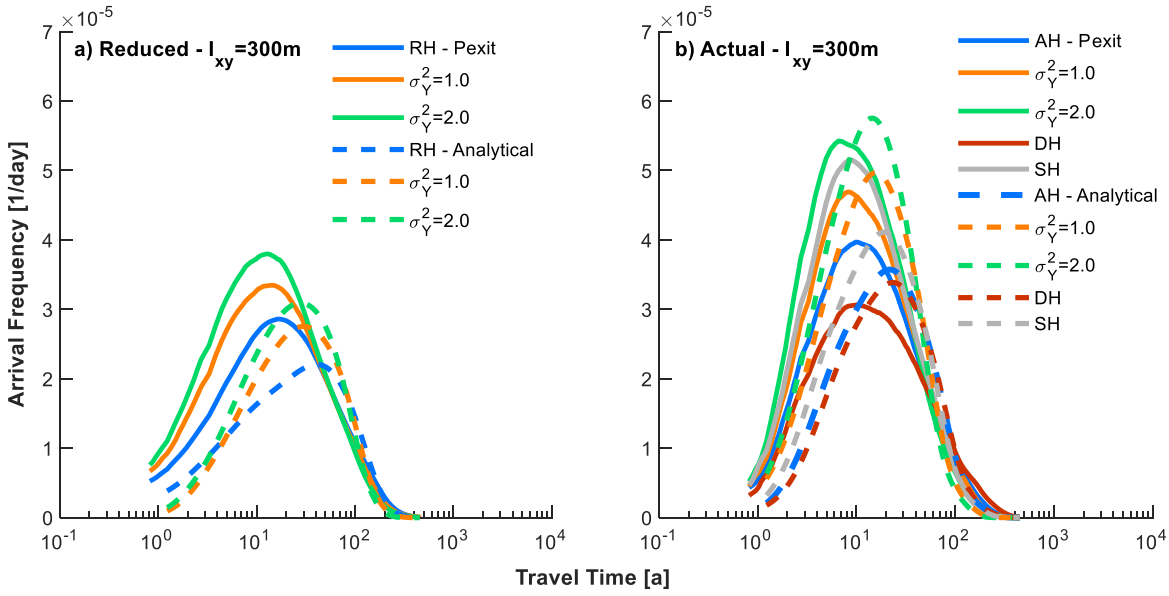


Figure 2-8. wMTT PDFs estimated using the analytical (dashed line) and numerical (solid line) methods for selected scenarios with $I_{xy}$=300m within both *a)* reduced and *b)* actual topographic models. Note that DH, AH, and SH distributions are very close to each other for the analytical method.

random variable decreases as the subsurface media of the modeled domain becomes more heterogeneous. Considering the type of heterogeneity imposed onto the porous media in this study, and for scenarios with the same topography, this result also indicates that preferential flow paths are widely present in the heterogeneous media allowing the early arrival of water particles to the point of discharge; as opposed to dispersion into the media of a hypothetical homogeneous case. A similar behavior is present for the actual topography model (Figure 2-8b), where the arrival frequency peaks at a higher value than for the homogeneous case, in the reduced topography, and keeps increasing with the degree of heterogeneity.

Together, these results suggest that both the mode and the median of the distributions have lower travel time values, which are associated with the effect of topography. The DH and SH scenarios are also plotted in Figure 2-8 to be compared against the actual-

topography homogeneous case (AH): for the numerical model, they plot below and above the AH scenario, respectively, as expected; as shorter travel times are associated with shallower subsurface geometries and longer flow paths occur when less restrictions to flow are present. In general, the mean travel time PDFs from the analytical approach do also discern among scenarios with varying aquifer depth, but not with the same degree of differentiation, and they miss, as in the other scenarios, the mode of the distribution defined by the peak of the numerical model PDFs. The mean of both the travel time and the arrival frequency that were estimated from the travel time CDF represent the mean values of the travel time distribution (i.e., PDF) for the entire watershed. The mean travel time and the mean arrival frequency estimated for each scenario were compared for both methods in Figure 2-9. The tendency of exhibiting shorter watershed travel times with increasing imposed heterogeneity (increased $\sigma_Y^2$) is again observed here for all the heterogeneous scenarios. Note that the range of estimated mean travel times varies from about 60 years to 77 years for all the heterogeneous scenarios in the reduced topography model regardless of the correlation length applied to them. Thus, the imposed heterogeneity in these scenarios is quite alike. Perhaps, a wider selection of correlation length ($I_{xy}$) values might have yielded greater differences in travel time. However, the examined values of $I_{xy}$ seem in agreement with the actual surficial geology features of the Alder Creek watershed. In addition, the imposed heterogeneity given by the $I_{xy}$ values and the variance of logconductivity ($\sigma_Y^2$) complies with the ergodicity hypothesis for the model domain.

The arrival frequency in the analytical approach is slightly underestimated in all the scenarios and less variable among scenarios than for the numerical method results. The higher arrival frequency (Figure 2-8b) corresponds to earlier arrival times for the entire watershed (Figure 2-9). For the analytical approach though, the range of estimated wMTTs is greater in the actual topography scenarios, favoring shorter travel times than those estimated by the numerical model. For both topographic models, and for both travel time methods, the homogeneous case constitutes an end-member scenario where the travel time is the longest because any imposed heterogeneity makes the MTT before discharge shorter (Figure 2-10a and Figure 2-10b, Table A1 in Appendix A). A watershed with similar

topography but with shallower aquifer depth would also have a shorter mean travel time for the entire watershed. This result was also replicated by the analytical method with less sensitivity to the imposed changes. When considering all 28 evaluated scenarios, the travel times derived from the calibrated analytical method explains well those estimated by the numerical model ($p_E(x,t)$, $r^2$=0.80). The mismatch on the peak of the mean travel time PDF is likely associated with the several observation points located near streams for which the analytical flow paths failed to intercept, mistakenly assigning larger flow paths instead. This pattern was somewhat compensated with the better agreement found for observation points located at mid- and far-distances away from the point of discharge, which both define a more regional groundwater flow within the watershed.

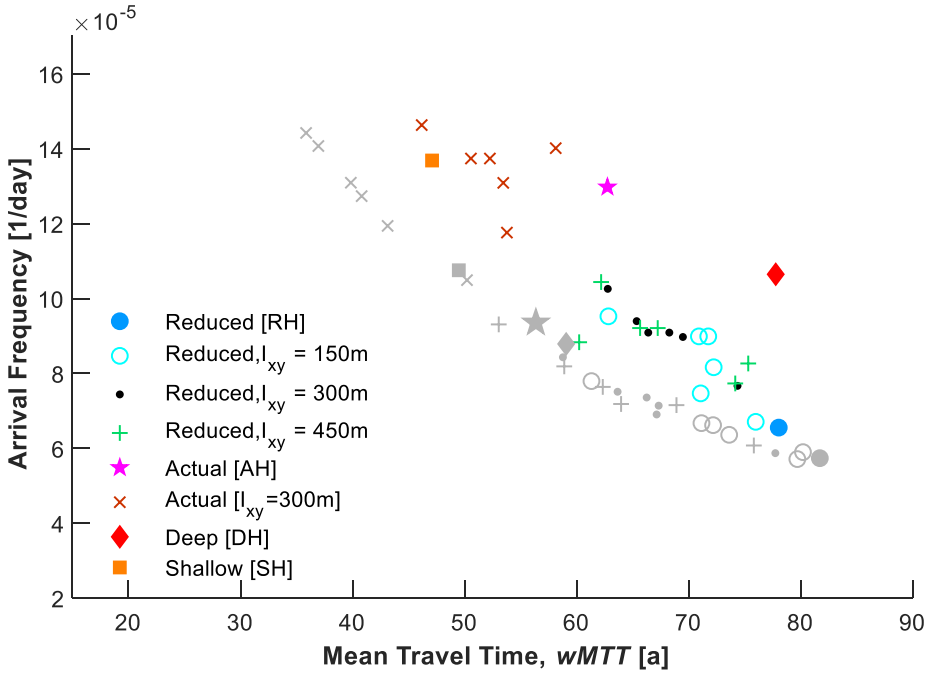


Figure 2-9. Estimated wMTTs and arrival frequencies for all scenarios. Colored symbols correspond to the numerical method estimates, gray symbols to the respective analytical method estimates.

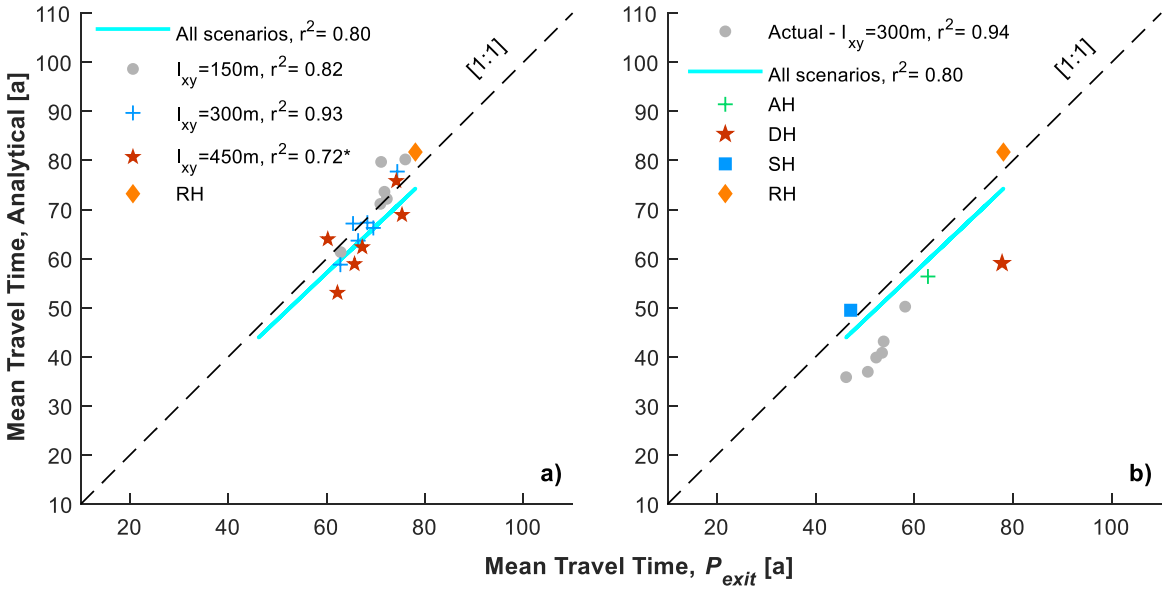


Figure 2-10. Estimated wMTTs by both methods are compared for a) reduced topography scenarios; and b) actual topography scenarios. Measure of agreement for each subset of data is presented, as well as for the entire set of scenarios (n=28). All Pearson correlation coefficients were significant ($p$<0.02), except for (*) where $p$=0.08.

The method developed by Haitjema (*1995*) to determine the watershed TTD was also applied to the actual topography scenarios (Figure A4, Appendix A): AH, DH, and SH. The wMTTs values obtained from the Haitjema method were overestimated by: 85, 158, and 52 percent difference with respect to the target set by the numerical model. Although, this method incorporates aquifer depth as main parameter, it also assumes that the θH/r ratio is constant throughout the entire aquifer, which does not hold in many areas in the watershed. Whereas, the percent differences for the analytical method were: -3%, -25%, and 32%, respectively. However, unlike the analytical method, the Haitjema approach properly followed the trend in wMTT by the changes in aquifer depth conditions (Figure A4), as an aquifer depth parameter is explicitly modeled in Haitjema's (*1995*) expression.

### 2.5.5 Calibrated *Uo* and Heterogeneity

The resulting calibrated *Uo* are proportional to the degree of imposed heterogeneity (Figure 2-11). The use of the initial Darcy velocities alone (before calibration) would have

grossly underestimated the bulk velocities required and, in turn, overestimated wMTT. The calibrated *Uo* required to match the imposed heterogeneity yields an almost linear response to the increasing degree of heterogeneity ($\sigma_Y^2$), for each size of heterogeneity ($I_{xy}$) evaluated. Actually, the slope of the relationship between *Uo* and $\sigma_Y^2$ is 0.012, 0.013, and 0.021 for the correlation lengths $I_{xy}$ = 150m, 300m, and 450m, respectively (not shown). The range of bulk velocities required by the imposed heterogeneity ranges between 0.079 m/d, for scenario 1 ($I_{xy}$=150m, $\sigma_Y^2$ =0.3), and 0.119 m/d, for scenario 18 ($I_{xy}$=450m, $\sigma_Y^2$ =2.0), which are a factor of 1.65 (0.079[m/d]/ 0.048[m/d]) and 2.5 (0.119[m/d]/0.048[m/d]), respectively, different from the initial Darcy velocity estimates for the reduced topography model (based on topography alone). A similar factor as for the reduced homogeneous case (RH), for the AH case, and for the actual topography scenarios ID 19 ($I_{xy}$=300m, $\sigma_Y^2$ =0.3), and ID 24 ($I_{xy}$=300m, $\sigma_Y^2$ =2.0), can also be estimated: 1.63 (RH), 1.33 (AH), 1.49 (ID 19) and 2.14 (ID 24). Considering that the slope of the actual topography model (2.53 degrees) is slightly above twice that of the reduced topography (1.24 degrees), the ratio of their initial Darcy velocities is 1.77 (0.085[m/d]/0.048[m/d]). While a linear correspondence was hardly expected, more data from watersheds could shed some light on how the mean Darcy velocity could vary with the watershed's slope, and how it can be used as a predictor of a calibrated velocity from a numerical groundwater model. For now, with the estimated data, it seems that with a greater slope, the mean Darcy velocity becomes a better predictor when comparing the correction factors for AH (1.33) against that of RH (1.63). Intuitively, this trend is expected as an increased hydraulic head provides a stronger similarity to the theoretical case where the effect of dispersion is reduced in the convective-dominated system. The effect of subsurface geometry is also evident in this plot, as the factor for DH (1.23) shows that the mean Darcy velocity can be a better predictor for deep aquifers than for shallow aquifers (SH factor: 1.55).

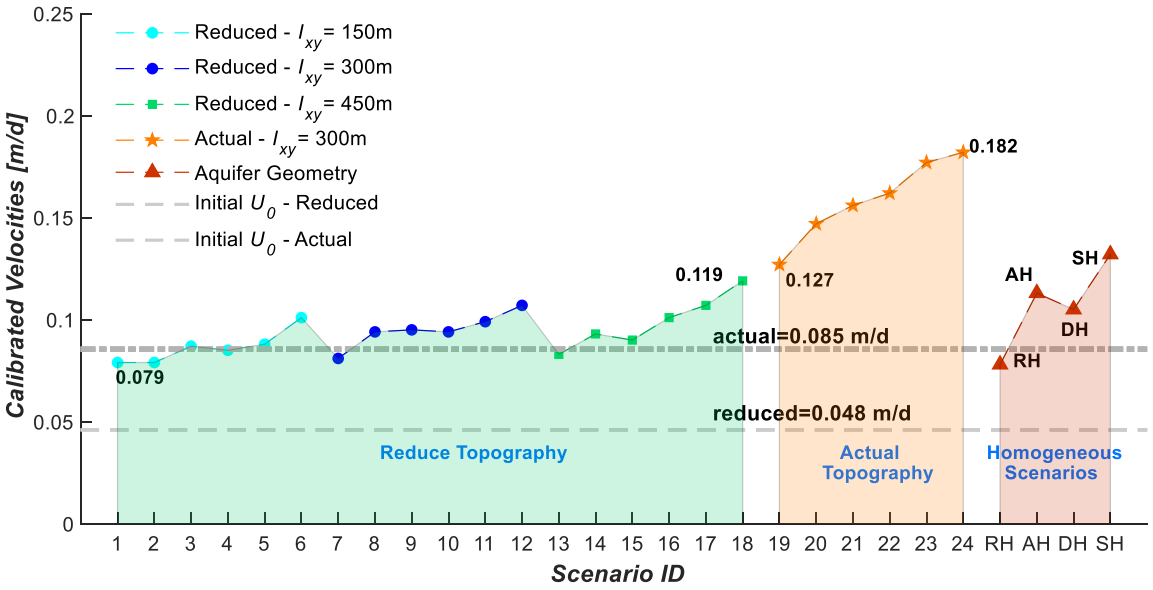


Figure 2-11. Summary of calibrated velocities assigned to each scenario in the analytical approach, along with the DEM-based bulk Darcy velocities for both reduced and actual topographic model.

### 2.5.6 Flow Path Analysis for Selected Transects (Homogeneous Aquifers)

A flow path analysis was performed in two stages: first, to observe the changes in stream traces among homogeneous scenarios (RH, AH, DH) in the numerical model, and second, to compare them against the analytical approach. Seven transects were created for this analysis. A more detailed description of the findings is presented in Appendix A. The flow path delineations for the RH scenario were used as baseline for comparison. The stream trace distances tend to increase for all transects except for transect 6, while transects 3 and 4 exhibited greater trajectory variations and had also greater slopes along the transect. The increase in topography generates deeper and longer flow paths as a consequence of a greater hydraulic head. Among the scenarios, the DH creates deeper and longer flow paths for all transects. The effect of subsurface geometry is significant in all transects except transects 4 and 5, based on the estimated pMTT. This effect is more evident at longer flow paths as they are more likely to sense the presence of the bedrock topography.

Transect 3 pMTTs are strongly underestimated by the analytical method. This transect is located in an area where heterogeneity makes the stream traces stagnant (Figure 2-4b, Figure 2-6b). In the homogeneous case, the regional groundwater flow within the watershed is heavily deviating the flow paths near the boundary towards farther points of discharge. Thus, it is the effect of both imposed heterogeneity and regional groundwater flow that explains the significant underestimation of the pMTTs around this area (Figure 2-3d, Figure 2-4b, Figure 2-5c, Figure 2-6b).

In general, the flow path lengths and the estimated pMTTs from both methods compares well for transects 1, 2, 5, and 7, are acceptable for transect 6, and not acceptable for transects 3 and 4. Thus, a good correlation in flow path lengths does guarantee a good estimate of pMTTs.

### 2.5.7 Effects of Topography and Aquifer Geometry on wMTT

Four modeled scenarios are considered to evaluate the effects of topography and aquifer geometry, separate from changes in thickness, without the influence of heterogeneity: RH, AH, DH, and SH (Table 2-4). The analytical method exhibits no sensitivity to the depth of bedrock surface as the triad of homogeneous scenarios with actual topography exhibit similar wMTTs. The variability of the reported calibrated velocities for these scenarios (Figure 2-11) is not, then, indicative of a pattern for the overall ensemble of flow paths. The results for $p_E(x,t)$ suggest that by flattening the overall slope in this watershed by half, the wMTT increases 15 years (24%) and the mean scale is reduced by 14 percent, highlighting the importance of hydraulic heads as the driving force of subsurface flow in steep watersheds. Also, the increase of the aquifer thickness by ~50 m also causes an increase in wMTT ($p_E(x,t)$) of 15 years (24%), but unlike the case of RH, the longer mean arrival time is accompanied by flow paths that are, on average, 49% longer. This analysis for DH can be extended to the SH scenario where both wMTT and scale are reduced by 25 and 5 percent, respectively. Considering that the changes in wMTT and scale are far from being proportional, SH results indicate of that not only topography but also the depth to a confining layer can be important controlling factors in the porous media's specific flow

velocities. The Peclet numbers are indicative of the type of transport conditions generated along the streamlines with the assigned values of calibrated $U_0$ and $\lambda_L$, which are in general dominated by convective transport.

Table 2-4. wMTTs, mode travel times, and mean flow path lengths and Peclet numbers for homogeneous scenarios.

| Scenario | Mean Stream Traces Length [m] | Peclet Number ($vL/2D$) Analytical | wMTT [a] | | Mode Travel Time [a] | |
|---|---|---|---|---|---|---|
| | | | $P_{exit}$ | Analytical | $P_{exit}$ | Analytical |
| RH | 1381 | 0.78±0.39 | 78.0 | 81.7 | 69.2 | 74.5 |
| AH | 1614 | 1.18±0.46 | 62.7 | 56.4 | 53.1 | 51.4 |
| DH | 2405 | 1.21±0.54 | 77.8 | 54.9 | 66.4 | 50.0 |
| SH | 1530 | 1.47±0.61 | 47.1 | 57.8 | 40.0 | 52.8 |

The mean peak travel times (i.e., mode travel time) for each scenario (Table 2-4) are measures of peak spreading. By examining the mean and mode values produced by the numerical and analytical methods, the spread of the two statistics compare relatively well between the two methods.

## 2.6 Discussion

We applied a one-dimensional analytical equation of travel time to a three-dimensional watershed setting. Results were calibrated against a numerical model for 28 scenarios. These included changes in potential drivers of subsurface flow distribution and discharge such as topography, subsurface geometry, and subsurface heterogeneity. We constructed a set of virtual watershed models in order to verify the efficiency of the analytical method in predicting travel time at a watershed scale. The spread of models was envisioned to promote situations of groundwater exchange with surface water, as we are interested in applying this methodology to biogeochemical problems. This was achieved by mainly using reduced-topography scenarios (n=19 out of 28). The reliability of our approach depends on

adequately assigning three parameters to the ensemble of streamlines: flow path length ($x$), macrodispersion ($\lambda_L$), and mean flow path bulk velocity ($U_0$). The last two parameters were used for calibration of the analytical travel time PDF to match the mode and arrival frequency of that from the numerical model for 24 observation points distributed across the watershed.

The flow path analysis (see section 2.5.6) highlights the important role played by both the flow path length in determining the travel time for individual water particles (Table A1 in Appendix A) and the mean value of travel times for the entire watershed (wMTT, Table 2-4). The model performance can be improved by incorporating as much knowledge as possible of the local conditions in relation to groundwater flow patterns. In areas where this information is unavailable, assumptions have to be made similarly to those used when building a numerical model. Data requirements for the development of subsurface numerical models are well established. However, the factors influencing the analytical model and its application to a 3-D groundwater system are more difficult to disentangle as there is no available literature. This study constitutes a first step in identifying some of these potential controls. However, factors such as drainage density and watershed size are not examined in this study as only one watershed is considered. These factors are evaluated in Chapter 3, where this methodology is applied to 8 additional watersheds. An aspect that became evident in the flow path analysis was the influence of regional groundwater flow in significantly controlling the travel times of particular areas within the watershed (transect 3, Figure 2-4b, Figure 2-6b). For these areas, deviation of the flow paths in the numerical model point to discharge locations beyond those inferred from the topography alone.

ArcNLET provides limited means to imitate the subsurface flow patterns generated by the numerical model. The flow patterns obtained from ArcNLET depend mostly on the value of the smoothing factor. For our study, a value of 20 provided the best overall match to numerical estimates. With values of 10, only limited regional flow occurs, as flow patterns would follow local topography more closely. On the other hand, using a smoothing factor of 30, would result in more regional groundwater flow patterns throughout the watershed. A

full sensitivity analysis is beyond the reach of this study. However, smoothing factors of 10 were applied to scenario 9 ($\sigma_Y^2$ =1.0) and 12 ($\sigma_Y^2$ =2.0) both with $I_{xy}$=300m, which resulted in lower wMTTs by 4 and 7 years, respectively. This reduction in wMTT was accompanied by a noticeable detriment in arrival frequency, as it did not increase with heterogeneity as the numerical model predicts. A smoothing factor of 30 was tested in actual topography scenarios with similar heterogeneity as above ($\sigma_Y^2$ =1.0, $\sigma_Y^2$ =2.0). This smoothing factor yielded similar behavior in both rendering of wMTTs and pMTT distribution. The difference in wMTT was 1 and 2 years for the $\sigma_Y^2$ =1.0 and $\sigma_Y^2$ =2.0 heterogeneities, respectively. The value of 20 for the smoothing factor is the one that is more aligned with the behavior exhibited by the numerical model in both reduced and actual topography scenarios. For other watersheds, further studies are needed to properly assign this parameter. In general, a higher value would be required in flat terrains, whereas, a lower value would give a better fit in steeper terrains. As detailed information on deeper flow paths are only available where numerical models have been developed, a value of 20 is deemed a conservative estimate given the sparse information of watershed-scale regional groundwater flow patterns. Regional groundwater flow patterns extending far outside of the model domain are not addressed in this study.

### 2.6.1 Calibration of $U_o$ and $\lambda_L$

Two calibration approaches were applied to the mean Darcy velocity defined by the differences in topographic elevation between the point of observation and its associated point of discharge. The second calibration option (i.e., adjusting $U_o$ to move the entire set of observation points (n=1784) along a 1:1 value) overestimates the mean travel time by a magnitude of 20-30 years, i.e., 38-56% with respect to the AH numerical estimates. The results for the first line of calibration (i.e., adjusting $U_o$ and $\lambda_L$ to match mode and frequency of numerical travel time PDFs for 24 observation points) provides a better fit to the watershed's MTT. The calibration of the Fickian longitudinal dispersivity term, which at field-scale studies is also known as macrodispersivity ($\lambda_L$) yields values ranging from 40 m to 160 m, for scale ($L$) distances of 200 m to 5500 m, respectively, and corresponding ratios

($\lambda_L/L$) of 20 to 3%. The latter ratios are in the mid-range of the values of $\lambda_L$ compiled by Gelhar (*1992*) from field data estimates. However, some of these compiled dispersivity measurements are regarded as unreliable, especially at larger scales, as few measurements were available for such long flow paths. The assumption of 10% of flow path length suggested by Gelhar (*1992*) as an approximation of field macrodispersion, has been widely used as starting point for calibration of groundwater transport models of contaminant plumes (*Fetter, 1993*). The calibrated curves in our study (Figure 2-2) are consistently below the $\lambda_L = 0.1 \cdot x$ line, especially for flow path lengths (scales) longer than 1000 m and 500 m in the reduced and actual topography models, respectively. If a solute were uniformly spread across the watershed, the values of dispersion will start increasing until they reach a plateau when all existing heterogeneity had been encountered (*Dagan, 1988*; *Fetter, 1993*). As the calibration of $\lambda_L$ should result in mirroring the macrodispersion introduced in the numerical model, which varies from 35 m to 45 m, the calibrated values are seemingly enhanced as the scale increases. However, this increase is not as high as reported by other 1-D models (*Kirchner et al., 2001*). We propose that this phenomenon is due to a compensation effect associated with the addition of two more dimensions to the expression that was developed to solve a one-dimensional problem. The scale effect observed in macrodispersion describes a non-Fickian behavior (*Dagan & Cvetkovic, 1996*) as, in theory, this parameter should be a unique property of the medium.

At longer scales (Figure 2-2), the actual topography model sustains a slightly steeper slope in the relationship of $\lambda_L$ and scale ($L$) than in the reduced model, even though both reach similar end values. Considering that the number of data points at longer scales is limited, observations at this scale are to be taken with caution. If what they represent is an actual trend, it could be stated that a larger $\lambda_L$ value is expected at larger scales in areas with steeper topography, and more so, in areas with an increased degree of heterogeneity (i.e., higher $\sigma_Y^2$). The core of the $\lambda_L$ correlation with flow path distance is that it can also be a proxy to a correlation with travel time. As discussed above, macrodispersion of solutes at a watershed scale increases with travel time. Based on theory from transport modeling, it could reach an asymptotic value at very long distances (*Dagan, 1988*; *Fetter, 1993*; *Dagan &*

*Cvetkovic, 1996*). In the numerical model, the ADE equation is used for transport of *age* throughout the model domain. Similarly, it is also used for the development of the analytical equation (*Soltani & Cvetkovic, 2013*). At the field scale, the ADE equation is dominated by the advective transport term (*Dagan, 1988*). Therefore, $\lambda_L$ is expected to exhibit similar behavior as in the numerical model in that it reaches an asymptotic value at long flow paths or travel times. We observed that at mild-slopes, the asymptotic value could be reached quite early on (Figure 2-2a).

### 2.6.2 Calibration Results and wMTTs

The numerical results suggested that, in general, the calibrated $\lambda_L$ values in the analytical model are slightly overestimated as the mean arrival frequency for the mean travel time (Figure 2-9) is systematically below that of the numerical model. This overestimation is more evident for the actual topography model scenarios, in which $\lambda_L$ was calibrated with better overall correlation (Table A1). The arrival frequency is actually closely matched at longer travel times (scales), for the reduced topography model scenarios. The overestimation of the $\lambda_L$ parameter by the analytical approach in the actual topographic model scenarios is accompanied by a wider range of travel times than those estimated using the $p_E(x,t)$ numerical approach (Figure 2-9). Contrary to expectations, a systematically better correlation between mean flow path velocity and flow path distance exists for the actual topographic model, but the resulting calibration of the actual topography scenarios is weaker in comparison to the reduced topography scenarios. The ratio of calibrated $U_o$ between the most heterogeneous case ($\sigma_Y^2$ =2.0) and the homogeneous case (AH) is 2.0 for actual topography, whereas, for reduced topography the same ratio is 1.4 (with $I_{xy}$= 300 m). The different velocities expressed by this ratio yield a greater variability in wMTT among the reduced topography scenarios (Figure 2-9). The wider range in bulk velocities applied to the analytical approach is not found for the numerical model responses in wMTTs. The increase in $U_o$ with the degree of heterogeneity is observed in both topographic settings. Given that in subsurface settings the wMTT signal is longer and more temporally-influenced by topography than in surficial settings, we speculate that a stronger relationship

between topographic characteristics and wMTT might be found in contrast to the large scatter in these relationships for surficial hydrology found by Tetzlaff et al. (*2009b*) for Scottish catchments. The scope of our study does not allow identifying these relationships. However, additional research could further develop these relationships by comparing watersheds with varying topography, subsurface geometry and heterogeneity. Such relationships would enable a path towards guidelines for the application of the analytical method in ungauged basins.

The distribution of travel times for the entire watershed is summarized by the wMTT PDF estimated for each scenario. As previously indicated, the analytical curves are less skewed to the right compared to their numerical counterparts. This is explained as the effect of deeper flow paths simulated in the analytical approach that do not intercept adjacent streams. If no evidence of a regional flow pattern exists, manually cutting short these flow paths in GIS is an alternative. However, they were left unmodified here to show their contribution to the overall distribution of travel times and to comply with the proposed methodology that relies on not having *a priori* knowledge on the existence of deeper flow paths. Simulated travel time PDFs like those presented here have been reported in others studies for surface hydrology (*McGuire et al., 2007*; *Kirchner et al., 2000*) and compared to various distributions (e.g. exponential, gamma). The unimodal distribution of travel times is characteristic of systems at steady state, as opposed to distributions for transient systems which can be multimodal and considerably less skewed. One advantage provided by the analytical equation is that it could be applied also to transient systems, which is not the case for the $p_E(x,t)$ numerical approach in FEFLOW that prevents from running both flow and transport simultaneously in a transient mode when transporting $p_E(x,t)$.

The degree of imposed, geostatistically distributed heterogeneity shows a positive correlation with *Uo* and a negative one with wMTT in both topographic settings. It is yet to be determined if this relationship holds true in other types of heterogeneity. For instance, in multi-layered settings, where different connectivity patterns in the subsurface may emerge. In such a setting, the vertical connectivity of the layers could determine whether the system

behaves as SH or DH. In cases with limited connectivity, an aquifer will tend to behave as the SH scenario, whereas in highly connected layers it will gravitate towards a DH-like scenario. A localized multi-layered setting might have occurred in our study for scenarios with the largest correlation length ($I_{xy}$=450m). For such conditions, the overall pattern of wMTT and flow path length could be different from those presented here.

Even for surface hydrology, a conclusive relationship between watershed size and wMTT remains to be found (*Wolock et al., 1997*; *Asano et al., 2002*; *Shaman et al., 2004*). Both approaches evaluated here (analytical and $p_E(x,t)$) can provide insight in this relationship for subsurface hydrology via the analysis of mean travel time PDFs across multiple watersheds. In cases where computationally efficient simulations are sought, it is necessary to reduce the mesh resolution of the numerical model. That is, by making the mesh coarser in larger watersheds, less exchange flux locations will be identified, thus limiting the accuracy of the $p_E(x,t)$ field in the numerical model. It is in cases where quick results are needed, limited background information is available, or the watershed scale is a limiting factor for building a numerical model that the analytical method presented here can be envisioned as a modeling alternative.

## 2.7 Conclusions

A detailed analysis on the implementation of a proposed analytical methodology to estimate wMTTs and pMTT PDFs at the watershed scale is presented. We assessed the performance of the methodology using a virtual watershed that was subjected to various potential controls of MTT including topography, subsurface geometry and heterogeneity. A total of twenty-eight (28) scenarios were created for this purpose and the topographic setting was modified to promote groundwater exchange fluxes with surface water. The results were evaluated against a numerical approach that relies on identifying the probability of exit of water particles distributed across the watershed. The proposed methodology compares well at mid- to long- flow path distances, and reproduces the variations exhibited by the numerical model from one scenario to the next. However, it overestimates the travel time of water particles located in the vicinity of streams as the flow path delineation used to

support the analytical model fails to intercept the stream channel. The generated particle travel time distributions for the entire watershed were slightly less skewed to higher pMTT values. This is likely due to deeper flow paths generated around stream segments compared to the pMTT's numerical estimates. This effect does not significantly alter the location of the centroid of the distribution as the resulting wMTTs from all scenarios compare well with those of the numerical approach ($r^2$=0.80, n=28, $p$<0.001). The effect of shallow confining units on the distribution of pMTTs at the watershed scale can be as significant as the effect of increasing the topographic slope. Our work advances the search for correlations between wMTT and topography for subsurface hydrology, but this will require going beyond the two topographic settings considered here.

The likely existence of preferential flow paths helped explain the increase in both the calibrated bulk velocity $U_o$ (analytical model) and the consequent decrease in pMTTs (both types of models) with increased heterogeneity ($\sigma_Y^2$). The relationship between $U_o$ and $\sigma_Y^2$ exhibits a linear trend that is maintained with increased slope and is accentuated with increasing size of heterogeneity ($I_{xy}$). Will this trend continue for steeper slopes? How about milder slopes? Is this trend still valid for other watersheds? Finding a more comprehensive relationship between calibrated velocities and DEM-derived Darcy velocities is crucial to guarantee that the methodology we propose is transferable to ungauged watersheds. This relationship needs to be established for other watershed characteristics, such as size, slope, and layered heterogeneity to verify if and under which circumstances it can be scaled up.

The method applied here, with the simplicity and ubiquity of the tools used (i.e., GIS and MATLAB), to estimate wMTT and pMTT distribution, and the process of comparing to the numerical model output, can be used to identify watershed-scale relationships relative to travel time. We presented a first step towards identifying an array of settings where the analytical approach is a viable alternative to the use of computationally expensive numerical modeling.

# Chapter 3

# Geomorphological Controls on Subsurface Mean Travel Times (MTT): Multi-Watershed Performance Assessment of an Analytical MTT Model


## Summary

The effects of a suite of geomorphological parameters on groundwater mean travel times (MTTs) at the watershed scale are investigated by simultaneously applying an analytical and a numerical model to 9 watersheds. This study builds on the work in Chapter 2, in which the effects on travel time distributions (TTD) of other contributing factors, in particular aquifer heterogeneity and thickness, were analyzed. The numerical watershed models are implemented under fully homogeneous and constant recharge conditions. Comparisons of travel times estimated by the analytical and numerical methods are carried out for individual observation points (pMTTs) distributed across the watershed and at the whole watershed scale (wMTT). With the exception of three study sites largely dominated by mountainous terrain where the numerical model fails to provide reliable results, the estimates of pMTTs and wMTT from the analytical model compare moderately and well, respectively, against the numerical model output ($0.18<r^2<0.52$, and 0% to 12% difference). The analytical TTDs and wMTTs match especially well and, hence, they can be used to provide a first assessment of groundwater flow and transport of conservative solutes. The goodness of fit between the numerical and analytical models is tested for 28 geomorphological indexes in order to delineate the physical watershed characteristics under which the analytical method works best. Optimal watershed characteristics include a topographic relief < 790 m and drainage density < 2.7 $km^{-1}$. Single and multiple linear regression (SLR and MLR) models are used for the determination of the necessary analytical model parameters, that is, the smoothing factor ($SF$), uniform flow path velocity ($Uo$), and macrodispersion coefficient ($\lambda_L$). Texture topography (e.g. drainage density and structure) and topographic relief emerge as the strongest predictors of the parameters; for wMTTs,

topographic relief yields the highest predictive ability. The regression relationships are tested in three watersheds: Carroll Creek, Schneider Creek, and Nith River, all located in Ontario, Canada. With the predicted values of *SF*, *Uo*, and $\lambda_L$, the analytical model performs satisfactorily, except for Schneider Creek. Our analysis indicates that there are structural characteristics (e.g., low Horton's law of slopes $R_S$, values) for which the analytical model does not perform adequately and underestimates wMTT for Schneider Creek's watershed. While the analytical model is not expected to capture all of the intricate flow paths dynamics in real watersheds, the simplicity of its implementation make it an attractive alternative to numerical flow models, particularly in the absence of detailed information on the subsurface. Further research should help widen the spectrum of potential applications of the analytical methodology.

## 3.1 Introduction

The need to better constrain water fluxes and storage at the watershed scale has motivated studies using comparative analyses based on geomorphological features with the mean travel time (MTT) as a key metric of watershed response (*McGlynn et al., 2003*; *Tetzlaff et al., 2009a*; *McNamara et al., 2011*). There has been a long history of efforts in trying to establish the links between geomorphology and hydrological processes. Early work by Horton (*1932, 1945*) identified physiographic characteristics that typically correlate with stream discharge using measures developed in the field of morphometry (*Gardiner & Park, 1978*). The Hortonian analysis provides the means, through stream ordering, to compare stream networks and their hydrological and erosional processes (*Bowden & Wallis, 1964*). In more recent years, the roles of intrinsic geomorphological features, have been examined in montane regions in order to assess surface hydrology, specifically those related to topography (*Tetzlaff et al., 2009a*, *Tetzlaff et al., 2009b*; *Capell et al., 2012*), watershed size (*McGlynn et al., 2003*; *Hrachowitz et al., 2010*; *Hale & McDonnell, 2016a*), soils (*Rodgers et al., 2005*; *Tetzlaff et al., 2009b*; *Hale and McDonnell, 2016a*), and drainage density (*Hrachowitz et al., 2009*; *Soulsby et al., 2010*; *Capell et al., 2012*) as potential controls of watershed's MTT (wMTT).

In examining topography, Tetzlaff et al (*2009a*) found that wMTT is inversely correlated with topographic indexes in 55 watersheds located in eight diverse geographical regions in the northern hemisphere. Furthermore, in flatter terrain the permeability of soils may play a more important role in regulating flow regimes. In another comparative analysis (*Tetzlaff et al., 2009b*), responsive soils (i.e., with poor drainage capacity) in 10 watersheds within the Cairngorm mountains in Scotland exhibited better predictive power of wMTT than topographic indexes, showing that potential landscape controls may play different roles in different regions. Rodgers et al. (*2005*) suggested that the interaction between topography and responsive soils represents a major control of wMTT. In these studies, wMTT estimates were obtained from isotope analyses (e.g. $\delta^{18}O$) of surface waters draining montane regions that are characterized by shallow, and not fully impermeable bedrock (*McDonnell, 2003*; *McGrane et al., 2014*), yielding ages not older than 4 years. Watershed MTT estimates obtained this way were used by Hrachowitz et al. (*2009*) to develop a predictive equation of wMTT in 20 montane watersheds in Scotland as a function of drainage density, responsive soils, precipitation, and topographic wetness index. The MTTs in Hrachowitz et al. (*2009*) and in the studies mentioned above were estimated using a lumped-parameter model developed by Maloszewski and Zuber (*1982*) typically applied to environmental tracers. Another inter-watershed comparison study evaluated the effect of bedrock permeability on stream base flow MTT at 15 nested watersheds distributed in two sites with distinct bedrock geology (*Hale and McDonnell, 2016a*). Hale and McDonnell (*2016a*) found longer MTTs (~6.2 years) in permeable rocks where 67% of the variance in MTT can be explained by the drainage area. On the other hand, in poorly permeable rocks 91% of the variance of shorter MTTs (1.8 years) was explained by the ratio of median flow path length to median flow path gradient. In contrast to these surficial hydrology studies, fewer studies have focused on the effects of topography (*Wörman et al., 2007*; *Cardenas, 2007*; *Marklund & Wörman, 2011*; *Welch et al., 2012*) and watershed size (*Wolock et al., 1997*) exerted over subsurface travel time.

Travel times distributions (TTDs) in non-mountainous settings are characterized by extended tails and MTTs that are on the order of decades (*Frisbee et al., 2013*; *Hale et al., 2016b*). Marklund and Worman (*2011*) showed that topography and bedrock overburden are

major controls on the TTDs at nuclear depository sites in Sweden. Wörman et al. (*2007*) verified: first, the fractal behavior of landscape topography initially identified in previous studies (*Rodriguez-Iturbe et al., 1992*); secondly, the influence of landscape topography on subsurface water residence times and the similarities of their distributions at multiple scales; and lastly, the scale effect of geomorphological features on subsurface flow. Cardenas (*2007*) used topographically-driven groundwater flow and transport in a homogeneous porous media to show that the observed fractal behavior on stream chemistry can be explained not only by heterogeneity, as suggested by previous studies, but also by the influence of topography. Wolock et al (*1997*) presented evidence that low-flow stream chemistry exhibited less variability as watershed size and subsurface contact time increased.

The impact of climate and geology as it relates to subsurface water residence times has also received attention. Maxwell et al (*2016*) developed the first surface and subsurface residence times for most of continental North America at a high spatial resolution of 1 km using a fully integrated model (PARFLOW, *Jones & Woodward, 2001*), and for a domain that reached a fixed depth of 102 m below the ground surface. Recharge was spatially estimated as $P - ET$ and, at the continental scale, constituted together with the mean hydraulic conductivity the major controllers of peak travel times in the subsurface. Maxwell et al. (*2016*) also showed the fractal behavior of travel time distributions of major watersheds, and presented evidence that high aridity (i.e., low recharge) yields to longer flow paths and travel times. However, their results also suggest that more accurate representations of TTDs require more detailed information on bedrock overburden, hydraulic properties, and a finer spatial resolution. Considering both the mobilization of old water during storm events and its persistent chemistry (*Kirchner, 2003*), and the potential inter-basin connectivity of longer flow paths associated with hundreds or thousands years of travel time, the analysis of water quality impacts from diffuse pollution of anthropogenic or geologic origin can be improved with a better understanding of travel time distributions.

Analytical approaches have been developed to obtain either watershed-scale TTDs (*Haitjema, 1995*) or simple, one-dimensional applications to estimate travel time probability

density functions (PDFs) (*Cornaton, 2012*; *Soltani and Cvetkovic, 2013*). The work presented in Chapter 2 is the first attempt at applying the 1-D analytical equation for travel time of Soltani and Cvetkovic (*2013*) at the watershed scale by comparing the analytical solution to a numerical subsurface model. In Chapter 2, this comparison was performed for a virtual watershed, to which 28 scenarios with different conditions of heterogeneity, topography, and aquifer depth were applied. The outcome was the development of an analytical methodology to estimate particle median travel times (pMTT), their distributions, and wMTT. The analytical distributions compared with the numerical estimates well ($0.34 < r^2 < 0.58$ for pMTT; and, $0.72 < r^2 < 0.94$ for wMTT). In Chapter 2, it was found that wMTT negatively correlates with heterogeneity ($I_{xy}$, $\sigma_Y^2$), which was explained by the formation of preferential flow paths along larger hydraulic conductivity lenses. The effect of bedrock overburden was to generate deeper and longer flow paths. The analytical model in Chapter 2 underestimated the arrival frequency of the peak of the travel time PDFs. This arrival frequency is primarily controlled by the macrodispersion coefficient, which in all scenarios remained under 10% of the total flow path length. The results also revealed the importance of flow path delineation in estimating particle travel times and the links with topography and the frequency of interception of the stream network. The uniform analytical flow velocities obtained in Chapter 2 exhibited a clear trend with heterogeneity, while a trend with topography was merely implied. The conclusion section of Chapter 2 suggested exploring further the effect of topography and stream density in other geomorphological settings as they may constitute important regulators of travel times in a watershed.

The geomorphological measures used as predictors of travel time in surficial hydrology have included topographic and slope indexes, soil type, and drainage density. The existing studies show there is no single universal controlling driver of travel time (*Tetzlaff et al., 2009a, 2009b*; *Hrachowitz et al., 2009*). However, topographic indexes are likely to be among the top controlling factors (*Tetzlaff et al., 2009a*; *Ali et al., 2012*). In the realm of subsurface travel times, inter-watershed comparisons remain very limited. The degree of complexity involved in developing subsurface watershed models, combined with the great variety of subsurface models used to simulate watershed-scale groundwater flow and transport, have

hindered the conduct of inter-watershed comparison studies. The transferability of knowledge on the mechanisms that potentially control subsurface travel time distributions, from well-studied basins to ungauged basins is yet to be explored.

In this paper we build on the work presented in Chapter 2 by applying the proposed methodology to eight watersheds in addition to Alder Creek. We include a total of 28 geomorphological indexes into the analysis to test their effects on numerically and analytically estimated travel times. The selected geomorphological indexes fit into five categories: elevation, shape, texture topography, fractal dimensions, and Horton's laws. A virtual watershed approach is used: the numerical model yields travel time PDFs for each watershed, under similar conditions of recharge and a homogeneous subsurface to facilitate the inter-basin comparison of wMTT. The effects of these geomorphological indexes are translated into transferable relationships to predict wMTT in ungauged watersheds. In our study, the calibrated Soltani-Cvetkovic analytical equation (*Soltani & Cvetkovic, 2013*) is compared against the travel time distribution estimates of a three-dimensional, watershed-scale subsurface numerical model in order to identify the more discerning indicators that can then inform future applications of the analytical TTD approach.

Here, the following major goals are targeted with our approach: first, compare TTDs, pMTT, and wMTT from both numerical and analytical models; second, identify significant discerning indexes based on the goodness of fit between numerical and analytical for future analytical model applications; third, develop regression models for predicting analytical model parameters and their evaluation on selected verification watersheds, for future implementations; and finally, identify major wMTT predictors from an array of geomorphological indexes through regression models.

Our study broadens the knowledge on the intrinsic geomorphic mechanisms controlling travel times in watersheds and yields an accessible method for MTT estimation using readily available tools (i.e., GIS and MATLAB).

## 3.2 Methods

For this study, both numerical and analytical models were developed for the estimation of MTTs and their distributions at the watershed scale for a total of 9 watersheds in North America. In this section, details on both types of models are provided together with a description of the study watersheds and the geomorphological indexes that were chosen for analysis.

### 3.2.1 Numerical and Analytical Travel Time

In Chapter 2, I developed an analytical method to estimate pMTTs, their distribution, and wMTT for an entire watershed. For the numerical model, a virtual watershed approach was used applying the ground surface and bedrock topography to a fully 3-D homogeneous subsurface model for each of the 9 study watersheds. The estimates derived from the analytical method were calibrated against those obtained with the numerical model and compared against the selected geomorphological indexes.

#### 3.2.1.1 Numerical Method

The numerical estimation of travel time was performed by using the probability of exit approach implemented in FEFLOW (DHI-Wasy GmbH). This approach was developed by Cornaton (*2004*) and Cornaton and Perrochet (*2006*). We refer the reader to these publications and to Cornaton (*2014*) where a recent update to the mathematical treatment can be found in more detail. A brief description of this method follows, which is specifically applied to subsurface travel time distributions at the watershed scale.

The backward adjoint model equations presented in (*Cornaton, 2004*) form the basis for calculating the life-expectancy probability density function ($g_E$) of a particle in the porous media, defined as the time left for the particle before exiting the domain through an outlet. The probability of exit CDF ($p_E(x,t)$) is similar to the life-expectancy CDF ($g_E$), however, by having $p_E$ being distributed as a random variable, it provides the means to estimate: i) the life-expectancy of any particle in the domain, and ii) the probability that a water particle will exit the domain. The $p_E(x,t)$ estimates can be calculated for a specific outlet that is part of a

multiple outlet system that could include, for example: wells, seepage surfaces, and exfiltration points along a river bed. This is accomplished by assigning a Cauchy boundary condition equal to unity (the maximum probability) to the target outlet. The target outlet in our case is the hundreds to thousands of exfiltration points along the stream bed. From this point backwards, a field of exit probability is created at every time step of the simulation depicting a break-through curve of exit probability at observation points (OPs) distributed in the watershed. Particles located in areas adjacent to the stream will exit the domain through this target outlet in their entirety with $p_E(x,t)$ values of 1.0. For particles located close to the boundaries of the watershed, $p_E(x,t)$ values are < 1, as these particles are affected by other potential outlets in the multiple outlet system. For this study, only two outlets are considered to be present: exfiltration through the stream bed and with groundwater flowing out near the watershed's outlet.

The numerical modeling approach available in FEFLOW for travel time requires that the subsurface flow system be at steady state while the transport of the non-reactive tracer (i.e., age), is simulated as a transient process. The resulting break-through curve from each observation point corresponds to the travel time cumulative density function (CDF). Similar to when defining capture zones for wells, a probability of exit threshold of 0.5 is applied to the raw data treatment to exclude those observation points that fall outside of the natural drainage area (i.e., the groundwatershed) defined by the $p_E(x,t)$ field. Observations points outside of the natural drainage area discharge through the porous media outlet, that is, the corresponding water particles exit as groundwater into the adjacent watershed controlled by a Dirichlet boundary condition.

The MTT for each observation point is estimated from the median's horizontal coordinate of the travel time CDF. For further analysis, the travel time CDF is numerically converted into a travel time PDF in MATLAB for calibration of the analytical pMTT estimates.

#### 3.2.1.2 Analytical Method

The analytical method consists of applying the 1-D travel time distribution equation developed by Soltani and Cvetkovic (*2013*) to a set of observation points or particles spread

out in a grid across the watershed. The equation provides a CDF of travel time for a particle leaving its point of origin in the watershed up to its point of discharge. The point of discharge is defined using the GIS application ArcNLET (*Rios et al., 2013*). ArcNLET uses topography as a proxy for the potentiometric surface for which the Dupuit-Forchheimer approximation is applied to obtain a groundwater flow velocity and direction field along the horizontal plane. The direction and velocity fields are intercepted in ArcNLET by rivers, lakes, and other waterbodies that form the local surface hydrology. The output from ArcNLET that is incorporated into the analytical method corresponds to the flow path delineation and the distance for each particle released in the watershed until it reaches a waterbody. The corresponding expression developed by Soltani and Cvetkovic (*2013*) is:

$$F_f(t;x) = \frac{1}{2} erfc\left(\frac{x - U_0\varphi(t)}{\sqrt{4\lambda_L U_0 \varphi(t)}}\right) \qquad \text{Eq. 3.1}$$

where, $x$ is the flow path distance of each particle obtained from ArcNLET, $U_O$ is the mean uniform bulk velocity, $\varphi(t)$ is a dimensionless factor for transient conditions, and $\lambda_L$, is the Fickian macrodispersion term. The 1-D analytical equation is applied on fully stationary condition, i.e., $\varphi(t) = 1$.

Equation 3.1 is derived from the solution of the 1-D ADE equation. Further details on its derivation and testing are provided in Soltani and Cvetkovic (*2013*). Two parameters in this equation are calibrated against the numerical MTT estimates: $\lambda_L$ and $U_O$. The numerical determination of travel time is limited to stationary conditions. The flow path distance ($x$) is a sensitive parameter controlling the value of MTT for each observation point. In ArcNLET, variations in the delineation of a flow path and its distance ($x$) are achieved by assigning different values to a parameter called the smoothing factor (*SF*). This parameter refers to how close the representation of the potentiometric surface mimics the ground topography, that is, with low *SF* values (1-20) the potentiometric surface closely resembles the ground surface, and for high values (30-50) the resulting potentiometric surface is more independent from topography.

With this in mind, in order to identify the configuration of parameters in the analytical method that provide the best match to the MTT estimates from the numerical model, the following considerations apply:

- Stream Network. In the numerical model, groundwater discharge does not occur everywhere along the riverbed. In a domain with no heterogeneity, the distribution of groundwater discharge is primarily controlled by ground and bedrock topography and by the density of the river network. Several delineations of stream networks are evaluated for the study catchments. During the calibration process, stream segments are added and excluded as specified by a minimum number of cells from a GIS flow accumulation analysis. In this analysis, the number of cells needed to initiate a stream segment corresponds to a specific minimum drainage area. For the homogeneous subsurface domain ($K_{xy}=K_z=5.26$ m/d) chosen in this study, the portion of the stream network that actively exchanges with groundwater corresponds to second and third Strahler stream orders. In presumably more realistic heterogeneous domain, however, first and second Strahler stream orders are likely to yield the best calibration results. First order stream only play a role when heterogeneity is incorporated in the headwater area of a watershed.
- Smoothing Factor (*SF*). For any observation point in the watershed, increasing this parameter tends to re-route the flow path to a point of discharge located further away from its origin. As this parameter is applied to the entire ensemble of observation points, the MTT for the entire watershed also increases (wMTT). Several SFs are tested in each study catchment during calibration, in combination with different stream network configurations. For future implementations of the analytical model, regression models that use the geomorphological indexes considered here can be used as predictors for *SF*, as well as $\lambda_L$ and *Uo* (see Section 3.3.3).
- Macrodispersion ($\lambda_L$) and Mean Bulk Velocity (*Uo*). These parameters are calibrated against the pMTTs estimated with the numerical model. Twelve out of the entire ensemble of observation points are selected for the calibration of the travel time

PDFs generated from the analytical model (by converting the travel time CDF) and the numerical model (as derived from the travel time break-through curve). When matching both PDFs, the $\lambda_L$ value modulates the spread of the bell-shaped curve (typically skewed to the right). That is, the greater $\lambda_L$, the wider the PDF becomes accompanied by lower arrival frequencies, whereas for lower $\lambda_L$ the PDF becomes more compressed (i.e., with a sharper peak) accompanied by greater arrival frequencies. The role of $U_O$ in the calibration process is that of matching the location of the travel time PDF peak along the time (horizontal) axis.

For a given study watershed, a calibrated set of parameters is obtained by first identifying the best configuration of the stream network and the SF. This is done by comparing the numerical MTT estimates against the analytical values for each configuration. The calibration of $\lambda_L$ and $U_O$ for the chosen calibration points is performed next using the best configuration obtained in the previous step. The final result of the calibration process is a mean bulk velocity and an equation of macrodispersion varying with flow path distance, both to be applied to the ensemble of observation points.

### 3.2.2 Case Study Watersheds

Nine watersheds are included in this study covering a wide range of slopes, sizes, and drainage density. All of them are located in North America (Figure 3-1, Table 3-1), five in Canada and four in the United States. Coincidentally, the study sites in Canada have mild to flat topographic relief, whereas the sites in the United States can be considered hillslope-dominated watersheds. These sites are chosen because subsurface models have been developed for them and are available in recent publications. Three types of data are extracted of the watersheds: the ground and bedrock topography, and the stream network GIS delineation. Note, however, that bedrock topography is not available for all watersheds. Information on subsurface heterogeneity and local climatology are also gathered, when available, and may be used in the continuation of this study in the future.

Three study sites are located in the Grand River basin (6800 km$^2$), Ontario (Canada): Upper Laurel Creek (31.2 km$^2$), Upper Nith (300.4 km$^2$), and Alder Creek (78.0 km$^2$). They have relatively muted topographic relief and slopes ranging from 67 to 122 m, and 1.17 to 3.27 degrees, respectively.

Table 3-1**.** Major watershed characteristics of study areas.

| Basin | ID | Area [km$^2$] | Strahler Order | DEM cell size [m] | Mean Elevation [m] | Topo. Relief [m] | Bedrock Surface Available | mean DEM-cell Slope [deg] |
|---|---|---|---|---|---|---|---|---|
| Alder Creek | AlC | 78.0 | 5 | 25 | 353 | 122 | Yes | 2.57 |
| des Anglais River | dAn | 701.3 | 5 | 30 | 226 | 372 | No[1] | 1.04 |
| Ganaraska River | Gan | 278.1 | 5 | 20 | 233 | 317 | Yes | 3.67 |
| Pamilco Canyon | Pam | 134.9 | 4 | 20 | 1898 | 1065 | No | 9.53 |
| Rattlesnake River | Rat | 49.5 | 4 | 20 | 2182 | 928 | No | 11.7 |
| Sagehen River | Sag | 37.2 | 4 | 20 | 2263 | 790 | No | 8.62 |
| Thomas Creek | ThC | 198.6 | 6 | 20 | 740 | 1211 | No | 15.4 |
| Upper Laurel Creek | uLc | 31.2 | 4 | 25 | 376 | 74 | Yes | 3.27 |
| Upper Nith River | uNi | 300.4 | 4 | 25 | 388 | 67 | Yes | 1.17 |

[1] bedrock surface was estimated based on either well data (dAn) or available hydrogeological maps (Pam, Rat, and ThC).

The Ganaraska River (498.5 km$^2$) discharges directly to Lake Ontario, with a significant topographic relief of 317 m. The thickness of the overburden deposits increases from south to north, that is, from the Lake Ontario shoreline to the Oak Ridges Moraine area, located in the headwaters of the basin (*Earthfx, 2006*).

Des Anglais River basin is located in Quebec, at the border with the United States. It is an extremely flat basin except for its headwaters surrounding against Covey Hill, on the outskirts of the Adirondacks Mountains, yielding a significant topographic relief of 372 m.

Rattlesnake River (49.5 km$^2$) and Pamilco Canyon (134.9 km$^2$) basins are both located within the Lower Walker River basin (10,230 km$^2$) in Nevada (USA). Their topographic relief is similar and significant, 928 and 1065 m, respectively. The drainage network is sparse

as this region is dominated by semi-arid hydrologic conditions with intermittent streams frequently present (*Allander et al., 2014*).

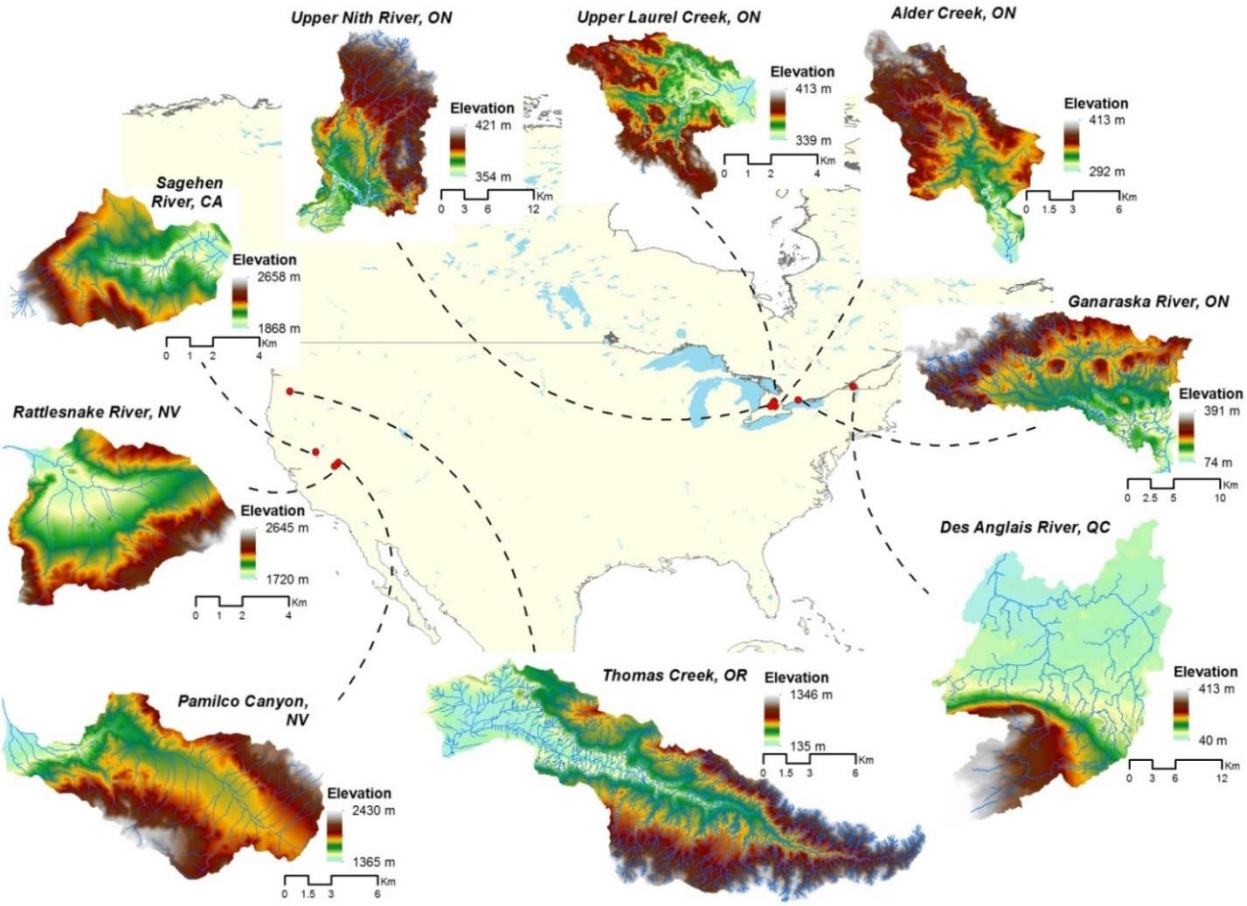


Figure 3-1. Distribution map of study areas in North America. Elevation ranking bars and drawing scales are shown for each study area.

The Sagehen River (37.2 km$^2$) basin is located in California (USA) on the eastern flank of the northern Sierra Nevada. It is a commonly used basin for local modeling efforts and available information is plentiful. It is a basin dominated by steep headwaters and a U-shaped valley, characteristic of glaciated terrain and meadow areas (*Essaid et al., 2014*). It has a topographic relief of 790 m and a steep mean slope of 8.62 degrees.

The Thomas Creek (198.6 km²) basin in Oregon (USA) is located within the Santiam River basin (4700 km²). This basin has the greatest topographic relief (1211 m) and the steepest mean slope (15.4 degrees), from all the basins included in this study.

### 3.2.3 Geomorphological Indexes

A large number of indexes of basin geomorphology are estimated for the study areas in order to establish how they relate to the distribution of travel times in the watersheds. These indexes were grouped in Table 3-2 in the following classes: texture topography, elevation, shape, fractal dimensions, and mixed indexes. They are estimated using either a mathematical expression or graphically, by plotting data extracted from collected information.

Empirical "laws" initially suggested by Horton (*1945*) for stream networks are included in this study (Table 3-2). In particular, we use a modified "law" of stream lengths ($R_L$) to estimate the total length of streams of order $w$ in the watershed, not the average length as originally presented by Horton (*1945*). A Strahler's stream-ordering scheme is applied to the watersheds.

Several elevation and slope measures are considered, many of which are self-explanatory except for the hypsometric curve and link slope (*LnkSlp*). The hypsometric curve provides a three-dimensional metric of the watershed by plotting relative height against relative area. The hypsometric curve can be used as an estimate of the age or activity stage of a watershed's geological evolution (*Bras, 1990*). The fluvial scaling of link slopes (*LnkSlp*) is examined using Shreve's (*1966*) stream ordering system as scaling index (i.e., the logarithm of magnitude) against the logarithm of link slopes. This relationship follows a power law scaling of the form: $ax^{-n}$, where $n$ has a reported average of 0.6 (*Tarboton et al., 1989*) and a range of 0.37-0.83 (*Flint, 1974*).

The shape of the watersheds is also quantified with several indexes that are typically based on comparing specific shapes and shape qualities to basin characteristics, such as area ($A$), perimeter ($P$), length ($L_T$) and width ($W$).

Table 3-2. Geomorphological indices included in present study.

| Parameter | Symbol | Formula | Units | Notes / Description | Reference |
|---|---|---|---|---|---|
| *Horton's Law measures* | | | | | |
| Horton's law of streams (Bifurcation ratio) | $N_S$, $R_B$ | $N_S = R_B \cdot SO + i$ | [-] | $N_S$: number of stream segments for each Strahler order (SO). $R_B$: is the slope of the SO vs. $N_S$ relationship; i: intercept. | Horton (1945); Strahler (1952); Tarboton et al. (1988); Brass (1990); Rodriguez-Iturbe and Rinaldo (1997) |
| Horton's law of stream length | mSL, $R_L$ | $mSL = R_L \cdot SO + i$ | [-] | mSL: mean stream length for each Strahler order (SO). $R_L$: is the slope of the SO vs. mSL relationship; i: intercept. | |
| Horton's law of stream slopes | mSS, $R_S$ | $mSS = R_S \cdot SO + i$ | [-] | mSS: mean stream slopes for each Strahler order (SO). $R_S$: is the slope of the SO vs. mSS relationship ; i: intercept. | |
| Link slope | *LnkSlp* | $Slp = LnkSlp \cdot N + i$ | [%] | Corresponds to the slope of the relationship between mSS [%] and Shreve order [or magnitude, N]; i: intercept. | Tarboton et al (1989) |
| *Texture topography measures* | | | | | |
| Drainage density | *Dd* | $Dd = L / A$ | [1/km] | L: stream segments length [km]; A: watershed area [$km^2$] | Horton (1945) |
| Texture ratio | *Tex* | $Tex = N_{mln} / P$ | [1/km] | $N_{mln}$: maximum number of intersected stream segments by an elevation contour line; P: watershed perimeter [km] | Gardiner (1975) |
| Drainage frequency | *DF* | $DF = N_S / A$ | [1/$km^2$] | $N_S$: number of stream segments; A:watershed area [$km^2$] | Horton (1945); Brass (1990) |
| Ruggedness number | *HDd* | $HDd = H \cdot Dd$ | [-] | H: mean stream segment drop [km]; Dd: drainage density [1/km] | Strahler (1964) |
| Texture - Perimeter | *TexPer* | $TexPer = N_{mln} / P_{UP}$ | [1/km] | $P_{UP}$: perimeter for upstream watershed encompassed by elevation contour line with maximum number of intersected stream segments. | Smith (1950); Leopold et al (1964) |
| *Elevation measures* | | | | | |
| Relief | *Relief* | Relief = Zmax-Zmin | [m] | Topographic relief, elevation difference within watershed | Strahler (1964) |
| DEM cell-size slope | *cSlope* | [-] | [deg] | Slope measurement given by the largest drop at each cell of the DEM, using Slope_3d GIS tool. | [-] |
| Main channel slope | *Schan* | [-] | [%] | Mean channel drop along segment. | Gardiner (1975) |
| Mean Gradient | *mGrad* | $mGrad = [Relief / L_T] \cdot 100$ | [%] | $L_T$: longitudinal length of watershed, longer dimension of watershed [km] | Gardiner (1975) |
| Hypsometric curve | [-] | [-] | [-] | Relationship between relative height (contour elevation minus outlet elevation) and relative area (area upstream of contour elevation divided by total area). | Leopold et al (1964); Brass (1990) |
| DEM slope probability histogram | [-] | [-] | [-] | Frequency occurrences of DEM cell-size slopes [deg] distributed in 100 bins. The DEM cell-size was kepth within 25-30m | [-] |

Table 3-2. Geomorphological indices included in present study. (continued)

| Parameter | Symbol | Formula | Units | Notes / Description | Reference |
|---|---|---|---|---|---|
| *Shape measures* | | | | | |
| Circularity | $R_C$ | $R_C = A / Aceq$ | [-] | Relates watershed area [A] with the area of a circle [Aceq] with the same perimeter length as the watershed. | Jarvis, R (1976) |
| Lemniscate ratio | $P_{LR}$ | $E\left(\frac{\pi}{2}\middle\vert m\right) = \int_0^{\pi/2} \sqrt{1 - m * \sin^2(\varphi)}\, d\varphi$ ; $m = \left(4A\sqrt{((L^2 * \pi/4A) - 1}/(L^2 * \pi)\right)^2$ ; $eP = 2L_T E(a\vert m)$ ; $P_{LR} = eP/P$ | [-] | Compares the perimeter of a lemniscate branch (eP) against that of the watershed (P). *eP* is estimated with the incomplete elliptical integral of the second kind (E(a \| m)). | Chorley et al. (1957); Gardiner, V. (1975) |
| Form factor | *FormF* | $FormF = A / L_T^2$ | [-] | Relates watershed area [A] with a square of length equivalent to the longer dimension of watershed, $L_T$ [km]. | Gardiner (1975) |
| Elongation ratio | *Er* | $Er = \sqrt{A} / L_T$ | [-] | Relates the square root of the watershed's area with $L_T$ [km] | Gardiner (1975) |
| Compactness | *C* | $C = P / \sqrt{A}$ | [-] | Relates the watershed's perimeter [P] with the square root of the area [A]. | MacEachren, A. (1985) |
| Relative distance variance | *RDV* | $RDV = \frac{A}{2\pi(\sigma_x^2 + \sigma_y^2)}$ | [km] | $\sigma^2_X$ and $\sigma^2_Y$: distance variance of 100-m cells across watershed with respect to its centroid, for the x and y axis. Equivalent to estimating the moment of an area. | MacEachren, A. (1985) |
| Main channel length | *MnChL* | [-] | [km] | Main stream length as defined by Shreve's (1966) stream order. | Gardiner (1975) |
| *Fractal dimensions* | | | | | |
| Stream fractal BC method - plane | $D_{BCst}$ | $N_B = D_{BCst} \cdot bs + i$ | [1/m] | BCst: box-counting method applied to a stream network; $N_B$: number of boxes; bs: box size [m] determined by GIS grid, which is increasingly varied to develop this relationship; i: intercept. » Steeper slope ~2.0 in Log [bs] vs Log [$N_B$] plot corresponding to larger box sizes, for $D_{BCst}$. » Flatter slope ~1.0 in Log [bs] vs Log [$N_B$] plot corresponding to smaller box sizes, for $d_{BCst}$. » Steeper slope ~1.0 Log [bs] vs Log [$N_B$]plot corresponding to larger box size, for $D_{BCp}$. | Mandelbrot (1983); Tarboton et al. (1988); Tarboton et al. (1989); Rodriguez-Iturbe and Rinaldo (1997) |
| Stream fractal BC method - 1D | $d_{BCst}$ | $N_B = d_{BCst} \cdot bs + i$ | [1/m] | | |
| Perimeter fractal BC method | $D_{BCp}$ | $N_B = D_{BCp} \cdot bs + i$ | [1/m] | | |
| Perimeter fractal WD method | $D_{WDp}$ | -- | [km] | Walking-Divider (WD) method applied to northing and easting coordinates of watershed's perimeter: an increasing chord length is used for each estimation of the perimeter as it 'walks' through its entire length. | |
| *Mixed measures* | | | | | |
| Link concentration | [-] | [-] | [-] | Relationship between number of stream segments intercepted by a contour elevation and relative height (contour elevation minus outlet elevation). | Mesa (1986); Gupta et al. (1986) |
| Hack's law | *LvAa*, *LvAb*, *LvAab* | $L_{MC} = a \cdot A^b$ | [-] | Relationship between main channel lenght ($L_{MC}$) and respective drainage area (A). *LvAa* , *LvAb* , and *LvAab* refers to the coefficient, exponent, and product of coefficient and product of this power law relationship. | Leopold et al. (1964); Rodriguez-Iturbe & Rinaldo (1997) |

The scaling behavior of the stream network of a watershed is quantified by calculating its fractal dimension using the box-counting technique (*Lovejoy et al., 1987*). The larger the box size the more space-filling the network is as its $D_{BCst}$ approaches 2, which corresponds to the dimension of the feature being captured by the river network (i.e., the watershed). The Walking-Divider method is also used to estimate the perimeter's fractal dimension. A FORTRAN code for this method is provided in Lam and De Cola (*1993*), modified from Shelberg et al. (*1982*). It is rewritten in MATLAB for this study.

## 3.3 Results

### 3.3.1 Analytical vs. Numerical Travel Times

The frequency distributions of the median travel times estimated with the numerical and analytical methods are compared for each watershed in Figure 3-2. Also shown on the figure are the values of descriptors of the shape of the distributions that can be used to estimate the goodness-of-fit between the two methods. For most watersheds, the distributions obtained with both methods are in fair agreement, except for Pamilco River, Rattlesnake River, and Thomas Creek watersheds where the numerical model exhibits extremely high frequencies at very short travel times. These watersheds are located in areas with hillslope-dominated geomorphological features typical of montane regions such as strong topographic relief and slopes. Sagehen River watershed is also located in a montane region; however, its distribution of pMTTs exhibits better agreement between models in spite of having the fourth largest topographic relief (790 m). Excluding these three watersheds, the mean, median, and standard deviation of the pMTT analytical model estimates follow closely those estimates from the numerical model, with in most cases, moderate underestimations of the mean and standard deviation.

Skewnesss of the analytical distributions is not well matched to the numerical ones in the Upper Laurel Creek and Ganaraska River watersheds. In terms of kurtosis, the occurrence of infrequent outliers is highest for Alder Creek, des Anglais River, and Ganaraska River watersheds, with the largest measure quantified for the analytical method estimates for des

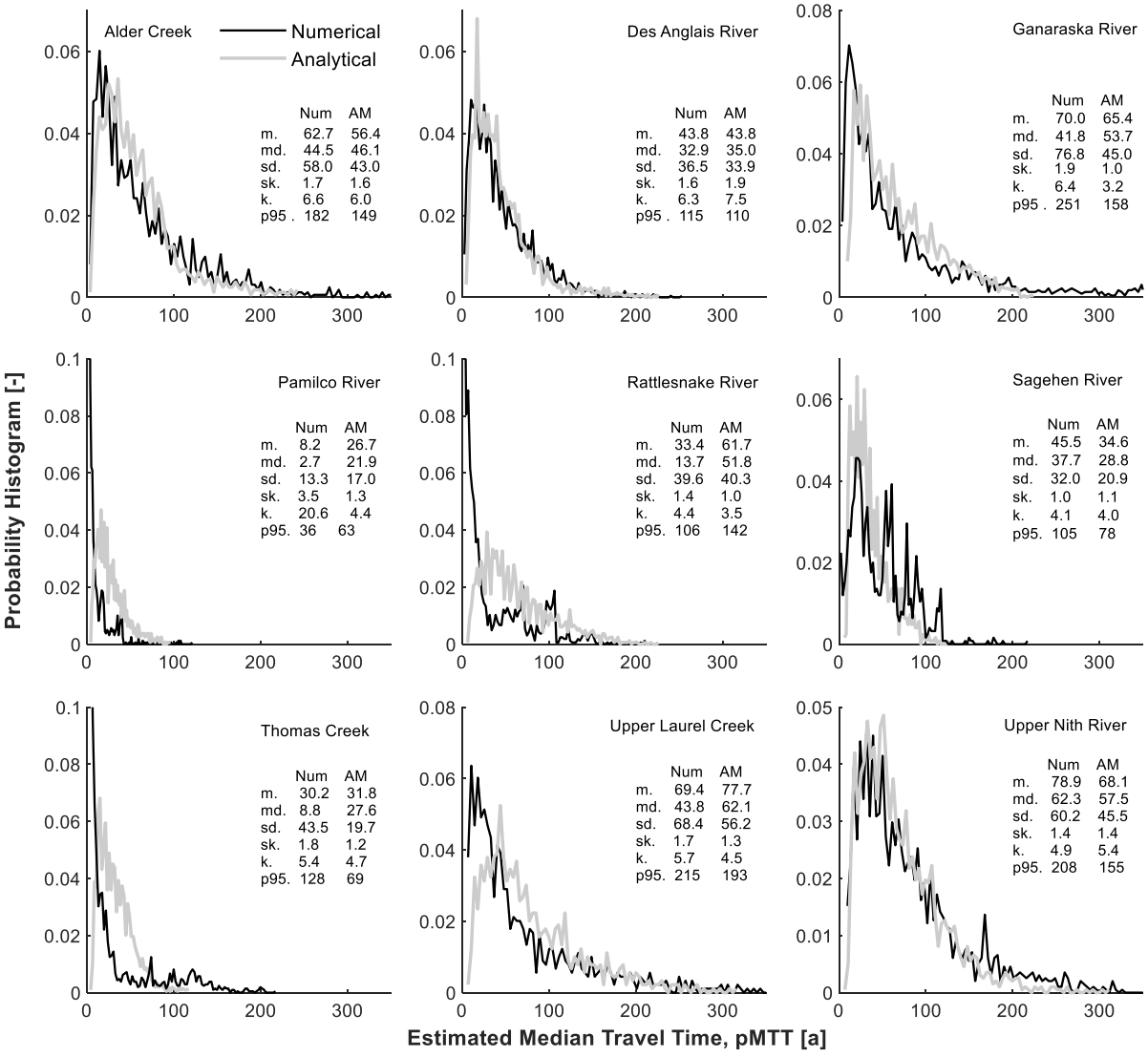


Figure 3-2. Frequency distribution of median travel times (pMTTs) estimated by both numerical (Num) and analytical (AM) methods for the nine watersheds. Measures of fit for the distributions are also presented (m.: mean, md.: median, sd.: standard deviation, sk.: skewness, k.: kurtosis, p95.: the 95$^{th}$ percentile) for both methods.

Anglais River. The closest kurtosis value to a normal distribution shape of 3.0 was for the analytical method pMTT estimates for Ganaraska River watershed, describing its smooth transition through the spectrum of travel times. Discrepancies between the magnitudes of

the frequencies are observed in most study sites especially for the Sagehen River watershed, where the occurrence of large and wide spikes of travel times are present likely at different locations in the watershed. These locations could be along the slopes of hillslope areas of this, rather montainous watershed, yielding clusters of water particles with long travel times. This phenomenon is replicated by the analytical method but only at shorter travel times. The underestimation in the standard deviation of the analytical model pMTTs is indicative of the wider spread of the travel times estimated by the numerical model. The number of occurrences of the longest travel times that exceed the 95$^{th}$ percentile is very small and adds little to the analysis. This 95$^{th}$ percentile value of travel time is encompassed by the range of travel times estimated by the analytical model indicating that the 95% of travel time occurrences in a watershed are predicted by the proposed methodology.

The mean difference in wMTTs is (+)5.3 years between the models. Out of the three "problematic" hillslope watersheds, the largest differences of 19 and 29 years are for Pamilco Canyon and Rattlesnake Flat, respectively. When excluding Rattlesnake Flat, Pamilco Canyon, and Thomas Creek (RPT watersheds, hereafter) watersheds, the mean error in wMTTs is only (+)0.33 years and a good correlation between analytical and numerical wMTT is observed ($r^2$=0.89, Figure 3-3). When including all watersheds, the correlation becomes weaker ($r^2$=0.71). Both correlations indicate a slight overestimation of wMTT by the analytical method, but it is more evident when the RPT watersheds are included.

The estimates of pMTTs and the wMTT computed with the analytical and numerical methods are compared for the study watersheds in Figure 3-4. The best performance, measured by r-squared, of the analytical model occurs in Alder Creek ($r^2$=0.52, Alc), followed by Upper Laurel Creek ($r^2$=0.30, uLa) and Upper Nith River ($r^2$=0.25, uNi), which coincidentally are all located in the Grand River watershed (Ontario, Canada). The goodness of fit for the pMTTs between these two methods is lowest for Rattlesnake Flat ($r^2$=0.03, Rat). The worst performance is found again on the RPT watersheds. The analytical method in Sagehen River (Sag) explains 18% of the variance of pMTT from the numerical. Additional

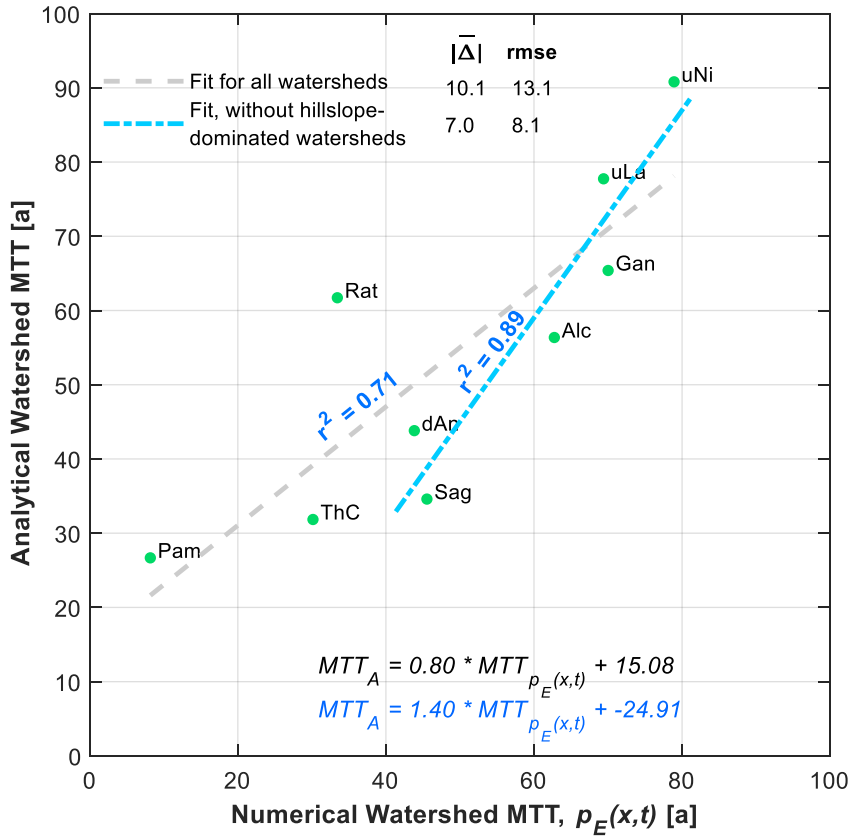


Figure 3-3. Watershed MTTs (wMTT in years) estimates by the calibrated analytical and numerical methods. Linear regression lines with and without RPT watersheds are shown together with their respective $r^2$ values. The root-mean-squared error (rmse) and mean absolute error ($|\bar{\Delta}|$) measures of fit are also shown.

measures of fit such as root-mean-squared error (rmse) and mean absolute error ($|\bar{\Delta}|$) are not sensitive to the agreement of the analytical model when estimating pMTT with respect to the numerical approach $p_E(x,t)$.

Some watersheds exhibit vertical 'banding' in the pMTTs estimated with the numerical model. That is, for OPs with similar $p_E(x,t)$-estimated MTTs their analytical counterpart exhibited a wide range of travel times. This vertical 'banding' is seen for the three hillslope-dominated watersheds (Figure 3-4d, Figure 3-4e, Figure 3-4g), and is most prominently expressed in Pamilco Canyon and Rattlesnake Flat. It extends to OPs with extremely short

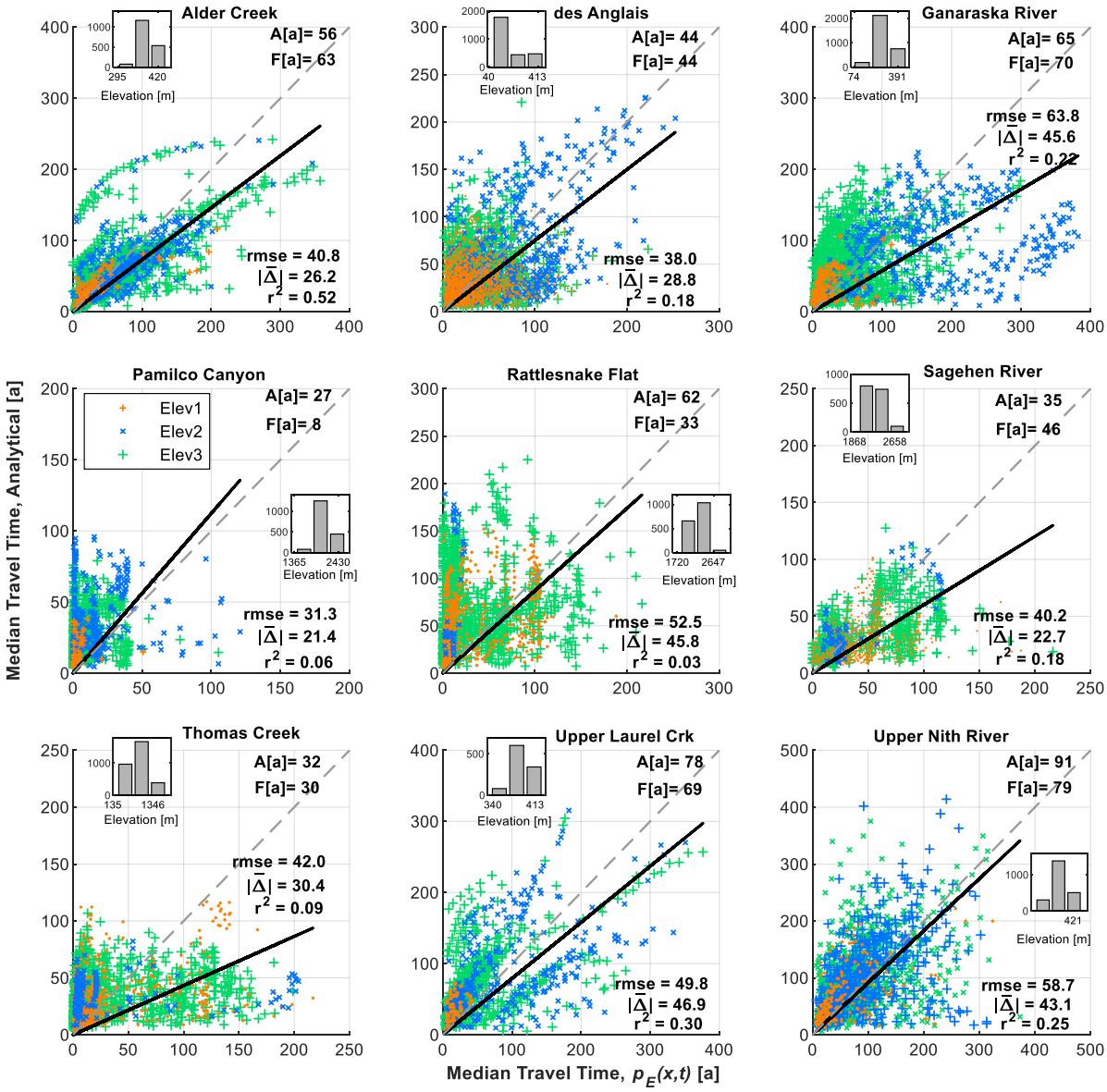


Figure 3-4. Scatter plots for calibrated analytical and numerical ($p_E$) particle MTTs for the nine watersheds. The watershed MTTs are also reported for the analytical (A) and numerical (F) models in years (a). Particle MTTs are discretized in color by three equal intervals of elevation: grey, green, and blue for interval Elev1, Elev 2 and Elev3. The histogram of elevation intervals for each watershed is shown as inset figure. The root-mean-squared error (rmse) and mean absolute error ($|\bar{\Delta}|$) measures of fit are also shown.

travel times, nearing zero. This, together with the extremely high frequency of short travel times shown in Figure 3-2, constitute in another line of evidence of the poor performance of the numerical model in the RPT watersheds.

As mentioned in Table 3-1, a depth-to-bedrock map is not available for several watersheds, including: des Anglais, Pamilco Canyon, Rattlesnake Flat, and Thomas Creek. In the case of des Anglais, a local well depth database was used to approximate aquifer depth. Regional hydrogeology maps taken from Maurer et al. (*2004*) guided the estimation of the aquifer depth for Pamilco Canyon and Rattlesnake Flat watersheds, and from McFarland (*1982*) for Thomas Creek. For these three last watersheds, assumptions on depth-to-bedrock were made in the hillslope areas. These assumptions were tested as potential reasons for the poor performance of the numerical model, however, different configurations of aquifer depth and mesh spatial resolution do not resolve the inconsistencies in travel time estimates. It is also likely that the steady flow field required by the transport model to simulate the transport of ages in FEFLOW becomes less reliable for steep hillslopes. This may create points of discharge that are dictated by steep topography and not by subsurface flow. For the analytical model, the original stream network delineation from NHD was modified several times to create first order streams following a fixed minimum number of cells in the flow accumulation raster in order to obtain a better agreement with numerical travel times, as it dictates the procedure outlined in section 3.2.1.2. Despite implementing many configurations, correlations do not improve for these three hillslope watersheds.

For some study watersheds, the pMTT agreement between the distributions from both methods depicted in Figure 3-2 does not match the measure of fit in Figure 3-4, which indicates that the travel times represented in the analytical model does not exactly coincide with the same locations than those registered in the numerical simulations.

Observation points are grouped according to their relative elevation in the watershed in three bins: low (Elev1), median (Elev2), and high (Elev3). The distributions of observation points (OPs, or particles) in these topographic elevation intervals shows that, generally, mid- and high-range OPs exhibits a wide range of travel times. Short travel times in

hillslope areas may occur, as well as in OPs located near the river network. Long travel times are not dominated by any elevation range, as at any point in the watershed local differential altitudes and distances exist where remote flow paths can be present. The range of flow paths at different altitudes along the stream network depends upon the shape of the watershed. In des Anglais (dAn) and Ganaraska (Gan) River watersheds a portion of OPs with long pMTTs is located at high elevations, but this is more accentuated in the Ganaraska River where the headwater area is more extensive. In Alder Creek, high elevation OPs yield mid- to long travel times, whereas, in Upper Laurel Creek and Upper Nith River travel times are spread across a larger range of elevations. The degree of agreement between analytical and numerical models does not vary with elevation for the same watershed. For any of the hillslope-dominated watersheds, there is no single elevation range that shows a better correlation than the overall value.

### 3.3.2 Where does the Analytical Model Performs Best?

In this section, a series of geomorphological features are examined and quantified (Table B1) to identify conditions under which the analytical method performs best against the numerical output. For this purpose, the measure of fit, r-squared, between the numerical and analytical methods is used as the discerning factor of performance for the geomorphological feature being evaluated as predictor. The measures of fit rmse and $|\bar{\Delta}|$ do not show enough sensitivity to the agreement between the models to be used as discerning factors. The analysis also seeks to shed light on the roles played by these geomorphological features in particle and watershed MTTs. Exclusive and non-exclusive ranges are created for a particular index, where the non-exclusive range does not yield optimal performance as it may either exclude the Sagehen River watershed or include any of the RPT watersheds.

#### 3.3.2.1 Horton's Analysis

Horton indexes $N$, $L$ and $S$ (Table 3-2) correlate well with the Strahler stream order ($w$) within the ranges 0.71-0.98, 0.69-0.98, and 0.73-1.0, respectively. The order in which the fitted lines are distributed for $N$ and $L$ does not strictly follow watershed size, however, its

influence is clearly present (Figure 3-5). Ganaraska River, for instance, is slightly larger than one third the size of des Anglais River (701 km$^2$), but the former exhibits a greater drainage density leading to both greater $N$ and $L$. Horton's $R_B$ law (i.e., the slope of $N$) does not produce any discretization with respect to the goodness of fit between the analytical and numerical methods (*NumAn* goodness of fit, hereafter) given by the r-squared value, but $R_L$, yields a narrow discretization between values of 2.5 and 3.4. The relationships of $S$, as well as $N$ and $L$, with stream order decreases as the upstream network feeds streams in the valleys. The steepest streams are located, in descending order, in the watersheds of Thomas Creek, Sagehen River, Rattlesnake Flat, and Pamilco Canyon, and the least steep ones in Upper Nith River, Upper Laurel Creek, and des Anglais River. Alder Creek and Ganaraska River are the mid-range in the set of study watersheds. For these two watersheds, these relationships with stream order actually yield a range of mean stream slopes with better *NumAn* goodness of fit. This range, highlighted in yellow in Figure 3-5, is encompassed by Upper Nith River and Ganaraska River. The law of slopes $R_S$, however, does not provide a useful discerning tool with respect to the *NumAn* goodness of fit.

3.3.2.2 Texture Topography Measures

Drainage density ($Dd$ = $L_S$/A) is a measure of the degree of development of a watershed (*Bras, 1990*). Its calculation depends on the resolution at which drainage maps (i.e., GIS shapefiles) or aerial photographs are used for delineation. There is a wide range of $Dd$ values among the study sites (Figure 3-6 and Table 3-1). The drainage density in Thomas Creek is the largest followed by Sagehen River, whereas, the smallest is in Des Anglais River. Its relation to *NumAn* goodness of fit is systematically poor. Drainage density and drainage frequency ($DF$) are measures of texture topography (*Smith, 1950*). Thus, $Tex$ (see Table 3-2) has a strong and positive relationship to $Dd$ (Figure 3-6, $r^2$=0.94). Both $DF$ and $Tex$ correlate poorly with *NumAn* goodness of fit (Figure B1, in Appendix B). No discerning ranges for these indexes are found for the study watersheds.

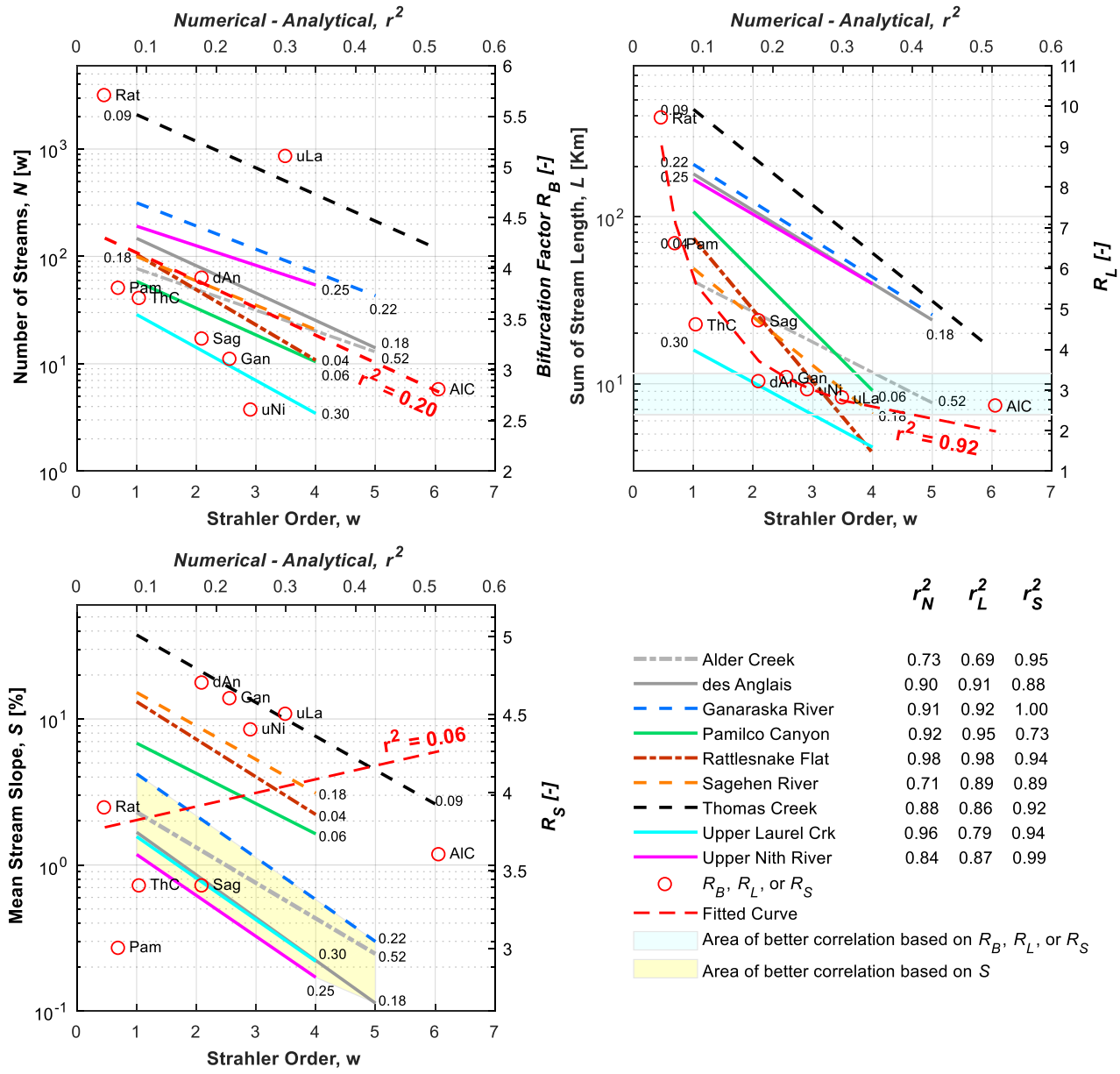


Figure 3-5. Horton analysis of stream networks: stream numbers (N), sum of lengths (L), and slopes (S). Fitted lines and r² values of these relationships are shown for the study sites as $r_N^2$, $r_L^2$, and $r_S^2$. The correlation (r²) between the analytical and numerical particle MTTs for each watershed is also presented next to the respective fitted line. The slopes of the above relationships yields $R_B$, $R_L$, and $R_S$ for each study site (red circles). The fitted line through these parameters against the correlation between the analytical and numerical method is also plotted (red dashed-line).

Strahler (*1950*) suggested that *Dd* increases with topographic relief (i.e., the difference between maximum and minimum elevation), which is verified here with a moderately strong, positive relationship ($r^2$=0.43). The box highlighting better *NumAn* goodness of fit shown on Figure 3-6b suggests that the analytical model works better at lower drainage densities (<2.7 $km^{-1}$) and topographic reliefs (<790 m). When *Dd* [1/km] is multiplied by the mean stream link drop (H [m]), it results in the dimensionless ruggedness number (*HDd*), which yields a relationship with a non-exclusive range. We propose that drainage density alone cannot be used to identify ranges with better *NumAn* goodness of fit. It is only when ground elevation (*Relief*) or stream network elevation (*HDd*) indexes are factored in that ranges discretizing the performance of the analytical model are obtained. When *Relief* alone is plotted against *NumAn* goodness of fit, it provides a range that clearly excludes the RTP watersheds (Figure B2d, in Appendix B).

3.3.2.3 Elevation Measures

Mean watershed gradient (*mGrad*, %), mean channel slope (*Schan*, %), mean DEM cell-size slope (*cSlope*, deg), and the probability distribution of the DEM-cell size slope are included in this category. The performance of the analytical method improves when *mGrad*, *Schan*, *cSlope*, and *Relief* decreases (Table 3-2, Figure 3-7). The above elevation indexes are both inversely related with the *NumAn* goodness of fit via either an exponential or a power law function, and defining a range of performance for the analytical model. *Relief* and *cSlope* are the indexes that provide a definite range for the best performance of the analytical model with *Relief* < 790 m and *cSlope* < 8.63 degrees. (Note that although Thomas Creek has the second largest *Schan*, it also exhibits the highest $R_S$ value. This apparent discrepancy is likely due to the fact that Thomas Creek has a more extensive valley in which the contribution of high order streams is more important than in Sagehen River).

The histogram describing the occurrence of slopes at the DEM-cell scale is indicative of the spectrum of slopes present throughout a watershed. These histograms are shown here in terms of probability of occurrence (Figure B2, Appendix B). Watersheds that yielded the best *NumAn* goodness of fit are mostly spread around lower DEM-cell size slopes (<2.5 deg).

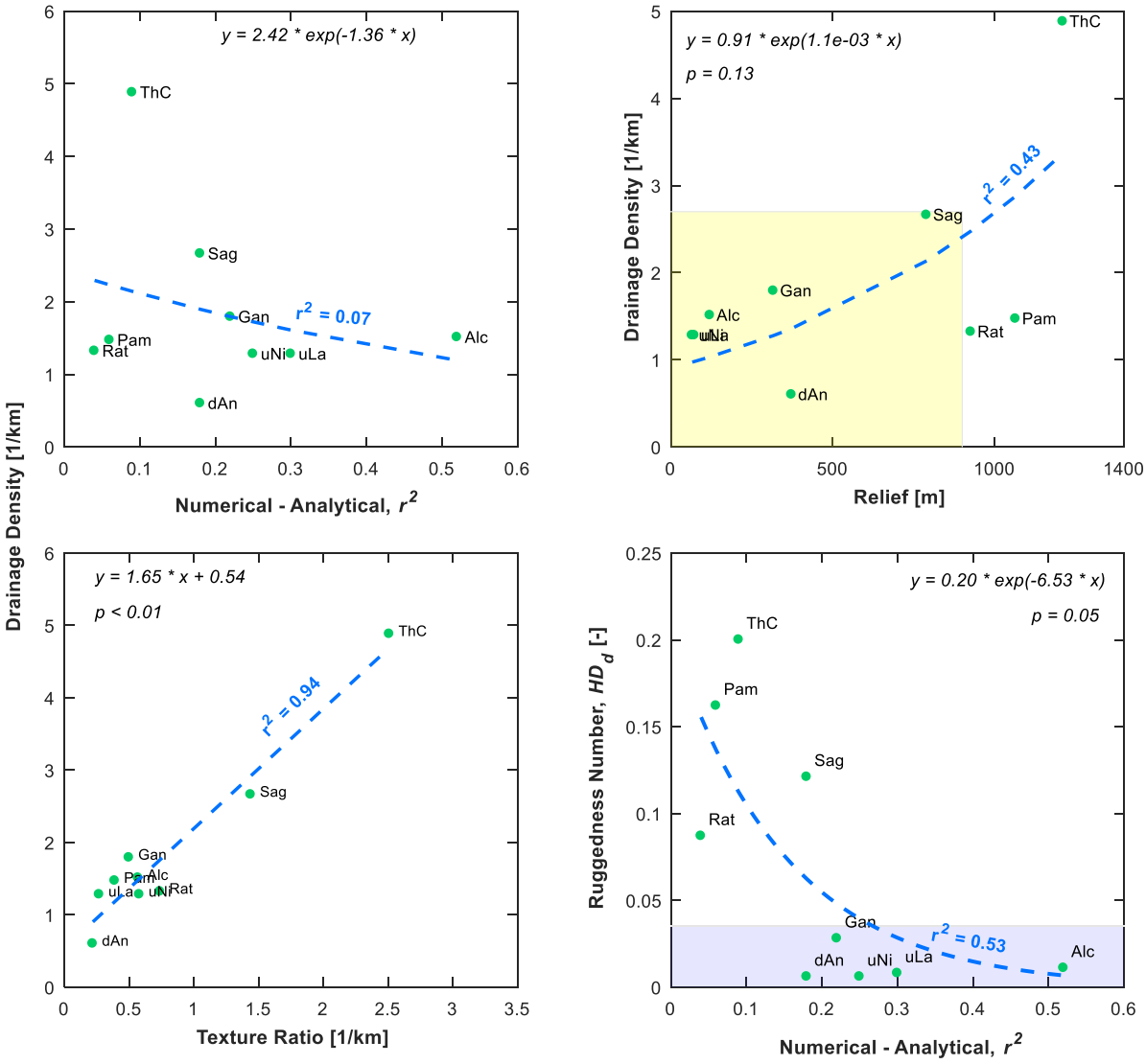


Figure 3-6. Drainage density (*Dd*) and ruggedness number ($HD_d$) as a function of the correlation between numerical and analytical results (*NumAn* goodness of fit). The relationship between *Dd* and texture ratio is also shown as well as between *Dd* and *Relief*.

Hypsometric curves were derived for all watersheds based on raster elevation data (Figure B3, in Appendix B). Characteristic profiles for geomorphologically young (or high activity), mature (medium activity), and old (low activity) watersheds can be associated

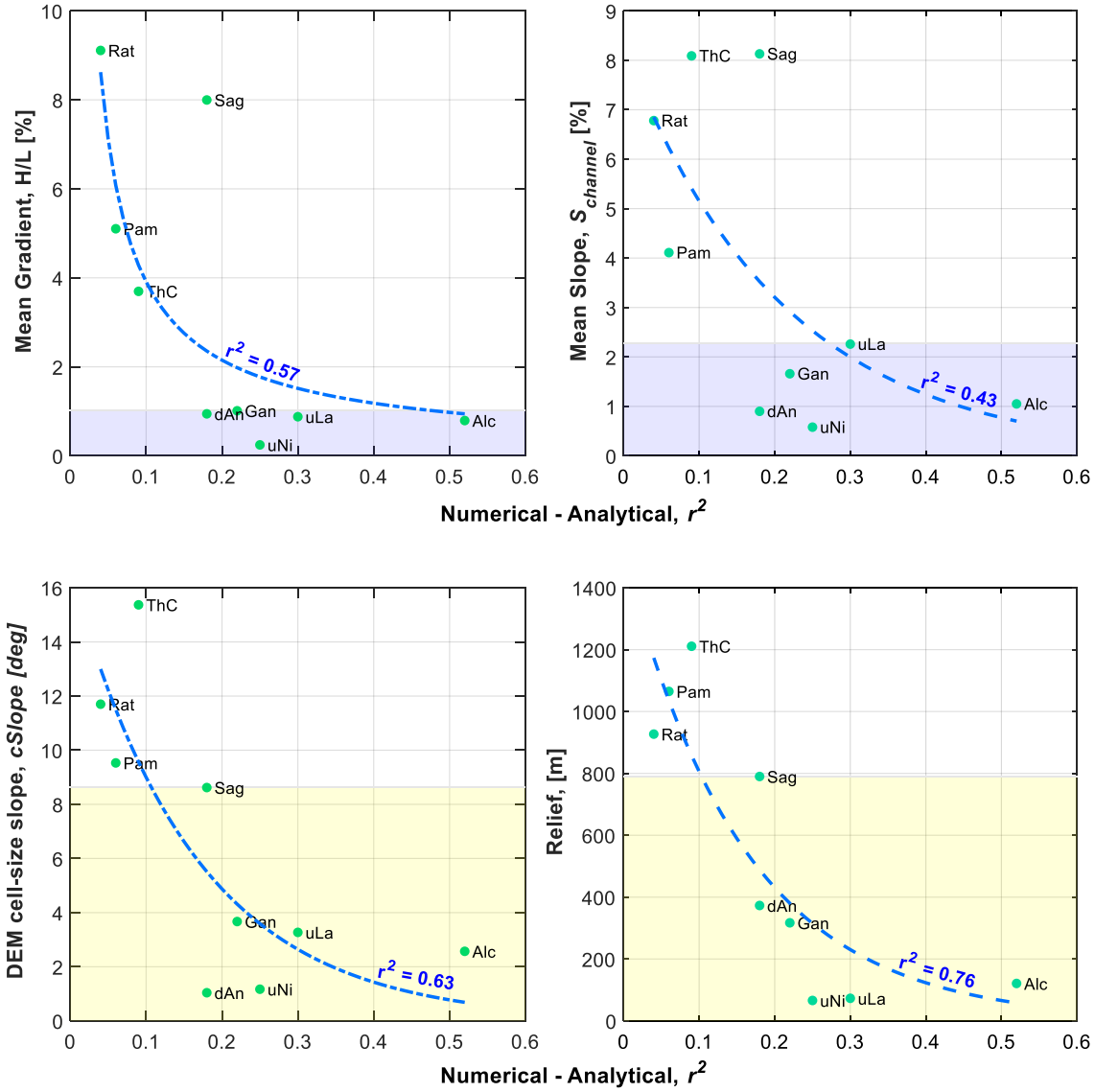


Figure 3-7. Elevation measures as a function of the degree of agreement between analytical and numerical methods (*NumAn* goodness of fit): a) mean gradient (mGrad), b) mean slope channel (*Schan*), c) mean DEM-cell size slope (*cSlope*), and d) topographic relief (*Relief*). Exclusive and non-exclusive ranges of these parameters are highlighted in yellow and blue, respectively, referring to the inclusion of Sagehen River watershed in the range.

with specific shapes of the hypsometric curve (*Bras, 1990*). Most of the study watersheds fall within the young (or high activity, concave down) and mature (medium activity, slightly concave down) categories except for des Anglais River whose strong concave up curve is associated with low activity (i.e., old age). This three-dimensional representation of the study sites, however, does not provide a means to discern among the *NumAn* goodness of fit. In other words, the analytical model performance is not constrained by the hypsometric curve.

A representation of the juxtaposition of watershed elevation and texture topography is provided by the link concentration plot that depicts the distribution of points at which the stream network dissects the topography at specific elevation contours throughout the watershed (Figure B4, Appendix B). Half of the study watersheds exhibited a single peak in their distribution of links: Sagehen River, Pamilco Canyon, Rattlesnake Flat, Alder Creek, and Upper Laurel Creek. The link concentration in the other half of watersheds follows a multi-modal behavior, where peaks occurred either consecutively or anywhere else in the watershed. However, an exclusive range of relative relief where the best *NumAn* goodness of fit dominates the link concentration distribution could not be determined.

#### 3.3.2.4 Measures of Shape

Circularity ($R_C$) compares the watershed area (A) against the equivalent area of a circle with the perimeter equal to that of the watershed (Jarvis, 1976). High values of *Rc* indicate more likeness to a 'circular' shape (Figure B5, Appendix B). This measure does not provide any discretization with respect to the performance of the analytical model. Both the lemniscate ratio ($P_{LR}$) and elongation ratio (*Er*) provide non-exclusive ranges for better performance of the analytical model. The $P_{LR}$ ratio identifies Sagehen River and Rattlesnake Flat as the most similar to a lemniscate shape (Figure 3-1). According to *ER*, the most elongated watersheds are Thomas Creek and Ganaraska River (Figure 3-1). A measure of compactness (*C*) given by $P/A^{0.5}$ again yields a weak range for best *NumAn* goodness of fit: *C* from 5.8 to 7.25. The lower *C* gets, the closer the perimeter length is to the length of the square-root of *A* and hence the watershed becomes more square shaped.

Another measure of compactness is given by the relative distance variance (RDV), which divides the watershed in infinitesimal areas. The variance of the distance to these areas from the watershed centroid is quantified for its estimation. A non-exclusive range of RDV values is obtained when Pamilco Canyon is included in it (Figure B6, Appendix B). These ranges, even though non-exclusive, indicate that best agreement between the analytical and the numerical models are, in general, likely to be obtained in not too elongated watersheds (*Er* and *C*). This result can be tied to the watershed size given that larger watersheds tend to be more elongated as the ratio $A/L^2$ (i.e., form factor) falls when $A$ increases (*Bras, 1990*). This can be observed in the relationship $L = a \cdot A^b$, where the exponent $b$ is always greater than 0.5 (*Leopold et al., 1964*).

3.3.2.5 Fractal Dimensions

The box-counting technique is applied to both stream network and watershed perimeter (Figure 3-8). This technique reveals a bi-fractal behavior for both the stream network data and the perimeter data. The bi-fractal behavior is characterized by two segments of different slope that fits the data defining distinct regions of self-similarity. The first line is traced along small box sizes and a great number of boxes are required to intersect the targeted shape (i.e., the perimeter or the stream network). This line has a mild slope with a value close to (-)1.0, as given by the exponent of the fitted power function. The trend of this line is interrupted as the box size increases and exceeds a certain value. A steeper slope is then needed, as fewer boxes are required to intersect the entire stream network. The second line is traced along large box sizes that require a smaller number of boxes to intersect the network. A similar bi-fractal behavior is observed by the box counting technique applied to the watershed's perimeters.

The steeper slope in the box-counting analysis represents the fractal dimension ($D_{BCst}$) of the evaluated feature (*Claps and Oliveto, 1996*). The milder slope of the box counting data of the stream network approaches unity as it more closely traces the uni-dimensional aspect of the network ($d_{BCst}$). The steeper slope, on the other hand, has a wider range of values from ~1.5 to 2.0. The steeper slope is interpreted by some researchers as a measure of how space-

filling the stream network is (*Tarboton et al., 1988*; *Rodriguez-Iturbe & Rinaldo, 1997*). The closer the fractal dimension is to 2 the more space filling the network is because, theoretically speaking, it approaches a surface dimension. This interpretation basically entails that a fractal dimension is another way of measuring texture topography using fractal analysis. However, this interpretation does not appear to apply to all watersheds in this study (Figure 3-8). Thomas Creek and Sagehen River have the largest drainage densities and fractal dimensions (~1.8), whereas Ganaraska River has the lowest fractal dimension. This does not correspond to the density of streams present in the latter watershed. The reason is likely that the space-filling interpretation of the fractal dimension of stream networks inherently assumes that all areas in the watershed contribute to the network, which is the reason why it has been challenged by other researchers (*Phillips, 1993*; *Veltri et al., 1996*). The mono-fractal dimensions estimated using the box-counting technique, when related to the respective *NumAn* goodness of fit, do not yield an exclusive range of values within which a better performance of the analytical model can be expected (Figure B7 in Appendix B).

The walking divider method is also used to estimate the fractal dimension of the perimeter curve. This method uses a chord length (step) and quantifies the number of chords required to cover the entire fractal curve. The result is an estimate of the length of the entire curve for a finite number of selected steps. Plotting the estimated length against the step size, the data increasingly underestimates the total length as step size increases, depicting a negative slope with values slightly above unity. The slope of this line corresponds to the fractal dimension in the walking divider method ($D_{WDp}$). Note that the perimeter's fractal dimension as estimated by both box-counting ($D_{BCp}$) and walking divider ($D_{WDp}$) methods yield different results (Figure B8). Neither method provides an exclusive range for better *NumAn* goodness of fit. However, the *D*-values estimated for the perimeter exceed unity for two watersheds using the box-counting method. This makes the box-counting method less suited for estimating fractal dimensions of this uni-dimensional feature.

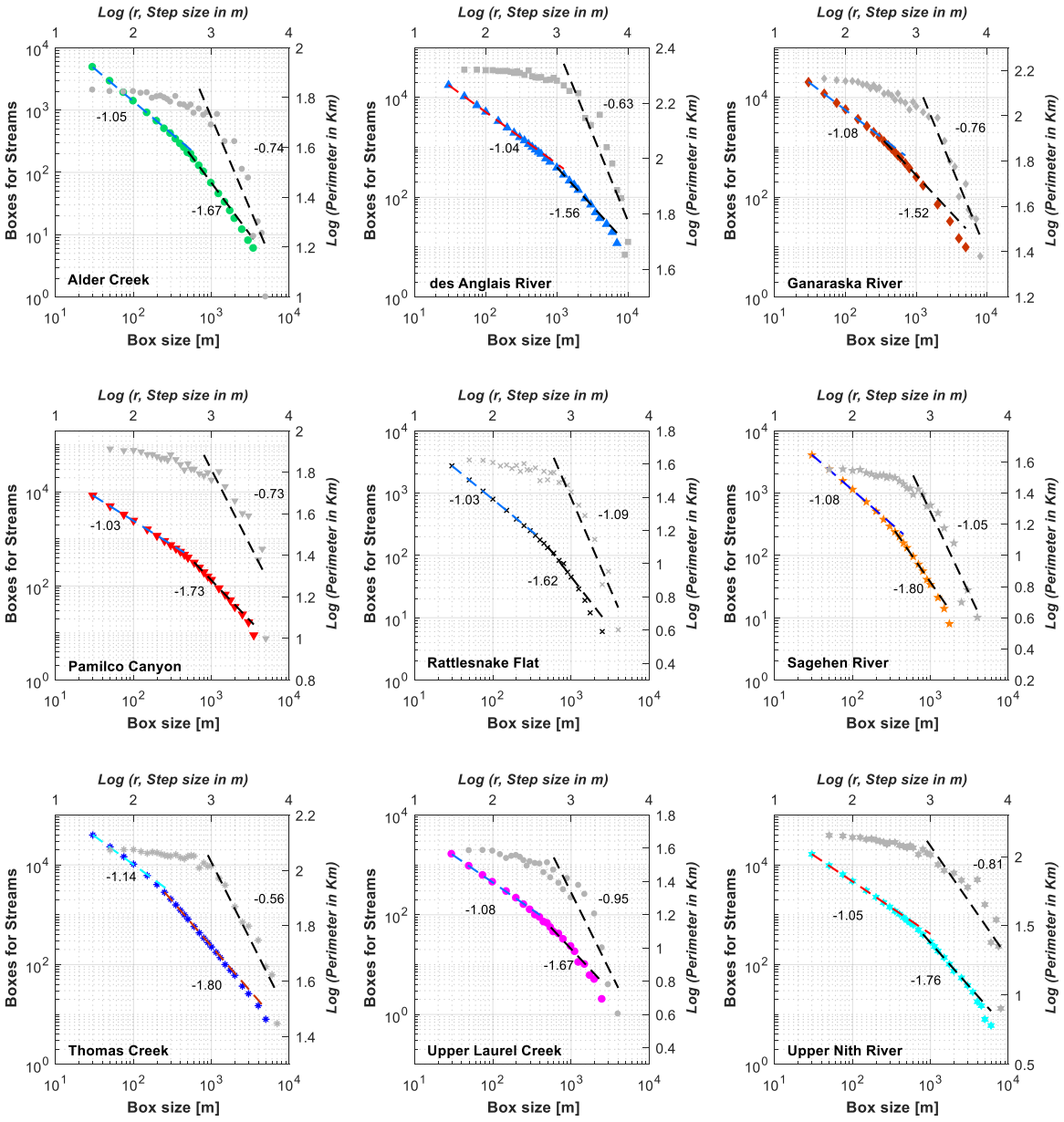


Figure 3-8. Fractal analysis of stream network and watershed perimeter using the box counting technique. The analysis on the stream network is in the principal logarithmic scale. A linear scale for the logarithmic values of perimeter and step (box) size is presented in the secondary set of axes. Power function curves ($y=a \cdot x^b$) are fitted to the bi-fractal behavior of the stream network data. The coefficient of the power function (slope of the line) is shown adjacent to the curve. A linear function is fitted to the perimeter data. The slope of this function is shown next to the trendline.

#### 3.3.2.6 Geomorphological Measures as Predictors of Analytical Model Performance - Summary

In the above analyses, a set of multiple indexes are related to the degree of agreement between the analytical and numerical models, as expressed by the square-root of the expected response (i.e., *NumAn* goodness of fit) for each study watershed. A two-tier approach is proposed to make use of these indexes as criteria to gauge whether the analytical model can effectively be used for any given watershed: i) The first tier corresponds to the two indexes that provided an exclusive range in the examined study sites: *Relief* (exclusive range: < 790 m) and *cSlope* (exclusive range: < 8.63 deg). A drainage density of less than 2.7 $km^{-1}$ can also be considered an additional selection criterion for apt watersheds for the implementation of the analytical model in cases where topographic relief is less than 790 m. ii) A second tier of indexes (Table 3-3) is obtained by including the non-exclusive ranges where either one watershed of the hillslope-dominated watersheds falls into the range, or one watershed with better correlation falls outside of it. Most of these indexes are relatively easy to estimate for any watershed, except for the walking divider method applied to estimate the fractal dimension on the perimeter. The MATLAB code for this fractal measure is provided in Appendix B. The second tier of indexes is to be used as a second level analysis should the first tier yield a positive or negative result.

### 3.3.3 Determination of $SF$, $U_0$, and $\lambda_L$ Values in Future Applications

For future applications of the analytical model to other watersheds, guidelines on what parameter values to use for the smoothing factor ($SF$), mean flow path bulk velocity ($U_0$), and macrodispersion coefficient ($\lambda_L$) are provided in this section. These guidelines are based on the relationships between these parameters and the geomorphological measures in Table 3-2. Note that values from the RPT watersheds are excluded from this analysis. Thus, the analysis consists in the development of single linear regressions (SLRs) and multiple linear regressions (MLRs) using the six remaining watersheds. A principal component analysis was also conducted, however, it is not deemed significant due to the scarcity of available

Table 3-3. Second tier, non-exclusive ranges obtained for better performance of the analytical model.

| Measure | Range | Measure | Range |
|---|---|---|---|
| Law of slopes ($R_L$) | 2.5 - 3.4 | Mean channel slope (*Schan*) | < 2.27% |
| Ruggedness number ($HD_d$) | < 0.03 | Mean gradient (*mGrad*) | < 1.2 |
| Lemniscate ratio ($P_{LR}$) | 0.56 to 0.68 | DEM slope histogram peak | < 2.5 deg |
| Elongation ratio (*Er*) | 0.53 to 0.68 | D one-dimensional box counting method on stream | 1.037 – 1.085 |
| Form factor (*FormF*) | 0.28 – 0.45 | D-walking divider method on perimeter | 1.039 - 1.062 |
| Relative distance variance (*RDV*) | 0.60 - 0.85 | | |

observations. Therefore, MLRs are reduced to two variables. The MLR models and their analysis can be found in Appendix B.

3.3.3.1 Single Linear Regressions

Macrodispersion power functions derived from the calibration of the analytical model relate the change in macrodispersion coefficient ($\lambda_L$) with respect to flow path distance ($x$) for the data collected from the 24 calibration points for each scenario. These power functions are developed for each watershed (Figure 3-9) and follow the form $y = a \cdot x^b$, where the exponent $b$ ranges from 0.43 (des Anglais River) to 0.92 (Sagehen River). Combined with the coefficient $a$, this yields a wide spectrum of values for $\lambda_L$. In order to apply a similar power function to future watersheds, both the exponent $b$ and the product '$a \cdot b$' should be used as the target variables (instead of $\lambda_L$).

The Pearson correlations between each of the parameters in the analytical equation (i.e., *SF*, $U_0$, plus $\lambda_L$'s power function exponent $b$, and $\lambda_L$'s power function product $a \cdot b$) and twenty-one (21) geomorphological indexes are shown in Figure 3-10. Additionally,

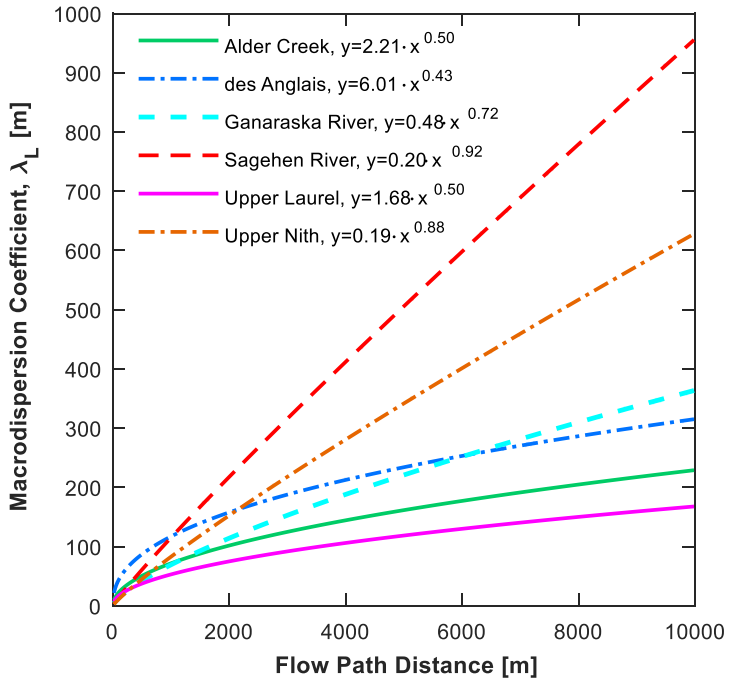


Figure 3-9. Macrodispersion coefficient fitted power functions ($y = a \cdot x^b$) based on the calibrated data for the study watersheds (12 observation points), excluding the RPT watersheds.

correlations between $R_B$, $R_L$, $R_S$, the coefficient $a$ (*LvAa*) of Hack's law ($L = c \cdot A_i^b$), the exponent $b$ of this function (*LvAb*), and the product $a{\cdot}b$ (*LvAab*) with respect to the above geomorphological measures including the parameters of the analytical model (not shown) are also performed. Here, $A_i$ corresponds to the composite drainage area associated with affluent streams converging to the main stream.

Both macrodispersion ($\lambda_L$) parameters $b$ and $a{\cdot}b$, on average, correlate equally better (0.47) than *SF* (0.38) and $U_0$ (0.40) against all geomorphological indexes (Figure 3-10). Among the different parameters, *Relief* and *LnkSlp* correlations with *SF* are significant. The smoothing factor is also highly correlated (0.92, not shown) with *LvAab*. The latter product is related to the *SF* via an increasing power function, whereas, *Relief* relates to the *SF* via a decreasing power function (Figure 3-10a). In general, *SF* correlates significantly better with texture topography and slope indexes (0.50) than with shape and fractal indexes (0.26).

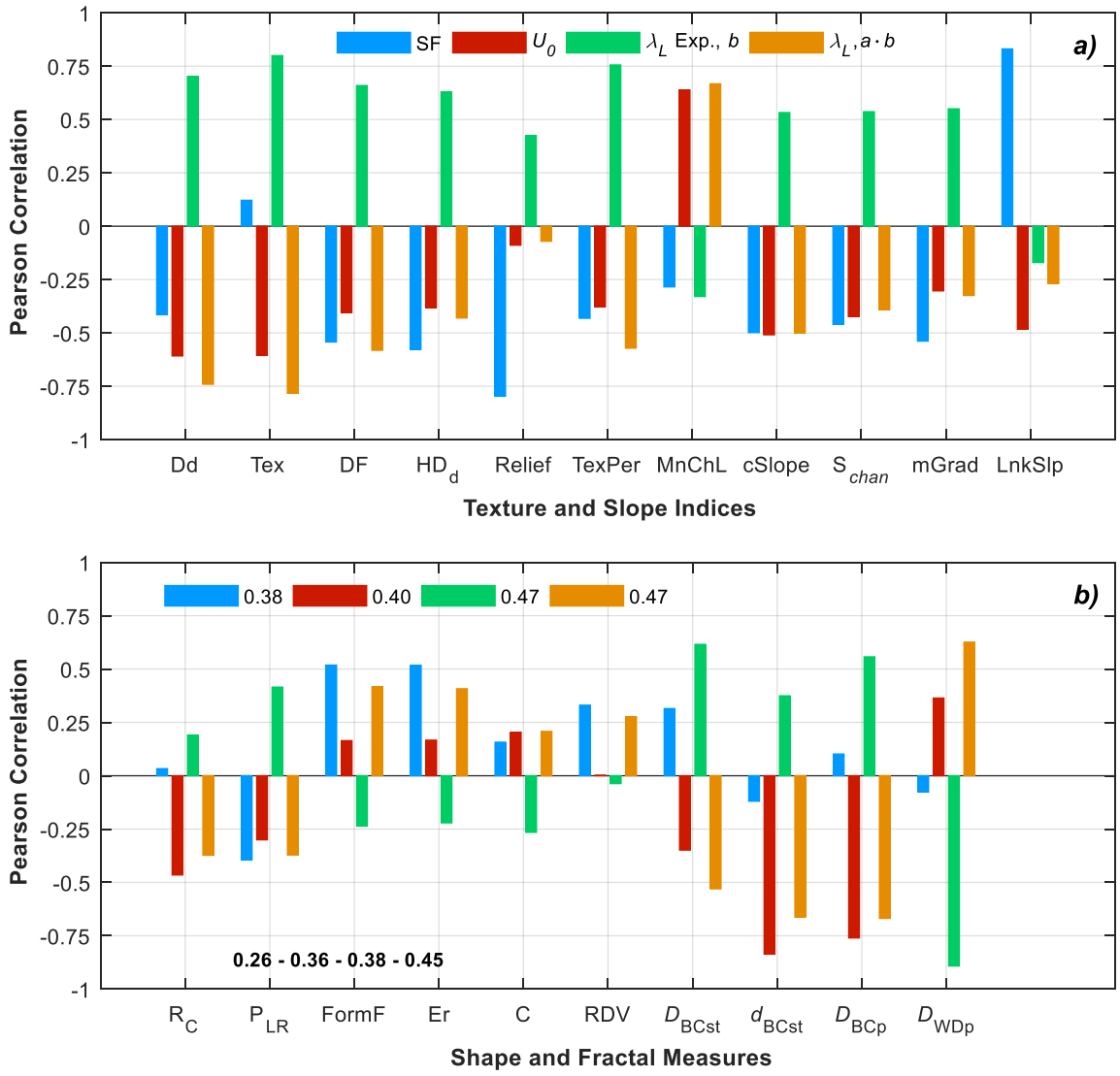


Figure 3-10. Pearson correlations of the parameters required by the analytical model, plotted against a) texture and slope indexes, and b) shape and fractal measures. The analytical parameters are: smoothing factor (*SF*), mean bulk velocity ($U_0$), exponent of macrodispersion ($\lambda_L$) power function ($y = a \cdot x^b$), $b$, and the product of coefficient (a) and exponent (b) of the power function, $a \cdot b$. Among the indexes are: drainage density (*Dd*), texture (*Tex*), drainage frequency (*DF*), texture for contour perimeter (*TexPer*), main channel length (*MnChL*), DEM cell size slope (*cSlope*), mean channel slope ($S_{chan}$), mean gradient (*mGrad*), slope of power function between link slopes and stream magnitude (*LnkSlp*), stream fractal dimension using the box-counting method ($D_{BCst}$), mild slope of stream fractal dimension using the box-counting method ($d_{BCst}$), and perimeter's fractal dimension using the walking divider method ($D_{WDp}$). Average correlation for each parameter is shown in the legend of plot b).

The mean flow path bulk velocity ($U_0$) is highly correlated with the unidimensional fractal dimension of the streams (i.e., mild slope, $d_{BCst}$ Figure 3-10b) and the fractal dimension of the perimeter ($D_{BCp}$), both estimated with the box-counting method. On average, the texture topography and slope indexes correlate better with $U_0$ (0.44, and 0.36, respectively) than with shape and fractal measures. Elevation and slope indexes exhibit, in general, lower correlations than expected. Using $d_{BCp}$ as predictor of $U_0$ (Figure 3-11b), des Anglais River (dAn) and Sagehen River (Sag) watersheds act as end members of the relationship. These watersheds exhibit, respectively, the lowest and highest values for both the *Dd* and mean DEM cell size slope (*cSlope*) indexes. However, other watersheds do not follow either of these ranges, suggesting that other mechanisms are at play in the relationship between the stream network's unidimensional fractal dimension and *Uo*. This fractal dimension is associated with an accurate determination of the stream length, given by the mild slope (Figure 3-8). How this fractal measure can exert control on $U_0$, it is not clear at this stage. A similar decreasing power function and degree of agreement was also found for $D_{BCp}$ ($Uo=0.04*D_{BCp}^{-2.59}$, $r^2=0.73$, not shown). The relationship with $D_{BCp}$ also had dAn and Sag watersheds as end members. A similarity in the distribution of stream and perimeter fractals can be explained by the concept that the watershed perimeter emulates the stream network that it encompasses. However, the relationship with the watershed scale subsurface velocity remains to be explained.

The exponent *b* and product $a \cdot b$ from the $\lambda_L$ power functions correlate, in general, better with texture topography and slope indexes (0.55 and 0.48, on average, respectively) than with shape and fractal measures (0.38 and 0.45, respectively). They tend to correlate well with the same indexes but negatively against each other. Texture (*Tex*), *TexPer*, and $D_{WDp}$ stand out as potential predictors, whereas *Relief*, $R_C$, *PLR*, *C* and *RDV* were poorly correlated with both *b* and $a \cdot b$. The influence of texture topography is important for this set of variables that are derived from calibrated observations points in the watershed. The best prediction for exponent *b* is by *TexPer*, which is directly proportional to *b* via a power function ($r^2=0.64$, $p<0.05$, Figure 3-11c). As *b* grows with *TexPer*, the larger $\lambda_L$ will become (Figure 3-9). For instance, in Sagehen River $\lambda_L$ grew faster with flow path length and simultaneously is the

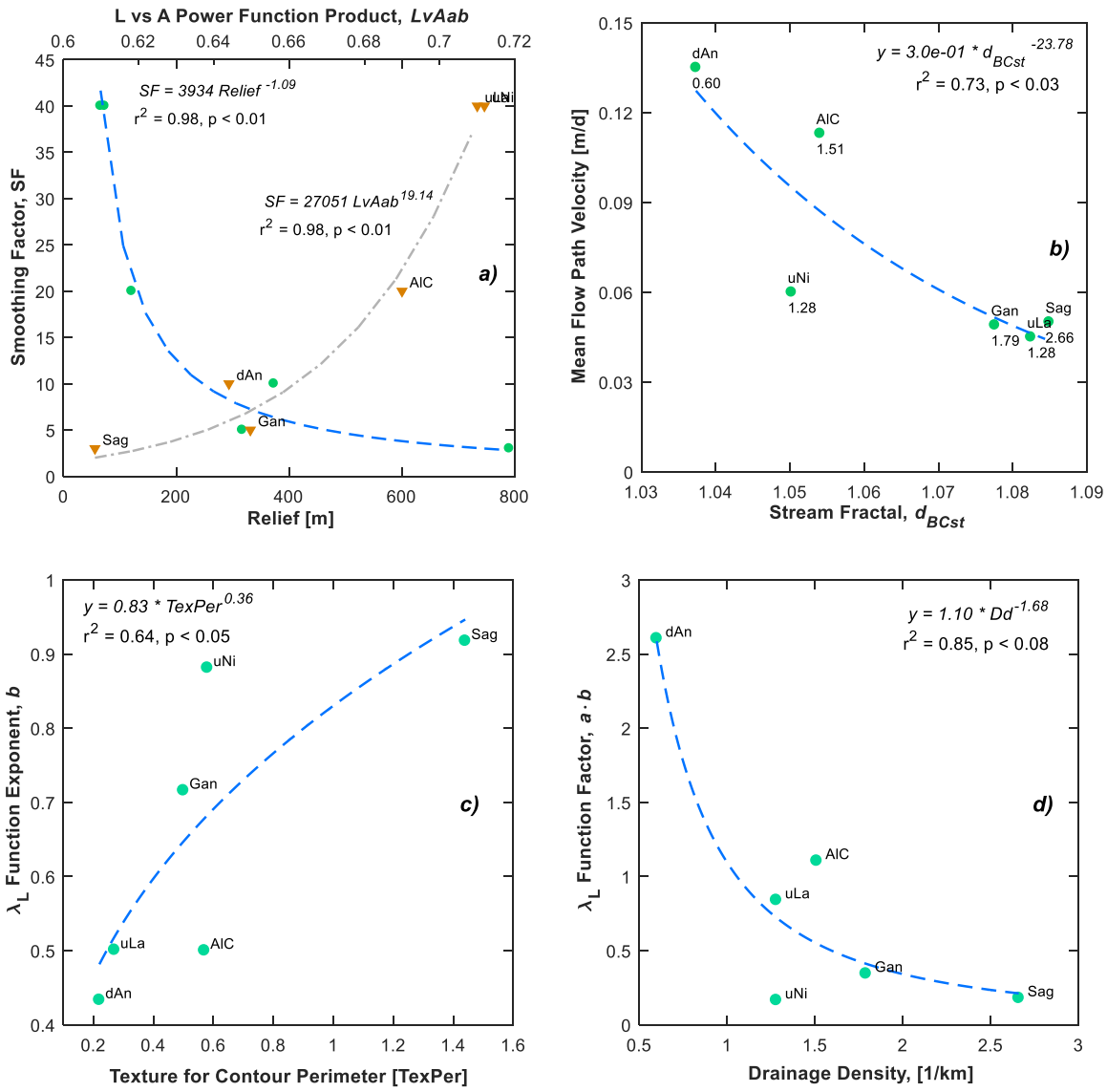


Figure 3-11. Single linear regression for the prediction of a) smoothing factor (*SF*), b) mean flow path velocity ($U_0$), c) $\lambda_L$ power function exponent (b), and d) $\lambda_L$ power function product ($a \cdot b$).

watershed with the largest *TexPer* value. For the product $a \cdot b$, *Dd* provided the best prediction ($r^2$=0.85, p=0.08, Figure 3-11d) but in this case, the relationship is a decreasing power function. Considering that *Dd* and *TexPer* are positively correlated, the decreasing power function suggests that the coefficient *a* significantly decreases with texture

topography. The product $a \cdot b$ in conjunction with Figure 3-11c provides the means to back-calculate both drivers of the $\lambda_L$ power function: coefficient $a$ and exponent $b$.

#### 3.3.3.2 Multiple Linear Regression

Alternatively, multiple linear regressions (MLRs) can be developed for predicting analytical model parameters. The MLR models are constructed using a backward stepwise approach, which is combined with the Lasso technique aimed at efficiently selecting predictors from a total of 27 indexes. The quality of the models is quantified from the mean square error (MSE), and also using information theory indexes such as the Akaike information criterion (AIC) and the Bayes information criterion (BIC). I refer to Appendix B for more details on the development of these MLR models.

The smoothing factor (*SF*) is better predicted by shape measures ($R_C$ and *LvAa*) than elevation and slope-related indexes (Table B2, Appendix B). The *Uo* is predicted by texture topography indexes (*Dd* and *DF*), for which the collinearity test (i.e., condition index) deems it as a weak near dependency ($n_j$<30). The dependence of $U_0$ on these indexes rather than gravity-oriented measures such as *cSlope*, *Relief*, and *mGrad*, is telling on the importance of the stream frequency and the watershed shape in controlling subsurface flow and travel times. The exponent of the $\lambda_L$-power function $b$ is predicted by shape (*C* and *LvAb*) and texture topography (*Tex* and *Dd*) measures. This is a reflection on the flow path distances that are constrained by the shape of the watershed, externally and internally by the interception of streams along the flow paths (i.e., texture topography). The product of the $\lambda_L$-power function $a \cdot b$ include texture topography indexes only as predictors: *HDd* and *Tex* (Figure B9, Appendix B).

### 3.3.4 WMTT and Geomorphological Indexes

A separate analysis was carried out to identifying predictors of wMTT using SLR and MLR models with a six-observation dataset that excludes the RPT watersheds. The MLR models and their analysis are presented in Appendix B.

3.3.4.1 SLR Models for wMTT

A strong relationship exists between the numerical and analytical models for the six watershed wMTTs ($r^2$=0.89, Figure 3-3). The wMTTs obtained with both methods correlate with geomorphological indexes and with the analytical model's parameters (*SF*, $U_0$, $a \cdot b$, and *b*). The analytical wMTTs closely follow the correlation trends exhibited by the numerical wMTT, except for the indexes *Tex*, *FormF*, *Er*, and $d_{BCst}$, where the analytical and numerical models yield opposite low correlations (Figure B10, Appendix B). Of the analytical method's parameters, only *SF* exhibits a strong relationship with wMTT ($r^2$=0.83). Several indexes correlate well with wMTT including *Relief*, *mGrad*, *LnkSlp*, *LvAb*, and *LvAab*. Among these indexes, *Relief* ($r^2$=0.64, p=0.05), *LnkSlp* ($r^2$=0.64, p=0.03), and *LvAab* ($r^2$=0.63, p=0.06) are the best predictors for individual SLR models (Figure 3-12). These results suggest a significant dependence of wMTT on the geomorphological properties represented by these two indexes.

The relationship between wMTT and with *Relief* is expected: the greater *Relief*, the shorter wMTT (*McGuire et al., 2005*; *Tetzlaff et al., 2009a*; *Hrachowitz et al., 2009*; *Capell et al., 2012*). As mentioned before, *Relief* has a positive relationship with *Dd* implying that shorter flow paths are more likely present in steep watersheds. The relationship with *LvAab* is not as straightforward as it involves the coefficient product $a \cdot b$, which varied in our dataset between 0.61 and 0.71 (n=6). Hack (*1957*) already proposed that the values of *a* and *b* remain remarkably constant, 1.4 and 0.6, respectively, when applied to a whole range of basins around the world. Later this relationship was verified by Montgomery and Dietrich (*1992*) by replacing the longest stream length (L) by the watershed length. The wMTT-*LvAab* relationship obtained here is different in that it was developed from drainage areas created by the inflow from tributaries flowing into the main stem of the watershed. In this way, the coefficients *a* and *b* are derived from significant (at least, p<0.09) power functions. They are inherent to each watershed, and not directly comparable to those derived from inter-basin analysis.

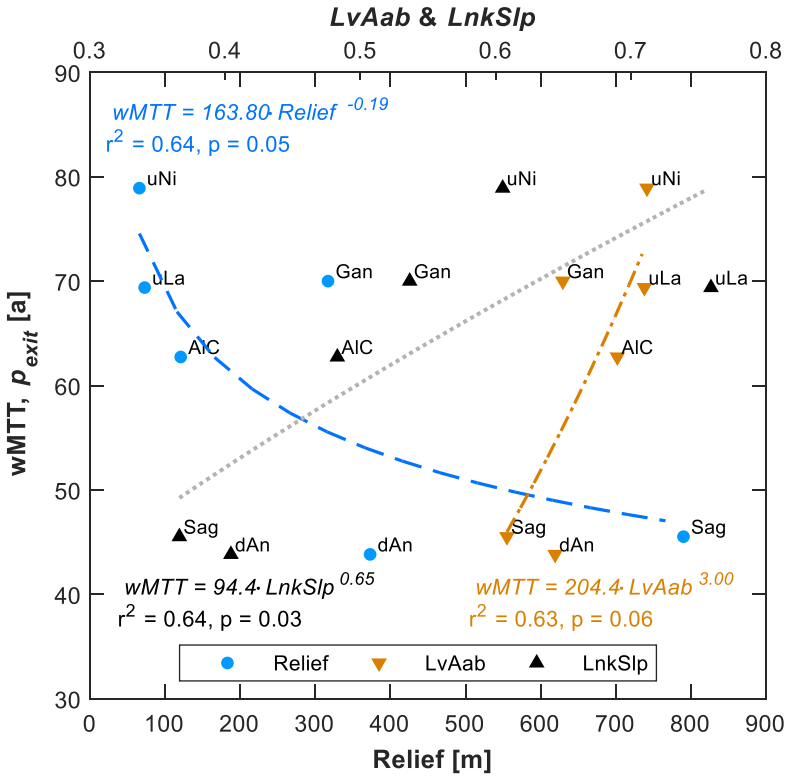


Figure 3-12. SLR models for watershed MTTs (wMTT in years) as estimated by the numerical model for the six watersheds. The predictors for these models are *Relief*, the power function product $a{\cdot}b$ (*LvAab*) for the fractal relationship between main stream length and drainage area ($L{=}a{\cdot}A^b$), and the exponent of the power function ($L_S{=}a{\cdot}N^b$) between stream slope and magnitude (*LnkSlp*).

A third relationship links wMTT to the predictor, *LnkSlp*. The latter, is a measure of stream slopes decreases with magnitude ($N$). Here, magnitude ($N$) refers to the Shreve stream order. A relationship between *LnkSlp* and *LvAab* can be expected, at least in some watersheds because, as stream slopes decrease downstream along the stream network (i.e., from headwaters to valley), so does the drainage area of affluent rivers to the main stem as it converges to the watershed outlet. This would explain the similarities in the distribution of wMTT with *LvAab* and *LnkSlp*. For both the relationships with *LnkSlp* and *LvAab*, Sagehen and des Anglais Rivers are one of the end members, and Upper Nith and Laurel Creek define the other. These end member groupings are not reflected in any of the other

geomorphological relationships considered in this study. More work is needed to fully unravel how and why *LvAab* relates to both wMTT and the analytical model parameter *SF* (Figure 3-11a and Figure B9a) for the study watersheds.

3.3.4.2 MLR for wMTT

Applying similar steps in the creation of MLR models as for the analytical parameters, several models predicting wMTT were generated. Five models with similar predictive power are presented in Appendix B (Table B3) where more details on their development can be found. In the resulting models, indexes related to Horton's law ($R_B$, $R_C$, and *LnkSlp*), texture topography (*DF*, *HDd*), and elevation (*Schan*) prevailed as predictors. The fourth model is considered the most relevant, for reasons explained in Appendix B (Figure B11). This is a Horton's law-based model using $R_B$ and *LnkSlp* indexes as predictors. The only difference between *LnkSlp* and $R_S$ is that the former uses the logarithm of magnitude (*N*) as opposed to Strahler ordering, in the stream ordering scheme. For this reason, it is considered under the Hortonian category of measures.

### 3.3.5 Verification of Proposed Models

After applying Tier 1 (*Relief* < 790 m with *Dd*<2.7 [1/km] and *cSlope*<8.63 deg) and Tier 2 (Table 3-3) indicators to a set of 19 subbasins located in the Grand River watershed, three subbasins (or tributary watersheds) were selected from seven that fulfilled the required conditions: Carroll Creek, Schneider Creek, and Nith River (Figure B12, Appendix B). Hence, the analytical model is assumed to yield estimates of travel time for these three subbasins that are comparable to numerical predictions. The verification process employs the same analytical and numerical model approaches as used earlier for the other watersheds, but not limited to homogeneous hydraulic conductivity ($K_{xy}$= $K_z$=5.26 m/d) and porosity (0.35). A bedrock surface map is available for the entire Grand River watershed and used here.

The predictive tools for *SF*, *Uo*, and $\lambda_L$ (Figure 3-12 for SLR models, and Figure B9 and Table B2 for MLR models), based on correlations with geomorphological indexes (Table 3-4)

are used in the analytical model calculations. In general, the SLR models provide better estimates that fell within the expected value ranges, compared to the MLR models (Table B4), which yielded in some cases negative values. Although the SLRs suggest that both *Relief* and *LvAab* are predictors for SF, only the *Relief* estimated *SF* values agree with the ranges

Table 3-4. Watershed characteristics, geomorphological indexes, and wMTT numerical and analytical estimates for the three selected subbasins used for verification. This list includes only the indexes used in the SLR and MLR models for predicting the analytical model parameters and wMTT.

| ***Parameters*** | ***Carroll Creek*** | ***Schneider Creek*** | ***Nith River*** |
|---|---|---|---|
| Area [$km^2$] | 78.1 | 70.3 | 47.7 |
| Perimeter [km] | 54.5 | 49.6 | 44.3 |
| *Dd* [1/km] | 1.63 | 1.05 | 1.63 |
| *DF* [1/$km^2$] | 2.24 | 1.56 | 2.47 |
| *Tex* [1/km] | 0.44 | 0.54 | 0.79 |
| *TexPer* [1/km] | 0.43 | 0.38 | 0.48 |
| *HDd* [-] | 14.5 | 7.1 | 9.0 |
| $R_C$ [-] | 0.16 | 0.18 | 0.26 |
| *C* [km/km] | 6.18 | 5.91 | 6.41 |
| *LvAa* | 1.24 | 0.50 | 0.50 |
| *LvAab* | 0.56 | 1.01 | 0.71 |
| $d_{BCst}$ | 1.059 | 1.043 | 1.064 |
| *Relief* [m] | 146 | 129 | 85 |
| *MnChL* [m] | 127233 | 73856 | 77884 |
| *Schan* [%] | 2.06 | 1.37 | 0.94 |
| *LnkSlp* | 0.41 | 0.35 | 0.60 |
| $R_L$ | 0.33 | 0.58 | 0.47 |
| $R_B$ | 3.62 | 5.77 | 3.31 |
| $R_S$ | 2.70 | 2.20 | 5.10 |
| *Predicted Analytical Model Parameters* | | | |
| $a \cdot b(\lambda_L)$ | 0.44 | 0.66 | 0.40 |
| $Uo$ | 0.067 | 0.076 | 0.065 |
| $SF$ | 17 | 20 | 31 |

expected for these watersheds' characteristics. The $d_{BCst}$ index tends to overestimate *Uo*, while *DF* appears to yield better *Uo* values. (Note: *DF* was initially identified as a potential *Uo* predictor in section 3.3.3.1). The analytical $\lambda_L$ parameters *b* and *a·b* were adequately estimated from *TexPer* and *Dd*, although, *Dd* tends to slightly overestimate *a·b*. Ultimately, index *DF* was used instead, as it generates better results. The MLR models for *SF* and *a·b* provided unreasonable, negative estimates, whereas for *Uo* and *b* the estimates are within the expected ranges. However, for all the predicted parameters, the estimates from the SLR models are preferred.

The analytical models for the verification watersheds were constructed with the predicted estimates for *SF*, *Uo*, and the dispersion parameters *b*, and *a·b*. The frequency of travel times estimated by both models is compared using measures of fit for the shape of the distributions (Figure 3-13a, Figure 3-13b, and Figure 3-13c). The measures of fit for Carroll Creek and Nith River watersheds show a similar degree of agreement obtained in the initial 9 study watersheds. This is not the case for the Schneider Creek watershed where the analytical model pMTT estimates yield a distribution with significantly less range, given by the standard deviation, which, in turn, lead onto the underestimation of the wMTT (Figure 3-13d). For these two watersheds, the 95$^{th}$ percentile of the numerical model estimates of travel time is still encompassed by the range of pMTTs estimated by the analytical method.

The level of agreement between methods measured by the measures of fit used on the particle-to-particle comparison (Figure 3-14) for the Schneider Creek watershed does not reflect the significant offset of the entire TTD. It is only the inclination of the trendline of the entire dataset that shows evidence of the TTD offset with respect to the numerical TTD.The inclinations of the particle cloud (i.e., pMTT) in the scatter plots for the three verification watersheds, are less than 45 degrees, suggesting that the predicted analytical *Uo* is faster than the mean velocity in the numerical model simulations. The effect on the overall wMTT does not appear to be that significant as the analytical and numerical wMTT in Carroll Creek and Nith River were similar. However, for the Schneider Creek watershed, where the

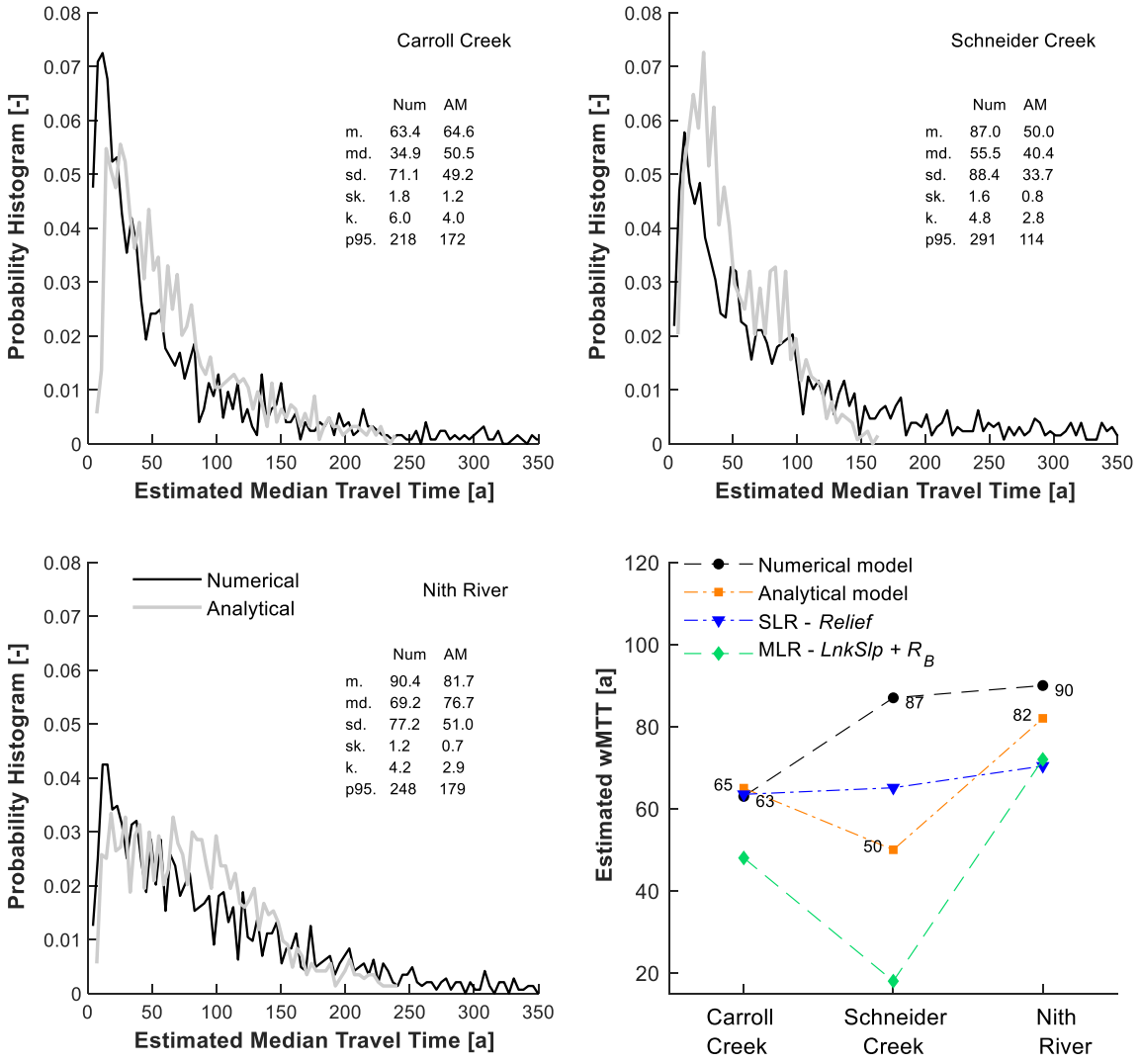


Figure 3-13. Frequency of travel times (pMTTs) estimated by both numerical (Num) and analytical (AM) methods for the verification watersheds: a) Carroll Creek, b) Schneider Creek, and c) Nith River. The predictive tools derived in this study for estimating watershed MTT based on geomorphological features are compared in panel (d). The SLR and MLR models used topographic *Relief* and Horton's law measures (*LnkSlp* & $R_B$) as predictors, respectively.

degree of inclination is much below 45 degrees, the analytical wMTT is significantly underestimated relative to the numerical estimate: 50 versus 87 years, respectively.

The regression models directly relating wMTT to geomorphological indexes are also applied on the verification watersheds. The wMTT estimates based on the *Relief* and *LnkSlp* SLR models range between 47 to 70 years, compared to the numerical model's values between 63 and 90 years (Table B5, in Appendix B). The predictive ability of *LvAab* and *LnkSlp* appears to be limited as they do not capture the trend in wMTT values generated by the numerical model (Table B5), possibly because the *LvAab* and *LnkSlp* values of the verification watersheds fall outside the ranges of values used to initially develop the SLR model. Given that the two indexes yield trends that are completely opposite to those of the numerical results, we do not recommended using *LvAab* and *LnkSlp* as predictors of wMTT. This leaves *Relief* as the main predictor of wMTT (Figure 3-14d) among the SLR models. Even though the *Relief*-based model follows the general numerical trend, its performance is least for the low topographic relief of the Nith River.

The geomorphological indexes of the verification watersheds are also used in the MLRs (Table B3, Appendix B). From the MLR models listed in Table B3, only models 2, 3, and 4 provide usable results highlighting the product $a \cdot b$ from the $\lambda_L$ power function as the key analytical predictor in models 2 and 3. The similar results produced by models 2 and 3 likely reflect the shared influence of $a \cdot b$. Model 4 captures the interaction between the geomorphological indexes $R_B$ and *LnkSlp*. Both indexes can be seen as Horton's law measures considering that the only difference between *LnkSlp* and $R_S$ is that, in the former, the logarithm of the stream's magnitude ($N$) is used instead of the Strahler order. The wMTT estimates of models 2 and 3 are clustered around 70 years, but do not capture the inter-watershed trend observed in the numerical model (Figure 3-14d). Model 4, interestingly, follows the wMTT trend of the analytical model characterized by a significant underestimation of wMTT for Schneider Creek (Figure 3-14d). Keeping in mind the caveats associated with all modeling approaches used, the regression models may present an alternative to the analytical model to obtain preliminary wMTT estimates.

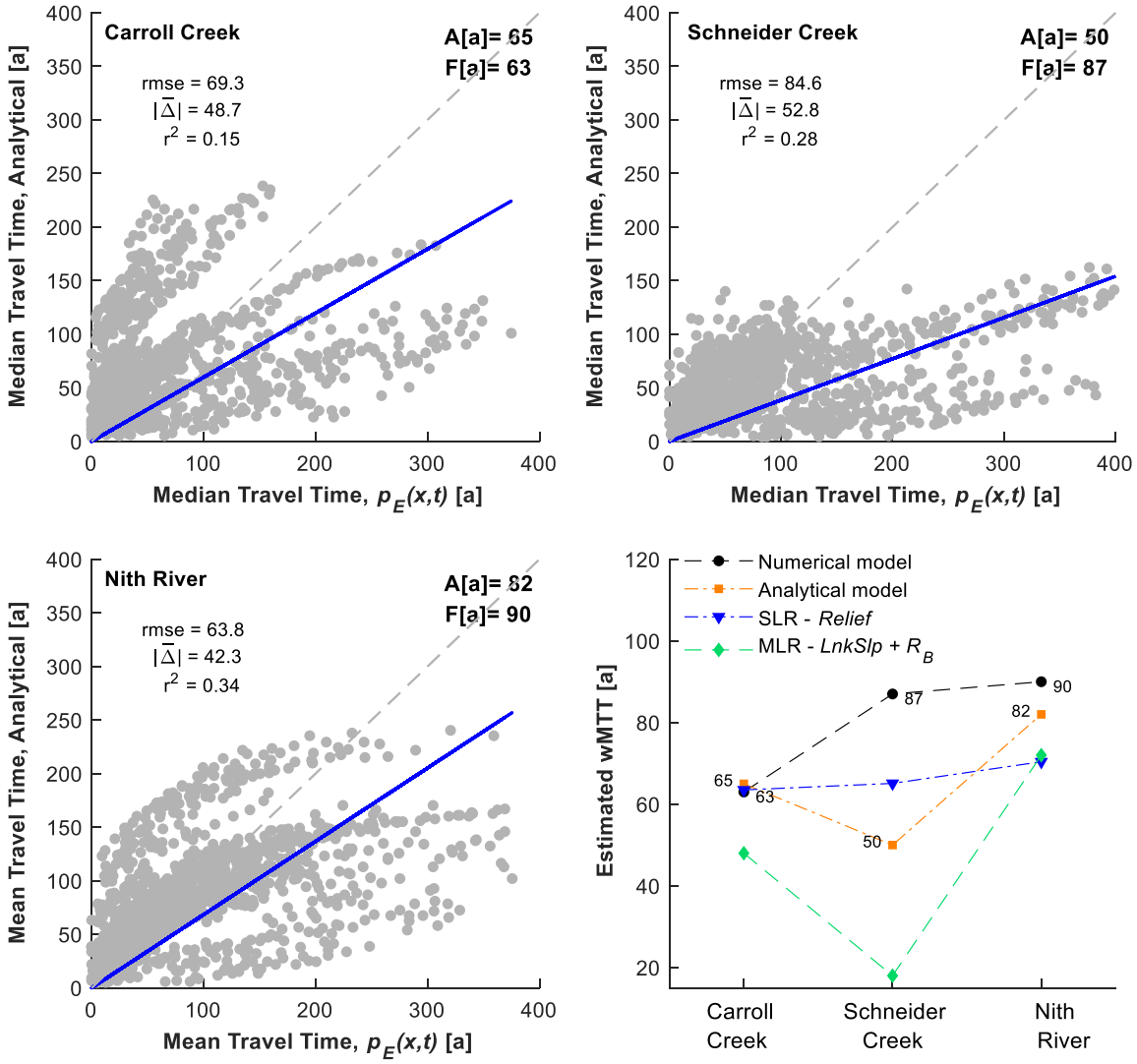


Figure 3-14. Scatter plots for analytical and numerical particle MTTs for verification watersheds: a) Carroll Creek; b) Schneider Creek; and c) Nith River. The watershed MTT are also reported for the analytical (A) and numerical (F) models. The predictive tools derived in this study for estimating watershed MTT based on geomorphological features are compared in panel (d). The SLR and MLR models used topographic *Relief* and Horton's law measures (*LnkSlp* & $R_B$) as predictors, respectively.

## 3.4 Discussion

The travel time distributions (TTDs) and watershed MTTs estimated by the numerical and analytical models are comparable in most of the study watersheds, except in the more mountainous RPT river basins. That is, we cautiously conclude that, in appropriate geomorphological settings, the analytical model performs well, regardless of watershed size. This is an important result from a watershed management point of view, because it provides a simple method to estimate the range of groundwater travel times in a given watershed, and it implies that local flow processes are replicated at larger scales. Ultimately, it is at the watershed scale that planning decisions should be made for regional and hydrologically connected areas (*Sivapalan et al., 2003*; *Wagener et al., 2010*).

The TTDs presented here provide crucial baseline information to assess the subsurface transport of diffuse pollutants infiltrating into a regional aquifer system. They yield insights into the hydrological and water quality responses to alterations in the watershed associated with land cover, land use, water management and climate change. A sustainable groundwater supply relies on the continued replenishment of the resource via recharge that, when exposed to contamination, may require an environmental risk assessment to be conducted to predict its impact on wellfields and receiving streams and reservoirs. The range of potential groundwater travel times in a watershed also impacts the fate of pollutant and nutrient legacies that have accumulated in the subsurface as a result of historical practices.

The analytical methodology used here, then, provides the means to obtain both an approximate distribution of groundwater ages and the MTT of a watershed by employing simple and readily available tools (here, GIS and mathematical software packages, and DEM). In comparison, the analytical method presented here performs more accordingly with the numerical output than the exponential function-type TTD from Haitjema (*1995*)'s approach (Figure 3-15, and Figure B14 in Appendix B). Notwithstanding the simplifying assumptions used in this study for both numerical and analytical methods, in particular steady-state flow and subsurface homogeneity, we believe the analytical equations and the

regression models yield useful information about the behavior of the groundwater system at the watershed scale. As shown in Chapter 2, these simplifying assumptions can be relaxed, for example by introducing heterogeneity in subsurface properties. In addition, the steady state flow assumption may offer a reasonable approximation for long travel time groundwater systems (*Beven, 2010*), such as found in lowland-dominated watersheds.

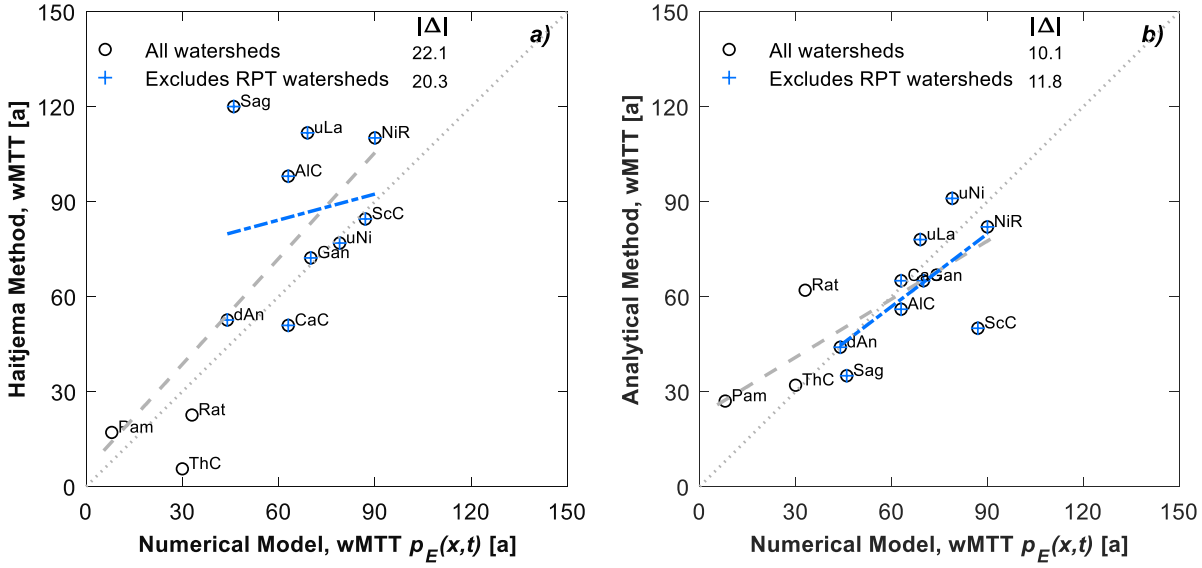


Figure 3-15. Estimates of the wMTT using both the Haitjema (*1995*) method (a) and the analytical methodology (b) developed in this study. Trendlines for both the 9 watersheds and the set excluding the RPT watersheds are compared to the numerical model estimates. The measure of fit mean absolute error is shown for each data set (|Δ|).

In contrast to the TTD range and wMTT, and not necessarily unexpected, the analytical approach only performs moderately well when estimating pMTT. Alder Creek scores best in the analytical-numerical comparison ($r^2$=0.52, Figure 3-4) followed by acceptable performances, except for the RPT watersheds where hillslope hydrology plays a decisive role. The watershed's shape controls the range of travel times observed in the lowland, midland, and upland portions of the watersheds, as short travel times occur in lowland regions and longer travel times in midland areas. The topographic slope controls the range of travel times in the upland regions. The analytical model's performance, however, remains

unaltered in the different elevation intervals of the observation points (OPs). As indicated in Figure 3-3 and Figure 3-2, the range of wMTTs and the variability of pMTT do not depend on watershed size.

The geomorphological analysis presented helps to identify those physical properties of a watershed that most significantly affect groundwater travel times, and to delineate the geomorphological conditions under which the analytical model performs well, or not. In general, among the geomorphological indexes considered, texture topography and elevation measures are the most revealing. A single geomorphological index, *Relief*, explains the poor agreement between the analytical and numerical results for the RPT watersheds. The best agreement occurs when *Relief* is less than 790 m. In addition, the analytical model performs best when *Dd* is less than 2.7 $km^{-1}$, probably as a result of the strong correlation between *Dd* and *Relief* (Figure 3-6b). In other words, the analytical model seems to be more suited at lower drainage densities and in flatter watersheds.

The similar wMTT estimates for the Sagehen River (37.2 $km^2$) and des Anglais River (701.3 $km^2$) watersheds provide an interesting test case, given the large differences in size and slope characteristics of the two watersheds: the drainage density for Sagehen River is almost five times higher than for des Anglais, while *Relief* is twice as high. However, the topographic conditions in the des Anglais' watershed are particular in that the ground elevation above 80 m occurs in only one isolated, steep slope location, Covey Hill, which constitutes the major water source for the watershed. The remaining terrain is very flat (Figure 3-1 and Figure B3). The steep drop in elevation between Covey Hill and the wide valley generates high bulk groundwater velocities. These high velocities in the numerical model are matched in the analytical method during calibration (Figure 3-11b). This yields pMTTs and wMTTs for des Anglais comparable to a smaller and steep watershed, such as Sagehen River, rather than values associated with a large and extremely-flat watershed.

The discrepancy between the apparent (steeper) and actual (flat-dominated terrain) *Relief* of des Anglais is evident in the *Dd-Relief* relationship where this watershed falls off the average trendline (Figure 3-6). In the same figure, Rattlesnake Flat and Pamilco Canyon also

exhibit lower than expected drainage densities relative to their *Relief*. The low drainage networks in these watersheds reflect the semi-arid climate conditions in which the actual (real) watersheds are located. To counteract the artifact of mapping the real drainage network onto the virtual watersheds, several denser drainage networks were created. However, none of these attempts improved the performance of the analytical model.

In terms of *Relief*, Sagehen River has the fourth highest value among the study watersheds, but in terms of *mGrad* and *Schan* it is one of the top two sites. The question then arises why a watershed with these steep characteristics performs better than the three RPT watersheds? The answer may lay in the hypsometric (Figure B3) and the link concentration (Figure B4) curves of these four watersheds. The hypsometric curve of Sagehen River suggests the presence throughout the watershed of milder slopes associated with an elongated and rather steep valley that dominates about 80 percent of the watershed (>0.2 sA/A). Along this valley, the density of streams is much greater than in the rest of the watershed as suggested by the link concentration curve. These characteristics, which are absent in the RPT watersheds, are not only better suited for implementing the analytical method, they also generate longer flow paths, pMTTs and wMTTs. In summary, the special, divergent geomorphological characteristics of Sagehen River and des Anglais River both converge to similar wMTT values.

The regression analyses show that elevation (*Relief* for *SF*), shape (*LvAab* for *SF*), fractal dimension (*dBCst* for *Uo*), and texture topography (*TexPer* and *Dd* for macrodispersion parameters $b$ and $a \cdot b$) indexes can be used as predictors for the analytical model parameters in the SLR models, but not the shape or Horton's law indexes. The parameters of the *LvA* power law relationship between main stream length and drainage area (i.e., *LvAb* and *LvAab*, section 3.3.4.1) serve as predictors not only for the analytical model parameters but also for wMTT (Table B3). However, the interpretation of the link between the *LvA* power function and wMTT is not straightforward. As shown in section 3.3.4.1, *LnkSlp* and *LvAab* are similarly distributed with respect to wMTT-$p_{exit}$ (Figure 3-12), because the two parameters are significantly correlated (r=0.82). This correlation with *LnkSlp* helps explain

the role of $a \cdot b$ of the *LvA* power function in wMTT. The index *LnkSlp* is a measure of the rate of drainage transition from the upstream to downstream portions of the watershed. Thus, the $a \cdot b$ product of the *LvA* power function can be seen as a measure of the drainage area per unit main stem length. Note, however, that in the verification watersheds, the *LvAab*-based regression models do not perform as well in predicting both analytical model parameters and wMTT.

Fractal dimensions, especially $d_{BCst}$, $D_{BCp}$, and $D_{WDp}$, exhibit strong correlations with $U_0$ and the macrodispersion parameter $b$, but only the contribution of $d_{BCst}$ is significant enough to be part of the $U_0$ SLR model. An MLR model based on texture topography indexes (i.e., *Dd* and *DF*, Table B2) for $U_0$ is also proposed. The macrodispersion parameters (i.e., $b$ and $a \cdot b$) appear well constrained by texture topography indexes in both SLR and MLR models. However, the SLR models perform better than the MLR models, and they are recommended to estimate the macrodispersion parameters for use in future applications of the analytical model (Table B4). The MLR models are likely more sensitive to the limited amount of observations that are available to constrain them properly. From the analysis of the results from the verification watersheds, the best predictors of the analytical model parameters that emerge are: texture topography (*DF*, *TexPer*, and *Dd*, for *Uo*, $b$, and $a \cdot b$), and elevation (*Relief* for *SF*) (Table 3-5).

Table 3-5. Summary of most relevant predictors used in the verification watershed analysis.

| **Predicted Parameter(s)** | **Type of Measure, Index & Model** |
|---|---|
| Analytical model parameters | *SF* : elevation (*Relief*) = $3934 * Relief^{1.09}$<br>*Uo* : texture topography (*DF*) = $0.089 * DF^{-0.35}$<br>$b$ ($\lambda_L$) : texture topography (*TexPer*) = $0.83 * TexPer^{0.36}$<br>$a \cdot b$ ($\lambda_L$) : texture topography (*Dd*) = $1.08 * DF^{-1.10}$ |
| wMTT | SLR : elevation (*Relief*) = $163.8 * Relief^{0.19}$<br>MLR : Horton's law (*LnkSlp* and $R_B$)<br>$= 41.3 + 109.7 * LnkSlp - 10.7 * R_B$ |

In the proposed MLR models for predicting wMTT the predominant types of indexes are Horton's law ($R_B$, $R_C$, *LnkSlp*), texture topography (*HDd*, *DF*), analytical model parameters ($a \cdot b$) and shape ($R_C$, *MnChL*). In the verification watersheds, *Relief* is the best predictor of wMTT among the SLR models but, surprisingly, it does not appear in any of the MLR models. The best MLR model (i.e., No. 4, *LnkSlp*- and $R_B$-based) follows the trend but not exactly the magnitude of the analytical wMTT estimates. Considering this and the fact that, in the case of Schneider Creek, the analytical method overestimates *Uo* when using *DF* as predictor, and that *LnkSlp* and $R_B$ are Horton's law indexes, the particular structural configuration of the stream network, which is related to *DF*, *LnkSlp* and $R_B$, may be the cause of the poor performance of the analytical model in this watershed. Schneider Creek exhibits by far the lowest $R_S$ value (= 2.2 Table 3-4) among the study watersheds, which is characteristic of a very smooth drainage transition from the upper reaches to the lowlands. However, more work is needed to support this explanation.

The predictions provided here for both the analytical model parameters and for wMTT are based on a limited number of observations, which strongly weighs on the performance of the MLR models. Nonetheless, the good results for Carrol Creek and Nith River, and the other study watersheds, are quite encouraging and indicate that the analytical model and the associated regression models provide a meaningful approach to generate first, rough estimations of groundwater travel time distributions in watersheds that lack the data or resources for the implementation of a full numerical hydrogeological model. When applying the analytical methodology, however, the various caveats and recommendations presented in this work should be taken into consideration.

## 3.5 Conclusions

The goals of this study were fourfold: 1) To test the performance of the analytical methodology for particle (p-) and watershed (w-) MTT developed in Chapter 2 in different environmental settings (i.e., nine virtual watersheds); 2) To identify the geomorphological properties that control particle travel times and, at the same time, yield metrics to evaluate the potential performance of the analytical model in future applications. (Note: this objective

emerged from the results in Chapter 2 where the effects of topography and depth to aquifer on TTDs and wMTTs were examined.) 3) To predict the parameters of the analytical model for future applications, by deriving regression equations from the physical characteristics of watersheds. 4) To identify, via the construction of SLR and MLR models, the geomorphological controls on watershed MTTs.

In order to assess the performance of the analytical method, the observed geomorphological data from nine real watersheds are mapped onto nine virtual analog watersheds. These virtual watersheds are further assumed to have homogeneous aquifers that are recharged at the same, uniform annual recharge of 227 mm per year. In four of the watersheds, aquifer depths are assigned based on the available maps of the bedrock surface. For the remaining watersheds, bedrock surfaces are created either from large scale hydrogeological maps that cover the valley regions and are then extended to the hillslope areas, or from groundwater well depth data assuming full penetration of the aquifer.

Based on the generated pMTT estimates, the TTDs of the analytical model compare reasonably well to those of the numerical model for most watersheds, except the RPT watersheds. The 95$^{th}$ percentile of the pMTTs estimated by the numerical model is encompassed by the analytical model estimates, which closely follow the shape descriptors of the distribution from the numerical model. For the wMTT estimates there is good agreement ($r^2$=0.89), with the analytical wMTTs remaining, on average, within 12% of the numerical values (excluding the RPT watersheds). This is an important result with implications for watershed management as TTDs and wMTTs are key metrics constraining watershed-scale groundwater tracer transport. However, the spatially bound analytical pMTT do not yield the same level of prediction. There are two reasons for this: 1) the numerical model yields unreliable travel times in the RPT watersheds, where hillslope hydrology plays a major role that is not well captured in the simulations, and 2) in the other six watersheds, the predicted analytical and numerical groundwater age distributions do not exactly coincide at the same watershed locations. This spatial disconnection between the TTDs and the pMTTs reveals a failure of the analytical model to capture the full intricacy of

groundwater flow paths. The best agreements between analytical and numerical pMTTs are for Alder Creek ($r^2$=0.52), Upper Laurel Creek ($r^2$=0.30), and Upper Nith River ($r^2$=0.25). Similar agreements are found for the three additional verification watersheds: $r^2$=0.15, 0.28, and 0.34 for Carroll Creek, Schneider Creek and Nith River, respectively.

The larger pMTTs are predominately generated at mid- and high-elevations in the watershed because longer flow paths tend to develop in these areas, thereby revealing an important control by the watershed shape. Thus, as expected from the findings in Chapter 2, flatter terrain generally yields longer travel times. The exception is des Anglais River where groundwater flow velocities are strongly affected by the only elevated part of the watershed, Covey Hill. The unique topography of des Anglais River results in fast flow velocities that ultimately lead to a wMTT comparable to that of Sagehen River's, despite the completely opposite geomorphological characteristics of the two watersheds in terms of relief, average slope and drainage density.

From the geomorphological indexes considered (27 in total), topographic relief (< 790 m) coupled with drainage density (< 2.7 $km^{-1}$) and mean channel slope (*Schan* < 8.63 deg) yield the most discriminatory conditions under which the analytical model performs best. A second tier of geomorphological constrains is also identified that can help guide future selection of watersheds where the analytical method could be applied (Table 3-3). From this analysis, single and multiple linear regression (SLR and MLR) models are derived from which the analytical model parameters (*SF*, $U_0$, *b*, and $a \cdot b$) can be estimated, which is essential for future implementations in other watersheds. Measures of, in order of importance, texture topography or drainage density, elevation, and shape (Table 3-5), emerge as the predictors in the SLR models. Overall, the MLR models do not perform as well as the SLR models, presumably because they are more sensitive to the limited number of observations (i.e., only six watersheds).

An important observation is that $U_0$ appears to depend on indexes related to texture topography rather than direct slope-related indexes. Similarly, the *b* exponent in the analytical model is also predicted to be controlled primarily by texture topography. This

exponent defines both how fast the macrodispersion power function changes with respect to flow path distance, and how large the $\lambda_L$ coefficient is. The fact that these parameters depend on texture topography indicate that they are influenced by the frequency at which the ensemble of groundwater flow paths intercept the streams in the watershed.

The application of the regression models to the verification watersheds reveals that *Relief* is the major predictor of wMTT and also the smoothing factor (SF). This suggests that gravity forcing is an important control on wMTT. In another transferable tool, a MLR model for wMTT (model 4 in Table B5), based on Horton's law indexes, produces a similar pattern as the analytical model in which Schneider Creek's wMTT is significantly underestimated (relative to the numerical prediction). This likely indicates that for certain structural watershed configurations the analytical model will perform poorly. Exactly what these configurations are will require further work.

Acceptable approximations of TTDs and wMTTs for ungauged river basins provide essential information to evaluate regional responses to changes in climate and land use. The analytical model and the regression models presented here are a step forward in building that capability. An important next step will be to determine how relaxing the key assumptions, that is, constant recharge and aquifer homogeneity, will affect the predictions and performance of these models. As recently suggested by Hale et al. (*2016b*), a more detailed analysis of subsurface heterogeneity as a predictor of groundwater travel times deserves further attention.

# Chapter 4
# A Coupled Hydrology-Nitrogen Catchment Model Incorporating Nitrogen Isotopes

**Note:** this is a prospective chapter presenting the preliminary development of a catchment-scale model simulating the fate and transport of nitrate and its stable isotopes. The planned application of the model to a tributary watershed in the Grand River basin is outlined as well as associated modeling scenarios. This work is ongoing in collaboration with Dr. Mahyar Shaffi of University of Waterloo.

## Summary

Nitrogen (N) nonpoint pollution management is an important environmental target in developed countries following the systematic elimination of point source discharges of raw wastewater. The reduction of N nonpoint sources has proven difficult due to ubiquitous anthropogenic sources and the occurrence of legacy stores in watersheds. Nitrogen isotopes in nitrate ($^{14}N$ and $^{15}N$) have been used to both track N sources in watersheds and trace N biogeochemical cycling through the various landscape compartments. Most N transformations and isotopic fractionations are directly or indirectly related to hydrological processes, yet attempts to fully couple them are fairly rare. Here, we initiate the development of a coupled hydrology-nitrogen biogeochemistry model platform and discuss its prospective application to the Carroll Creek watershed (78 $km^2$) in the 6800 $km^2$ Grand River basin in Southern Ontario. The study watershed is predominantly agricultural (86%). Annual loads of organic and inorganic fertilizers, biological N fixation, and atmospheric deposition are considered as inputs to the N isotope model. The external inputs of N and their respective $^{15}N/^{14}N$ ratios replenish the subsurface N compartments where the following N transformations can take place: organic N mineralization, ammonia volatilization, nitrification, plant uptake, and denitrification. The N exports from each hydrologic response unit are then collated from the various N compartments to form the overall N export from the watershed. The base flow N loads account for the travel times

estimated from the analytical model developed in Chapter 3 for Carroll Creek watershed. The ongoing work aims to calibrate the N isotope model using the concentrations and N isotope compositions of nitrate measured in Carroll Creek. This will be accomplished by fitting the N transformation rates and source N isotopic compositions using non-linear least square regressions or Monte Carlo simulations. A preliminary analysis indicates that the likelihood of finding a global minimum that closely matches the observed streamwater N isotope compositions is low, considering the uncertainties associated with assigning source N isotopic compositions and the current absence of representing the N redox transformations in the groundwater-surface water transition zones (e.g. riparian and hyporheic zones, and wetlands). Thus, this work is only a first step in the development of a process-based modeling platform to predict and analyze the watershed scale N isotopic imprints resulting from land use practices and subsurface N transformations.

## 4.1 Introduction

The concentrations and isotopic compositions of dissolved nitrogen (N) species change as they move along different the hydrological and biogeochemical pathways in the subsurface. This is of most importance in agricultural watersheds, where the demand of N to increase crop production has altered the allocation of N in soil ecosystems at the global scale (*Vitousek et al., 1997*; *Vitousek et al., 2013*). Watershed N exports occur chiefly through outflow of the oxidized, dissolved form of N (i.e., nitrate, $NO_3^-$), and gaseous emissions (i.e., $N_2O$ and $N_2$) to the atmosphere. While the riverine inputs to coastal zones have increased as a result of rising agricultural inputs, they are just a fraction of the N inputs to the landscape because of N retention in soils and gaseous losses primarily driven by denitrification (*Boyer et al., 2002*; *Wollheim et al., 2008*; *Hale et al., 2013*). Notwithstanding this N removal, projections for food production and wastewater effluents have been used to estimate that the global riverine N flux will increase by 13% in 20 years, whereas developing countries are projected to see a 27% increase (*Bouwman et al., 2005*).

The reduction of point-source pollutants to waterbodies has been significant in the last 50 years, at least in developed countries (*Alexander & Smith, 2006*; *Schulz & Bischoff, 2008*;

*Ballantine & Davies-Colley, 2014*). On the other hand, non-point source pollution remains a challenge as it involves a wider spectrum of human activities (e.g. fertilizer application, septic tank leachates, burning of fossil fuel, industrial releases to the atmosphere) being applied at different spatial and temporal rates over the entire landscape. Mitigating non-point N pollution has quickly become one of the main watershed management targets in developed countries (*Carpenter et al., 1998*; *Hardy & Koontz, 2008*). This management task has been proven difficult due to the myriad of N sources in watersheds with mixed land use (*Carpenter et al., 1998*).

Stable N isotopes provide a means to identify sources and assess the reactive transport of N in surface and subsurface environments (*Kendall, 1998*), at various spatio-temporal scales. In several studies, researchers have been able to identify the origin of the distinct N isotopic imprints of nitrate ($\delta^{15}N\text{-}NO_3^-$) in areas dominated by a particular land use (*Spoelstra et al., 2001*; *Karr et al., 2001*; *Burns et al., 2009*; *Kaushal et al., 2011*). Because different N sources may exhibit overlapping N isotopic compositions (*Fogg et al., 1998*), the task of identifying the sources of $NO_3^-$ in a mixed land use scenario is more complex. It has, however been accomplished successfully (*Aravena et al., 1993*; *Wassenaar, 1995*; *Robertson & Schiff, 2008*). Another use of $^{15}N$ abundances is to provide evidence for the occurrence of specific N transformations by keeping track of the $^{15}N$ enrichment of the substrates and the depletion of the products (*Mariotti et al., 1988*; *Lehmann et al., 2003*), which, again, may be difficult to achieve in the case where N is subjected to a series of transformations as it moves from terrestrial to aquatic systems (*Bottcher et al., 1990*).

Considering the complexities associated with the interpretation of $\delta^{15}N\text{-}NO_3^-$ data under mixed land uses and at the watershed scale, Burns et al. (*2009*) suggested limiting the analysis to a smaller portions of a few hundred $km^2$ in large watersheds. For example, in a large watershed (26,000 $km^2$, 27% of South Korea), Lee et al. (*2008*) were able to identify the major source of $NO_3$-N in the northern branch of the watershed (~40% of total area), however, the isotopic signatures for the southern branch could not distinguish between manure and sewage. When considering streamwater isotopic N compositions, the sources

and transformations are not limited to landscape units next to the stream, they may in fact originate from nonpoint sources much farther away and involve long flow paths (*Kaushal et al., 2006*; *Kaushal et al., 2011*). Potential N transformations involve N volatilization, vegetation uptake, nitrification, and denitrification, with the latter occurring both in shallow and deeper aquifers (*Wassenaar, 1995*, *Cey et al., 1999*; *Robertson and Schiff, 2008*).

Nitrogen transformation processes in the soil and aquifers occur in parallel to hydrological processes. Thus, a biogeochemical model describing the N transformation in the subsurface must be accompanied by a hydrological model that simulates the transport fluxes among the different N reservoirs in the landscape. Here, we started developing an N isotope model which we link to the RAVEN hydrological model for the Carroll Creek watershed (78 $km^2$). This watershed is located in the much larger the Grand River basin (6,800 $km^2$) and is dominated by agricultural land use (86%). The N isotope model emulates the compartments in the hydrological partitioning used by RAVEN and follows a mass balance approach similar to those employed by Mary et al. (*1998*) for $^{15}N$ tracing methods, and by Amundson and Baisden (*2000*) and later by Brenner et al. (*2001*) for the natural $^{15}N$ abundance in a soil-plant system. The soil-plant system model presented in Brenner et al. (*2001*) is an improved version of the model in Amundson and Baisden (*2000*) and since its inception it has been applied in several studies (*Amundson et al., 2003*; *Houlton et al., 2006*; *Bai & Houlton, 2009*; *Hilton et al., 2013*).

Amundson et al. (*2003*) applied their soil-plant model to a worldwide database of $\delta^{15}N$ and found that soil and plant $\delta^{15}N$ values are negatively and positively correlated with mean annual precipitation and temperature, respectively. The phenomenon of the under-expression of the isotopic effect associated with denitrification is a recurrent topic in N biogeochemistry (*Houlton et al., 2006*; *Bai & Houlton, 2009*), which Amundson et al. (*2003*) soil-plant N isotope model is able to reproduce. The phenomenon refers to the apparent reduction in the denitrification's isotopic imprint with increasing scale of observation. In most environmental settings, denitrification is limited to clustered areas where the right biogeochemical conditions prevail. The isotopic (heavy) signatures of the residual $N\text{-}NO_3^-$

from these areas eventually mix with the $N\text{-}NO_3^-$ from other areas where denitrification is inhibited, e.g., by the presence of molecular oxygen (*Brandes & Devol, 1997*). The increasing in-mixing of isotopically lighter $N\text{-}NO_3^-$ dilutes, and possibly masks, the isotopic expression of denitrification at the watershed scale (*Houlton et al., 2006*).

Lehmann et al. (*2003*) following Brenner et al. (*2001*), applied a diffusion-reaction isotope model to a lacustrine environment accounting for denitrification in both water column and bottom sediments. The isotopic imprint associated with denitrification in this system was diminished by the input of fresh $NO_3^-$. In light of the limited number of observations, Lehmann et al. (*2003*) determined the model parameters using a weighted least square method for the most uncertain parameters (i.e., the isotopic enrichments of N and oxygen, and the denitrification rate constant), and a Monte Carlo simulation for the inhibition constants, Michaelis-Menten parameters, mixed sediment height, and turbulent diffusivity. In the $^{15}N$ tracing model literature, Mary et al. (*1998*) developed the FLUAZ program, which solves a similar system of differential equations but includes a greater number of N transformations with the goal of calculating gross N transformation rates. The calculation of the final gross N rates is done in FLUAZ by applying a non-linear fitting technique based on Levenberg-Marquardt's algorithm to find the global minimum (*Mary et al., 1998*). Significant improvements to the original FLUAZ model were made by Müller et al. (*2004*) by adding more N transformations. Later, Müller et al. (*2007*) replaced the Levenberg-Marquardt's algorithm with a Monte Carlo sampling approach, due to the greater number of parameters to be estimated with only limited numbers of observations.

This chapter proposes the development of an N isotope model linked to a hydrological model at the watershed scale in order to match observations of stream concentrations and $\delta^{15}N\text{-}NO_3^-$ signatures, similar to the modified version of DAYCENT of Bai and Houlton (*2009*), but for agriculture dominated watersheds. In our model the key N transformation processes below specified land use coverages are simulated. All the N exports from the different hydrological compartments are then collated into the watershed's total N export via surficial (overland and tile flow) and subsurface (shallow and deep baseflow) pathways.

The contributions from baseflow generated in each hydrologic response unit (HRU) take into account the mean travel times of the shallow and deep baseflow in the HRU. These travel times are obtained from the analytical model developed in Chapter 3 for Carroll Creek watershed. For this watershed, historical N inputs, from both anthropogenic and natural sources, have been determined in previous research (*Zhang, 2016*). Typical ranges of N isotopic compositions ($\delta^{15}N$) of N sources and fractionation factors ($\alpha$) of $^{15}N$ discriminating biogeochemical processes are used. The construction of this model is a work in progress and the preliminary achievements are reported here.

## 4.2 Methodology

The proposed modeling framework builds on an existing hydrological model for the Grand River watershed, which passes computed water flows on to a biogeochemical mass balance model for N transformations in the soil and groundwater compartments of the hydrologic response units (HRUs) (M. Shafii, personal communication). The linked hydrological-N model calculations yield the $NO_3^-$ fluxes associated with interflow, tile flow, and baseflow from all the HRUs in the watershed, and predict the $NO_3^-$ concentration and export flux at the watershed stream.

In the existing RAVEN hydrological model, the baseflow contributions are estimated using an exponential function to relate flow routes to concentrations at the watershed scale (*van der Velde et al., 2010*). This convenient distribution has been widely used since its inception to account for groundwater travel time distributions (*Rinaldo & Marani, 1987*). However, it lacks a physical representation of the watershed. Here, instead, we replace the exponential function with the mean of the probability density functions (PDFs) of the particle median travel times (pMTT) computed for each HRU in the watershed, applying the methodology developed in Chapter 2. The study watershed (Carroll Creek) is used for verification of the analytical model whose parameters are obtained from the regression models based on the geomorphological watershed characteristics (Chapter 2). The analytical model provides estimates of the pMTTs (and their distributions) and the whole-watershed MTT (wMTT) for

Carroll Creek (Ontario, Canada) For the wMTT of Carroll Creek, the analytical model estimates 65 years, while the numerical model yields 63 years.

Next, we add an explicit representation of the stable isotopes $^{14}N$ and $^{15}N$ in the biogeochemical N model. The existing N reaction model, which is externally linked to the hydrological model, is further modified to include intermediate reaction steps for nitrification. Descriptions of the existing hydrological-N model and the proposed N model for the study site are presented below, followed by that of the proposed N isotope model. General characteristics of the study site and measured $NO_3^-$ concentrations and $\delta^{15}N$ compositions are also provided.

### 4.2.1 Hydrological Model

The existing hydrological model for the Grand River watershed was built in RAVEN, a flexible, open source, semi-distributed modelling framework (*RAVEN Development Team, version 2.7*). A detail description can be found in Snowdon (*2009*) and in the user and developer manual version 2.7. The RAVEN approach is based on hydrological response units (HRUs) as the minimum expression of physical discretization. Within each HRU, multi-layer soil and aquifer compartments are user-defined. The aggregation of HRUs creates subbasins, whose aggregation in turn creates the watershed. For this study, the HRUs are defined based on singular combinations of land use and soil type. The RAVEN model includes most hydrological surface and subsurface partitioning processes, including, among others, evapotranspiration, soil and canopy evaporation, snowmelt, infiltration, percolation, baseflow and runoff. For each of these processes, RAVEN provides a wide selection of possible algorithms.

For the partitioning processes, RAVEN offers, in addition to the typical operator splitting (or ordered series) method, three options of the Runge-Kutta numerical solver methods. The latter options differ from the operator splitting method in treating the water and energy storages simultaneously for all the processes involved instead of following a sequential source-depleting order (*Snowdon, 2009*). Two routing methods are available in RAVEN: (1) the

aggregation of the exported flows from all HRUs by applying a convolution of the discretely exported flow rates and the distribution of arrival times to the main channel of the subbasin, given by the unit hydrograph (UH), and (2) the unidirectional transfer (downstream only) of flow among subbasins along an open channel, with the diffusive wave method as the routing algorithm. The first routing method is called 'in-catchment routing' in RAVEN parlance, and can use a Gamma unit hydrograph for the time allocations of the HRU exports within the subbasin.

Carroll Creek is included in the RAVEN model as one subbasin, comprised of a total of four HRUs. In each of the four HRUs, the fluxes among the different water storage units (canopy, surface, double soil layers, and aquifer layers) are calculated. Besides these internal HRU fluxes, the following external fluxes result from the hydrological partitioning: overland flow, tileflow, baseflow, and deep baseflow. Using the in-catchment routing method, these exported fluxes are routed to the main channel of the subbasin (here, Carroll Creek) by applying a Gamma distribution function. These exported fluxes then carry the various solutes of interest to the outlet of the subbasin.

### 4.2.2 Isotope Nitrogen Model

The mass balance model for nitrogen (N) and N isotopes emulates the compartments included in the hydrological model: upper, lower active, and lower passive layers (Figure 4-1). In the lower compartments only nitrate ($NO_3^-$) is explicitly represented. It is assumed to be the primary form of dissolved N exported from the HRU to the receiving stream. Note that this assumption can be relaxed in future model versions, for example by allowing export of dissolved organic N. In the upper compartment, the N pool is divided into organic N in soil and plants, soil $NH_4^+$, and $NO_3^-$. Ammonium is treated as a reactive intermediate whose concentration remains low. Mobile N (i.e., $NO_3^-$) from the upper compartment is leached both downwardly by percolation and through different processes laterally (overland flow, tileflow, and baseflow exports). Nitrogen cycling in the soil and aquifer compartments are sustained by atmospheric N deposition (*AD*) and land use N sources (e.g. organic (*Fo*) and inorganic (*Fi*) fertilizer). The separate compartments for soil and plants

organic N is a configuration that provides benefits that are threefold: the soil becomes the direct recipient of *Fo*, the leguminous plants receives transformed atmospheric $N_2$ into available N through biological fixation (*BNF*), the loss of N through crop harvest can be assessed separately as well as the N recycling associated with litterfall and crop residue (L&CR).

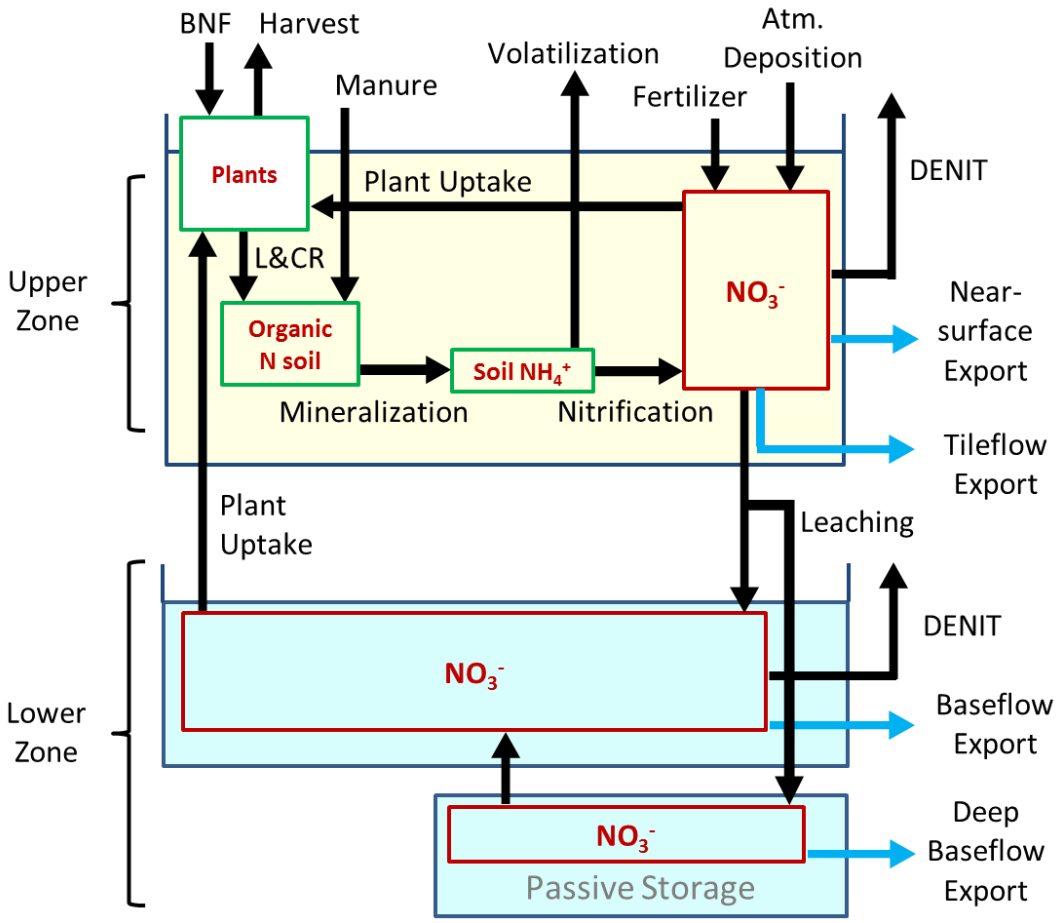


Figure 4-1. Schematic of the nitrogen model. L&CR: litter and crop residue, BNF: biological N fixation.

Although ammonium can also be a source of N for a limited number of plants (*Högberg, 1997*), it is the final product of nitrification (i.e., $NO_3^-$), which the most utilized soil N substrate for plants in near neutral pH soils. In addition to nitrification, ammonium can be

lost by volatilization to the atmosphere as ammonia ($NH_3$) (*Högberg, 1997*; *Kendall, 1998*). Ammonia volatilization depends on weather and soil conditions (*Karr et al., 2003*; *Kendall et al., 2007*; *Robertson & Schiff, 2008*). In agricultural lands, manure is the main source of readily available $NH_3$, which in turn is most efficiently removed during hot summer days (*OMAFRA, 2017*).

Nitrification produces $NO_3^-$, which can leave the HRU laterally, depending on the local topography, or vertically, with the infiltration of rainfall (i.e., leaching). Denitrification removes $NO_3^-$ to the atmosphere as reduced $N_2$-gas. Nitrate leaching out of the soil first encounters the upper, active groundwater layer (i.e., the LA compartment), where denitrification and plant uptake processes act as sinks of $NO_3^-$. A deeper, less-active groundwater compartment (i.e., the LP compartment) acts as a buffer for the active groundwater layer and helps simulate the hydrological lag times of watershed responses to changes in the external forcings. In what follows, detailed descriptions of the N biogeochemical processes in the model that induce isotopic fractionations are given, as well as estimates of the natural and anthropogenic N inputs applied as model forcings.

### 4.2.3 $^{15}$N Discriminating Reactions

Of the N cycling processes mentioned above, not all discriminate significantly against the heavier $^{15}$N isotope. In general, mineralization and plant uptake produce minimum fractionations. This has been observed in undisturbed forest soils with limited nitrification such that the $\delta^{15}$N of the soils is within a few permil (<2‰) from that of the tree roots (*Nadelhoffer & Fry, 1994*). The isotopic fractionations accompanying assimilation of $NO_3^-$ by 38 types of plants (-2.2 to +0.6‰) were found to be influenced by the substrate concentration (*Mariotti et al., 1980*). The isotopic enrichment in a treatment of soybeans at 5 mM $NO_3^-$ concentration was +2‰ (*Bergersen et al., 1988*). Application to soils of a model for isotopic fractionation in aquatic algae predicts a maximum value of -4‰ for N assimilation (*Fogel & Cifuentes, 1993*). On average, however, nitrate assimilation by plants yields small fractionations, around -0.25‰.

Volatilization isotopically affects recently mineralized organic N from soil and stored manure, be it in liquid or solid form. The effect in $\delta^{15}N$ in long-term stored liquid manure is significant varying from +10‰ in winter to +30.8‰ in the summer days (*Karr et al., 2003*). In a local study at Strawberry Creek (Ontario, Canada), a few kilometers away from Carroll Creek, the N isotopic composition at the creek (+15.9‰) was attributed to the application of manure in the watershed (*Mengis et al., 1999*). Karr et al. (*2003*) observed a positive correlation between the changing isotopic composition of liquid manure (slurry from storage lagoons) and air temperature for a period of over a year. Local information for the use of liquid manure in Wellington County (*Goss et al., 2001*) suggests that the rate of manure application corresponds to half of that from solid manure, making the solid manure two-thirds the total volume of applied in the county. In the model, volatilization occurs in non-rainy days, as runoff and infiltrating rainfall dilutes and mobilizes $NH_4^+$ eventually towards a path of nitrification. The emissions of volatilized $NH_3$ occurs during the first days of storage in solid manure, and can be similar to liquid manure's emissions in the first month of storage, after which emissions from liquid manure keep increasing at a steady rate (*Dewes, 1999*). No isotopic data has been collected in solid manure during long-term storage, which in Ontario is stored at least for 180 days.

The degree of fractionation during nitrification is greatly dependent on the amount of anthropogenic N inputs to the soil-vegetation system (*Kendall et al., 2007*). In non-agricultural lands, nitrification tends to yield similar $\delta^{15}N$ values of soil water nitrate (~0 to +3‰) compared to the uncultivated organic N soil (+2 to +5‰), indicative of slight $^{15}N$ depletion of $NO_3^-N$ and slight $^{15}N$ enrichment of soil N (*Garten et al., 2007*). The long-term leaching of depleted $^{15}N$-$NO_3^-$ may lead to the gradual enrichment of $^{15}N$ in uncultivated soil N. In cultivated soils, however, much larger $^{15}N$ discrimination, between -12‰ to -29‰, is observed because the soils are not N-limited. Here, an average fractionation factor was chosen ($\alpha_N$ = 0.979, (Table 4-1). In soils with manure application, volatilization and nitrification of organic-N can occur sequentially yielding a complex imprint in the isotopic composition of $NO_3$-N. First, volatilization enriches $^{15}N$ in the remaining $NH_4^+$-N, which is

then oxidized into a $^{15}N$ depleted $NO_3^-$ via nitrification. Considering that both processes generate similar enrichments, the resulting isotopic nitrate composition can vary from slightly enriched (~+8 ± 2 ‰) to more significantly enriched (+8 to +16‰) with respect to the isotopic composition of the cultivated soil N (*Wassenaar, 1995*).

In denitrification, nitrate is the electron acceptor and organic carbon is the electron donor in the enzymatic (kinetic) transformation of nitrate in solution into N-gas ($N_2$ or $N_2O$). In this reaction, the residual substrate, as in all isotopic processes, is enriched in $^{15}N$-$NO_3^-$, whereas the lighter gaseous species are released to the atmosphere. The occurrence of denitrification in cultivated fields is primarily controlled by the spatial distribution and availability of organic carbon, as well as soil moisture. In natural soils the availability of nitrate is often an additional limiting factor for denitrification. Because of these various controls the isotopic imprint of denitrification on soil water $NO_3^-$ is quite variable, from -5‰ to -33‰ (*Högberg, 1997*). At this stage, the distribution of organic carbon is not represented in the model, and a mean fractionation factor ($\alpha_D$=0.981) for denitrification is used throughout (Table 4-1).

### 4.2.4 Nitrogen Inputs and Model Stocks

Natural and anthropogenic N forcings are included in the model through the N inputs to the soil system: atmospheric deposition, fertilizer, manure, and biological N fixation. A brief description on the development of time series for N loads and their isotopic compositions is presented in this section, followed by the initial estimates of the compartment stocks in the model.

Table 4-1. Nitrogen fractionating processes, their isotopic effect, and the fractionation factor applied in the model.

| N Process | Reaction | Isotopic Effect | $\alpha_{P/S}$ |
|---|---|---|---|
| Mineralization | org-N → $NH_4^+$ | Minimum to null fractionation has been reported, depleting $^{15}N$-$NH_4^+$. | 0.999 |
| Volatilization | $NH_4^+$→ $NH_{3(g)}$ | Dependent on temperature, wind, rainfall, soil pH, and available light. Fractionation > 20‰ are reported resulting in enriched $^{15}N$-$NH_4^+$ and depleted $^{15}N$-$NH_{3(g)}$. | $f(T)$[1] |
| Nitrification | $NH_4^+$→ $NO_3^-$ | Two-step reaction with conversion to $NO_2^-$ being rate limiting of the overall process. Large fractionation reported -12‰<ε<-29‰ | 0.979 |
| Plant Uptake | $NO_3^-$→ org-N | Or assimilation, with limited fractionation within -0.25‰<ε<-4‰. | 0.998 |
| Denitrification | $NO_3^-$ →$N_{2(g)}$ | Highly variable and dependent on soil saturation and temperature. Fractionation may vary between -5‰<ε<-33‰. | 0.981 |

[1] Fractionation is a function of daily temperature (T) following changes in $\delta^{15}N$ observed in liquid manure at a site in North Carolina (*Karr et al., 2003*). To be used, unmodified, where liquid manure is applied. A similar relationship was adjusted for solid manure (see Appendix C).

#### 4.2.4.1 Nitrogen Inputs

The estimation of a fixed daily atmospheric deposition N load is based on the historical analysis made by Zhang (*2016*) of $NO_3^-$ in wet deposition collected during the period 1978-2001 in several stations in the Grand River watershed. These data were collected by Environment Canada and accessible through its NatCHEM database. The historical analysis indicates that the trend of N loading in atmospheric deposition has been declining since the early 1990's, when it reached a maximum of 20 kg/ha/yr. In the last decade (i.e., as of 2011) the estimated atmospheric N load is ~10 kg/ha/yr. These loads fall between typical values for unpolluted (5 kg/ha/yr) and polluted (28 kg/ha/yr) environments (*Van Miegroet et al., 1992*). In precipitation, $NO_3^-$ and $NH_4^+$ are the most common forms of N in atmospheric deposition (*Holland et al., 1999*). For this study, the oxidized form of N is assumed to be the only N species in atmospheric deposition. The mean N isotopic composition in $NO_3^-$ of

precipitation reported by Kendall (*1998*) is -2.5 ± 3‰. (Note: in many instances $NH_4^+$ in precipitation is slightly depleted in $^{15}N$ with respect to $NO_3^-$ precipitation, *Kendall, 1998*, but not in all cases, *Heaton, 1986.*) The mean N isotopic composition of 10 rain samples collected in Turkey Lake's watershed (Ontario), located 600 km northwest of Carroll Creek, is -2.1‰ (*Spoelstra et al., 2001*). This $\delta^{15}N$ value is used as representative of the N isotopic composition of atmospheric deposition (AD) in the model.

The N requirements for crop growth published by the Ontario Ministry of Agriculture, Food and Rural Affairs (OMAFRA) in the document "Agronomy Guide for Field Crops" (*2017*) is used as a guideline for allocating N fertilizer and manure application loads. In Carroll Creek, there are four major land uses associated to agricultural activities: row crops (crop rotation), small grains (buckwheat, flax, and sunflower), forages (hay), and pastures (grass). A common crop rotation in the Grand River watershed (*Liu et al., 2016*) is: soybean, winter wheat, and corn. According to OMAFRA, only corn requires an annual N application that depends on soil texture (Table C1 in Appendix C). An area-weighted estimate of N required for corn (142 kg/ha) is included in the two-year rotation with a nominal N requirement of 20 and 15 kg/ha for soybean and winter wheat, respectively. For small grains, an average value of the recommended N requirements for buckwheat, flax, and sunflower is to be applied in the model (57 kg/ha in Table 4-2).

Symbiotic N fixing soil bacteria use the enzyme nitrogenase to catalyze the reduction of $N_2$ from the atmosphere to $NH_3$ (*Buresh, 1980*). This self-reliant ability regulates N supply to the vegetation. However, the intense cultivation of legumes combined with fossil fuel combustion has altered the ratio of biological $N_2$ fixation and total $N_2$ fixation at the global scale (*Cleveland et al., 1999*; *Vitousek et al., 2013*). Locally, Zhang (*2016*) has estimated the biological N fixation (BF) in the Grand River watershed as a function of crop coverage and rotation. After meeting with a local agricultural specialist, Liu et al. (*2016*) estimate that the most frequently occurring crop rotation in the Grand River watershed is: soybean, winter wheat, and corn. The mean BF value for this two-year rotation is used in the model. Although winter wheat and corn are not considered $N_2$ fixing crops, they have been found

to create associative $N_2$ fixation habitats with bacteria that fix N within the rhizosphere of the host plants (*Hubbell & Kidder, 2009*). In addition to plants, free-living heterotrophs in soils can also fix N drawing available energy from organic carbon leaching from decomposing material (litter). Their contribution to the overall global $N_2$ fixation rates is minor, however (*Hubbell & Kidder, 2009*). In three Ontario forests, the asymbiotic $N_2$ fixation in surface soils was estimated at <1 kg/ha/yr (*Hendrickson, 1990*). In the model presented here, BF of N is only provided by plants.

OMAFRA (*2017*) recommends applying an N fertilizer to manure ratio of two-thirds to supply the total N crop requirement (Table 4-2). The liquid form of manure provides almost twice as much readily available $NH_4^+$ than solid manure (42% versus 21%), however, the organic-N in solid manure has a more long-term benefit to the cultivated soil, even into the next year harvest.

Table 4-2. Annual nitrogen crop requirements and rates of N fertilizer and manure to be applied in the model.

| Land Use Category | Area [ha] | N Crop Requirement [kg/ha] | N Rate of Fertilizer [kg/ha] | N Rate of Manure [kg/ha] |
|---|---|---|---|---|
| Row crops | 1952 | 49 | 16 | 33 |
| Small grains | 766 | 57 | 19 | 38 |
| Forages | 2222 | 60 | 20 | 40 |
| Pasture | 646 | 44 | 15 | 29 |
| **Area Weighted [kg/ha/a]** | | **54** | **18** | **36** |

Litterfall and crop residue are important components in the N cycle and are highly dependent on the type of trees present in the watershed and the harvesting practices in the area. Coniferous and deciduous forests, that both make 4.1 and 4.5 % of the total area in Carroll Creek, respectively, differ in the amount of litter produced. The vegetation of coniferous forests tends to be more permanent year around, a characteristic that is utilized to control streamflow in watersheds, whereas, deciduous trees such as oak, maple, beech

lose their leaves each year. An estimation of this N flux for each vegetation type is presented in Appendix C (Table C2 and Table C3) based on published data.

#### 4.2.4.2 Compartment Model Stocks and Initial $\delta^{15}N$

The stocks of soil organic and mineral N are presented here for the upper (U), lower active (LA), and lower passive (LP) compartments. In the lower compartments, only N as nitrate is modeled. The stock of N in soil refers to N contained in the soil organic matter. Soil organic N constitutes the second largest N reservoir after atmospheric $N_2$ (*Schlesinger, 1997*). The source of this organic-N is the decomposition of litter from vegetation through millennia of balancing organic and mineral N inputs and mineral-N outputs (*Marty et al., 2017*). Thus, natural, uncultivated lands tend to be relatively rich in organic-N. The mean of the total soil N pool in 21 forests in Québec was 915 g N/m$^2$, while the N concentrations of mineral soil horizons (1.3 g N/kg) are just a fraction of those of the usually thinner organic soil horizon (16.7 g N/kg) (*Marty et al., 2017*). In southern Ontario, Ellert & Gregorich (*1996*) sampled surface and deeper soils of both cultivated lands and adjacent forests to identify pools of carbon, N, and phosphorus. They found that the mean N surface concentrations of cultivated and forest soils were 586 and 724 g N/m$^2$, respectively, with an average difference of 19%; whereas, the mean N subsurface values were 129 and 111 g N/m$^2$ with an average difference of -16%.

It is recognized that the inorganic N in soils only corresponds to around 1% of the total soil N (*Kendall et al., 2007*). This 1% consists mostly of $NO_3^-$ and some $NH_4^+$. With an average $NO_3^-/NH_4^+$ ratio in dissolved inorganic N (DIN) in the upper compartment of 5, 1% of total soil N gives, on average, 3.54 and 4.24 g $NO_3^-$-N/m$^2$ and 0.88 and 1.06 g $NH_4^+$-N/m$^2$, for cultivated and uncultivated soils, respectively. The N stocks for the lower compartments follow similar values as the estimated above for the upper $NO_3^-$ compartment.

The isotopic composition of liquid and solid manure changes throughout the year due to the effect of $NH_3$ volatilization. In the proportional relationship of temperature and $\delta^{15}N$ quantified by Karr et al. (*2003*), $\delta^{15}N$ changes during the rising temperatures of spring and

summer at a faster rate than the declining limb of this relationship during the late summer, fall, and winter temperatures (Figure C1, Appendix C). Details on the rising and declining linear equations describing this behavior in liquid manure are presented in Appendix C. A similar analysis is not available in the literature for solid manure. Thus, it is assumed that solid manure's $\delta^{15}N$ varies following the range of values reported by Bateman & Kelly (*2007*): 3.4 to 20.4‰ $\delta^{15}N$, occurring at the same time of the year as the liquid manure. The isotopic composition of the mixture is weighted by the 2:1 ratio of solid to liquid manure that is reportedly applied in Wellington County (*Goss et al., 2001*).

Table 4-3. Summary of annual N inputs, and their nitrogen isotopic compositions ($\delta^{15}N$). Initial δ15N is also provided for compartments for those HRUs dominated by either fertilizer or manure application.

| **N Inputs** | **Estimate [kg N/ha]** | **$\delta^{15}N$ (‰)** | | | |
|---|---|---|---|---|---|
| Atmospheric Deposition (AD) | 10 | -2.1[1] | | | |
| Biological N Fixation (BNF) (soybeans/hay) | 252/222 | 0[2] | | | |
| Litter & Crop Residue (forests/row crops) | (26-53)/19 | +8[3] | | | |
| | | **Source** | **Upper** | **LA** | **LP** |
| Fertilizer (Fi) | 18 | +1 | +4.7[4] | +12[6] | +18[6] |
| Manure (Fo) | 36 | $f_S$(T), $f_L$ (T)[5] | +16[5] | +20[5,6] | +8[5,6] |

[1] Measured by Spoelstra et al. (*2001*); [2] From atmospheric $N_2$ -BF Kendall (*1998*); [3] Nadelhoffer & Fry (*1994*); [4] Soil NO3- from fertilizer and manure as in Kendall & Aravena (*2000*); [5] $\delta^{15}N$ function based on Karr et al.(*2003*); [6] Robertson & Schiff (*2008*).

## 4.3 Coupling of Hydrological and Nitrogen Models

The nitrogen model (Figure 4-1) mimics the compartment scheme used in the hydrological model. It simulates the internal transformation and exchange fluxes within each HRU, as well as the export fluxes leaving the HRU. These internal and external fluxes are incorporated into the nitrogen balance equations that define the change in time of each N form. For the light isotope, we have:

$$\frac{dNorg}{dt} = Fo + Cr - k_M Norg$$

$$\frac{dNveg}{dt} = BF + k_U NO_{3U} + k_{UL} NO_{3LA} - Cr - Hv$$

$$\frac{dNH_4}{dt} = k_M Norg - k_N NH_4 - k_V NH_4$$

$$\frac{dNO_{3U}}{dt} = AD + Fi + k_N NH_4 - k_U NO_{3U} - k_1 k_2 k_D NO_{3U} - k_T NO_{3U} - k_{Lch} NO_{3U}$$

$$\frac{dNO_{3LA}}{dt} = k_{Lch} NO_{3U} * a - k_1 k_2 k_D NO_{3LA} - k_{UL} NO_{3LA} - k_B NO_{3LA} + (1-a) k_{Ex} NO_{3LP}$$

$$\frac{dNO_{3LP}}{dt} = (1-a) k_{Lch} NO_{3U} - (1-a) k_{Ex} NO_{3LP}$$

And, for the heavy isotope:

$$\frac{d^{15}Norg}{dt} = R_{Fo} Fo + R_{Cr} Cr - k_M \alpha_M {}^{15}Norg$$

$$\frac{d^{15}Nveg}{dt} = R_{BF} BNF + k_U \alpha_U R_{oNu} NO_{3U} + k_{UL} \alpha_U R_{oNLA} NO_{3LA} - R_{Cr} Cr - R_{Hv} Hv$$

$$\frac{d^{15}NH_4}{dt} = k_M \alpha_M R_{Or} Norg - k_N \alpha_N {}^{15}NH_4 - k_V \alpha_V {}^{15}NH_4$$

$$\frac{d^{15}NO_{3U}}{dt} = R_{AD} AD + R_{Fi} Fi + k_N \alpha_N R_{Am} NH_4 - k_U \alpha_U {}^{15}NO_{3U} - k_1 k_2 k_D \alpha_D {}^{15}NO_{3U} - k_T {}^{15}NO_{3U} - k_{Lch} {}^{15}NO_{3U}$$

$$\frac{d^{15}NO_{3LA}}{dt} = a * k_{Lch} {}^{15}NO_{3U} - k_1 k_2 k_D \alpha_D {}^{15}NO_{3LA} - k_{UL} \alpha_U {}^{15}NO_{3LA} - k_B {}^{15}NO_{3LA} + (1-a) k_{Ex} {}^{15}NO_{3LP}$$

$$\frac{d^{15}NO_{3LP}}{dt} = (1-a) k_{Lch} {}^{15}NO_{3U} - (1-a) k_{Ex} {}^{15}NO_{3LP}$$

The formulations used for the heavier N isotope are similar to those applied in previous studies by Brenner et al. (*2001*) and Lehmann et al. (*2003*), where i) the N inputs are multiplied by their isotopic compositional ratio ($R$), and ii) the rates of the N processes that discriminate against $^{15}N$ are multiplied by the corresponding fractionation factor ($\alpha_{P/S}$). The fractionation factor, as previously indicated (Table 4-1), is expressed with the $^{15}N$-enriched form in the denominator yielding $\alpha_{P/S} < 1$. The hydrologic fluxes are represented in the form of fractions of a specific flow withdrawing from a reservoir source (Table 4-4). First-order reaction constants control the consumption of the substrates (Table 4-4).

The existing hydrological model extends over Carroll Creek with four HRUs for two agricultural land use types. For this spatial configuration, N transformation processes in the upcoming work will be sequentially activated in the simulation until reaching quasi steady-state conditions. The spin-up period of simulation required to reach quasi steady-state is likely to be longer than the duration covered by time series data used for the N inputs. Several configurations of N transformation processes combined with spatial resolution increments (i.e., in number of HRUs and agricultural land uses) are planned to match observations with the minimal set of reactions and spatial discretization.

## 4.4 Study Watershed

The Carroll Creek watershed (78 km$^2$) is located in the Grand River basin (6,800 km$^2$). This region receives on average 916 mm of annual precipitation, and the mean annual temperature is 7$^o$C. The upper and lower portions of the watershed are dominated by clay loam till soils and loam till soils, respectively (Figure 4-2a). In the lower portion of the watershed, pockets of organic, gravelly, and sandy soils are also present. Five agricultural-related land uses can be recognized, including pasture (8.3%), which together amount to 86.5% of the total watershed area (Figure 4-2b). Row crops and forage occupy more than half of area, with 25 and 29% coverage, respectively. All land use categories are uniformly distributed across the watershed, except for forests that are mostly adjacent to streams. Carroll Creek is an order five stream, in the Strahler-stream ordering scheme.

Table 4-4. Flow partitioning and N first-order reaction parameters in N balance model.

| Parameter | Units | Definition | Value - Range |
|---|---|---|---|
| $k_U$ | [-] | Plant uptake fraction [*U*[1]/*VZ*] | tbdbhm[2] |
| $k_{UL}$ | [-] | Plant uptake fraction from lower compartment [*UL*/*SAT*] | tbdbhm |
| $k_T$ | [-] | Tileflow fraction [*T*/*VZ*] | tbdbhm |
| $a$ | [-] | Partial mixing coefficient | tbdbhm |
| $Lch$ | [-] | Leaching fraction from U to L compartment [*Lch*/*VZ*] | tbdbhm |
| $B$ | [-] | Baseflow fraction [*B*/*SAT*] | tbdbhm |
| $Ex$ | [-] | Exchange ratio, similar to *a* | tbdbhm |
| $k_M$ | [day$^{-1}$] | Mineralization rate constant | 0.006 to 0.04[3,4] |
| $k_N$ | [day$^{-1}$] | Nitrification rate constant | 0.05 to 0.30[5] |
| $k_V$ | [day$^{-1}$] | Volatilization rate constant | 5.1e-3[6] |
| $k_D$ | [day$^{-1}$] | Denitrification rate constant | 0.002-0.06[5,7]<br>1.3e-3 to 0.09[8,9] |

[1] hydrological fluxes and compartments: U, UL, evapotranspiration from top and lower compartments; T, tileflow; Lch, percolation from upper to lower compartment; B, baseflow; VZ, vadose zone compartment; SAT, saturated-lower compartment.
[2] tbdbhm: to be determined by hydrological model.
[3] Stanford & Smith (***1972*****).**
[4] Zhang et al. (*2017*).
[5] literature review therein, Ramos & Carbonell (*1991*) [for top soils]
[6] Asada et al. (*2013*)
[7] surficial soils in Mariotti et al. (*1982*) [for top soils]
[8] sandy material with impermeable clay, Frind et al. (*1990*) [for lower soils/surficial geology]
[9] sand, silt, and clay, McMahon et al. (*2008*) and Tesoriero & Puckett (*2011*) [for lower soils/surficial geology]

Cummings (*2015*) included Carroll Creek as one of four watersheds in his study of the seasonality of stream $NO_3^-$ concentrations and isotopic compositions of N and oxygen in $NO_3^-$. A common trend of low $NO_3^-$ concentrations and high $\delta^{15}N\text{-}NO_3^-$ and $\delta^{18}O\text{-}NO_3^-$ during the growing season was identified in all watersheds (Figure 4-3), both indicative of the occurrence of denitrification (*Cummings, 2015*). The values for the N isotopic composition of $NO_3^-$ ($\delta^{15}N\text{-}NO_3^-$) are indicative of significant N fractionation processes

occurring in the watershed. The agricultural nature of the watershed is also evident in the $\delta^{15}N\text{-}NO_3^-$ values, which are farther away from values typically observed in uncultivated watersheds ($+1‰ < \delta^{15}N\text{-}NO_3^- < +7‰$, *Bai & Houlton, 2009*).

Carroll Creek is one of the verification watersheds used to test the regression models for estimating both the analytical model parameters of the methodology developed in Chapter 2 and the watershed mean travel time (wMTT). These regression models use easily measured geomorphological features as predictors. The analytical model created from the predicted parameters yield, in turn, estimates of particle median travel times (pMTT), which, together with their distribution and wMTT, are compared against the numerical model predictions (i.e., FEFLOW's) (Figure 4-4). The goodness of fit ($r^2$=0.15) for pMTT is comparable to the initial watersheds used to develop the regression models (Figure 4-4a). The wMTT predicted by the analytical model differs from the numerical counterpart by only 2 years (3 %). The distribution of ages simulated by the analytical model covers most of the occurrences and frequencies of travel times (Figure 4-4b), except for the longest ones where a relatively few occurrences of particles with travel times longer than 250 years were not reproduced by the analytical model. Also, the frequencies for short travel times (<50 years) is slightly misrepresented in the analytical model.

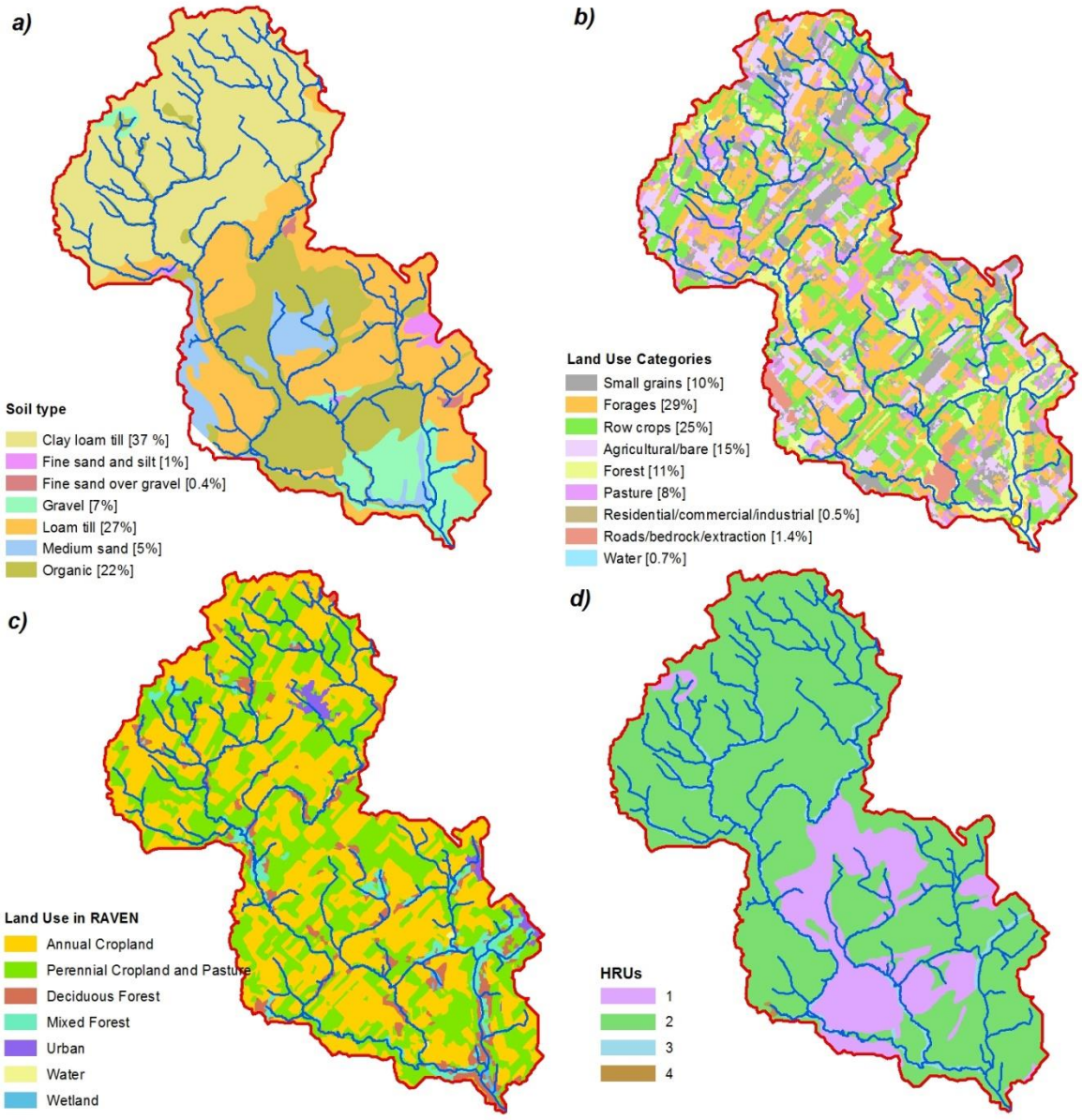


Figure 4-2. Soil type (a) and land use (b) distribution in the Carroll Creek subbasin, and consolidated land use categories (c) and HRUs (d) currently in the existing RAVEN model.

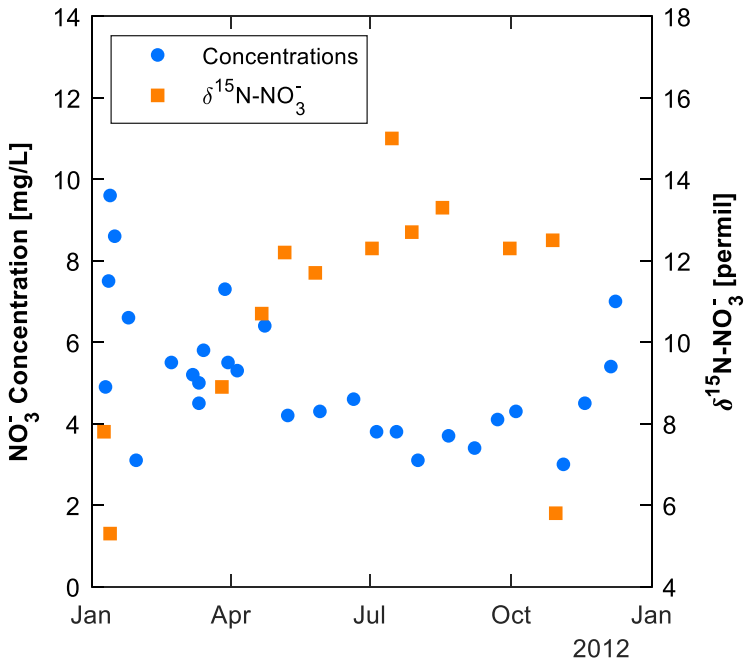


Figure 4-3. Nitrate concentrations and N isotopic composition in $NO_3^-$ ($\delta^{15}N$- $NO_3^-$) measured in the Carroll Creek stream waters by Cummings (*2015*).

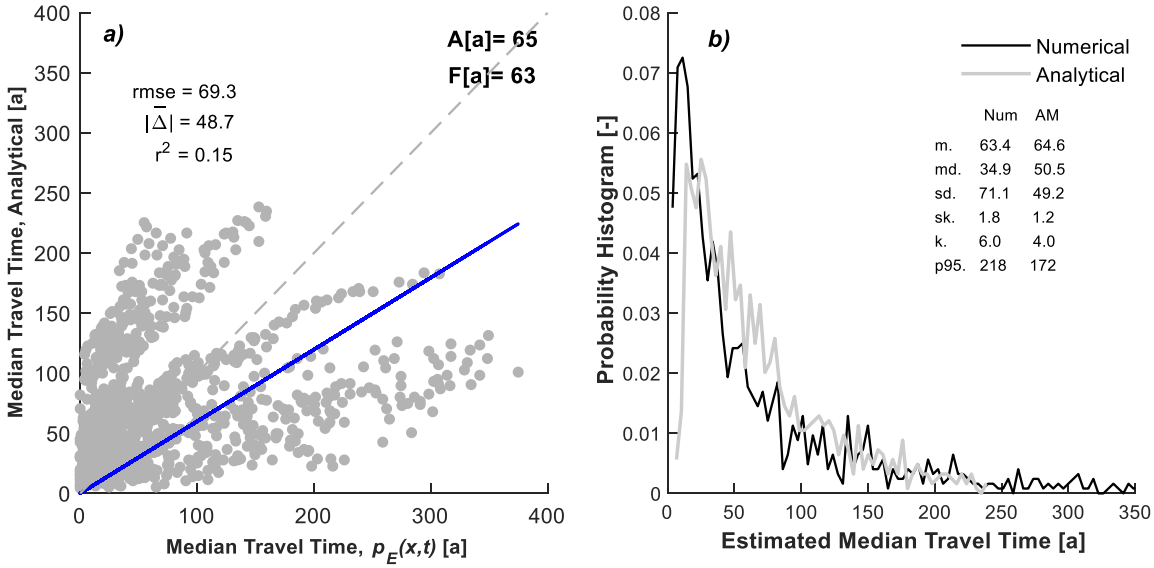


Figure 4-4. Particle median travel times (pMTT) and watershed mean travel time (wMTT) (a) and pMTT distribution (b) estimated with the analytical model are compared against the respective numerical model estimates. On panel (a) A stands for analytical and F for numerical.

## 4.5 Prospective Directions

A method for optimization of the parameters in the N isotope model being considered is that used in the FLUAZ model (*Mary et al., 1998*) (i.e., Levenberg-Marquardt's algorithm), or other similar ones, such as those available in the OSTRICH optimization software (*Matott, 2017*). Once the model is ready to run simulations, different configurations of N transformation processes and spatial watershed discretization are planned (Table 4-5). These configurations will evaluate the influence of single and sequential N transformation processes under varying spatial discretizations. The targeted N transformation processes are those that discriminate against $^{15}N$ as the reproduction of both N-$NO_3$ concentrations and $\delta^{15}$N-$NO_3^-$ signatures are sought. The observed N isotopic composition in Carroll Creek (Figure 4-3) is likely the result of the combination of the N isotopic composition of the sources, which are applied in all the configurations in Table 4-5, and one or more $^{15}N$ discriminating process.

Besides the configurations listed in Table 4-5, the contribution from either surface or subsurface fluxes in explaining the measured observations will be evaluated for each simulation. This discretization in the contribution can also be performed on natural versus anthropogenic N sources. Statistics to compare the generated time series against the observations will be applied to each simulation to measure performance.

Table 4-5. List of planned simulations for configurations of varying N transformation processes and spatial discretization.

| Configuration | N Transformations Included | Spatial Discretization | |
|---|---|---|---|
| | | Number of HRUs | Number of Agricultural Land Uses |
| Sim1 | NIT[1] | 2 | 1 |
| Sim2 | NIT | 4 | 2 |
| Sim3 | NIT + DENIT | 2 | 1 |
| Sim4 | NIT + DENIT | 4 | 2 |
| Sim5 | VOL + NIT | 2 | 1 |
| Sim6 | VOL + NIT | 4 | 2 |
| Sim7 | NIT + PU | 2 | 1 |
| Sim8 | NIT + PU | 4 | 2 |
| Sim9 | VOL + NIT + DENIT | 2 | 1 |
| Sim10 | VOL + NIT + DENIT | 4 | 2 |
| Sim11 | VOL + NIT + DENIT + PU | 2 | 1 |
| Sim12 | VOL + NIT + DENIT + PU | 4 | 2 |
| Sim13 | VOL + NIT + DENIT + PU + MIN | 2 | 1 |
| Sim14 | VOL + NIT + DENIT + PU + MIN | 4 | 2 |

[1] NIT: nitrification; DENIT: denitrification; VOL: volatilization; PU: plant uptake; MIN: mineralization.

# Chapter 5
# General Conclusions

Travel time distributions (TTDs) provide key information about the hydrological functioning of watersheds that is essential for understanding and ultimately predicting the response of water quality to anthropogenic pressures, including changes in land use and regional climate change. Several approaches exist to determine TTDs of watersheds. These include tracer-assisted models and water balance calculations linked to tracer information, which have mostly been applied to watersheds in mountainous areas. In addition, analytical and numerical modeling approaches are also available for lowland watersheds with deeper aquifers. In this thesis, I present a simple, transferable methodology to estimate the groundwater TTD for the entire watershed, as well as TTDs for water particles entering the groundwater table at multiple, spatially distributed locations across the watershed. The proposed approach offers the advantage of separating subsurface flow and transport of locally leaching solutes from diffusive pollution sources spread across a watershed.

The proposed methodology is based on applying a 1-D analytical model to generate a travel time probability distribution function (PDF) that describes the groundwater TTD of a 3-D watershed. The approach is developed using virtual watersheds for which the predictions of the analytical model are compared to the output of a 3-D numerical hydrological model (FEFLOW), under variable surface topography and subsurface heterogeneity. For the 28 individual scenarios evaluated in a virtual watershed, whose geomorphology and hydrogeology are inspired by that of Alder Creek, the TTDs, median particle travel times (pMTTs), and mean (whole-)watershed travel times (wMTTs) estimated with the analytical and numerical models are in good agreement, especially for mid- to long- distance flow paths. Furthermore, the analytical method responds correctly to imposed changes in subsurface heterogeneity. In the numerical model, an increase in the degree of aquifer heterogeneity ($\sigma_Y^2$) results in a reduction of wMTT, a response matched by

the analytical method. This response, explained by the creation of preferential flow paths, is also matched when increasing the magnitude of heterogeneity ($I_{xy}$).

The analytical travel time estimations verify the already well-known watershed responses to variation in topography, in particular, the expected negative relationship between mean watershed slope and wMTT. However, while the numerical model predicts an increase in wMTT for a reduced topography scenario but with a deeper aquifer, the analytical model fails to reproduce this feature. In light of these results, I set out to explore the influence of watershed geomorphology on groundwater travel times in more detail using a series of nine virtual watersheds.

In Chapter 3 a set of empirical relationships are developed that allow the application of the analytical method in ungauged basins. The inter-watershed comparison approach includes eight virtual watersheds, in addition to the Alder Creek virtual analog, all subject to similar hydrologic forcing (that is, precipitation) and assuming fully homogeneous subsurface conditions. The analytical method performs well when estimating the watersheds' TTDs and wMTTs, but less so in the case of pMTT. The results of the analyses imply that the analytical methodology could be used to guide watershed management and nonpoint source pollution risk assessment, provided the limitations of the approach are properly understood and taken into account.

To develop the relationships between geomorphological watershed attributes, the analytical model parameters, and wMTT estimates, a total of 28 geomorphological indexes are considered. The resulting predictive relationships are geared toward enabling the transferability of the analytical methodology to ungauged basins. The transferability is tested in three additional local verification watersheds. In these verification watersheds, the degree of agreement for the targeted watershed properties (i.e., TTD, wMTT and pMTT) is maintained relative to the original nine watersheds. The analytical method input parameters and wMTT are primarily related to elevation (i.e., *Relief*), texture topography (i.e., *Dd*, *TexPer*, *DF*), and Horton's law (i.e., $R_B$ and *LnkSlp*) parameters. The wMTT estimated for Schneider Creek, one of the verification watersheds, is significantly underestimated,

however. Tentatively, it would appear that the structural configuration of the watershed's stream network (as manifested by the variables *DF*, $R_B$ and *LnkSlp*) causes the analytical model to fail in accurately estimating wMTT.

The final chapter (Chapter 4) provides a preliminary outline for the development of an N isotope model linked to a hydrological watershed model. The aim is to replace the commonly used exponential lumped-parameter equation for representing groundwater TTD in hydrological models by the analytical modeling framework outlined in this thesis. To illustrate the proposed approach, a watershed with predominant agricultural land use is selected, Carroll Creek, a small tributary of the Grand River in Southern Ontario. I present the proposed approach for the N isotope reaction model that includes the most relevant N transformation processes that discriminate against $^{15}N$. A stepwise strategy to represent the relevant N processes and implement the spatial discretization of the watershed is discussed, as well as a preliminary assessment of the available data on stream $NO_3^-$ concentrations and $\delta^{15}N\text{-}NO_3^-$ compositions.

## 5.1 Future Work

Subsurface heterogeneity remains to be more precisely incorporated in the predictive relationships for the analytical model parameters and wMTT estimations. Hale and McDonnell (*2016*) and Hale et al. (*2016*) recently showed that subsurface bedrock permeability is an important predictor of baseflow MTT in montane watersheds. For the two montane watersheds with distinct bedrock permeability used in their research they show evidence for distinctly longer stream water MTTs (~6 years) in the permeable bedrock watershed. In Chapter 2, the analytical model responded consistently to changes in heterogeneity by increasing the calibrated *Uo* and reducing wMTT. Thus, some measures of subsurface heterogeneity are required as potential predictors of wMTT. The following approaches could prove useful in this respect: 1) using imposed, geostatistically defined heterogeneity metrics similar to that used in Chapter 2, and 2) implementing the 3-D sedimentary hydrofacies from numerical model domains developed by other authors. A

brief commentary on incorporating each approach on the original watersheds (excluding the RPT watersheds) is provided below.

1) Imposed heterogeneity. In Chapter 2, imposed heterogeneity was applied to 28 scenarios on a single watershed (i.e., the virtual Alder Creek watershed). An improvement to the imposed heterogeneity in Chapter 2 would be to consider larger planar correlation lengths, say $I_{xy}$ = 1 or 2 km, to evaluate structural heterogeneity similar to multi-layered aquifer systems. Overall, many opportunities exist to further assess how calibrated *Uo* values depend on heterogeneity, but also how heterogeneity influences the predicted MTT in variable geomorphological settings (i.e., watersheds).

2) Heterogeneity from numerical models. This information was actually collected at the beginning of this study for some of the original watersheds. The subsurface heterogeneity for these watersheds is incorporated in numerical models other than FEFLOW. A significant amount of work is required to make this 3-D data usable in FEFLOW, hence, explaining why aquifer homogeneity was assumed when testing the 28 geomorphological indexes in Chapter 3. Note that such 3-D data is not yet available for Ganaraska River, for which Earthfx (*2006*), a Toronto consultant, has developed a model for the Oak Ridges Moraine that includes this watershed. More realistic representations of the actual permeability fields for subsurface flow at each watershed will help to evaluate the effects of heterogeneity in wMTT. The estimates of wMTT and TTD for each watershed can also be compared with an equivalent heterogeneity scenario evaluated in the former approach.

After the implementation of the analytical methodology to a number of watersheds, a couple of potential changes to the methodology have emerged in order to strengthen its weaknesses. First, identifying distinct geomorphological areas within the watershed to apply different model parameters: *SF*, *Uo*, and $\lambda_L$, instead a single set of parameters for the entire watershed. The greater the number of distinct areas, the more intricated the development of the model will become, which defies the original conceptual framework in

two ways: ease in its implementation and being untethered by scale. Second, replacing the flow path delineation currently obtained from ArcNLET, with a new one where the flow paths in the vicinity of streams are better represented. An automated tool developed in Python working in interface with GIS could create similar flow path delineations without inputing any groundwater parameters, relying fully on a varying topographic surface. This topographic surface can be varied to create local and regional flow paths by resampling the DEM to small cell-sizes, for local discharges, and to large cell-sizes, for regional flow paths.

The current outline for the development of the N isotope model follows the spatial discretization of the existing hydrological model, that is, four HRUs. Additional HRUs may be required to match observed measurements in Carroll Creek, which will demand further spatial discretization and hydrological modeling. This can be achieved by considering two additional agricultural land uses present in the area that are, at the moment, consolidated in the two current agricultural land use categories of the model. Increased level of discretization will be achieved with this addition, considering that the HRUs will be integrated by spatial overlays of land use and soil type.

One of the main sought outcomes from the preliminary work on the N isotope model for Carroll Creek is that the relative contributions of surface and subsurface N exports will be crucial to explaining stream-based nitrate concentrations and isotopic compositions. In the case that the base flow contributions play an important role in describing the stream water observations, the temporal refinement of these N export pathways will be required. The current outline for the N isotope model further works under the assumption that the N input sources, both natural and anthropogenic, have remained constant for a period of time similar to that of the base flow wMTT, estimated at around 63 years. This wMTT will actually be shorter if the heterogeneity in aquifer permeability is significant. To address this temporal issue, the following historical data will be necessary for the last 50 years in Carroll Creek: land use coverages, N fertilizer applications, and annual crop productions. If both spatial and temporal (historical) discretizations are needed to refine N exports from the

baseflow compartments, the proposed model modifications will provide the means to allocate the N fluxes according to the improved watershed TTDs.

# References


Aisopou, A., Binning, P. J., Albrechtsen, H. J., & Bjerg, P. L. (2015). Modeling the factors impacting pesticide concentrations in groundwater wells. *Groundwater*, *53*(5), 722–736. http://doi.org/10.1111/gwat.12264

Alexander, R. B., & Smith, R. A. (2006). Trends in the nutrient enrichment of U.S. rivers during the late 20th century and their relation to changes in probable stream trophic conditions. *Limnology and Oceanography*, 51(1_part_2), 639–654.

Almasri, M. N., & Kaluarachchi, J. J. (2007). Modeling nitrate contamination of groundwater in agricultural watersheds. *Journal of Hydrology*, *343*(3–4), 211–229.

Ali, G., Tetzlaff, D., Soulsby, C., McDonnell, J.J., and Capell, R., (2012). A comparison of similarity indices for catchment classification using a cross-regional dataset. Advances in *Water Resources*, 40, 11-22.

Allander, K.K., Niswonger, R.G., and Jeton, A.E., (2014). Simulation of the Lower Walker River Basin hydrologic system, west-central Nevada, Using PRMS and MODFLOW models: *U.S. Geological Survey Scientific Investigations Report 2014-5190*, 93 p.

Amundson, R., & Baisden, W. T. (2000). Stable isotope tracers and mathematical models in soil organic matter studies. In "*Methods in Ecosystem Science*", E. Sala, R. Jackson, H. Mooney, R. Howarth (eds.). Springer-Verlar, New York, Inc., 117–137.

Amundson, R., Austin, A. T., Schuur, E. A. G., Yoo, K., Matzek, V., Kendall, C., Baisden, W. T. (2003). Global patterns of the isotopic composition of soil and plant nitrogen. *Global Biogeochemical Cycles*, 17(1). http://doi.org/10.1029/2002GB001903

Aravena, R., Evans, M. L., & Cherry, J. A. (1993). Stable isotope of oxygen and nitrogen in source identification of nitrate from septic systems. *Ground Water*, 31(2), 180–186.

Asada, K., Eguchi, S., Urakawa, R., Itahashi, S., Matsumaru, T., Nagasawa, T., Katou, H. (2013). Modifying the LEACHM model for process-based prediction of nitrate leaching from cropped Andosols. *Plant and Soil*, 373(1–2), 609–625.

Asano, Y., T. Uchida, and N. Ohte (2002). Residence times and flow paths of water in steep unchannelled catchments, Tanakami, Japan, *Journal of Hydrology*, 261, 173– 192.

Ashby, S. F., and R. D. Falgout, (1996). A parallel multigrid preconditioned conjugate grandient algorithm for groundwater flow simulations. *Nuclear Science Engineering*, 124, 145–159.

Ballantine, D. J. and Davies-Colley, R.J., (2014).Water quality trends in New Zealand rivers: 1989–2009, *Environmental Monitoring and Assessment*, 186(3): 1939-1950.

Bai, E., & Houlton, B. Z. (2009). Coupled isotopic and process-based modeling of gaseous nitrogen losses from tropical rain forests. *Global Biogeochemical Cycles*, 23(2), 1–10.

Beauvais, A. A., & Montgomery, D. R. (1997). Are channel networks statistically self-similar? *Geology*, *25*(12), 1063–1066.

Belsley, D.A., Kuh, E., and Welsch, R.E., (1980). *Regression diagnostics: identifying influential data and sources of collinearity*. Wiley Publishing, 292p.

Bergersen F.J., Peoples M.B., Turner G.L. (1988). Isotopic discriminations during the accumulation of nitrogen by soybeans. *Aust. J. Plant Physiol*. 15:407-20.

Beven, K. J., and M. J. Kirkby (1979). A physically based, variable contributing area model of basin hydrology, *Hydrological Science Bulletin*, 24(1), 43– 69.

Beven, K. (1982). On subsurface stormflow: An analysis of response times. *Hydrol. Sci. J.*, 27, 505–521

Beven, K.J., (2000). On uniqueness of place and process representations in hydrological modelling. *Hydrology and Earth Systems Science* 4: 203–212.

Beven K.J., (2001). How far can we go in distributed hydrological modelling? *Hydrology and Earth System Sciences* 5(1): 1–12

Beven, K. J., (2010). Preferential flows and travel time distributions: defining adequate hypothesis tests for hydrological process models. *Hydrological Processes*, 24, 1537-1540.

Bijay-Singh, Yadvinder-Singh, and G.S. Sekhon, (1995). Fertilizer-N use efficiency and nitrate pollution of groundwater in developing countries. *Journal of Contaminant Hydrology*, 20, 167-184.

Birkel, C., & Soulsby, C. (2015). Advancing tracer-aided rainfall-runoff modelling: A review of progress, problems and unrealised potential. *Hydrological Processes*, *29*(25), 5227–5240. http://doi.org/10.1002/hyp.10594

Bischoff, K. B. (1964), Axial dispersion with time variable flow, *Chemical Engineering Science*, (19), 989–990.

Boegh, E., Thorsen, M., Butts, M. B., Hansen, S., Christiansen, J. S., Abrahamsen, P., … Thomsen, A. (2004). Incorporating remote sensing data in physically based distributed agro-hydrological modelling. *Journal of Hydrology*, *287*(1–4), 279–299.

Böhlke, J.K., and Denver, J.M. (1995). Combined use of groundwater dating, chemical, and isotopic analyses to resolve the history and fate of nitrate contamination in two agricultural watersheds, Atlantic coastal plain, Maryland. *Water Resources Research*, 31(9), 2319-2339.

Böhlke, J.K., M.E. O'Connell, and K.L. Prestegaard, (2007). Ground water stratification and delivery of nitrate to an incised stream under varying flow conditions. *Journal of Environmental Quality*, 36, May-June.

Botter, G., E. Bertuzzo, and Andrea Rinaldo (2011), Catchment residence and travel time distributions: The master equation. *Geophysical Research Letters*, 38, L11403, doi: 10.1029/2011GL047666.

Bowden, K. L. and Wallis, J. R., (1964). Effect of stream ordering techniques on Horton's laws of drainage composition. *Bulletin of the Geological Society of America* 75, 767-74.

Bouwman, A. F., Van Drecht, G., Knoop, J. M., Beusen, A. H. W., & Meinardi, C. R. (2005). Exploring changes in river nitrogen export to the world's oceans. *Global Biogeochemical Cycles*, 19(1), 1–14. http://doi.org/10.1029/2004GB002314.

Boyer, E. W., Goodale, C. L., Jaworski, N. A., & Howarth, R. W. (2002). Anthropogenic Nitrogen Sources and Relationships to Riverine Nitrogen Export in the Northeastern U.S.A. *Biogeochemistry*, 57/58, 137–169.

Bottcher, J., Strebel, O., Voerkelius, S., & Schmidt, H. L. (1990). Using fractionation of nitrate-nitrogen and nitrate-oxygen for evaluation of microbial denitrification in a sandy aquifer. *Journal of Hydrology*, 114, 413–424.

Brandes, J. A., & Devol, A. H. (1997). Isotopic fractionation of oxygen and nitrogen in coastal marine sediments. *Geochimica et Cosmochimica Acta*, 61(9), 1793–1801.

Brenner, D. L., Amundson, R., Baisden, W. T., Kendall, C., & Harden, J. (2001). Soil N and 15N variation with time in a Californian annual grassland ecosystem. *Geochimica et Cosmochimica Acta*, 65(22), 4171–4186.

Bras, R.L., 1990. *Hydrology: an introduction to hydrologic science*. Massachusetts Institute of Technology, Addison-Wesley Publishing Company, Inc. ISBN 0-201-05922-3.

Broxton, P. D., Troch, P. a., & Lyon, S. W. (2009). On the role of aspect to quantify water transit times in small mountainous catchments. *Water Resources Research*, *45*(8). http://doi.org/10.1029/2008WR007438

Brown, R.H. (1964). Hydrologic factors pertinent to groundwater contamination. *Ground Water*, 2:5-12.

Buresh, R. J., Casselman, M. E., & Patrick, W. H. (1980). Nitrogen Fixation in Flooded Soil Systems , a Review. *Advances in Agronomy*, 33, 149–192. http://doi.org/10.1016/s0065-2113(08)60166-2.

Burns, D. A., Boyer, E. W., Elliott, E. M., & Kendall, C. (2009). Sources and Transformations of Nitrate from Streams Draining Varying Land Uses: Evidence from Dual Isotope Analysis. *Journal of Environment Quality*, 38(3), 1149–1159.

Busenberg, E., and L.N. Plummer. (1992). Use of chlorofluorocarbons (CCl3F and CCl2F2 ) as hydrologic tracers and age-dating tools: The alluvium and terrace system of central Oklahoma. *Water Resources Research*, 28:2257–2283.

Capell, R., Tetzlaff, D., Hartley, A.J., and Soulsby, C., (2012). Linking metrics of hydrological function and transit times to landscape controls in a heterogeneous mesoscale catchment. *Hydrological Processes*, 26, 405-420.

Cardenas, M.B. (2007), Potential contribution of topography-driven regional groundwater flow to fractal stream chemistry: Residence time distribution analysis of Tóth flow. *Geophysical Research Letters*, 29(13), 1640, doi:10.1029/2006GL029126.

Carle, S. F. (1996), *T-PROGS: Transition probability geostatistical software*, report, Univ. of Calif., Davis.

Carpenter, S. R., Caraco, N. F., Correll, D. L., Howarth, R. W., Sharpley, A. N., & Smith, V. H. (1998). Nonpoint pollution of surface waters with phosphorus and nitrogen. Technical Report. *Ecological Applications*, 8(3), 559–568.

Cey, E. E., Rudolph, D. L., Aravena, R., & Parkin, G. (1999). Role of the riparian zone in controlling the distribution and fate of agricultural nitrogen near a small stream in southern Ontario. *Journal of Contaminant Hydrology*, 37(1–2), 45–67.

Chen, Z., Ding, W., Xu, Y., Müller, C., Rütting, T., Yu, H., Zhu, T. (2015). Importance of heterotrophic nitrification and dissimilatory nitrate reduction to ammonium in a cropland soil: Evidences from a $^{15}N$ tracing study to literature synthesis. *Soil Biology and Biochemistry*, 91, 65–75. http://doi.org/10.1016/j.soilbio.2015.08.026

Chorley, R.J., Malm, D.E., & Pogorzelski, H.A., (1957). A new standard for estimating drainage basin shape. *American Journal of Science*, vol. 255, 138-141.

Claps, P., and G. Oliveto, (1996). Reexamining the determination of the fractal dimension of river networks. *Water Resources Research*, vol.32, 10, 3123-3135.

Cleveland, C. C., Townsend, A. R., Schimel, D. S., Fisher, H., Hedin, L. O., Perakis, S., … Wasson, M. F. (1999). Global patterns of terrestrial biological nitrogen ($N_2$) fixation in natural ecosystems. *Global Biochemical Cycles*, 13(2), 623–645.

Cornaton, F.J. (2004). Deterministic models of groundwater age, life expectancy and transit time distributions in advective-dispersive systems. PhD thesis, Faculty of Sciences of the University of Neuchâtel.

Cornaton, F. J. (2012). Transient water age distributions in environmental flow systems: The time-marching Laplace transform solution technique. *Water Resources Research*, 48, W03524, doi:10.1029/2011WR010606.

Cornaton, F.J. (2014). *A 3-D ground water and surface water flow, mass transport and heat transfer finite element simulator - Ground Water (GW) version 3.6.5*. Groundwater Modelling Centre, DHI-Wasy GmbH, Berlin, Germany.

Cornaton, F., P. Perrochet (2006). Groundwater age, life expectancy and transit time distributions in advective–dispersive systems: 1. Generalized reservoir theory. *Advances Water Resources*, 16, 1267-1291.

Corwin, D.L., Loague, K., and Ellsworth, T.R., (1999). Assessment of non-point source pollution in the vadose zone. *Geophysical Monograph Series*, 108, American Geophysical Union, Washington, DC, 369p.

Cummings, T. F. (2015). Assessment of Nitrate Export in Agricultural Sub-Catchments of the Grand River Watershed : An Isotope Approach. Master of Science Thesis in Earth Science, University of Waterloo, pp. 120.

Cvetkovic, V., & Dagan, G. (1994). Transport of kinetically sorbing solute by steady random velocity in heterogeneous porous formations. *Journal of Fluid Mechanics*, *265*(1), 189. http://doi.org/10.1017/S0022112094000807

Dagan, G. (1988). Time-dependent macrodispersion for solute transport in anisotropic heterogeneous aquifers. *Water Resources Research*, 24(9),1491-1500.

Dagan, G., & Nguyen, V. (1989). A comparison of travel time and concentration approaches to modeling transport by groundwater. *Journal of Contaminant Hydrology*, *4*, 79–91.

Dagan, G., and V. Cvetkovic (1996). Reactive transport and immiscible flow in geological media. I. General theory. *Proceedings: Mathematical, Physical and Engineering Sciences*, Vol. 452, No. 1945, pp. 285-301.

Darracq, A., G. Destouni, K. Persson, C. Prieto, J. Jarsjö (2010), Quantification of advective solute travel times and mass transport through hydrological catchments. *Environmental Fluid Mechanics*, 10:103-120. doi: 10.1007/s10652-009-9147-2.

DeCoursey, D.G., Ahuja, L.R., Hanson, J., Shaffer, M., Nash, R., Rojas, K.W., Hebson, C., Hodges, T., Ma, Q., Johnsen, K.E., Ghidey, F., (1992). *Root zone water quality model, Version 1.0, Technical Documentation*. United States Department of Agriculture, Agricultural Research Service, Great Plains Systems Research Unit, Fort Collins, Colorado, USA.

De Bartolo, S. G., Veltri, M., & Primavera, L. (2006a). Estimated generalized dimensions of river networks. *Journal of Hydrology*, *322*(1–4), 181–191.

De Bartolo, S. G., Primavera, L., Gaudio, R., D'Ippolito, A., & Veltri, M. (2006). Fixed-mass multifractal analysis of river networks and braided channels. *Physical Review E - Statistical, Nonlinear, and Soft Matter Physics*, *74*(2), 1–8.

Del Grosso, S. J., et al. (2001), Simulated effects of land use, soil texture, and precipitation on N gas emissions using DAYCENT, in *Nitrogen in the Environment: Sources, Problems and Management*, edited by R. F. Follett and J. L. Hatfield, pp. 413–431, Elsevier Sci., Amsterdam.

Delhez, E. J. M., and E. Deleersnijder (2002), The concept of age in marine modelling II. Concentration distribution function in the English Channel and the North Sea, *J. Mar. Syst.*, 3(1), 279–297.

Dewes, T. (1999). Ammonia emissions during the initial phase of microbial degradation of solid and liquid cattle manure. *Bioresource Technology*, 70, 245–248. http://doi.org/10.1016/s0960-8524 (99)00046-2.

Diersch, H.J. (2014). *FEFLOW – Finite element modeling of flow, mass, and heat transport in porous and fractured media*. Springer-Verlag 2014. DOI 10.1007/978-3-642-38739-5.

Dooge, J. C. I. (1986), Looking for hydrologic laws, *Water Resources Research*, 22(9), 46–58.

Earthfx Incorporated. (2006). *Groundwater Modelling of the Oak Ridges Moraine Area*. CAMC-YPT Technical Report #01-06.

EC, (2007). *Report from the Commission to the Council and the European Parliament on implementation of Council Directive 91/676/EEC concerning the protection of waters against pollution caused by nitrates from agricultural sources for the period 2000–2003*. SEC(2007)339}/COM/2007/0120 final

EEA, (2007). *Europe's Environment; The Fourth Assessment*, European Environmental Agency, Copenhagen, DK, 452 pp.

Ellert, B. H. & E. G. Gregorich, (1996). Storage of carbon, nitrogen, and phosphorus in cultivated and adjacent forested soils of Ontario. *Soil Science*, 161(9): 587-603.

Essaid, H., & Hill, B. R. (2014). Watershed-scalemodeling of streamflow change in incised montanemeadows. *Water Resource Research*, *50*, 2657–2678. http://doi.org/10.1002/2013WR014420

Etcheverry D, Perrochet P. 2000. Direct simulation of groundwater transit- time distributions using the reservoir theory. *Journal of Hydrogeology* 8: 200–208.

Fetter, C.W. (1993). *Contaminant hydrogeology*. Macmillan Publishing Company, 458 pages.

Fiori, A., and D. Russo (2008), Travel time distribution in a hillslope: Insight from numerical simulations. *Water Resources Research*, 44, W12426, doi:10.1029/2008WR007135.

Flint, J. J. (1974). Stream gradient as a function of order, magnitude and discharge. *Water Resources Research*, 10(5), 969-973.

Fogel, M. L. & Cifuentes, L. A. (1993). Isotope Fractionation during primary production. In *Organic Geochemistry,* Micheael H. Engel, S. A. M., ed., pp. 73-88. New York: Plenum Press.

Fogg, G. E., Rolston, D. E., Decker, D. L., Louie, D. T., & Grismer, M. E. (1998). Spatial variation in nitrogen isotope values beneath nitrate contamination sources. *Ground Water*, *36*(3), 418–426.

Freer, J., J. J. McDonnell, K. J. Beven, N. E. Peters, D. A. Burns, R. P. Hooper, B. Aulenbach, and C. Kendall (2002). The role of bedrock topography on subsurface storm flow. *Water Resources Research*, 38(12), 1269, doi:10.1029/2001WR000872.

Frind, E. O., Duynisveld, W. H. M., Strebel, O., & Boettcher, J. (1990). Modeling of Multicomponent Transport With Microbial Transformation in Groundwater: The Fuhrberg Case. *Water Resources Research*, 26(8), 1707–1719.

Frind, E.O., J. Molson, M. Sousa, and P. Martin (2014). Insights from four decades of model development on the Waterloo Moraine: A review. *Canadian Water Resources Journal*, (39-2), 149-166.

Frisbee, M.D., Wilson, J.L., Gomez-Velez, J.D., Phillips, F.M., and Campbell, A.R., (2013). Are we missing the tail (and the tale) of residence time distributions in watersheds? *Geophysical Research Letters*, 40, 4633-4637, doi:10.1002/grl.50895.

Fritz, P. and Fontes, J.Ch., 1980. Introduction. In: P. Fritz and J.Ch. Fontes (Editors), *Handbook of Environmental Isotope Geochemistry*, Vol. 1, The Terrestrial Environment, A. Elsevier, Amsterdam, pp. 1--19.

Gardiner, V., Park C.C., (1978). Drainage basin morphometry: review and assessment. *Progress in Physical Geography: Earth and Environment*, 2(1): 1-35.

Garten, C.T., J.P. Hanson, D.E. Todd, B.B. Lu, and D.J. Brice. (2007). Natural $^{15}N$ and $^{13}C$ abundance as indicators of forest nitrogen status and soil carbon dynamics. Chapter 3

in *Stable isotopes in ecology and environmental science*. Micheener, R. H., Lajtha, K., (eds). Blackwell Pub.

Gelhar, L.W., C. Welty, K.R. Rehfeldt (1992). A critical review of data on field-scale dispersion in aquifers. *Water Resources Research*, 28(7), 1955-1974.

Ginn, T. R. (1999), On the distribution of multicomponent mixtures over generalized exposure time in subsurface flow and reactive transport:: Fundations, and formulations for groundwater age, chemical heterogeneity, and biodegradation. *Water Resources Research*, 35, 1395–1407.

Goode, D.J. (1996). Direct simulation of groundwater age. *Water Resources Research,* 32(2), 289–296. doi:10.1029/ 95WR03401.

Goss, M. J., Rollins, K. S., Mcewan, K., Shaw, J. R., & Lammers-Helps, H. (2001). *The Management of Manure in Ontario with Respect to Water Quality*. University of Guelph.

Green, C. T., Böhlke, J. K., Bekins, B. A., & Phillips, S. P. (2010). Mixing effects on apparent reaction rates and isotope fractionation during denitrification in a heterogeneous aquifer. *Water Resources Research*, *46*(8), 1–19.

Hack, J. T., (1957). Studies of longitudinal profiles in Virginia and Maryland. U.S. Geol. Surv. Prof. Paper, 294-B.

Haitjema, H. M. (1995). On the residence time distribution in idealized groundwater sheds. *Journal of Hydrology*, *172*, 127–146.

Hale, R. L., Hoover, J. H., Wollheim, W. M., & Vörösmarty, C. J. (2013). History of nutrient inputs to the northeastern United States, 1930-2000. *Global Biogeochemical Cycles*, 27(2), 578–591. http://doi.org/10.1002/gbc.20049

Hale, V. C., and J. J. McDonnell, (2016). Effect of bedrock permeability on stream base flow mean transit time scaling relations: 1. A multiscale catchment intercomparison, *Water Resources Research*, 52, 1358–1374, doi:10.1002/2014WR01612.

Hale, V. C., J. J. McDonnell, M. K. Stewart, D. K. Solomon, J. Doolitte, G. G. Ice, and R. T. Pack, (2016). Effect of bedrock permeability on stream base flow mean transit time scaling relationships: 2. Process study of storage and release. *Water Resources Research*, 52, 1375–1397, doi:10.1002/ 2015WR017660.

Hamilton, S. K. (2012). Biogeochemical time lags may delay responses of streams to ecological restoration. *Freshwater Biology*, 57(SUPPL. 1), 43–57.

Han, X., Shen, W., Zhang, J., & Müller, C. (2018). Microbial adaptation to long-term N supply prevents large responses in N dynamics and N losses of a subtropical forest. *Science of the Total Environment*, 626, 1175–1187.

Hansen, S., Jensen, H.E., Nielsen, N.E., Svendsen, H., (1991). Simulation of nitrogen dynamics and biomass production in winter wheat using the Danish simulation model Daisy. *Fertilizer Research* 27, 245–259.

Hardy, S. D., & Koontz, T. M. (2008). Reducing nonpoint source pollution through collaboration: Policies and programs across the U.S. States. *Environmental Management*, 41(3), 301–310. http://doi.org/10.1007/s00267-007-9038-6

Harman, C. J. (2015), Time-variable transit time distributions and transport: Theory and application to storage-dependent transport of chloride in a watershed, *Water Resources Research*, 51, 1–30, doi:10.1002/2014WR015707.

He, X., Koch, J., Sonnenborg, T. O., Flemming, J., Schamper, C., & Refsgaard, J. C. (2014). Transition probability-based stochastic geological modeling using airborne geophysical data and borehole data. *Water Resources Research*, *50*, 3147–3169.

Heaton, T. H. E. (1986). Isotopic studies of nitrogen pollution in the hydrosphere and atmosphere: A review. *Chemical Geology: Isotope Geoscience Section*, 59(C), 87–102.

Hendrickson, O.Q. (1990). Asymbiotic nitrogen fixation and soil metabolism in three Ontario Forests. Soil Biol. Biochem. 22(7), 967-971.

Hilton, R. G., Galy, A., West, A. J., Hovius, N., & Roberts, G. G. (2013). Geomorphic control on the δ15N of mountain forests. *Biogeosciences*, 10(3), 1693–1705.

Högberg, P. (1997). $^{15}N$ natural abundance in soil – plant systems. Tansley Review No. 95, *New Phytol.*, 137(95), 179–203. http://doi.org/10.1046/j.1469-8137.1997.00808.x.

Holland, E.A., Dentener FJ, Braswell BH & Sulzman J.M. (1999) Contemporary and pre-industrial global reactive nitrogen budgets. *Biogeochemistry*, 46: 7-43.

Horton, R.E., (1932). Drainage basin characteristics. *Trans. AGU*, 13: 350-361.

Horton, R.E., (1945). Erosional development of streams and their drainage basins: hydrophysical approach to quantitative morphology. *Bulletin of the Geological Society America*, 56:275-370.

Houlton, B. Z., Sigman, D. M., & Hedin, L. O. (2006). *Isotopic evidence for large gaseous nitrogen losses from tropical rainforests*. Proceedings of the National Academy of Sciences, 103(23), 8745–8750. http://doi.org/10.1073/pnas.0510185103

Hrachowitz, M., Soulsby, C., Tetzlaff, D., Dawson, J. J. C., & Malcolm, I. A. (2009). Regionalization of transit time estimates in montane catchments by integrating landscape controls. *Water Resources Research*, *45*(5). http://doi.org/10.1029/2008WR007496

Hrachowitz, M., Soulsby, C., Tetzlaff, D., & Speed, M. (2010). Catchment transit times and landscape controls — does scale matter ? *Hydrological Processes*, *125*(June 2009), 117–125.

Hrachowitz, M., Savenije, H. H. G., Blöschl, G., McDonnell, J. J., Sivapalan, M., Pomeroy, J. W., Cudennec, C. (2013). A decade of Predictions in Ungauged Basins (PUB)-a review. *Hydrological Sciences Journal*, *58*(6), 1198–1255.

Hrachowitz, M., Benettin, P., van Breukelen, B. M., Fovet, O., Howden, N. J. K., Ruiz, L., Wade, A. J. (2016). Transit times - the link between hydrology and water quality at the catchment scale. *WIREs Water*, *3*, 629–657. http://doi.org/10.1002/wat2.1155

Hubbell, D. H. & Kidder, G. (2009). *Biological Nitrogen Fixation*. University of Florida IFAS Extension Publication SL16. 1-4.

Indelman, P., & Rubin, Y. (1996). Solute transport in nonstationary velocity fields. *Water Resources Research*, *32*(5), 1259–1267.

Inselsbacher, E., Wanek, W., Strauss, J., Zechmeister-Boltenstern, S., & Müller, C. (2013). A novel15N tracer model reveals: Plant nitrate uptake governs nitrogen transformation rates in agricultural soils. *Soil Biology and Biochemistry*, 57, 301–310.

Jacobsen, B. H., & Hansen, A. L. (2016). Economic gains from targeted measures related to non-point pollution in agriculture based on detailed nitrate reduction maps. *Science of the Total Environment*, 556, 264–275. http://doi.org/10.1016/j.scitotenv.2016.01.103

Jarvis, R.S., (1976). Classification of nested tributary basins in analysis of drainage basins shape. *Water Resources Research*, vol. 12(6), 1151-1164.

Jerabkova, L., Prescott, C. E., & Kishchuk, B. E. (2006). Nitrogen availability in soil and forest floor of contrasting types of boreal mixedwood forests. *Canadian Journal of Forest Research*, 36(1), 112–122. http://doi.org/10.1139/x05-220

Jiang, Y., & Somers, G. (2009). Modeling effects of nitrate from non-point sources on groundwater quality in an agricultural watershed in Prince Edward Island, Canada. *Hydrogeology Journal*, *17*(3), 707–724.

Johannesson, G. H., Lauzon, J., Crolla, A., Gilroyed, B., Vanderzaag, A., & Gordon, R. (2017). Impact of manure storage conditions and time on decomposition of and losses from liquid dairy manure stored in a temperate climate. *Canadian Journal of Soil Science*, 98(1), 148–160. *http://doi.org/10.1139/cjss-2017-0083*

Jones, J.E. and Woodward, C.S. (2001). Newton–Krylov-multigrid solvers for large-scale, highly heterogeneous, variably saturated flow problems. *Advances in Water Resources*, 24(7), 763–774, doi:10.1016/S0309-1708(00)00075-0.

Karr, J.D., Showers, W.J., Gilliam, J.W., Andres, A.S., (2001). Tracing nitrate transport and environmental impact from intensive swine farming using delta nitrogen-15. *Journal of Environmental Quality*, 30, 1163–1175.

Karr, J. D., Showers, W. J., & Jennings, G. D. (2003). Low-level nitrate export from confined dairy farming detected in North Carolina streams using δ15N. *Agriculture, Ecosystems and Environment*, 95(1), 103–110. http://doi.org/10.1016/S0167-8809(02)00103-2

Kaushal, S. S.; Lewis, W. M., Jr.; McCutchan, J. H., Jr. (2006). Land use change and nitrogen enrichment of a Rocky Mountain watershed. *Ecol. Appl.*, 16, 299–312.

Kaushal, S. S., Groffman, P. M., Band, L. E., Elliott, E. M., Shields, C. A., & Kendall, C. (2011). Tracking nonpoint source nitrogen pollution in human-impacted watersheds. *Environmental Science and Technology*, 45(19), 8225–8232.

Kazemi, G. A., J. H. Lehr, P. Perrochet, 2006. *Groundwater age*. Wiley-Interscience, a John Wiley & Sons, Inc., Publication, Hoboken, New Jersey.

Kendall, C., Sklash, M.G., Bullen, T.D., 1995. Isotope tracers of water and solute sources in catchments. In: *Solute modeling in catchment systems*, Trudgill, S.T. (ed), Wiley, 261-303.

Kendall, C., (1998). Tracing nitrogen sources and cycling in catchments. Chapter 16, in '*Isotope tracers in catchment hydrology*', C. Kendall and J.J. McDonnell (Eds.) Elsevier Science B.V., Amsterdam, pp. 519-576.

Kendall, C., & Aravena, R. (2000). Nitrate isotopes in groundwater systems. In *'Environmental Tracers in Subsurface Hydrology*' **Cook,** P.G., **Herczeg,** A. L. (Eds.) Springer: pp. 261–297.

Kendall, C., Elliott, E. M., & Wankel, S. D. (2007). Tracing anthropogenic inputs of nitrogen to ecosystems. In '*Stable Isotopes in Ecology and Environmental Science*', Michener, R., Lajtha, K. (eds), Blackwell Pub., Maiden, MA.

Kirchner, J.W., X. Feng, and C. Neal (2000), Fractal stream chemistry and its implications for contaminant transport in catchments. *Nature*, 403, 524-527.

Kirchner, J.W., X. Feng, and C. Neal (2001), Catchment-scale advection and dispersion as a mechanism for fractal scaling in stream tracer concentrations. *Journal of Hydrology*, 254, 82-101.

Kirchner, J.W., and Colin Neal (2013), Universal fractal scaling in stream chemistry and its implications for solute transport and water quality trend detection. *PNAS*, 110, No. 30, 12213-12218.

Knisel, W.G., Williams, J.R., 1995. Hydrology component of CREAMS and GLEAMSmodels. In: Singh, V.P. (Ed.). *Computer Models of Watershed Hydrology*, Water Resources Publication, pp. 1069–1114

Kollet, S.J., and R.M. Maxwell (2008), Demonstrating fractal scaling of baseflow residence time distributions using a fully-coupled groundwater and land surface model. *Geophysical Research Letters*, 35, L07402.

Kourakos, G., Klein, F., Cortis, A., & Harter, T. (2012). A groundwater nonpoint source pollution modeling framework to evaluate long-term dynamics of pollutant exceedance probabilities in wells and other discharge locations. *Water Resources Research*, *48*(5), 1–19. http://doi.org/10.1029/2011WR010813

Lam, N.S.-N, and De Cola, L. (1993). *Fractals in geography*. Edited by Nina Siu Ngan Lam and Lee De Cola. PTR Prentice Hall, ISBN 0-13-105867-3.

Lee, K. S., Bong, Y. S., Lee, D., Kim, Y., & Kim, K. (2008). Tracing the sources of nitrate in the Han River watershed in Korea, using $\delta^{15}N\text{-}NO_3^-$ and $\delta^{18}O\text{-}NO_3^-$ values. *Science of the Total Environment*, 395(2–3), 117–124. http://doi.org/10.1016/j.scitotenv.2008.01.058

Lehmann, M. F., Reichert, P., Bernasconi, S. M., Barbieri, A., & McKenzie, J. A. (2003). Modelling nitrogen and oxygen isotope fractionation during denitrification in a lacustrine redox-transition zone. *Geochimica et Cosmochimica Acta*, 67(14), 2529–2542.

Leonard, R.A., Knisel, W.G., Still, D.A., (1987). GLEAMS: groundwater loading effects of agricultural management systems. *Transactions of ASAE* 30, 1403–1418.

Leopold, L.B., Wolman, M.G., Miller, J.P., (1964). *Fluvial processes in geomorphology*. Published by W.H. Freeman and company. Printed in San Francisco, USA.

Leray, S., Engdahl, N. B., Massoudieh, A., Bresciani, E., & McCallum, J. (2016). Residence time distributions for hydrologic systems: Mechanistic foundations and steady-state analytical solutions. *Journal of Hydrology*, *543*, 67–87.

Li, X., R. B. Ambrose, and R. Araujo. (2004). Modeling mineral nitrogen export from a forest terrestrial ecosystem to streams. *Trans. ASAE* 47(3): 727-739.

Lin, L., Yang, J.Z., Zhang, B., Zhu, Y., (2010). A simplified numerical model of 3-D groundwater and solute transport at large scale area. *Journal of Hydrodynamics*, Ser. B. 22(3), 319-328.

Lindgren, G. A., G. Destouni, and A. V. Miller (2004), Solute transport through the integrated groundwater-stream system of a catchment, *Water Resources Research*, 40, W03511, doi:10.1029/2003WR002765.

Liu, Y., Yang, W., Leon, L., Wong, I., McCrimmon, C., Dove, A., & Fong, P. (2016). Hydrologic modeling and evaluation of Best Management Practice scenarios for the Grand River watershed in Southern Ontario. *Journal of Great Lakes Research*, 42(6), 1289–1301. http://doi.org/10.1016/j.jglr.2016.02.008

Lovejoy, S., D. Schertzer, and A. A. Tsonis, (1987). Functional box counting and multiple elliptical dimensions in rain, *Science*, 235, 1036-1038.

Luther, K.H., Haitjema, H.M., (1998). Numerical experiments on the residence time distributions of heterogeneous groundwatersheds. *Journal of Hydrology*, 207 (1–2), 1–17.

MacEachren, A., (1985). Compactness of geographic shape: comparison and evaluation of measures. Geografiska Annaler, Series B, *Human Geography*, vol. 67, No.1, 53-67.

Malmström, M.E., G. Destouni, and P. Martinet (2004). Modeling expected solute concentration in randomly heterogeneous flow systems with multicomponent reactions. *Environmental Science & Technology*, 38, 2673-2679.

Maloszewski, P., & Zuber, A. (1982). Determining the turnover time of groundwater systems with the aid of environmental tracers. *Journal of Hydrology*, 57, 207–231.

Mariotti A, Mariotti F, Amarger N, Pizelle G, Ngambi JM, Champigny ML, Moyse A. (1980). Fractionements isotopique de I'azote lors des processes d'absorption des nitrates et de fixation de I'azote atmospherique par les plants. *Physiologie Vegetale*, 18: 163-181.

Mariotti, A., Germon, J. C., & Leclerc, A. (1982). Nitrogen isotope fractionation associated with the $NO_2^- \rightarrow N_2O$ step of denitrification in soils. *Canadian Journal of Soil Science*, 62, 227–241.

Mariotti, A., Landreau, A., & Simon, B. (1988). 15N isotope biogeochemistry and natural denitrification process in groundwater: Application to the chalk aquifer of northern France. *Geochimica et Cosmochimica Acta*, 52(7), 1869–1878.

Marklund, L., & Wörman, A. (2011). The use of spectral analysis-based exact solutions to characterize topography-controlled groundwater flow. *Hydrogeology Journal*, *19*(8), 1531–1543. http://doi.org/10.1007/s10040-011-0768-4

Martin, J. C., & Wegner, R. E. (1979). Numerical solution of multiphase, two-dimensional incompressible flow using stream-tube relationships. *Society of Petroleum Engineers Journal*, *19*(5). http://doi.org/10.2118/7140-PA

Martin, P.J., and E. Frind, (1998). Modeling a complex multi-aquifer system: The Waterloo Moraine, *Groundwater*, 36(4), 679-690.

Marty, C., Houle, D., Gagnon, C., & Courchesne, F. (2017). The relationships of soil total nitrogen concentrations, pools and C:N ratios with climate, vegetation types and nitrate deposition in temperate and boreal forests of eastern Canada. *Catena*, 152(3), 163–172. http://doi.org/10.1016/j.catena.2017.01.014.

Mary, B., Recous, S., & Robin, D. (1998). A model for calculating nitrogen fluxes in soil using $^{15}N$ tracing. *Soil Biology and Biochemistry*, 30(14), 1963–1979.

Matott, LS. 2017. *OSTRICH: an Optimization Software Tool*, Documentation and User's Guide, Version 17.12.19. 79 pages, University at Buffalo Center for Computational Research, www.eng.buffalo.edu/~lsmatott/Ostrich/OstrichMain.html.

Maurer, D.K., Lopes, T.J., Medina, R.L., and Smith, J.L., (2004), Hydrogeology and hydrologic landscape regions of Nevada. *U.S. Geological Survey Scientific Investigations Report 2004–5131*, 35 p.

Maxwell, R. M., Condon, L. E., Kollet, S. J., Maher, K., Haggerty, R., & Forrester, M. M. (2016). The imprint of climate and geology on the residence times of groundwater. *Geophysical Research Letters*, *43*, 701–708. http://doi.org/10.1002/2015GL066916

Mengis, M., Schiff, S. L., Harris, M., English, M. C., Aravena, R., Elgood, R. J., & MacLean, A. (1999). Multiple geochemical and isotopic approaches for assessing ground water NO3 elimination in a riparian zone. *Ground Water*, 37(3), 448–457.

McDonnell, J.J. (2003), Where does water go when it rains? Moving beyond the variable source area concept of rainfall-runoff response. *Hydrological Processes*, 17, 1869-1875.

McDonnell, J. J., M. Sivapalan, K. Vache´, S. Dunn, G. Grant, R. Haggerty, C. Hinz, R. Hooper, J. Kirchner, M. L. Roderick, J. Selker, and M. Weiler (2007). Moving beyond heterogeneity and process complexity: A new vision for watershed hydrology, *Water Resources Research*, 43, W07301, doi:10.1029/2006WR005467.

McDonnell, J. J. et al. (2010), How old is streamwater? Open questions in catchment transit time conceptualization, modelling and analysis, *Hydrological Processes*, 24, 1745–1754, doi: 10.1002/hyp.7796.

McFarland, W.D., (1982). A description of aquifer units in western Oregon. *U.S. Geological Survey, Open-File Report 82-165*.

McGuire, K. J., McDonnell, J. J., Weiler, M., Kendall, C., McGlynn, B. L., Welker, J. M., & Seibert, J. (2005). The role of topography on catchment-scale water residence time. *Water Resources Research*, 41(5), 1–14. http://doi.org/10.1029/2004WR003657

McGuire, K. J., & McDonnell, J. J. (2006). A review and evaluation of catchment transit time modeling. *Journal of Hydrology*, 330(3–4), 543–563.

McGuire, K.J., M.Weiler, and J.J.McDonnell (2007). Integrating tracer experiments with modeling to assess runoff processes and water transit times. *Advances in Water Resources*, 30, 824-837.

McGlynn, B., McDonnell, J., Stewart, M., & Seibert, J. (2003). On the relationships between catchment scale and streamwater mean residence time. *Hydrological Processes*, *17*(1), 175–181. http://doi.org/10.1002/hyp.5085

McGlynn, B.L., J.J. McDonnell, J. Seibert, and C. Kendall (2004), Scale effects on headwater catchment runoff timing, flow sources and groundwater-streamflow relations. *Water Resources Research*, 40, W07504, doi:10.1029/2003WR002494.

McGrane, S.J., Tetzlaff, D., and Soulsby, C., (2014). Influence of lowland aquifers and anthropogenic impacts on the isotope hydrology of contrasting mesoscale catchments. *Hydrological Processes*, 28(3), 793-808.

McGuire, K. J., J. J. McDonnell, M. Weiler, C. Kendall, B. L. McGlynn, J. M. Welker, and J. Seibert (2005), The role of topography on catchment-scale water residence time, *Water Resources Research*, 41, W05002, doi:10.1029/2004WR003657.

McLaren, R.G. (2011). GRID BUILDER – A pre-processor for 2-D, triangular element, finite-element programs. University of Waterloo, Groundwater Simulations Group.

McMahon, P.B., and J.K. Bohlke (1996). Denitrification and mixing in a stream-aquifer system: effects on nitrate loading to surface water. *Journal of Hydrology*, 186, 105-128.

McMahon, P. B., Böhlke, J. K., Kauffman, L. J., Kipp, K. L., Landon, M. K., Crandall, C. A., … Brown, C. J. (2008). Source and transport controls on the movement of nitrate to public supply wells in selected principal aquifers of the United States. *Water Resources Research*, 44(4), 1–17. http://doi.org/10.1029/2007WR006252

McNamara, J.P., Tetzlaff, D., Bishop, K., Soulsby, C., Seyfried, M., Peters, N.E., Aulenbach, B.T.,and Hooper, R., (2011). Storage as a metric of catchment comparison. *Hydrological Processes*, 25, 3364-3371.

Mesa, O.J., (1986). Analysis of channel networks parameterized by elevation. University, Miss.: University of Mississippi. PhD dissertation.

Montgomery, D. R. & Dietrich, W. E., (1992). Channel initiation and the problem of landscale scale. *Science*, (255), 826-830.

Müller, C., Stevens, R. J., & Laughlin, R. J. (2004). A15N tracing model to analyse N transformations in old grassland soil. *Soil Biology and Biochemistry*, 36(4), 619–632.

Müller, C., Rütting, T., Kattge, J., Laughlin, R. J., & Stevens, R. J. (2007). Estimation of parameters in complex15N tracing models by Monte Carlo sampling. *Soil Biology and Biochemistry*, 39(3), 715–726. http://doi.org/10.1016/j.soilbio.2006.09.021

Nadelhoffer, K.J., Fry, B., (1994). Nitrogen isotope studies in forest ecosystems. In: *Stable Isotopes in Ecology and Environmental Science*, Lajtha, K., Mitchener, R.H. (Eds.), Blackwell Scientific Publications, Oxford, pp. 22-44.

Neuman, S. (1993). Eulerian-lagrangian theory of transport in space-time nonstationary velocity fields: exact nonlocal formalism by conditional moments and weak approximation. *Water Resources Research*, *29*(3), 633–645.

OMAFRA and University of Guelph, (2012*). Ontario field crop residue survey of availability and properties as potential feedstock's for the bioeconomy*. Agricultural Adaptation Council.

OMAFRA Field Crop Team, (2017). *Agronomy guide for field crops*. Publication 811. Published by the Ministry of Agriculture, Food and Rural Affairs, Queen's Printer for Ontario, Toronto, ISBN 978-1-4606-9021-5.

Pearce, A. J., M. K. Stewart, and M. G. Sklash (1986), Storm runoff generation in humid headwater catchments: 1. Where does the water come from?, *Water Resources Research*, 22, 1263–1272.

Phillips, J.D. (1993). Interpreting the fractal dimension of river networks. Chapter 7 in *Fractals in Geography, vol. 7*, edited by N. S. Lam and L. De Cola, pp. 142-157, Prentice-Hall, Englewood Cliffs, N.J., 1993.

Przewlocki K, Yurtsever Y. (1974). Some conceptual mathematical models and digital simulation approach in the use of tracers in hydrological systems. *Isotope techniques in groundwater*, Vol. IIIAEA, Vienna, pp. 425–450.

Radcliffe, J.A., (2000). Physical hydrogeology and impact of urbanization at the Waterloo West Side: a groundwater modelling approach. MSc. in Earth Science, University of Waterloo.

Ramos, C., & Carbonell, E. A. (1991). Nitrate Leaching and Soil-Moisture Prediction with the Leachm Model. *Fertilizer Research*, 27(2–3), 171–180.

Raven Development Team, *RAVEN: User's and Developer's Manual v2.7*.

Raimbault, B. a. (2011). *Litter input, soil quality and soil carbon dioxide production rates in varying riparian land uses along a first order stream in Southern Ontario, Canada*. Thesis, Master of Environmental Studies, University of Waterloo, Canada.

Refsgaard, J.C., M. Thorsen, J.B. Jensen, S. Kleeschulte, & S.Hansen. (1999). Large scale modelling of groundwater contamination from nitrate leaching. *Journal of Hydrology*, *221*, 117–140. http://doi.org/10.1016/S0022-1694(99)00081-5

Rinaldo, A., K. J. Beven, E. Bertuzzo, L. Nicotina, J. Davies, A. Fiori, D. Russo, and G. Botter (2011), Catchment travel time distributions and water flow in soils. *Water Resources Research*, 47, W07537, doi:10.1029/2011WR010478.

Rios, F.J., M. Ye, L. Wang, P.Z. Lee, H. Davis, and R. Hicks (2013). ArcNLET: A GIS-based software to simulate groundwater nitrate load from septic systems to surface water bodies. *Computers & Geosciences*, 37 (7), 822-830.

Rinaldo, A., & Marani, A. (1987). Basin scale model of solute transport. *Water Resource Research*, *23*(11), 2107–2118.

Robertson, W. D., & Schiff, S. L. (2008). Persistent Elevated Nitrate in a Riparian Zone Aquifer. *Journal of Environmental Quality*, 37(2), 669–679.

Robin, M.J.L., A.L. Gutjahr, E.A. Sudicky, and J.L. Wilson (1993). Cross-correlated random field generation with the direct Fourier transform method. *Water Resources Research,* 29, 2385-2397.

Rodgers, P., C. Soulsby, S.Waldron, and D.Tetzlaff. (2005). Using stable isotope tracers to assess hydrological flow paths residence times and landscape influences in a nested mesoscale catchment. *Hydrol. Earth Syst. Sci.*, 9, 139-155.

Rodriguez-Iturbe, I., A. Rinaldo, R. Rigon, R. L. Bras, A. Marani, and I. Ijjasz-Vasquez (1992), Energy-dissipation, runoff production, and the 3-dimensional structure of river basins, *Water Resources Research*, 28(4), 1095.

Rodríguez-Itube, I., and A. Rinaldo, 1997. *Fractal river basins, chance and self-organization*. Cambridge University Press, New York, USA.

Rubin, J., & James, R. V. (1973). Dispersion-affected transport of reactive solutes in saturated porous media: Galerkin method applied to equilibrium-controlled exchange in unidirectional steady state water flow. *Water Resource Research*, *9*(5), 1332–1356.

Rubin, Y. (2003). *Applied stochastic hydrogeology*. Oxford University Press, pg. 391.

Rudolph, D. L., 1985. A quasi three dimensional finite element model for steady-state analysis of multiaquifer systems, B. Application to the Greenbrook well field. M.Sc. thesis, Department of Earth Sciences, University of Waterloo.

Rütting, T., Clough, T. J., Müller, C., lieffering, M., & Newton, P. C. D. (2010). Ten years of elevated atmospheric carbon dioxide alters soil nitrogen transformations in a sheep-grazed pasture. *Global Change Biology*, 16(9), 2530–2542.

Schilling, K. E., & Zhang, Y. K. (2012). Temporal scaling of groundwater level fluctuations near a stream. *Ground Water*, 50(1), 59–67.

Schlesinger, W. H. (1997). *Biogeochemistry: an analysis of global change*. Academic Press, San Diego, California, USA.

Schulz, M. and Bischoff, M. (2008). Variation in riverine phosphorus between 1994 and 2003 as affected by land-use and loading reductions in six medium-sized to large German rivers, *Limnologica - Ecology and Management of Inland Waters*, 38, 2, (126).

Shaman J, M. Stieglitz, D. Burns (2004). Are big basins just the sum of small catchments? *Hydrological Processes*, 18: 3195–3206.

Shapiro, A. M., & Cvetkovic, V. D. (1988). Stochastic analysis of solute arrival time in heterogeneous porous media. *Water Resources Research*, *24*(10), 1711–1718.

Shelberg, M.C., Moellering, H., and Lam N.S.-N. 1982. Measuring fractal dimensions of empirical cartographic curves. *Proceedings, Fifth International Symposium on Computer-Assisted Cartography* (Auto-Carto 5), Washington, D.C., pp. 481-490.

Shreve, R.L. (1966). Statistical law of stream numbers. *Journal of Geology*, 74:17-37.

Smil, V. (1999). Crop Residues: Agriculture ' s Largest Harvest. *BioScience*, 49(4), 299–308. http://doi.org/10.2307/1313613.

Sivapalan, M., Takeuchi K, Franks SW, Gupta VK, Karambiri H, Lakshmi V, Liang X, McDonnell JJ, Mendiondo EM, O'Connell PE, Oki T, Pomeroy JW, Schertzer D, Uhlenbrock S, Zehe E. (2003). IAHS decade on Predictions in Ungauged Basins (PUB), 2003–2012: Shaping an exciting future for the hydrological sciences. *Hydrological Sciences Journal-Journal des Sciences Hydrologiques* 48: 857–880.

Smith, K.G., (1950). Standards for grading texture of erosional topography. *American Journal of Science*, 248:655-668.

Snowdon, A. P., (2009). Improved numerical methods for distributed hydrological models. Master of Applied Science Thesis in Civil Engineering. University of Waterloo.

Spoelstra, J., Schiff, S. L., Elgood, R. J., Semkin, R. G., & Jeffries, D. S. (2001). Tracing the sources of exported nitrate in the Turkey Lakes Watershed using $^{15}N/^{14}N$ and 18O/16O isotopic ratios. *Ecosystems*, 4(6), 536–544.

Soltani, S. S., and V. Cvetkovic (2013). On the distribution of water age along hydrological pathways with transient flow. *Water Resources Research*, 49, 5238–5245,

Soulsby, C., Malcolm, R., Helliwell, R., Ferrier, R.C., and Jenkins, A. (2000). Isotope hydrology of the Allt a' Mharcaidh catchment, Cairngorms Scotland: implications for hydrological pathways and residence times. *Hydrological Processes*, 14, 747-726.

Soulsby, C., P.J. Rodgers, J. Petry, D.M. Hannah, I.A. Malcolm, S.M. Dunn (2004). Using tracers to upscale flow path understanding in mesoscale mountainous catchments: two examples from Scotland. *Jounral of Hydrology*, 291, 174-196.

Soulsby, C., Tetzlaff, D., Dunn, S. M., & Waldron, S. (2006). Scaling up and out in runoff process understanding: insights from nested experimental catchment studies. *Hydrological Processes*\, *20*, 2461–2465. http://doi.org/10.1002/hyp

Soulsby, C., and D. Tetzlaff (2008). Towards simple approaches for mean residence time estimation in ungauged basins using tracers and soil distributions. *Journal of Hydrology*, 363, 60-74. doi: 10.1016/ j.jhydrol.2008.10.001

Soulsby, C., Tetzlaff, D., & Hrachowitz, M. (2009). Tracers and transit times: windows for viewing catchment scale storage? *Hydrological Processes*, *23*, 3503–3507.

Soulsby, C., Tetzlaff, D., and Hrachowitz, M., (2010). Are transit times useful process-based tools for flow prediction and classification in ungauged basins in montane regions? *Hydrological Processes*, 24, 1685-1696.

Soulsby, C., K. Piegat, J. Seibert, and D. Tetzlaff (2011). Catchment-scale estimates of flow path partitioning and water storage based on transit time and runoff modelling. *Hydrological Processes,* 25, 3960-3976.

Soulsby, C., Birkel, C., Geris, J., Dick, J., Tunaley, C., & Tetzlaff, D. (2015). Stream water age distributions controlled by storage dynamics and nonlinear hydrologic connectivity: Modeling with high-resolution isotope data. *Water Resources Research*, *51*, 7759–7776.

Souza, M.R., Frind, E.O., Rudolph, D.L., (2013). An integrated approach for addressing uncertainty in the delineation of groundwater management areas. *Journal of Contaminant Hydrology*, 148, 12-24.

Stanford, G. and Smith, S. (1972) Nitrogen Mineralization Potential of Soils. *Soil Science Society of America Journal*, 36, 465-472.

Statistics Canada, (2006). A geographical profile of livestock manure production in Canada, 2006. *https://www150.statcan.gc.ca/n1/pub/16-002-x/2008004/article/10751-eng.htm*

Stewart, M. K., & McDonnell, J. J. (1991). Rainfall samples were collected sequentially within the increments during each storm event. *Water Resources Research*, 27(10), 2681–2693.

Strahler, A. N. (1950). Equilibrium theory of erosional slopes approached by frequency distribution analysis. *Americal Journal of Science*, 248, 673–696.

Strahler, A. N. (1964). *Quantitative geomorphology of drainage basins and channel networks*. Handbook of applied hydrology, McGraw-Hill Book Co., New York.

Styczen, M., Storm, B., (1993). Modelling of N-movements on catchment scale—a tool for analysis and decision making. 1. Model description. 2. A case study. *Fertilizer Research* 36, 1–17.

Tarboton, D.G., Bras, R.L., & Rodríguez-Iturbe, I., (1988). The fractal nature of river networks. *Water Resources Research*, vol. 24 (8), 1317-1322.

Tarboton, D.G., Bras, R.L., & Rodríguez-Iturbe, I., (1989). Scaling and elevation in river networks. *Water Resources Research*, vol. 25(9), 2037-2051.

Tesoriero, A. J., & Puckett, L. J. (2011). $O_2$ reduction and denitrification rates in shallow aquifers. *Water Resources Research*, 47(12522), 1–17.

Tetzlaff, D., J. Seibert, K.J. McGuire, H. Laudon, D.A. Burns, S.M. Dunn, and C. Soulsby (2009a). How does landscape structure influence catchment transit time across different geomorphic provinces? *Hydrological Processes*, 23, 945-953.

Tetzlaff, D., J. Seibert, C. Soulsby (2009b), Inter-catchment comparison to assess the influence of topography and soils on catchment transit times in a geomorphic province; the Cairngorm mountains, Scotland. *Hydrological Proceses*, 23, 1874-1886, doi: 10.1002/hyp.7318.

Therrien, R., and E.A. Sudicky, (1996). Three-dimensional analysis of variably-saturated flow and solute transport in discretely-fractured porous media. *Journal of Contaminant Hydrology*, 23(1-2), 1--44.

Tibshirani, R., (1996). Regression shrinkage and selection via the Lasso. *Journal of the Royal Statistical Society*, series B, 58(1), pp. 267-288.

Turner JV, Macpherson DK, Stokes RA. (1987). The mechanisms of catchment flow processes using natural variations in deuterium and oxygen-18. *Journal of Hydrology* 94: 143–162.

Uhlenbrook, S. and Ch. Leibundgut (2002). Process-oriented catchment modelling and multiple-response validation. *Hydrological Processes,* 16, 423-440. doi: 10.1002/hyp.330.

Uhlenbrook, S., M. Frey, C. Leibundgut, and P. Maloszewski (2002). Hydrograph separations in a mesoscale mountainous basin at event and seasonal timescales. *Water Resources Research*, 38(6), 1096, doi:10.1029/ 2001WR000938.

USEPA (United States Environmental Protection Agency) (2002). Section 319 Success Stories Volume III: The Successful Implementation of the Clean Water Act's 319 Nonpoint Source Pollution Program. EPA 841-S-01-0001. Washington, DC: EPA, Office of Water.

van Breemen, N.,E.W. Boyer, C.L. Goodale, N.A. Jaworski, K. Paustian, S.P. Seitzinger, K. Lajtha, B. Mayer, D. Van Dam, R.W.Howarth, K.J. Nadelhoffer, M. Eve & G. Billen, (2002). Where did all the nitrogen go? Fate of nitrogen inputs to large watersheds in the northeastern USA. *Biogeochemistry*, 57-58: 267–93.

van der Velde, Y., G. H. de Rooij, J. C. Rozemeijer, F. C. van Geer, and H. P. Broers (2010). Nitrate response of a lowland catchment: On the relation between stream concentration and travel time distribution dynamics, *Water Resources Research*, 46, W11534, doi:10.1029/2010WR009105.

Van Drecht, G., A. F. Bouwman, J. M. Knoop, A. H. W. Beusen, and C. R. Meinardi, (2003) Global modeling of the fate of nitrogen from point and nonpoint sources in soils, groundwater, and surface water, *Global Biogeochem. Cycles*, 17(4), 1115, doi:10.1029/2003GB002060.

Van Meter, K.J., N.B. Basu, J.J. Veenstra, and C.L. Burras. (2016). The nitrogen legacy: emerging evidence of nitrogen accumulation in anthropogenic landscapes. *Environmental Research Letters*. 11, doi:10.1088/1748-9326/11/3/035014.

Van Meter, K. J., N. B. Basu, and P. Van Cappellen (2017), Two centuries of nitrogen dynamics: Legacy sources and sinks in the Mississippi and Susquehanna River Basins, *Global Biogeochemical Cycles*, 31, 2–23, doi:10.1002/2016GB005498.

Van Miegroet, H.; Johnson, D. W.; Cole, D. W. (1992). Analysis of N cycles in polluted versus unpolluted environment. In '*Atmospheric Deposition and Forest Nutrient Cycling*'; Johnson, D. W.; Lindberg, S. E., Eds.; Springer-Verlag: NewYork; pp199- 202.

Veltri, M., Veltri, P., & Maiolo, M. (1996). On the fractal description of natural channel networks. *Journal of Hydrology*, *187*, 137–144.

Vitousek, P. M., Aber, J. D., Howarth, R. W., Likens, G. E., Matson, P. A., Schindler, D. W., … Tilman, D. G. (1997). Human Alteration of the Global Nitrogen Cycle: Sources and Consequences. Technical Report. *Ecological Applications*, 7(3), 737–750.

Vitousek, P. M., Menge, D. N. L., Reed, S. C., & Cleveland, C. C. (2013). Biological nitrogen fixation: rates, patterns and ecological controls in terrestrial ecosystems. *Philosophical Transactions of the Royal Society*, 368:20130119.

Vogt, K. A., Grier, C. C., & Vogt, D. J. (1986). Production, turnover, and nutrient dynamics of above- and belowground detritus of world forests. *Advances in Ecological Research*, 15, 303–377.

Wagener, T., Sivapalan, M., Troch, P. A., McGlynn, B. L., Harman, C. J., Gupta, H. V., Wilson, J. S. (2010). The future of hydrology: An evolving science for a changing world. *Water Resources Research*, 46(5), 1–10. http://doi.org/10.1029/2009WR008906

Wassenaar, L. I. (1995). Evaluation of the origin and fate of nitrate in the Abbotsford Aquifer using the isotope of 15N and 18O in NO3. *Applied Geochemistry*, 10, 391–405.

Welch, L. a. a., Allen, D. M. M., & (Ilja) van Meerveld, H. J. (2012). Topographic Controls on Deep Groundwater Contributions to Mountain Headwater Streams and Sensitivity to Available Recharge. *Canadian Water Resources Journal*, *37*(4), 349–371.

Wollheim, W. M., Vörösmarty, C. J., Bouwman, A. F., Green, P., Harrison, J., Linder, E., Syvitski, J. P. M. (2008). Global N removal by freshwater aquatic systems using a spatially distributed, within-basin approach. *Global Biogeochemical Cycles*, 22(2), 1–14.

Wolock, D.M., J. Fan, and G.B. Lawrence (1997), Effects of basin size on low-flow stream chemistry and subsurface contact time in the Neversink River watershed, New York. *Hydrological Processes*, 11, 1273-1286.

Wörman, A., A.I. Packman, L. Marklund, J.W. Harvey, and S.H. Stone (2007), Fractal topography and subsurface water flows from fluvial bedforms to the continental shield. *Geophysical Research Letters*, 34, L07402, doi:10.1029/2007GL029426.

Yang, Y., Yanai, R. D., See, C. R., & Arthur, M. A. (2017). Sampling effort and uncertainty in leaf litterfall mass and nutrient flux in northern hardwood forests. *Ecosphere*, *8*(11). http://doi.org/10.1002/ecs2.1999

Zhan, H., (1999). On the ergodicity hypothesis in heterogeneous formations. *Mathematical Geology*, 31(1): 113-134.

Zhang, D., Andricevic, R., Sun, A. Y., & Hu, X. (2000). Solute flux approach to transport through spatially nonstationary flow in porous media. *Water Resources Research*, *36*(8), 2107–2120.

Zhang, H., & Hiscock, K. M. (2011). Modelling the effect of forest cover in mitigating nitrate contamination of groundwater: A case study of the Sherwood Sandstone aquifer in the East Midlands, UK. *Journal of Hydrology*, *399*(3–4), 212–225.

Zhang, J. B., Zhu, T. B., Cai, Z. C., Qin, S. W., & Müller, C. (2012). Effects of long-term repeated mineral and organic fertilizer applications on soil nitrogen transformations. *European Journal of Soil Science*, 63(1), 75–85.

Zhang, J., Müller, C., & Cai, Z. (2015). Heterotrophic nitrification of organic N and its contribution to nitrous oxide emissions in soils. *Soil Biology and Biochemistry*, 84, 199–209. http://doi.org/10.1016/j.soilbio.2015.02.028

Zhang, X. (2016). Spatio-temporal patterns in net anthropogenic nitrogen and phosphorus inputs across the Grand River watershed. Master of Science Thesis in Earth Science, University of Waterloo.

Zhang, J., Tian, P., Tang, J., Yuan, L., Ke, Y., Cai, Z., Müller, C. (2016). The characteristics of soil N transformations regulate the composition of hydrologic N export from terrestrial ecosystem. Journal of Geophysical Research: *Biogeosciences*, 121(6), 1409–1419. http://doi.org/10.1002/2016JG003398

Zhang, Y., Xu, W., Duan, P., Cong, Y., An, T., Yu, N., Zhang, Y. (2017). Evaluation and simulation of nitrogen mineralization of paddy soils in Mollisols area of Northeast China under waterlogged incubation. *PLoS ONE*, 12(2), 1–19.

Zheng, C., G.D., Bennett. (2002). *Applied contaminant transport modeling*. Second edition, Wiley-Interscience, a John Wiley & Sons, Inc. New York.

# Appendix A

# Supplementary Material: Chapter 2

## Introduction

The supplementary material provides further details on the theoretical formulation for the estimation of travel time in the numerical model. A flow chart summarizing the calibration process followed in the analytical method is presented. Additionally, details are also included on the estimated groundwater flow path analysis of seven transects distributed across the watershed that are used to compare their distances and pMTTs estimated using the analytical and numerical methods.

## Travel Time Distribution using the Numerical Model

The mathematical approach incorporated in FEFLOW (DHI-WASY GmbH) for the estimation of groundwater age was developed by Cornaton (*Cornaton, 2004*; *Cornaton and Perrochet 2006*; *Cornaton, 2014*). Three independent time variables are derived from this approach: age (*A*), life time expectancy (*E*), and transit time (*T*). Age is defined as the time a water particle has spent since the time of injection up to a location $\boldsymbol{x}$ in the aquifer. Life expectancy is the time that is left for a water particle at a location $\boldsymbol{x}$ before it leaves the aquifer. Transit time corresponds to the time since injection up until it exits the aquifer, which is equivalent to T = A + E. Under this approach, each of these time variables has its associated probability density function (PDF): $g_A$, $g_E$, and $g_T$, derived from evaluating the respective time variable at any position $\boldsymbol{x}$ in the domain. Both $g_A$ and $g_E$ are distributed and transported using the ADE equation by solving the boundary value problem (i.e., for $g_E$ only):

$$\frac{\partial \theta g_E}{\partial t} = \nabla \cdot \mathbf{q} g_E + \nabla \cdot \mathbf{D} \nabla g_E - q_I g_E \quad in\ \Omega,$$

And its boundary conditions:

$$g_E(\boldsymbol{x}, 0) = g_E(\boldsymbol{x}, \infty) = 0 \quad in\ \Omega,$$

$$[\mathbf{q}g_E(\boldsymbol{x},t) + \mathbf{D}\nabla g_E(\boldsymbol{x},t)] \cdot \boldsymbol{n} = (\mathbf{q} \cdot \boldsymbol{n})\delta(t) \;\; on \;\; \Gamma_+,$$

$$-\mathbf{D}\nabla g_E(\boldsymbol{x},t) \cdot \boldsymbol{n} = 0 \;\; on \;\; \Gamma_0,$$

where $\Omega$, $\Gamma_+$, $\Gamma_0$, represent the entire domain, the outlet of interest, and the domain's impervious boundary, respectively; θ, is porosity or mobile water content; $q$, is the Darcy flux vector; $D$, is the tensor of macro-dispersion; $\delta(t)$, is the time-Dirac delta function; and $q_I g_E$, is a source term to represent recharge. The second and third boundary conditions (BC) correspond to a Cauchy- and Neumann-type BC, respectively. This set of equations is referred as the 'backward-in-time' model, which was derived from the forward model by reversing the velocity field. The result of solving these boundary value equations is the respective density function that is transported, $g_A$ and $g_E$, which should be interpreted as the probabilities of a water particle to arrive at (for the age PDF) position $\boldsymbol{x}$ after $t$ years or less, and to exit the aquifer (for the life expectancy PDF) departing from position $\boldsymbol{x}$ after $t$ years or less. The transit time probability is defined by the convolution of both $g_A$ and $g_E$ at every position $\boldsymbol{x}$ in the domain so that $g_T(\boldsymbol{x},t) = g_{A+E}(\boldsymbol{x},t)$. According to this definition, the maximum value of $g_T(\boldsymbol{x},t)$ corresponds to either the maximum value of $g_A(\boldsymbol{x},t)$, which occurs at the outlet ($\Gamma_+$), or the maximum value of $g_E(\boldsymbol{x},t)$, at the inlet ($\Gamma_-$).

## Generated Heterogeneity Fields

Using the FGEN program we generated hydraulic conductivity fields following the parameters specified in Table 2-3 for different correlation lengths ($I_{xy}$) and variance of logconductivity ($\sigma_Y^2$). Figure A1 shows a subset of these generated fields in which iso-conductivity areas become larger as the correlation length increases in both horizontal and vertical views, for a constant $\sigma_Y^2$ value of 1.0.

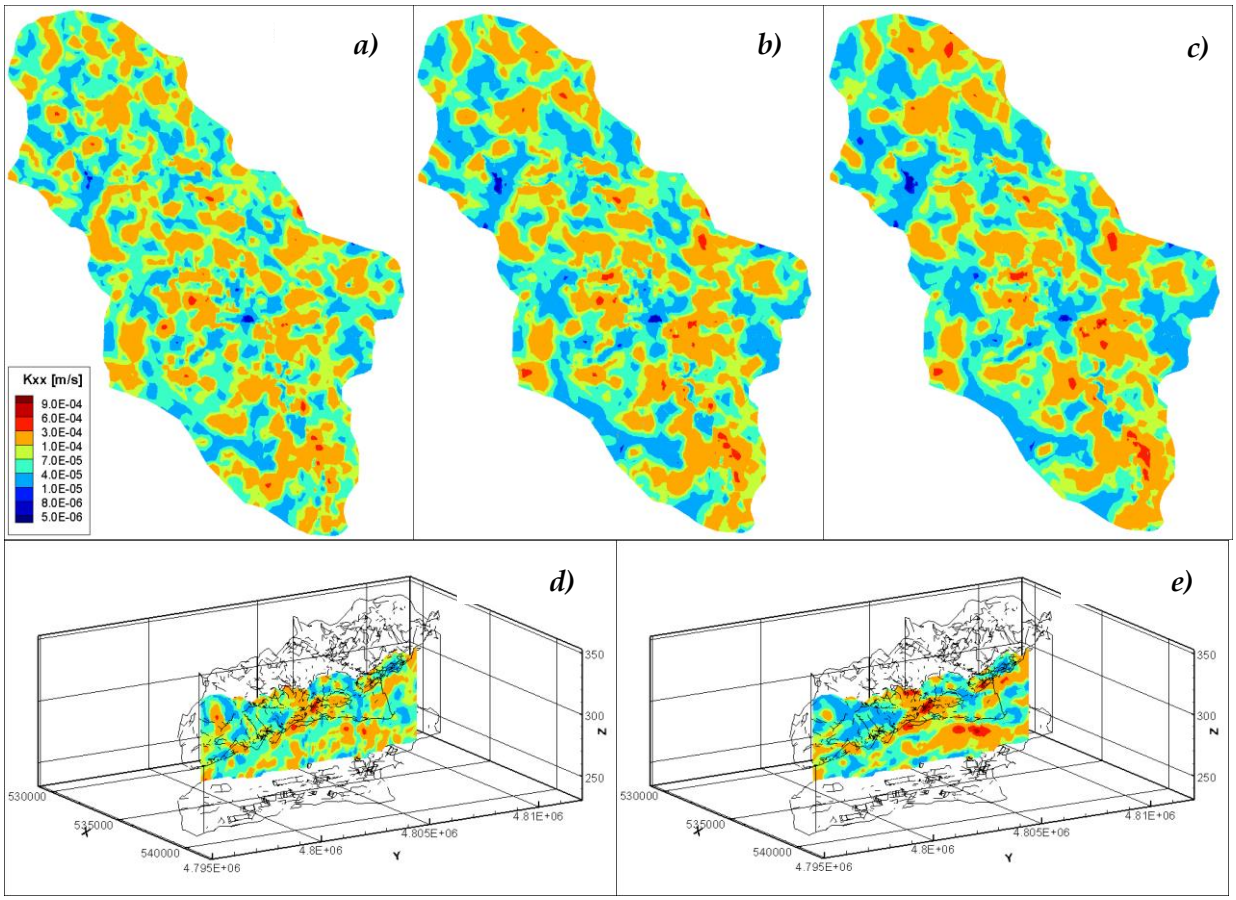


Figure A1. Hydraulic conductivity fields generated with FGEN, an example for $\sigma_Y^2$ = 1.0 in top view and cross section; a) $I_{xy}$ = 150m; b) $I_{xy}$ = 300m; c) $I_{xy}$ = 450m; d) $I_{xy}$ = 150m; and, e) $I_{xy}$ = 450m. All these panels were created with a vertical correlation length ($I_z$) of 2.7m.

## Calibration Flow Chart

The process used for calibrating the analytical method is presented here (Figure A2). It begins with the delineation of flow paths matching that of the numerical model by adjusting the smoothing factor in ArcNLET. There are two parameters in the analytical model that could be modified to match the numerical travel time PDF: bulk velocity ($U_0$) and macrodispersion ($\lambda_L$). The bulk velocity moves the travel time PDF along the x-axis (i.e., travel time), and the $\lambda_L$ displaces the peak along the y-axis (i.e., arrival frequency). This is an iterative process that could also involve re-adjusting the smoothing factor in the case that

these calibration parameters require significant adjustments. The calibration process was applied to twenty-four observation points in the watershed for each scenario (n=28).

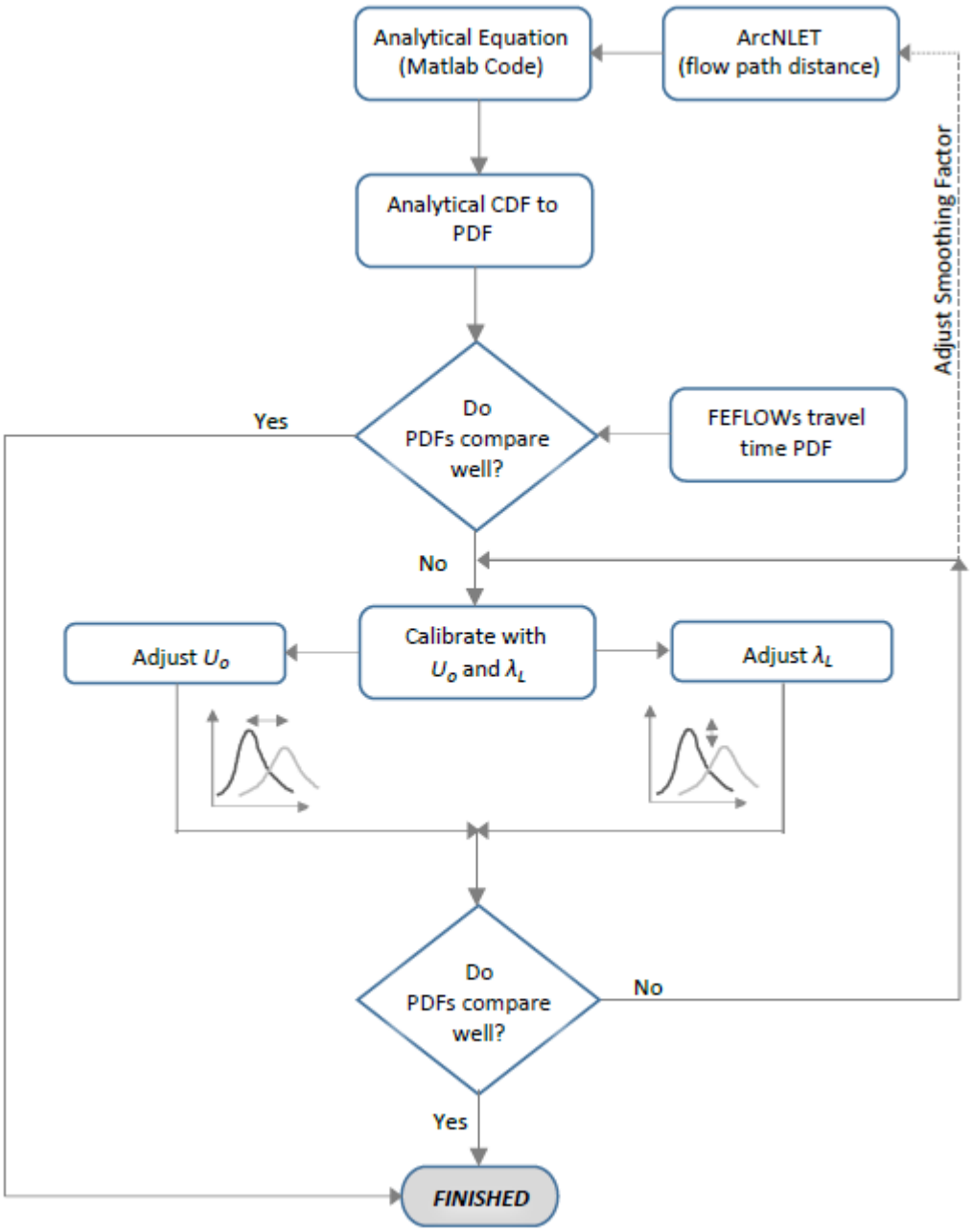


Figure A2. Flow chart summarizing the calibration process used for the analytical model.

## Calibrated Parameters for Analytical Model and MTT Estimates

The analytical model was calibrated using two approaches: i) by adjusting the travel time PDFs for 24 particle locations estimated from both analytical and numerical models, and ii) by adjusting the mean bulk velocity ($U_o$) in order to have the data cloud of travel time estimates to fall in a $45^o$ alignment with respect to the numerical estimates. These calibrated parameters from each approach are presented in Table A1. The analytical model parameters from the first calibration approach were applied to the respective scenario to obtain first the pMTTs, from which the wMTTs were calculated. The corresponding pMTTs from the numerical model were used for this calculation of numerical wMTTs.

## Analytical and Numerical pMTT Comparison [Worst Case]

The greatest discrepancies (>500%) between the analytical and numerical model occurred next to streams for both reduced and actual topography models. In Figure A3, we are identifying these particle locations independently in both RH and AH scenarios. This figure is complementary with Figure 2-7, where the location of incremental discrepancies is represented as percent difference from the numerical estimate.

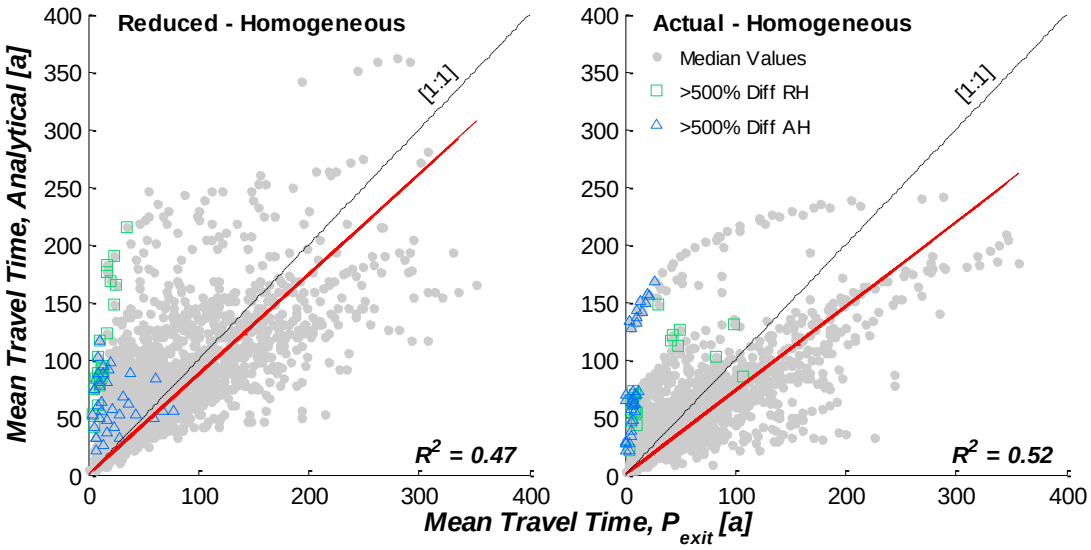


Figure A3. Data sets with pMTTs 500 % difference or greater with respect to the numerical estimates spatially, and independently, identified in Figure 2-7 for both a) RH and b) AH scenarios.

Table A1. Calibrated parameters for analytical approach along with the estimated mean travel time and their correlation with the numerical model estimates.

| Scenario | ID | Calibration with 24 Streamlines | | Analytical vs. $P_{exit}$, [2] $r^2$ | wMTT[3] $P_{exit}$ *(a)* | wMTT, Analytical, *(a)* |
|---|---|---|---|---|---|---|
| | | Bulk vel $Uo$ [m/d] | Calibrated Macrodispersion, $\lambda_L$ | | | |
| *Reduced Topography* | | | | | | |
| Homogeneous | RH | 0.078 | 13.32·X^0.272, $r^2$=0.48 | 0.47 | 78.0 | 81.7 |
| K15hv03[1] | 1 | 0.079 | 13.03·X^0.271, $r^2$=0.57 | 0.47 | 76.0 | 80.2 |
| K15hv07 | 2 | 0.079 | 12.09·X^0.291, $r^2$=0.41 | 0.51 | 71.1 | 79.7 |
| K15hv10 | 3 | 0.087 | 6.79·X^0.359, $r^2$=0.69 | 0.53 | 72.2 | 72.2 |
| K15hv125 | 4 | 0.085 | 8.02·X^0.34, $r^2$=0.49 | 0.55 | 71.7 | 73.6 |
| K15hv150 | 5 | 0.088 | 8.94·X^0.321, $r^2$=0.49 | 0.58 | 70.9 | 71.1 |
| K15hv200 | 6 | 0.101 | 7.51·X^0.34, $r^2$=0.69 | 0.56 | 62.8 | 61.3 |
| K3hv03 | 7 | 0.081 | 8.75·X^0.338, $r^2$=0.44 | 0.50 | 74.4 | 77.7 |
| K3hv07 | 8 | 0.094 | 9.45·X^0.322, $r^2$=0.42 | 0.55 | 65.4 | 67.1 |
| K3hv10 | 9 | 0.095 | 4.93·X^0.398, $r^2$=0.78 | 0.56 | 69.5 | 66.3 |
| K3hv125 | 10 | 0.094 | 10.28·X^0.30, $r^2$=0.44 | 0.58 | 68.3 | 67.3 |
| K3hv150 | 11 | 0.099 | 10.58·X^0.295, $r^2$=0.44 | 0.56 | 66.4 | 63.7 |
| K3hv200 | 12 | 0.107 | 6.27·X^0.358, $r^2$=0.73 | 0.51 | 62.8 | 58.8 |
| K45hv03 | 13 | 0.083 | 12.88·X^0.28, $r^2$=0.46 | 0.50 | 74.2 | 75.8 |
| K45hv07 | 14 | 0.093 | 11.68·X^0.285, $r^2$=0.50 | 0.47 | 60.2 | 64.0 |
| K45hv10 | 15 | 0.09 | 5.61·X^0.375, $r^2$=0.75 | 0.56 | 75.3 | 68.9 |
| K45hv125 | 16 | 0.101 | 12.76·X^0.270, $r^2$=0.46 | 0.57 | 67.2 | 62.3 |
| K45hv150 | 17 | 0.107 | 12.26·X^0.272, $r^2$=0.43 | 0.55 | 65.7 | 58.9 |
| K45hv200 | 18 | 0.119 | 6.79·X^0.348, $r^2$=0.72 | 0.52 | 62.2 | 53.0 |
| *Actual Topography* | | | | | | |
| Homogeneous | AH | 0.113 | 2.23·X^0.503, $r^2$=0.92 | 0.46 | 62.7 | 56.4 |
| K3hv03 | 19 | 0.127 | 2.93·X^0.458, $r^2$=0.9 | 0.47 | 58.1 | 50.2 |
| K3hv07 | 20 | 0.147 | 4.94·X^0.39, $r^2$=0.91 | 0.43 | 53.8 | 43.1 |
| K3hv10 | 21 | 0.156 | 3.73·X^0.435, $r^2$=0.93 | 0.42 | 53.5 | 40.8 |
| K3hv125 | 22 | 0.162 | 4.54·X^0.406, $r^2$=0.9 | 0.42 | 52.3 | 39.8 |
| K3hv150 | 23 | 0.177 | 2.90·X^0.467, $r^2$=0.91 | 0.41 | 50.6 | 36.9 |
| K3hv200 | 24 | 0.182 | 3.26·X^0.453, $r^2$=0.93 | 0.40 | 46.2 | 35.9 |
| Deep Aquifer | DH | 0.105 | 3.96·X^0.418, $r^2$=0.87 | 0.34 | 77.8 | 54.9 |
| Shallow Aquifer | SH | 0.132 | 2.80·X^0.466, $r^2$=0.91 | 0.42 | 47.1 | 57.8 |

[1] Nomenclature used to refer to heterogeneous scenarios, e.g. K15hv03 for $I_{xy}$=150m; $\sigma_Y^2$ =0.3

[2] correlations are all significant ($p$<0.001).

[3] wMTT: mean travel time, taken as median from the travel time CDF.

### Haitjema's Method

Haitjema (*1995*) developed an analytical solution for the distribution of residence times in a groundwatershed. As summarized in section 1.3.1, this method depends on porosity (θ), aquifer depth (i.e., H, saturated thickness), and recharge rate ($r$), following the expression:

$$F(\mathrm{t}) = 1 - \exp\left(-\frac{\mathrm{t}}{\overline{\mathrm{T}}}\right); \text{where } \overline{\mathrm{T}} = \frac{\theta \mathrm{H}}{r}$$

The correction to this equation for unconfined conditions was not used here as the ratio of $r$[m/s]/$K_{avg}$[6.09x10$^{-5}$m/s]= 1.2x10$^{-4}$ is similar to the case plotted in his Figure 7a ($r/K_{avg}$ = 1.0x10$^{-4}$) in which the unmodified equation can be used to approximate the actual residence time distribution. Considering the subsurface parameters used in the numerical models for θ (0.35) and $r$ (6.5e-4 m/d), and the saturated thickness estimated from the FEFLOW steady state model, H, the TTD for the AH, DH, and SH scenarios was estimated with the expression above (Figure A4a). Haitjema (*1995*) demonstrated that the MTT for the groundwatershed, given by the centroid of the area above the curve, corresponds to $\overline{\mathrm{T}}$. The wMTTs estimated from the Haitjema method were overestimated by 85% (AH), 158% (DH), and 52% (SH) with respect to the target set by the numerical model (Figure A4b). Notwithstanding this overestimation, the wMTT values are positively correlated with the increase and decreased in wMTT to changes to a deeper (DH) and a shallower (SH) aquifer is modeled in FEFLOW. Although, specifically including aquifer depth in his mathematical expression, the assumption of a constant θH/r ratio everywhere in the watershed does not hold for Alder Creek.

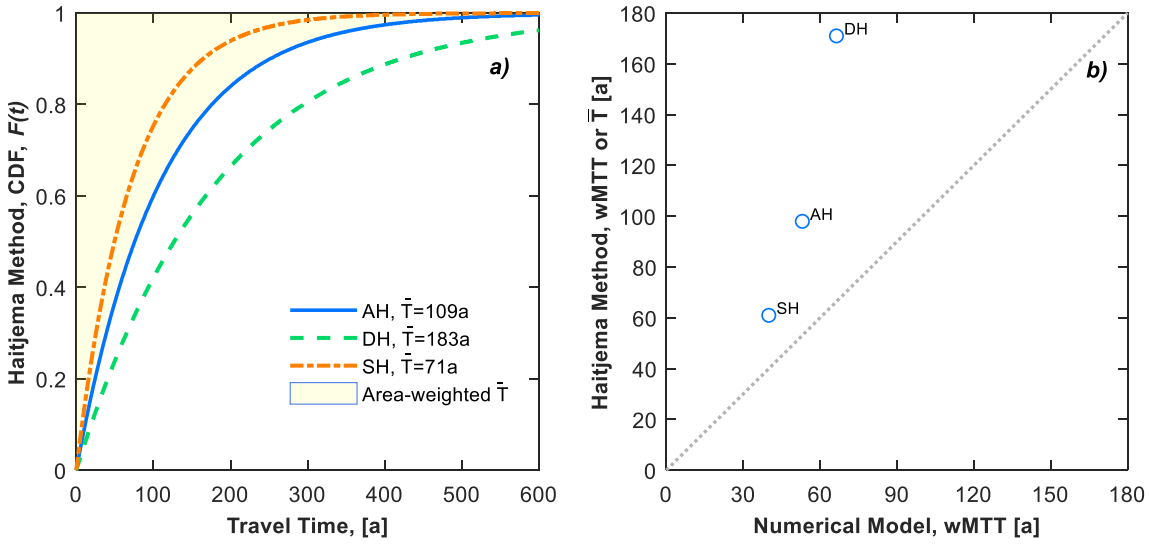


Figure A4. Travel time distributions for AH, DH, and SH scenarios using the Haitjema (*1995*)'s method (a), and their associated MTT (or $\overline{T}$) estimates compared to the numerical output (b).

### Flow Path Analysis on Selected Transects for Homogeneous Cases

The use of individual stream traces from the numerical model (FEFLOW) has proven to be somewhat unreliable (see Section 5) when defining a potential water particle flow path, especially, in heterogeneous domains. However, the homogeneous case, as discussed before, is not subjected to interception in low permeability zones disconnected from fully saturated groundwater tables. Thereby, flow paths along seven transects in the watershed are evaluated in scenarios RH, AH, DH, and SH to further discuss the influence of topography and subsurface geometry (Figure A5). The seven transects along with their respective flow paths were delineated using the reduced topography model. Therefore, the stream traces for the reduced topography model (RH) are used as reference for comparison with the traces from the AH and DH scenarios. Traces for scenario SH are not shown for clarity as they mostly fall in between the RH and AH traces. The transects are defined so that the points of discharge of the chosen set of flow paths did align as close as possible. For all transects and scenarios considered, except for transects 1 and 6, their three-dimensional trajectory ended at a point of discharge downstream from that of the reduced topography, seemingly

favoring longer flow patterns. For transect 6, however, the actual topography and applied aquifer depth have forced its flow paths to discharge at a location upstream. The three flow paths with the northernmost entry points completely miss the stream intersection, resulting in very long flow paths ending in points of discharge much further downstream. Flow paths in transects 3 and 4 exhibited greater trajectory variations (Table A2) from this visual top perspective. The difference in elevation along the transects varies from 14.0 m to 27.0 m, for transect 5 and 4, respectively; yielding for the latter the largest slope from all transects (1.79%) with reduced topography. Transect 1 and 7 have a similar elevation difference, however, the slope is 50% larger in transect 7 as its total length is shorter, which (Figure A5**)** is not so evident. The transects on the east bank of the river's main stream have the highest slopes. A similar analysis applies to the actual topography model as these variables are proportional to the difference in topography, except for the mean stream trace length (Mean X). This variable slightly decreased for transect 6 and remained constant for transect 5; whereas, it increases for all other transects by as much as 41% and 33%, for transects 3 and 4, respectively. The longer flow paths in the AH scenario, according to these data, are attributed mainly to the effect of higher topography and greater hydraulic head, forcing the system to find equilibrium within a new groundwater flow by diverging into zones that will intercept other, often farther, points of discharge.

In order to tie this flow path evaluation with the proposed analytical approach for all four homogeneous models, the flow path distances are compared against the respective stream trace distance; also, the estimated mean travel time from the analytical approach is compared against that from the numerical model for all flow paths, and for each transect (Figure A6). The scale of correlation between the compared parameters from the analytical and numerical approaches is highly variable (Figure A6). Transects 1, 2, 5, and 7 exhibited a good correlation between the methods, for both parameters (flow path distance and mean travel time); whereas, transects 3, and 6 exhibit an acceptable correlation that is conditioned to a subset of flow paths within each transect. In general, a good agreement of the flow path distance parameter in the analytical approach with the numerical counterpart guarantees a similar correlation on the mean travel time plot. Besides calibrating $U_0$ in the analytical

model, it is the assignation of an adequate flow path distance to each observation point that provides an equally adequate spread of ages for the transects evaluated, and for the watershed as a whole.

Table A2. Transects topographic information as well as their respective mean flow path distance derived from stream traces in homogeneous models.

| Transect (n) | Length [m] | Reduced Topography (RH) | | | | Actual Topography (AH) | | | |
|---|---|---|---|---|---|---|---|---|---|
| | | Mean X [m][1] | Slope | Mean Z [m] | ΔZ [m] | Mean X [m][2] | Slope | Mean Z [m] | ΔZ [m] |
| 1 (13) | 3114 | 1526 | 0.60% | 332.3 | 19.8 | 1732 | 1.20% | 378.7 | 39.3 |
| 2 (11) | 2619 | 1368 | 0.55% | 327.2 | 16.7 | 1504 | 1.09% | 368.7 | 33.2 |
| 3 (6) | 1438 | 1119 | 1.45% | 324.8 | 20.7 | 1583 | 2.87% | 363.9 | 40.8 |
| 4 (7) | 1702 | 1190 | 1.79% | 323.7 | 27.0 | 1585 | 3.55% | 361.7 | 53.7 |
| 5 (11) | 3607 | 2145 | 0.35% | 320.7 | 14.0 | 2146 | 0.70% | 355.8 | 27.8 |
| 6 (11) | 2704 | 1788 | 0.65% | 320.5 | 14.9 | 1739 | 1.32% | 355.4 | 29.7 |
| 7 (9) | 2161 | 1287 | 0.88% | 311.7 | 21.8 | 1563 | 1.75% | 337.9 | 43.2 |

[1] mean stream trace length for all transects is 1489 m.
[2] mean stream trace length for all transects is 1693 m.

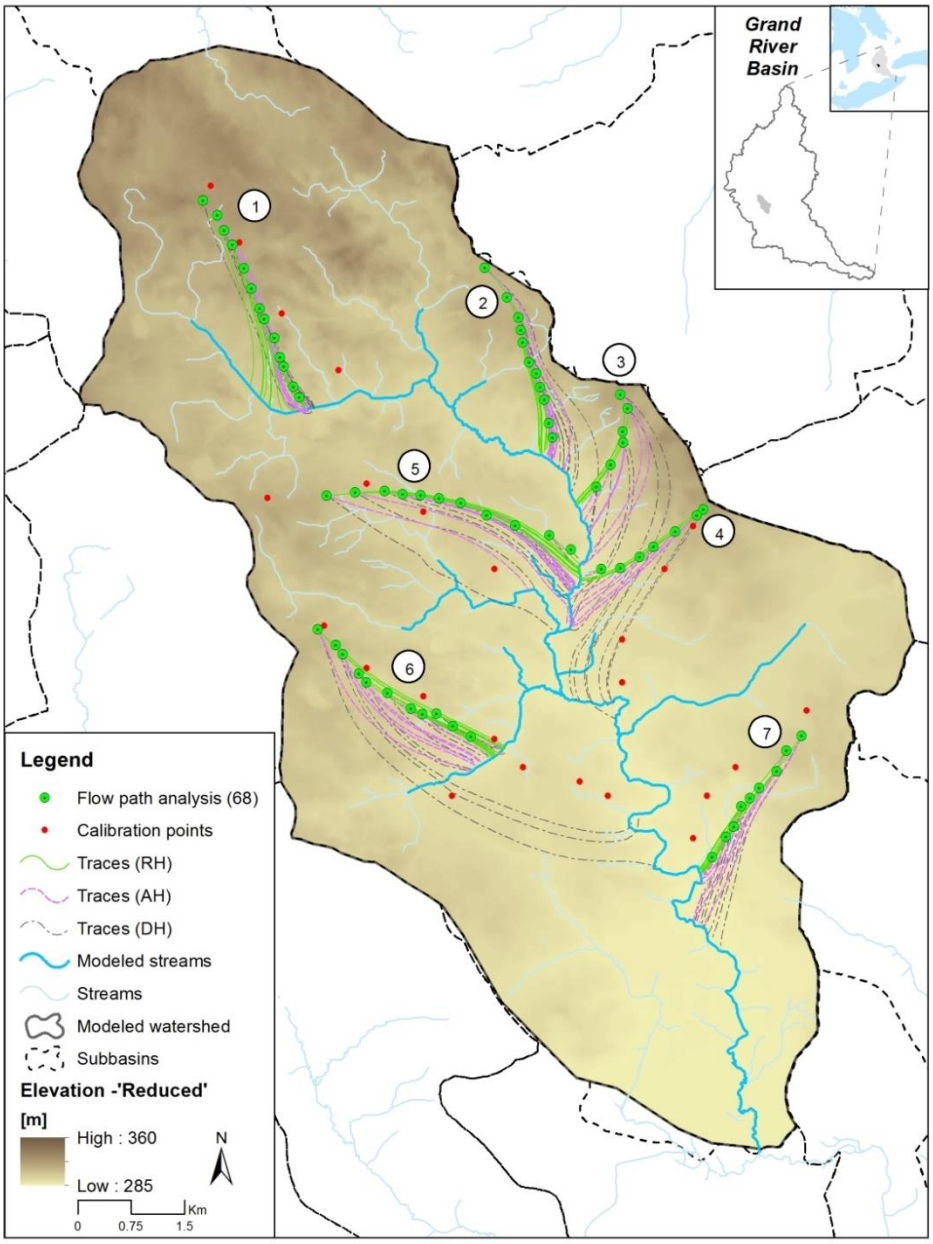


Figure A5. Location of transects for which a flow path analysis was performed based on the stream traces obtained from homogeneous model scenarios RH, AH, and DH in FEFLOW.

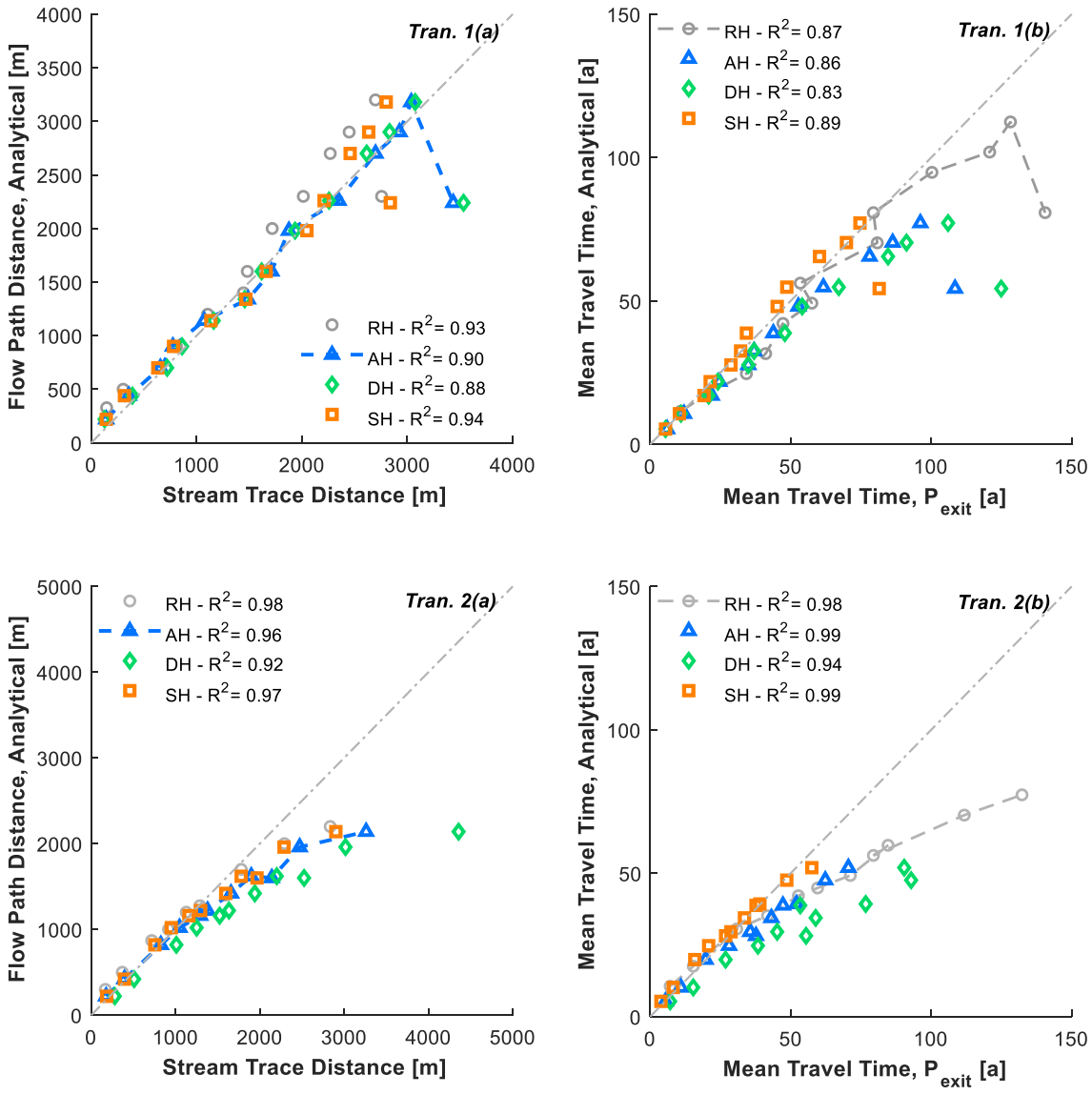


Figure A6a. Analytical (a) flow path distances and (b) pMTTs are compared against their numerical estimates for transects 1 and 2.

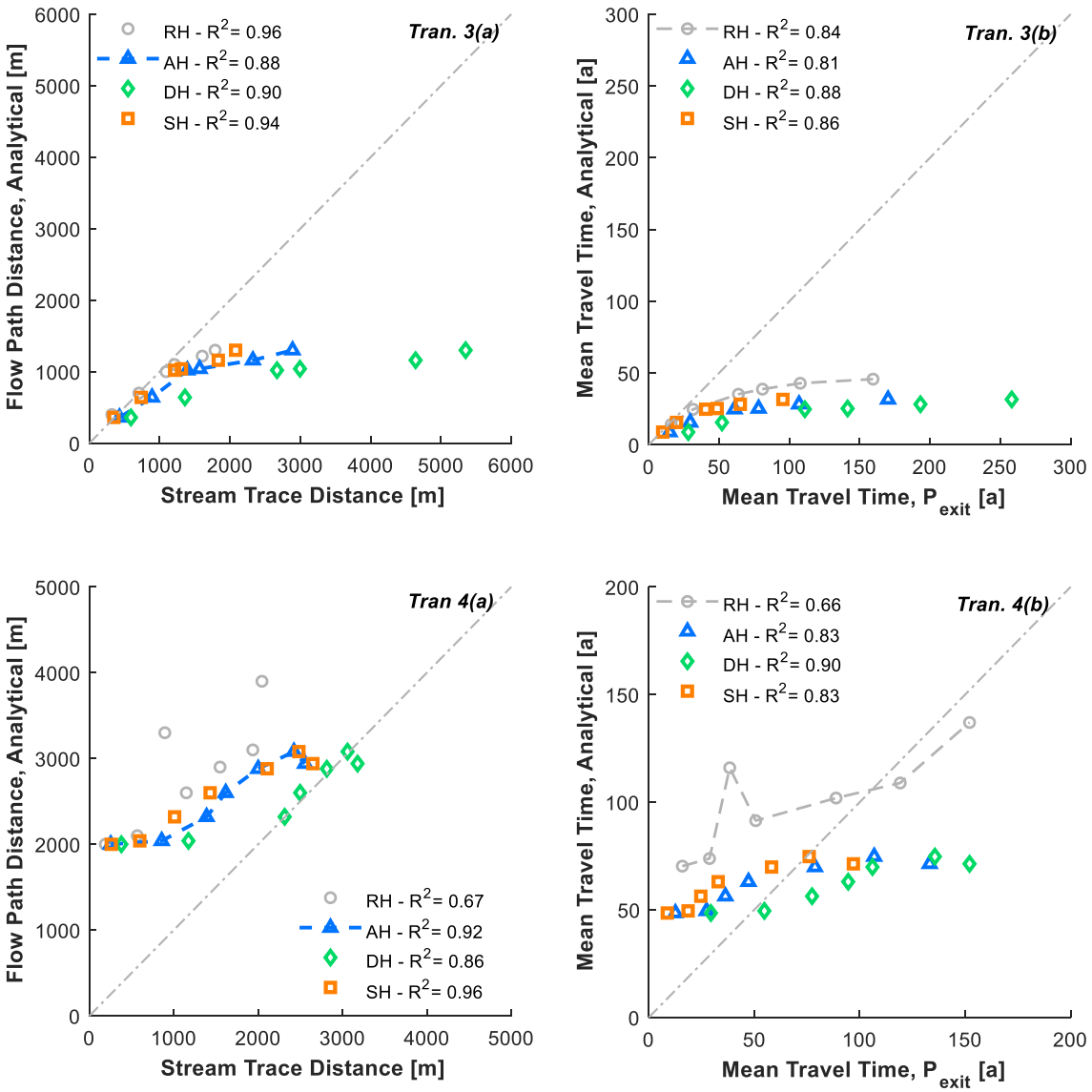


Figure A6b. Analytical (a) flow path distances and (b) pMTTs are compared against their numerical estimates for transects 3 and 4.

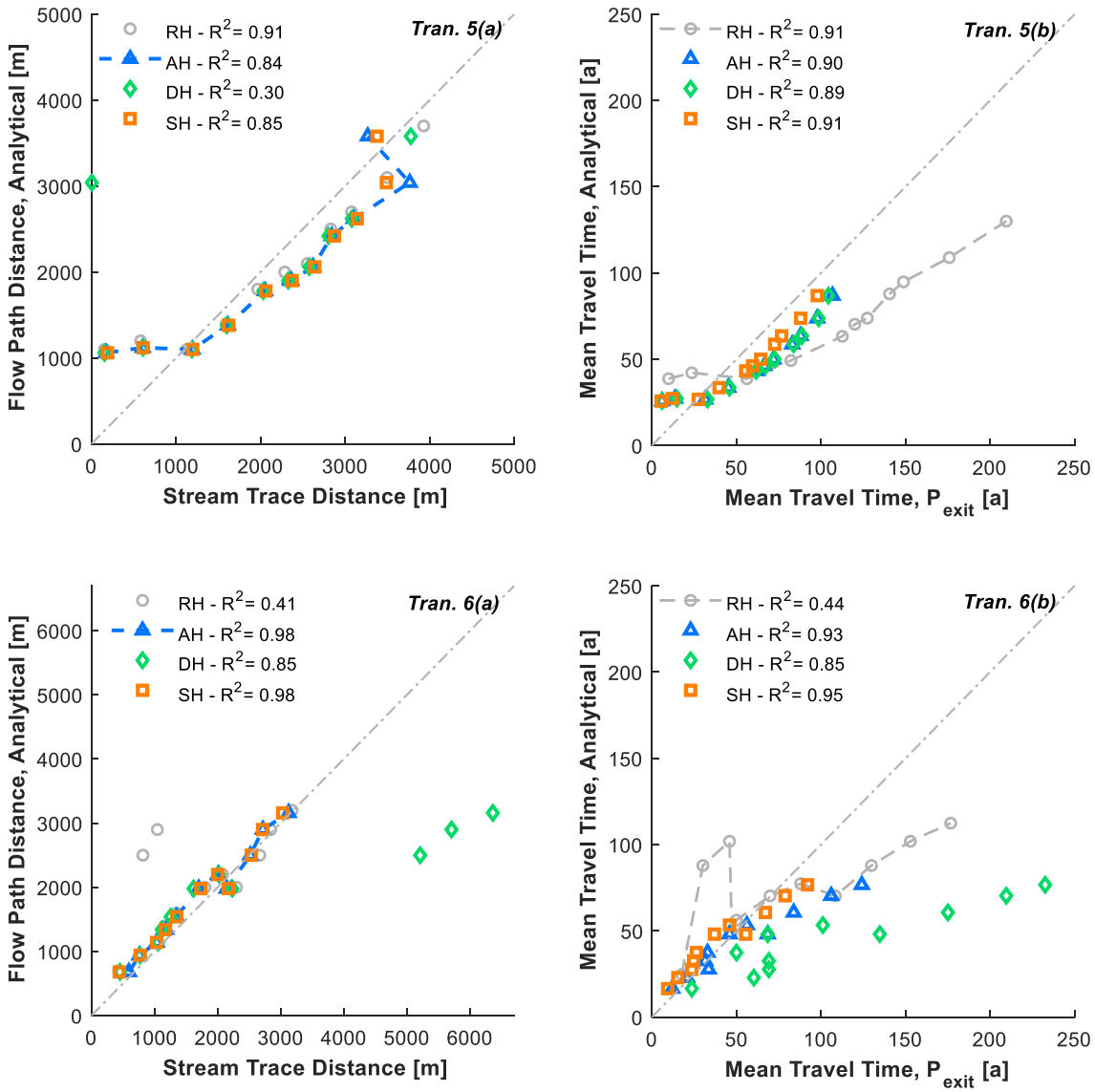


Figure A6c. Analytical (a) flow path distances and (b) pMTTs are compared against their numerical estimates for transects 5 and 6.

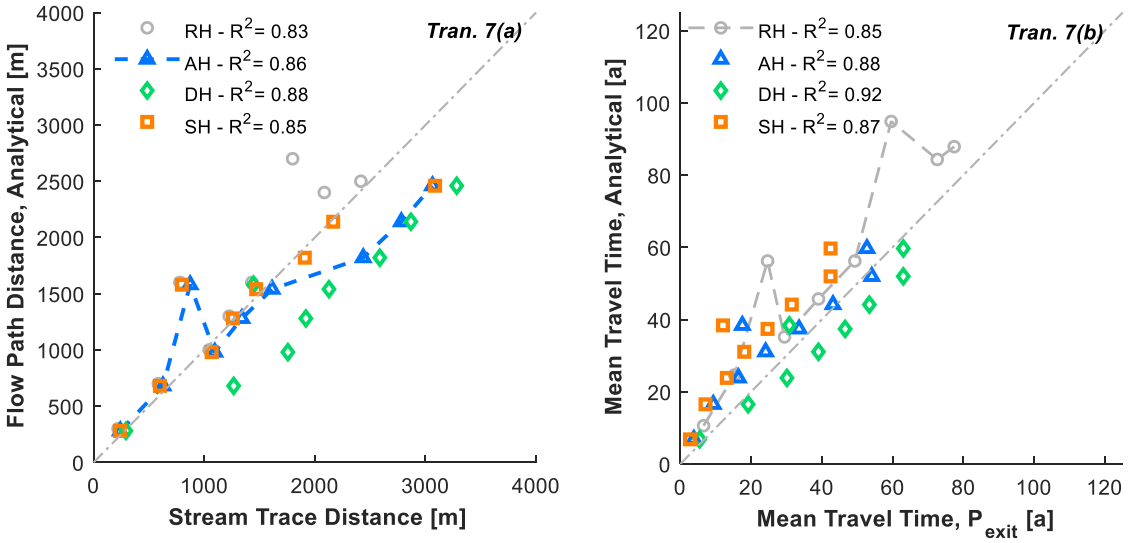


Figure A6d. Analytical (a) flow path distances and (b) pMTTs are compared against their numerical estimates for transect 7.

Transect 3 is located in an area that has been previously identified as problematic for the analytical method to reproduce the numeric model's estimates of travel time. The fact that not only for the heterogeneous (Figure 2-5b, Figure 2-7b) but also for the homogeneous case (Figure A6b) the problem persists is indicative that issues other than topography and subsurface geometry are at play to explain both the degree of underestimation by the analytical method and the wide range of travel times predicted by the numerical model. Note that in panel (a) for this transect, the stream trace distance in the RH scenario for the last observation point is approximately 1900 m, which was moderately underestimated by the analytical method with 1300m. However, this under-estimation grows larger for the AH model and even more for the DH scenario, making the difference in travel times estimated from both methods to grow proportionally. From all the homogeneous scenarios SH is the one that is least affected by underestimation. Therefore, it is a combination of the watershed geometry and the location of this area with respect to the dominant regional groundwater flow that creates the disparity in flow path lengths and travel times along transect 3. The deviation caused by regional groundwater flow pattern is especially reinforced in the DH

scenario, likely due to the enhanced momentum exerted by a larger water mass. However, if the transect was drawn in a more extensive regional model, and considering that the deviation of the flow paths occurred largely on the last two observation points of the transect, that is, at the edge of the model's boundary, these flow paths would have likely discharged into another stream outside the Alder Creek watershed. For the current model, this general area seems to be 'compressed' towards the model boundary by the incoming groundwater from the northwest portion of the watershed driven by a locally deep groundwater table. Regional groundwater flow is not at play in areas located west highlighted for scenario 24 ($I_{xy}$=300m, $\sigma_Y^2$ =2.0), for 'location set 2' (Figure 2-7b). Then it is both heterogeneity and regional groundwater flow that are creating the largest disparities between stream traces distances and travel times in the numerical model. These disparities lead to underestimations in travel time using the analytical model.

In transect 4, the correlation is the worst of all, and it does not depart from nowhere near the origin, indicating that the flow direction of the entire transect was not captured by the analytical method by any of the flow paths. Likewise, in transect 5, this also occurs for the first two flow paths closer to the point of discharge, however, the flow path length correlation improves significantly for locations farther away from it. In this transect, almost undiscernible changes in flow paths for the RH scenario, created a significant difference in travel times from other actual topography scenarios, which in turn, provided similar travel times all along the transect regardless of the subsurface geometry applied to them. This indicates that this region is strongly controlled by topography, and potentially by heterogeneity, which is not evaluated in this section. The effect of geometry is mostly evident at mid-range and longer travel times (see transects 1, 2, 6, and 7), which is expected considering the lengths of their stream traces and the likelihood of sensing the aquifer depths along their trajectory. Especially in transect 6 this observation is more evident for the last three flow paths, where they intercept a surface water feature located further downstream from the point of discharge of other flow paths, yielding longer travel times (Figure A6c).

The analytical method applies one single bulk velocity ($U_o$) to the entire watershed which may result in a different response at various locations in the watershed. The effect of this response on each transect can be seen in the plots comparing median travel times. Those observation points with travel times depicting a trend line with slope lower than unity (1:1) would have required a lower bulk velocity; whereas, a larger slope means that a lower velocity would have been a better fit locally. The areas that would require a lower bulk velocity for better agreement in median travel times are those around transect 4 and 6, both located east and west at the middle of the watershed.

In summary, after considering correcting analytical flow paths for potentially strong deviation caused by regional groundwater flows, there is a relatively good agreement between the methods at the transect scale, for all transects except for transect 4 that systematically missed the local groundwater flow direction.

# Appendix B

# Supplementary Material: Chapter 3

## Introduction

The supplementary material provides further analysis on: i) multiple linear regression models applied to both analytical model parameters (i.e., *SF*, *Uo*, *a*, and *a·b*), ii) wMTT using geomorphological indexes from study sites as predictors, iii) the performance of the analytical method with respect to the approach developed by Haitjema (*1995*). In addition, this supplementary material also includes figures of some of the geomorphological indexes estimated from study sites. The material herein is presented in the order as it was introduced in the main text.

## Geomorphological Features as Predictors of Analytical Model Performance

In order to ease future implementations of the analytical model used here, the geomorphological indexes (Table 3-2) were used as predictors of its potential performance, once implemented. This was accomplished by plotting the estimates of these indexes (Table B1) against the goodness of fit ($r^2$) between the numerical and analytical pMTT. It was sought to identify ranges in these indexes estimates where the analytical model would yield an acceptable performance. In practice, this meant defining a range of values that excluded the hillslope-dominated watersheds: Thomas Creek (ThC), Rattlesnake Flat (Rat), and Pamilco Canyon (Pam). A small portion of indexes yielded an exclusive range, whereas others either yielded a non-exclusive range or did not show any discernable pattern. A non-exclusive range is that where either one of the hillslope-dominated watersheds is within the range of values or one of the watersheds with acceptable performance does not fall within the specified range. This non-exclusivity adds a degree of uncertainty to the prediction of acceptable performance.

Table B1. Estimates of geomorphological indexes for study sites. For details in their definition and estimation refer to Table 3-2 and section 3.2.3 in the main text.

| *Index* | des Anglais River | Ganaraska River | Alder Creek | Upper Laurel Creek | Upper Nith River | Pamilco Canyon | Rattlesnake River | Sagehen River | Thomas Creek |
|---|---|---|---|---|---|---|---|---|---|
| *ID* | dAn | Gan | Alc | uLc | uNr | Pam | Rat | Sag | ThC |
| *Dd* [$km^{-1}$] | 1.51 | 0.60 | 1.79 | 1.47 | 1.32 | 2.66 | 4.88 | 1.28 | 1.28 |
| *Tex* [$km^{-1}$] | 1.01 | 0.25 | 0.71 | 0.57 | 1.02 | 1.91 | 2.97 | 1.02 | 1.45 |
| *DF* [$km^{-2}$] | 2.71 | 0.46 | 2.79 | 0.90 | 3.72 | 6.20 | 25.1 | 1.13 | 1.57 |
| *HDd* [-] | 0.011 | 0.006 | 0.028 | 0.162 | 0.087 | 0.121 | 0.200 | 0.008 | 0.006 |
| *Relief* [m] | 121 | 373 | 317 | 1065 | 927 | 790 | 1211 | 73 | 66 |
| *TexPer* [$km^{-1}$] | 0.57 | 0.22 | 0.50 | 0.39 | 0.74 | 1.44 | 2.51 | 0.27 | 0.58 |
| *MnChL* [m] | 25550 | 71690 | 45199 | 26461 | 12379 | 11800 | 41665 | 11512 | 37461 |
| *cSlope* [deg] | 2.57 | 1.04 | 3.67 | 9.53 | 11.7 | 8.62 | 15.4 | 3.27 | 1.17 |
| *Schan* [%] | 1.05 | 0.9 | 1.66 | 4.11 | 6.78 | 8.13 | 8.09 | 2.26 | 0.58 |
| *mGrad* [%] | 0.79 | 0.94 | 1.01 | 5.10 | 9.11 | 8.00 | 3.70 | 0.88 | 0.25 |
| $R_C$ [-] | 0.23 | 0.07 | 0.11 | 0.19 | 0.37 | 0.45 | 0.13 | 0.38 | 0.11 |
| $P_{LR}$ [-] | 0.67 | 0.57 | 0.59 | 0.72 | 0.76 | 0.84 | 0.73 | 0.64 | 0.57 |
| *FormF* [-] | 0.33 | 0.45 | 0.28 | 0.31 | 0.48 | 0.38 | 0.19 | 0.45 | 0.42 |
| *Er* [-] | 0.58 | 0.67 | 0.53 | 0.56 | 0.69 | 0.62 | 0.43 | 0.67 | 0.65 |
| *C* [-] | 6.06 | 6.57 | 7.15 | 5.75 | 4.87 | 4.63 | 6.76 | 5.84 | 6.70 |
| *RDV* [km] | 0.65 | 0.82 | 0.62 | 0.68 | 0.88 | 0.80 | 0.42 | 0.83 | 0.77 |
| $D_{BCst}$ [1/m] | 1.671 | 1.556 | 1.518 | 1.728 | 1.619 | 1.803 | 1.801 | 1.669 | 1.762 |
| $d_{BCst}$ [1/m] | 1.054 | 1.037 | 1.078 | 1.034 | 1.029 | 1.085 | 1.143 | 1.082 | 1.050 |
| $D_{BCp}$ [1/m] | 0.741 | 0.630 | 0.760 | 0.733 | 1.094 | 1.054 | 0.560 | 0.953 | 0.812 |
| $D_{WDp}$ [1/m] | 1.057 | 1.061 | 1.059 | 1.034 | 1.038 | 1.042 | 1.046 | 1.061 | 1.041 |
| *LnkSlp* [%] | 0.48 | 0.40 | 0.54 | 0.70 | 0.80 | 0.37 | 0.33 | 0.76 | 0.61 |
| $R_B$ [-] | 2.8 | 3.9 | 3.1 | 3.8 | 5.7 | 3.3 | 3.7 | 5.1 | 2.6 |
| $R_L$ [-] | 2.6 | 3.2 | 3.3 | 6.6 | 9.7 | 4.7 | 4.6 | 2.8 | 3.0 |
| $R_S$ [-] | 3.6 | 4.7 | 4.6 | 3.0 | 3.9 | 3.4 | 3.4 | 4.5 | 4.4 |
| *LvAa* [-] | 0.92 | 0.92 | 0.89 | 0.80 | 0.93 | 0.78 | 1.16 | 1.00 | 1.13 |
| *LvAb* [-] | 0.75 | 0.70 | 0.73 | 0.72 | 0.69 | 0.78 | 0.61 | 0.71 | 0.63 |
| *LvAab* [-] | 0.69 | 0.64 | 0.65 | 0.58 | 0.64 | 0.61 | 0.71 | 0.71 | 0.71 |

## Texture Topography

Not all the texture topography indexes behave similarly with respect to the performance of the analytical model. Texture ratio (*Tex*), for instance, did not exhibit a discernable pattern (Figure B1a), whereas *Dd* (Figure 3-6b) did (*Dd*<2.7 [1/km]), even though *Tex* is clearly related to *Dd* (Figure 3-6c).

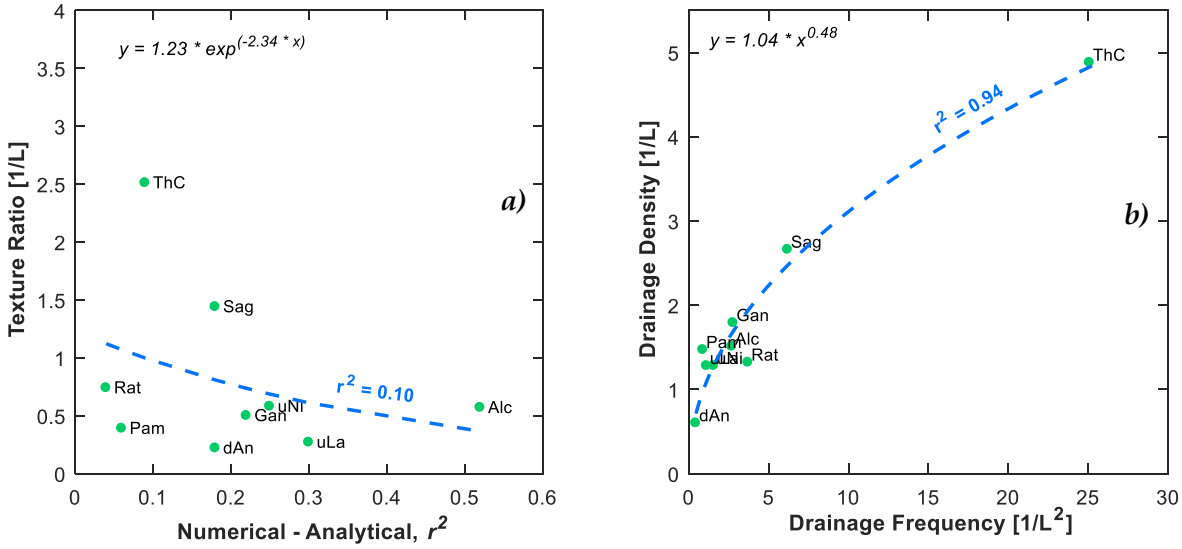


Figure B1. a) Relationship between texture ratio (*Tex*) and the goodness of fit between numerical and analytical models, and, b) relationship between *Dd* and *DF*.

**Elevation Measures**

The frequency of occurrences of the DEM-cell size slopes within the watershed can show both the shape distribution of slopes present and the range of the most dominant slopes that could be controlling how the analyticam method performs. These histograms are shown here in terms of probability of occurrence (Figure B2, Appendix B). The study watersheds exhibit a wide variety of spectra of slopes. The histograms vary from clear narrow peaks to very flat and even distributions. For the latter case, Thomas Creek is unique among these watersheds and shows a flat distribution. The modes of the distribution for Pamilco Canyon, Rattlesnake Flat, and Sagehen River are around 3, 4, and 5 degrees, respectively. The distribution of DEM-cell size slopes for des Anglais River is almost exponential as most of its terrain is flat, only rising at by the headwaters around Covey Hill. Watersheds that yielded the best *NumAn* goodness of fit are mostly spread around lower DEM-cell size slopes (<2.5 deg). However, this geomorphological measure did not provide an exclusive range of DEM-cell size slopes.

The hypsometric curve is associated with the stage of the geological evolution of the watershed (Figure B3). This structural characteristic of the watershed, tells on the interaction of the geological forcings experienced by the watershed, namely: uplifting, tectonic-build-up, and erosion. A particular behavior of the hypsometric curves was not recognized in these watersheds.

The link concentration plot constitutes of a three-dimensional representation of texture topography (i.e., drainage density-related indexes), by examining how the density of streams changes with elevation. No distinctive region in this plot was dominated by high values of pMTT correlations between the numerical and analytical methods (Figure B4).

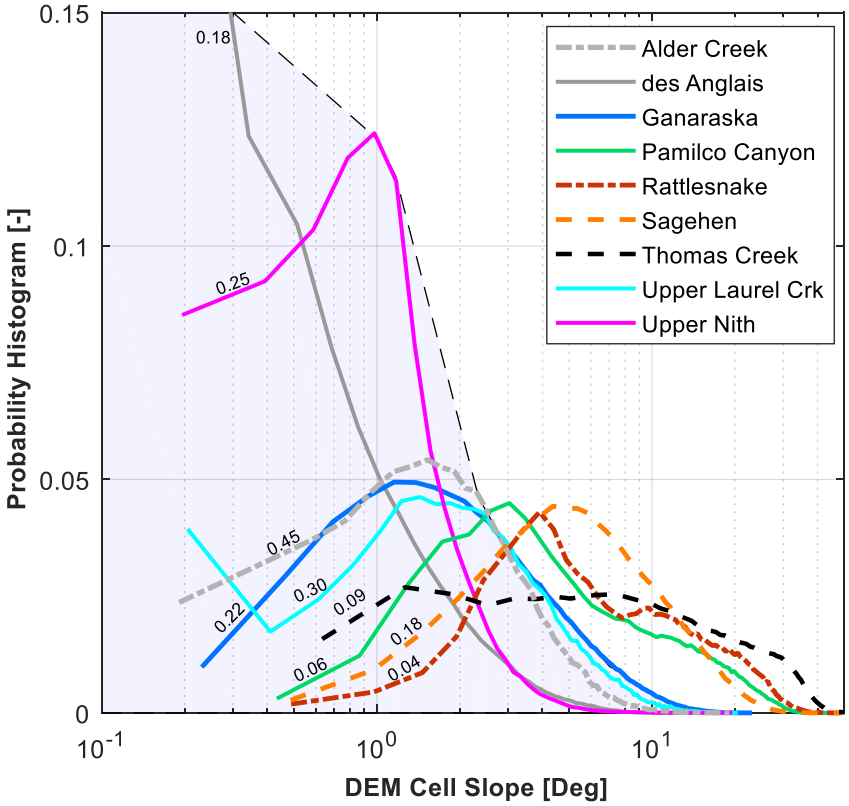


Figure B2. Probability histograms of slopes in degrees derived from available digital elevation model (DEM) data. The correlation between numerical and analytical model (*NumAn*) is shown on top of the curve. The region of best *NumAn* goodness of fit is highlighted in purple.

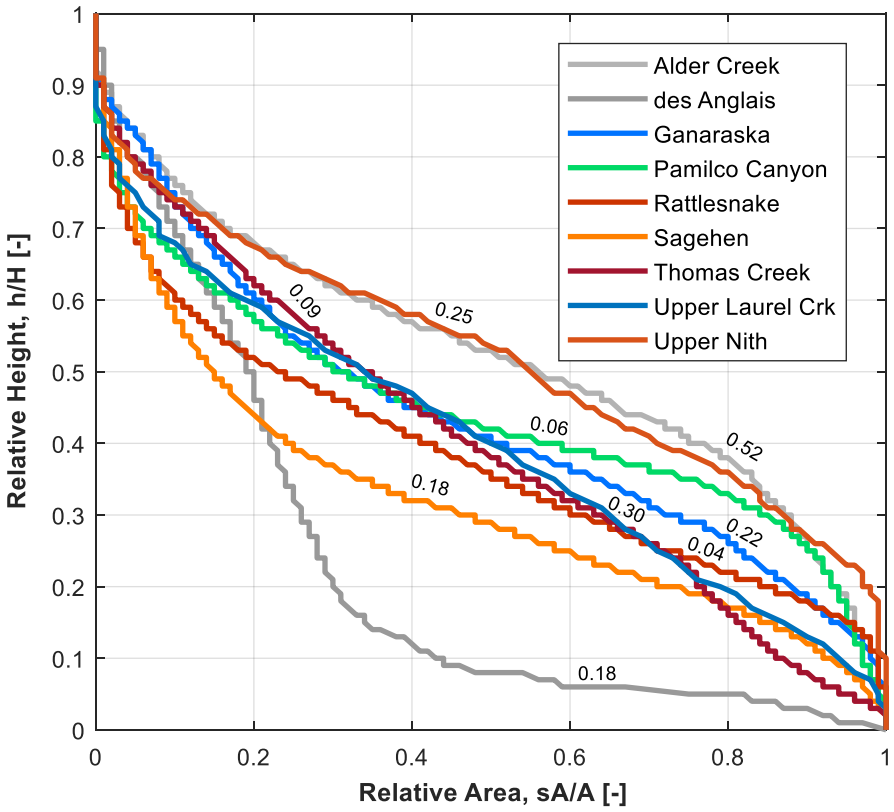


Figure B3. Hypsometric curves for study sites. Particle MTT correlations between numerical and analytical methods (*NumAn* correlations) are shown on top of respective curve.

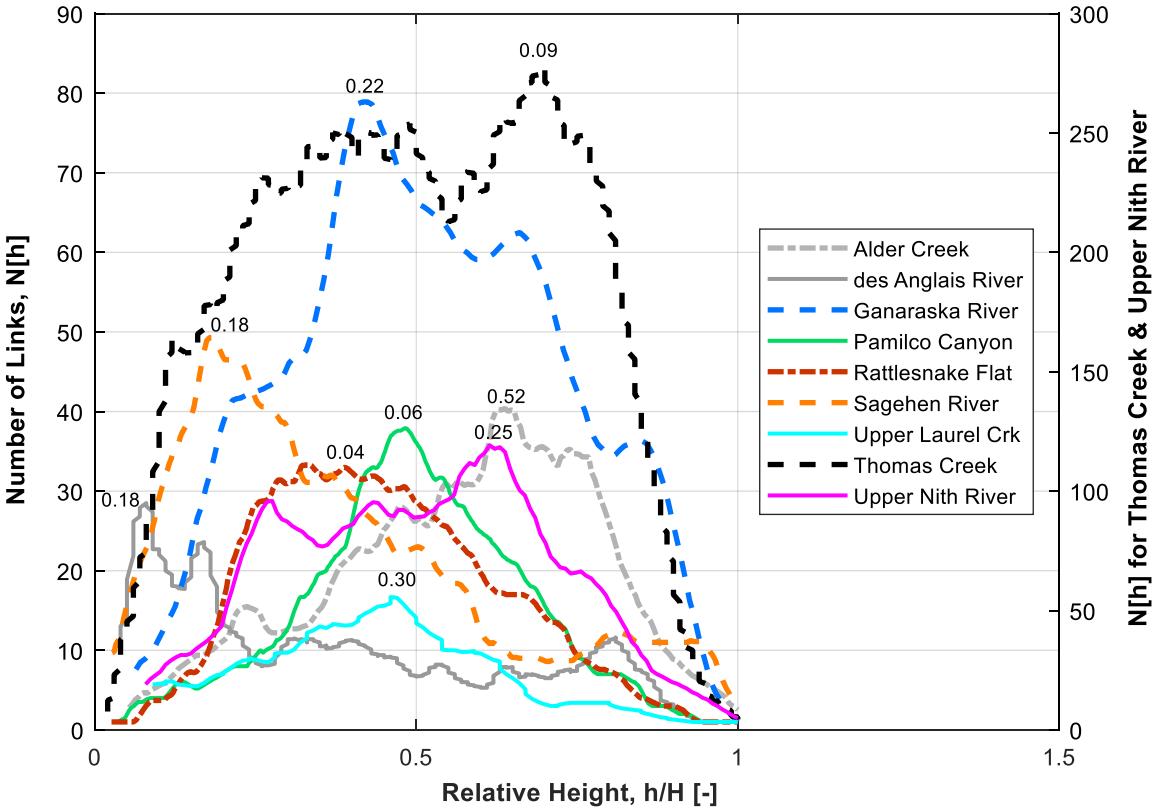


Figure B4. Link concentration plot for study sites. Particle MTT correlations between numerical and analytical methods (*NumAn* correlations) are shown at the peak of each curve.

## Shape Measures

Several shape measures have yielded non-exclusive ranges: $P_{LR}$, $Er$, $C$, and $RDV$ (Figure B5 and Figure B6). In two of these indexes, $P_{LR}$ and $C$, Sagehen River (Sag) has fallen outside of the non-exclusive range, sharing similar index estimates with hillslope-dominated watersheds. According to these indexes, Sag is the most compact among the examined watersheds, (i.e., lowest $C$ estimate) and its perimeter is the most similar to that of a lemniscate branch (i.e., closest value to unity). It is interesting to notice that Alder Creek (Alc) always occupies a median value in all shape measures and among all watersheds.

The lemniscate ratio ($P_{LR}$) was defined by Chorley et al. (*1957*) and involves in its calculation the area of the loop, the longest diameter of the loop ($l$), and the perimeter of the loop, which corresponds to a complete elliptic integral of the second kind:

$$P = 2l \int_0^{\pi/2} \sqrt{1 - K^2 sin^2\varphi}\ d\varphi$$

where, $K = \sqrt{(k^2 - 1)}/k$, $k = l^2\pi/4A$, and $\varphi$ varies from 0 to $\pi/2$ radians. This equation was solved using the function *ellipticE* in MATLAB. Another measure of compactness was applied, different from the perimeter-area ratio, called the relative distance variance (RDV). The RDV is a dispersion measure of compactness for which the shape of the watershed is comprised by infinitesimal elements of area $dA$ (*MacEachren, 1985*). Dispersion of these $dA$ elements is measured with respect to the watershed's centroid. In that, it is similar in physics to the moments of area, but an alternative formulation is used in terms of the variance of the distance of these elements in the $x$ and $y$ –direction:

$$RDV = \frac{A}{2\pi(\sigma_x^2 + \sigma_y^2)}$$

Where, $\sigma_x^2$ and $\sigma_y^2$ are the variance of the $x$ and $y$ distances to each $dA$ element.

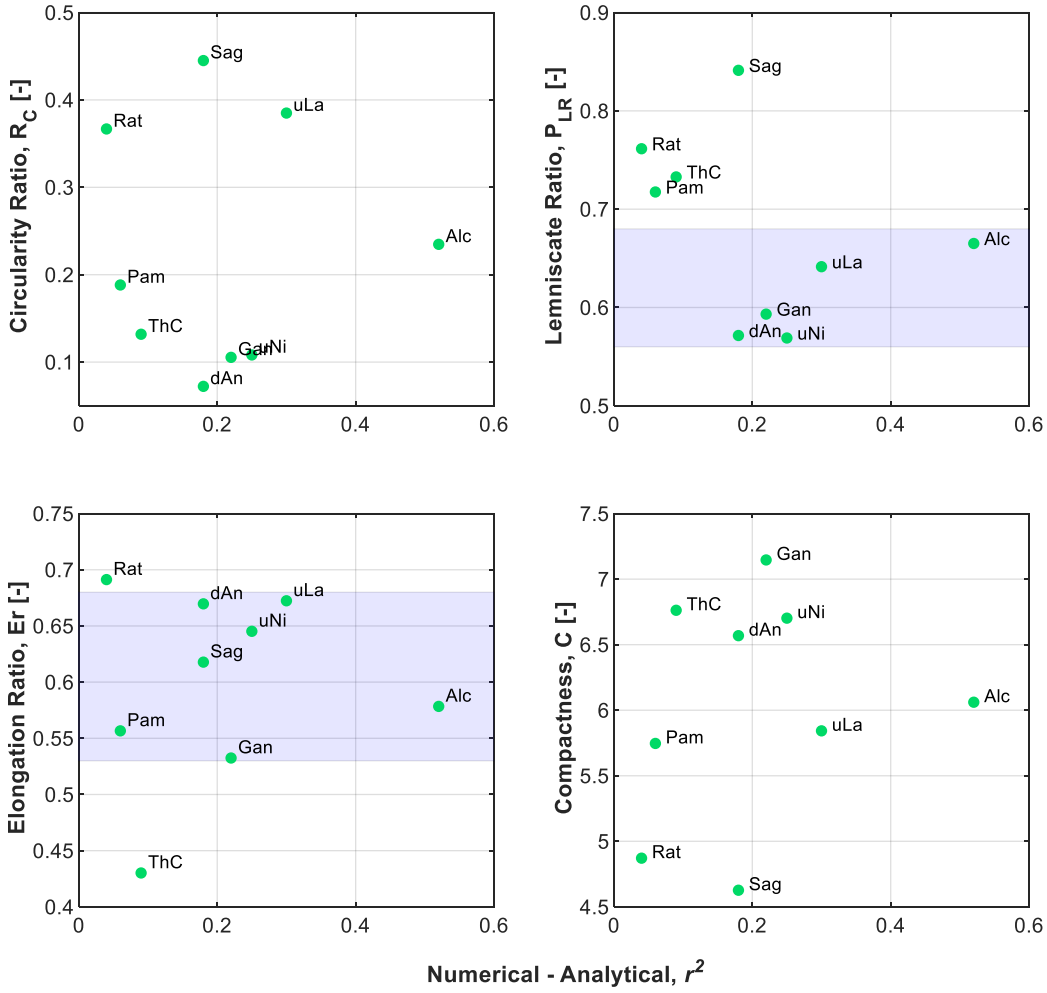


Figure B5. Measures of shape as determined by circularity ratio ($R_C$), lemniscate ratio ($P_{LR}$), elongation ratio ($ER$), and compactness ($C$) for study sites. Uncertain ranges of these parameters are highlighted in blue for values with best *NumAn* correlations.

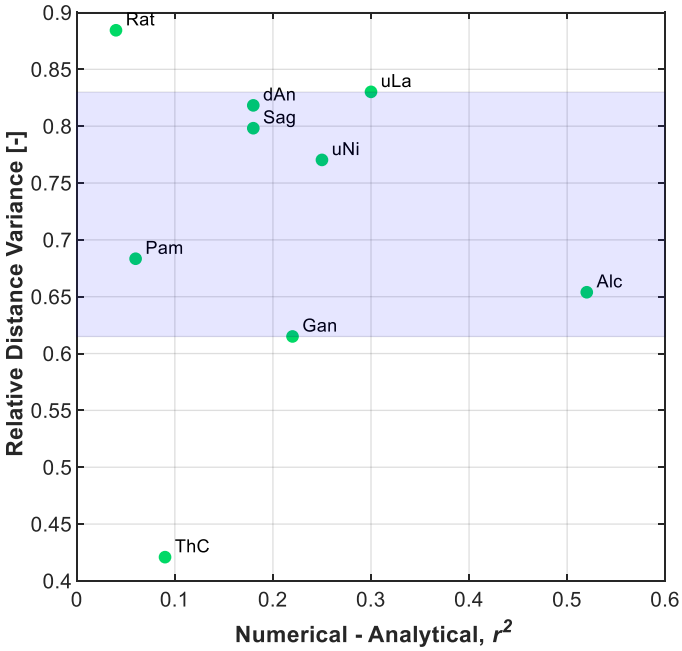


Figure B6. Measures of shape as determined by relative distance variance (*RDV*) for study sites. Uncertain ranges of these parameters are highlighted in blue for values with best *NumAn* correlations.

## Fractal Dimensions

The interpretation of fractal dimension of stream networks as classifying the feature as space-filling has been challenge by other researchers (*Phillips, 1993*; *Veltri et al., 1996*). Phillips (*1993*) suggested that the fractal dimension of stream networks does not have a physical representation on the processes occurring in geomorphic systems and that could rather be interpreted as a degree of geological constraints on network evolution. Other researchers (*Beauvais and Montgomery, 1997*) had also tested the principle of self-similarity in stream networks and found that they are not statistically self-similar at all scales but only at specific ranges. These earlier findings in mono-fractal analysis paved the way to develop a multifractal analysis that recognizes stream networks as multifractal objects, characterized by non-plane filling structures with a fractal dimension less than 2 (*De Bartolo et al., 2006a*; *De Bartolo et al., 2006b*). This multifractal analysis provides a whole array of fractal dimensions relative to multiple river structures, each yielding different scale patterns. This latter approach was not utilized here as it does not allow for simple response comparisons among watersheds relative to both *NumAn* goodness of fit and geomorphological parameters.

Fractal dimensions estimated with the box-counting method applied on streams ($D_{BCst}$, Figure B7) indicated that, under the umbrella of the space-filling theory, the stream networks of Thomas Creek (ThC) and Sag are the most space-filling among these watersheds. Whilst, Ganaraska River (Gan) and des Anglais River (dAn) are the least space-filling, meaning that their stream networks do not properly drain their drainage area. $D_{BCst}$ did not provide a range, exclusive or otherwise. The $D_{BCst}$ value of Alder Creek falls also within the median range of all watersheds.

The fractal dimension of the watershed's perimeter was estimated using: the box-counting method ($D_{BCp}$) and the walking-divider method ($D_{WDp}$) (Figure B8). The walking-divider method uses a chord length (step) and quantifies the number of chords required to cover the entire fractal curve. The result is an estimate of the length of the entire curve for a finite number of selected steps. Plotting the estimated length against the step size, the data

increasingly underestimates the total length as step size increases, depicting a negative slope with values slightly above unity. The slope of this line corresponds to the fractal dimension in the walking divider method ($D_{WDp,}$ Figure B8). From these methods, the most appropriate to define the fractal dimension for this feature is the walking-divider method. This method 'walks' the feature by also following changes in direction in a more rigorous fashion than the box-counting method could do.

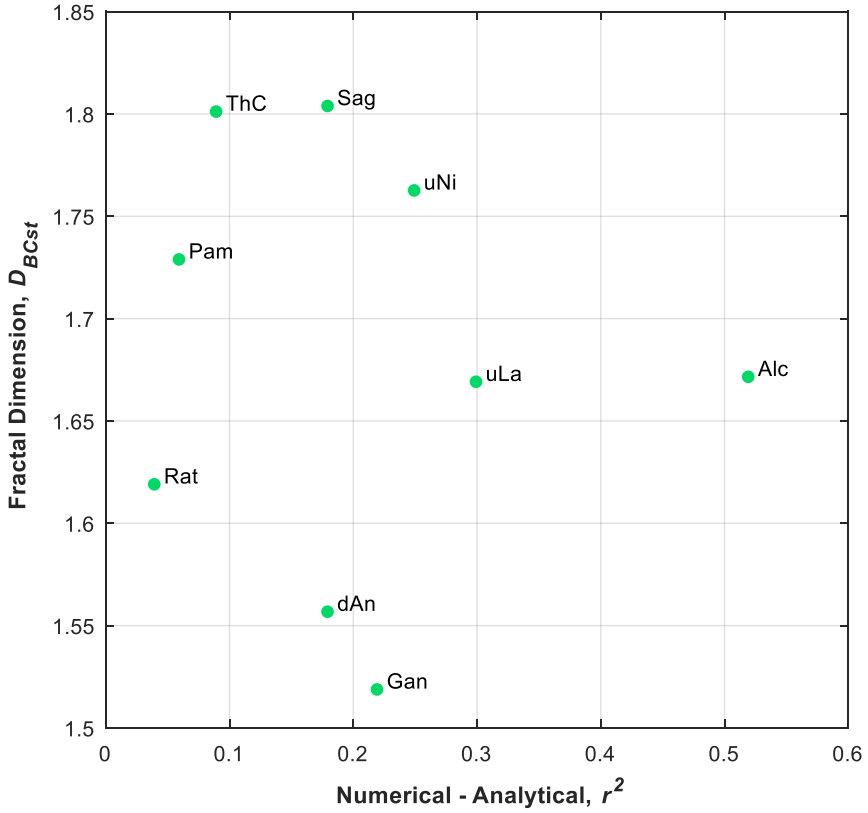


Figure B7. Mono-fractal dimensions estimated from the box counting technique ($D_{BCst}$) applied on stream networks. Values correspond to slopes of power function (exponent) fitted to the relationship: log $N_{boxes}$ vs. log Box size.

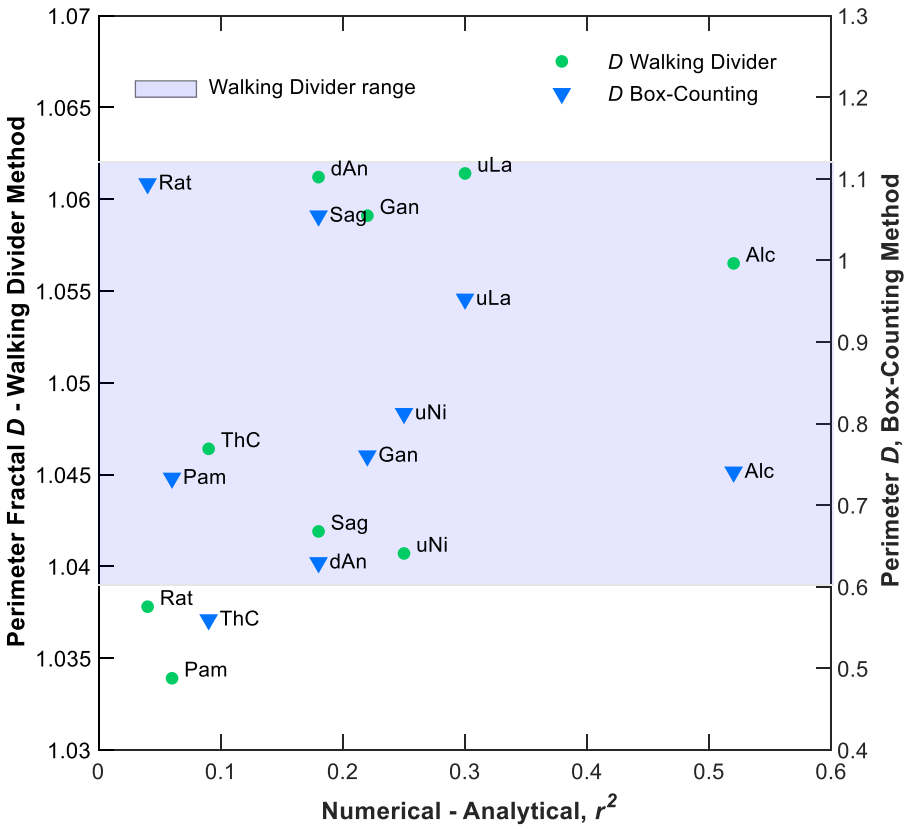


Figure B8. Mono-fractal dimensions estimated using the Walker Divider method, and the box counting technique applied on watershed's perimeter. Values correspond to slopes of power functions fitted to log Perimeter vs. log step size. A non-exclusive range for better *NumAn* correlation is highlighted based on the walking divider estimates.

## The Walking-Divider Method - MATLAB Code

This MATLAB code is based on the FORTRAN code put together by Lam and De Cola (*1993*) from previous work of other researchers.

```
load 'XY.mat'           % XY data matrix, x-coord and y-coord in 1,2
columns
IX= XY(:,1);
IY= XY(:,2);

%
================================================================================
SumCL=0;
```

```
% I=I+1;
X(1)=IX(1);
Y(1)=IY(1);
np=length(IX);           %number of points

for p=2:np
    X(p,1)=IX(p);
    Y(p,1)=IY(p);
%     if ~i==1
    X1(p-1,1)=X(p)-X(p-1);
    Y1(p-1,1)=Y(p)-Y(p-1);
    DIST(p-1,1)= sqrt(X1(p-1)^2 + Y1(p-1)^2);
    SumCL(p-1,1) = sum(DIST(1:end,1));
%     else
%     end
end

AVD=SumCL(end,1)/(np-1);
STDIST = sqrt((X(1)-X(np))^2 + (Y(1)-Y(np))^2);
SINUO = SumCL(end,1)/STDIST;

fprintf('No. of points = %f   Mean Distance = %f\n',np,AVD)
fprintf('Total Length = %f   Sinuosity = %f\n',SumCL(end,1), SINUO)

% Factor=input('\n Enter the starting Chord Length ==>> \n');
% READ(*,'(F)') FACTOR        FACTOR is variable in input file

NW=input('\nEnter number of walks  ==>> ');
% READ(*,'(I)') NW          NW not in input file.


% MEASURE THE TOTAL LENGTHS OF THE LINE WITH DIFFERENT DIVIDER OPENINGS

File6 = [];
% File6 columns:  'WALKS    CL  LOG(CL)  STEPS   LENGTH   LOG(LENGTH)'

CL = AVD*0.5;

for j=1:NW
    CL = CL*1.1;
    K=2;
    IPNUM = 0;
    X1 = X(K-1);
    Y1 = Y(K-1);
    while K < np
        X2 = X(K);
        Y2 = Y(K);
        Proceed = true;
        DISTA = sqrt((X2-X1)^2+(Y2-Y1)^2);
        while (DISTA >= CL && Proceed ==true)
```

```
        DISTA = sqrt((X2-X1)^2+(Y2-Y1)^2);
        Xnew = X1 +(CL/DISTA) * (X2-X1);
        Ynew = Y1 +(CL/DISTA) * (Y2-Y1);
        IPNUM = IPNUM + 1;
        X1 = Xnew;
        Y1 = Ynew;
        continue
    end
    while DISTA < CL
        X3 = X(K+1);
        Y3 = Y(K+1);
        X2 = X(K);
        Y2 = Y(K);
        DISTC=sqrt((X3-X1)^2 + (Y3-Y1)^2);
        if DISTC < CL
            INDICA = np - 1;
            if K < INDICA
                K = K+1;
            else
                K = K+1;
                break
            end
            continue
        else
            DISTB=sqrt((X3-X2)^2 + (Y3-Y2)^2);
            DISTA=sqrt((X2-X1)^2 + (Y2-Y1)^2);
            if ~DISTB==0 || ~DISTA==0
                F = (DISTA^2 + DISTB^2 - DISTC^2) / (2*DISTA*DISTB);
                if F >0.999  ||  F<-0.999
                   DIST = CL - DISTA;
                else
                    C = acos(F);
                    A = asin(DISTA*sin(C)/CL);
                    B = 3.14159 - A - C;
                    DIST = DISTA * sin(B) / sin(A);
                end
            else
                DIST = CL - DISTA;
            end
            Xnew =  X2 + (DIST/DISTB) * (X3-X2);
            Ynew =  Y2 + (DIST/DISTB) * (Y3-Y2);
            IPNUM = IPNUM + 1;
            X1 = Xnew;
            Y1 = Ynew;
            K = K+1;
            Proceed = false;
            break
        end
    end
end

FLENGTH = (CL * IPNUM + sqrt((X(np)-X1)^2 + (Y(np)-Y1)^2))/1000;
```

```
    PX(j) = log10(CL/1000);
    PY(j) = log10(FLENGTH);
    File6(j,1)=j;       File6(j,2)=CL;      File6(j,3)=PX(j);
    File6(j,4)= IPNUM;  File6(j,5)=FLENGTH; File6(j,6)=PY(j);
end

fold1 ='C:\Folder\';
savfil=strcat(fold1,'pfix_File6.mat');
save(savfil,'File6')

XD = 0.0;
YD = 0.0;
XY = 0.0;
XA = 0.0;
YA = 0.0;

for m = 1:NW
    XA = XA + PX(m)^2;
    YA = YA + PY(m)^2;
    XD = XD + PX(m);
    YD = YD + PY(m);
    XY = XY + PX(m)*PY(m);
end
B = (XY-XD*YD/NW) / (XA-XD^2/NW);
D = 1 - B;

ABOVE = (XY - XD*YD/NW)^2;
BELOW = (XA - XD^XD/NW) * (YA - YD*YD/NW);
RSQ = ABOVE/BELOW;


figure('position',[10 550 380 360],'name','Log[Length vs CL]')
plot(File6(:,3),File6(:,6),'o','color',or2,ms,4)
hold on
xlabel('\bf Log(Chord Length [km])',fs,9)
ylabel('\bf Log(Length [km])',fs,9)
```

## Multiple Linear Regressions for Analytical Model Parameters

Multiple linear regressions (MLRs) were developed to better constraining analytical model parameters (Figure B9). The solutions defined by the MLR were estimated with six independent observations. For each parameter, several MLRs were available from different configurations of indexes. However, the ones selected here incorporated a wide range of predictor values to increase their applicability to a larger variety of possible environmental settings. They were also selected because they predict the analytical parameter in a continuous fashion without favoring a limited range of the independent variables. The MLRs presented here achieved at least a 96% probability allowing neglecting the null hypothesis. This hypothesis corresponds to that of the F-statistic and it is neglected when the model is a better fit than the intercept-only model. In other words, the model's prediction is better than the mean of the dependent variable. The probability of each predictor to reject the null hypothesis (*rho*) is also included (Figure B9), which provides insight on the degree of significance of the contribution from each predictor to the entire MLR. The stochastic behavior in the residuals of these MLRs was not thoroughly verified considering the difficulty in identifying potential deterministic patterns on a six-point scatter plot. However, no definite deterministic patterns were recognized. In some cases, the form of the MLR includes an interaction term of the product between predictors. A collinearity test was performed for each set of predictors in any given MLR. This test estimated the condition index ($n_j$) for a set of predictors based on their singular values ($n_j = \mu_{max}/\mu_j$), for which high $n_j$ values are indicative of separate near dependencies in the data (*Belsley et al., 1980*). The number of $n_j$-values equals the number of near dependencies. A condition index tolerance (i.e., $n_j$<10) was used as threshold to select values of variance decomposition proportions ($\pi_{ij}$) higher than 0.5 to identify predictors with some degree of collinearity (*Belsley et al., 1980*). When dependencies among predictors are identified, a ridge regression technique was applied to estimate whether or not the collinearity should be corrected, which can also be done by the same technique. This technique reduces the variance of the coefficient estimates, which in turn, may reduce the mean square-error (MSE) when collinearity exists. Taking advantage of this tell-tale, an increase in the MSE,

after applying this technique, was used as an indicator of no significant collinearity among predictors (*Belsley et al., 1980*).

The Lasso technique (*Tibshirani, 1996*) was implemented to help identify potential predictors which are likely more significant in explaining the response parameter of an MLR. With twenty-seven potential indexes to consider, the *stepwiselm* function in MATLAB simplified the process of including and excluding predictors to the working MLR model. The results from the *stepwiselm* function were optimized with manual pairing of predictors. In general, the *stepwiselm* function provided an MLR model with as many as four predictors, with highly significant fit, given by the root mean-squared error (RMSE), the R-squared, and the p-value of the F-statistic. Additionally, the quality of these models was measured using information theory indexes such as the Akaike information criterion (AIC) and the Bayes information criterion (BIC). Models with larger numbers of parameters are always better fitted, but both AIC and BIC penalizes them, as models with fewer predictors are sought. The resulting models with better fit are associated with having low AIC and BIC indexes and RMSE values. Predictors in a model with not significant p-values (>0.10) were removed and in some cases replaced with the product of the remaining two predictors. Predictors suggested by the Lasso technique as significant, were brought into the model to evaluate their contribution. In reducing the amount of predictors, the use of interactions between the remaining predictors increased the model performance. These interactions either decreased or increased collinearity, which was maintained below 30 for the models presented here (Table B2). This threshold is a typical condition index value that separates weak (< 30) from moderate to high dependencies ($30<n_j<100$). The ridge regression analysis deemed these weak dependencies as not significant for the final models. By reducing the number of terms to two in the final models, their overall significance as dictated by RMSE, AIC and BIC estimates was also reduced. However, considering that the number of observations was limited and that a significant fit was attained with lower number of predictors, the MLR models are satisfactory for the purpose of serving as guidelines in estimating the analytical model parameters.

The MLR model for *SF* includes the $R_C$ and *LvAa* indexes (Figure B9a). From the calibration process it was noticed that the SF varies the slope of the watershed: the greater the slope the smaller the SF would be. The SF is positively correlated with the coefficient of the Hack's law *LvAa* ($r^2$=0.69) whereas it has no correlation with $R_C$ ($r^2$=0.01). The strong correlation with *LvAa* remains unexplained, as *LvAa*, at the most, it can represent a planar distribution factor of the watershed, which is different from the association between watershed slope and the SF. A near dependency was identified between *LvAa* and the model's intercept but it was a weak one ($n_j$=23.8) and no correction was required based on the ridge regression analysis.

Texture topography indexes (Figure B9b, *Dd* and *DF*) are predictors of $U_0$, and their individual contribution is also significant. The parent of this model included an interaction term that yielded better AIC and BIC indexes but its own contribution to the entire model was not relevant ($p_{Dd:DF}$=0.16), which motivated its removal. A weak collinearity was present between *Dd* and *DF* ($n_j$=21.5), but the ridge regression analysis did not force a correction. The dependence of $U_0$ on texture (*Dd*, *DF*, and $d_{BCs}$) and shape (*LvAb*) measures rather than gravity-oriented indexes such as *cSlope*, *Relief*, and *mGrad*, is telling on the importance of the stream frequency and the watershed shape in controlling subsurface flow and travel times. A second best option for this model included $d_{BCs}$ and *LvAb*, where $U_0$ specifically grew with greater *LvAb* and $d_{BCs}$ values. Greater *LvAb* values are characteristic of elongated watersheds. A wider range of growth for $U_0$ is achieved with the selected model.

The macrodispersion function for prospective watersheds is described by the $\lambda_L b$ and the product $\lambda_L ab$ from the power function that typically defines it. The exponent of this function, $\lambda_L b$, is predicted (Figure B9c) with *Tex* and *C* (Compactness). The fact that $\lambda_L b$ is predicted by shape and texture topography measures is expected as it heavily depends on the flow path distances constrained by the shape of the watershed, externally, and internally by the interception of streams along the flow paths. Another model included the indexes: *TexPer*, *PLR*, $D_{BCp}$, and *LvAa* all contributing in a significant way with minimum RMSE, AIC, and BIC estimates, and where, again, texture topography and shape measures are predictors. *Tex*

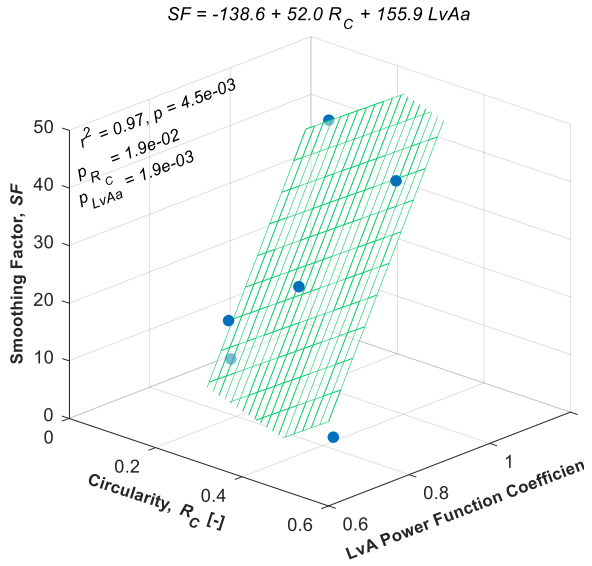
SF = -138.6 + 52.0 R_C + 155.9 LvAa
r² = 0.97, p = 4.5e-03
p_RC = 1.9e-02
p_LvAa = 1.9e-03
Smoothing Factor, SF
Circularity, R_C [-]
LvA Power Function Coefficien

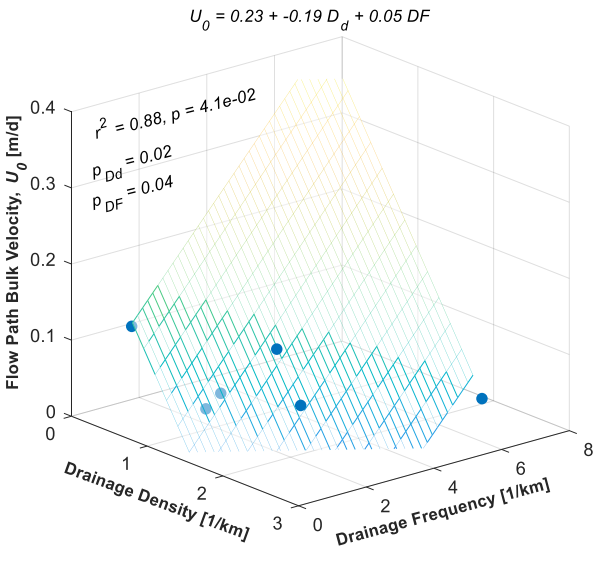
U_0 = 0.23 + -0.19 D_d + 0.05 DF
r² = 0.88, p = 4.1e-02
p_Dd = 0.02
p_DF = 0.04
Flow Path Bulk Velocity, U_0 [m/d]
Drainage Density [1/km]
Drainage Frequency [1/km]

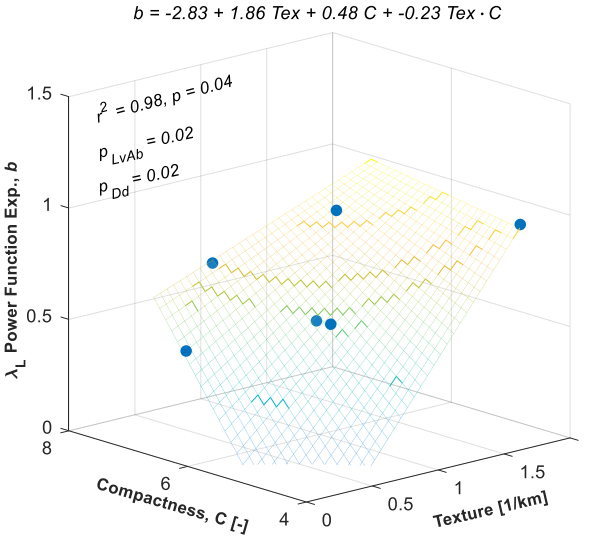
b = -2.83 + 1.86 Tex + 0.48 C + -0.23 Tex · C
r² = 0.98, p = 0.04
p_LvAb = 0.02
p_Dd = 0.02
λ_L Power Function Exp., b
Compactness, C [-]
Texture [1/km]

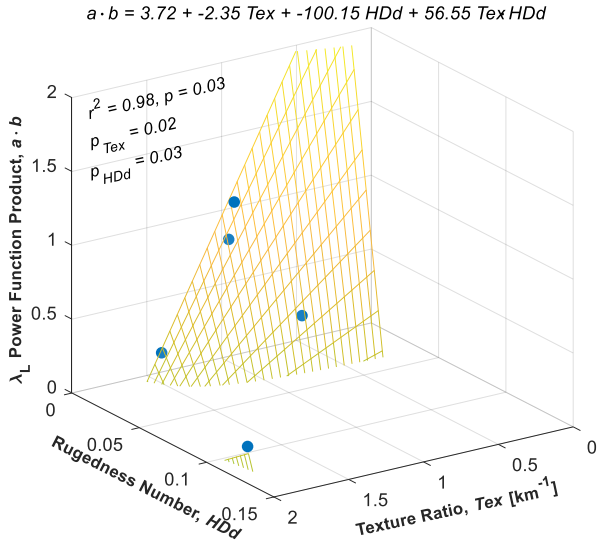
a · b = 3.72 + -2.35 Tex + -100.15 HDd + 56.55 Tex HDd
r² = 0.98, p = 0.03
p_Tex = 0.02
p_HDd = 0.03
λ_L Power Function Product, a · b
Rugedness Number, HDd
Texture Ratio, Tex [km^-1]

Figure B9. Multiple linear regression of a) smoothing factor (*SF*), b) mean flow path velocity ($U_0$), c) $\lambda_L$ power function exponent (b), and d) $\lambda_L$ power function product (a·b). The probability of neglecting the null hypothesis of the F-statistic is shown for entire MLR and for each of its predictors.

and *C*, in the selected model, exhibited a weak, near dependency ($n_j$=15.4), which did not require a correction of the terms according to the ridge regression analysis. The model for $\lambda_L ab$ is predicted by two texture topography measures: *HDd* and *Tex*. The model exhibited some collinearity ($n_j$=28.1) between HDd and the interaction term but it was not deemed significant.

Table B2. MLR models to predict analytical model parameters for future applications. Model quality measures are also included.

| Analytical Parameter | Expression | $R^2$ | RMSE | AIC | BIC | Condition number |
|---|---|---|---|---|---|---|
| *SF* | $SF$ = -138.6+52·$Rc$ + 155.9·$LvAa$ | 0.97 | 3.58 | 34.2 | 33.6 | 23.9 |
| *Uo* | $Uo$ = 0.23 - 0.19·$Dd$ + 0.05·$DF$ | 0.88 | 0.02 | -29.9 | -30.5 | 21.5 |
| *λLb* | $\lambda Lb$ = -2.83 + 1.86·Tex + 0.48·$C$ - 0.23·$Tex$·$C$ | 0.98 | 0.05 | -17.2 | -18.0 | 15.4 |
| *λLab* | $\lambda Lab$ = 3.66 - 2.31·$Tex$ - 0.10·$HDd$ + 5.53e-2·$Tex$·$HDd$ | 0.98 | 0.22 | 0.03 | -0.80 | 28.1 |

## MLRs for wMTT

Applying similar steps in the creation of MLR models as for the analytical parameters several models predicting wMTT were developed. The Pearson correlation among wMTT from the numerical and analytical models as they relate to the geomorphological indexes (Figure B10) were used with the stepwise technique to create the initial models. These models included up to four predictors (Table B3) which were reduced using the Lasso technique together with the goodness of fit measures(R-square, RMSE, AIC, and BIC indexes) and the collinearity analysis (condition index and ridge regression technique).

Elevation, texture topography, and analytical parameters are among the predictors: $\lambda_L ab$, *HDd*, *DF*, *Schan*, $R_B$, $R_C$, *MnChL*, and *LnkSlp*. The coefficient product $a \cdot b$ of the $\lambda_L$ power function is the base of three reduced models (Table B3) indicating its strong predictive value, which is shared with *HDd*, *DF*, and *Schan* in separate models. The analytical parameter $\lambda_L ab$ can be derived from the SLR and MLR relationships defined in the previous section for future watershed applications. From these indexes, *Schan* is a measure of slope, *DF* of texture topography, *HDd*, of texture with an elevation component, and $R_B$, $R_C$, and *LnkSlp* are Horton's law measures. After reducing the models to two terms, the collinearity was diminished from a strong to either moderate (first three models) or weak (last two models) dependencies. The interaction term tended to increase collinearity in the final models and was excluded, with the exception of model 5. The moderate dependency in the first three models is mainly dominated by *λLab* and the model's intercept. Note that *Relief*'s predicting abilities were not significant enough to appear in the reduced models. Considering the goodness of fit measures employed to evaluate the quality of the models, the model with *HDd* and $\lambda_L ab$ was the best fitted among the reduced models (Figure B11). However, this model appears to limit its predictive capacity to watersheds with MTTs lower than 83 years, as indicated by its intercept and the negative signs of the following terms in the model. For this reason, and for exhibiting moderate collinearity, the *LnkSlp*- and $R_B$-based model is a better option (i.e., model 4 in Table B3). *LnkSlp* is also a predictor of the wMTT SLR model (Figure 3-14), whereas, $R_B$ is weakly ($r^2$=0.22), and negatively correlated with wMTT. Both indexes are similar measures in the way a watershed converges headwaters to lowlands. A weak ($n_j$=10) collinearity is present in this model between $R_B$ and the intercept. The ridge regression analysis did not deem it necessary to correct this dependency.

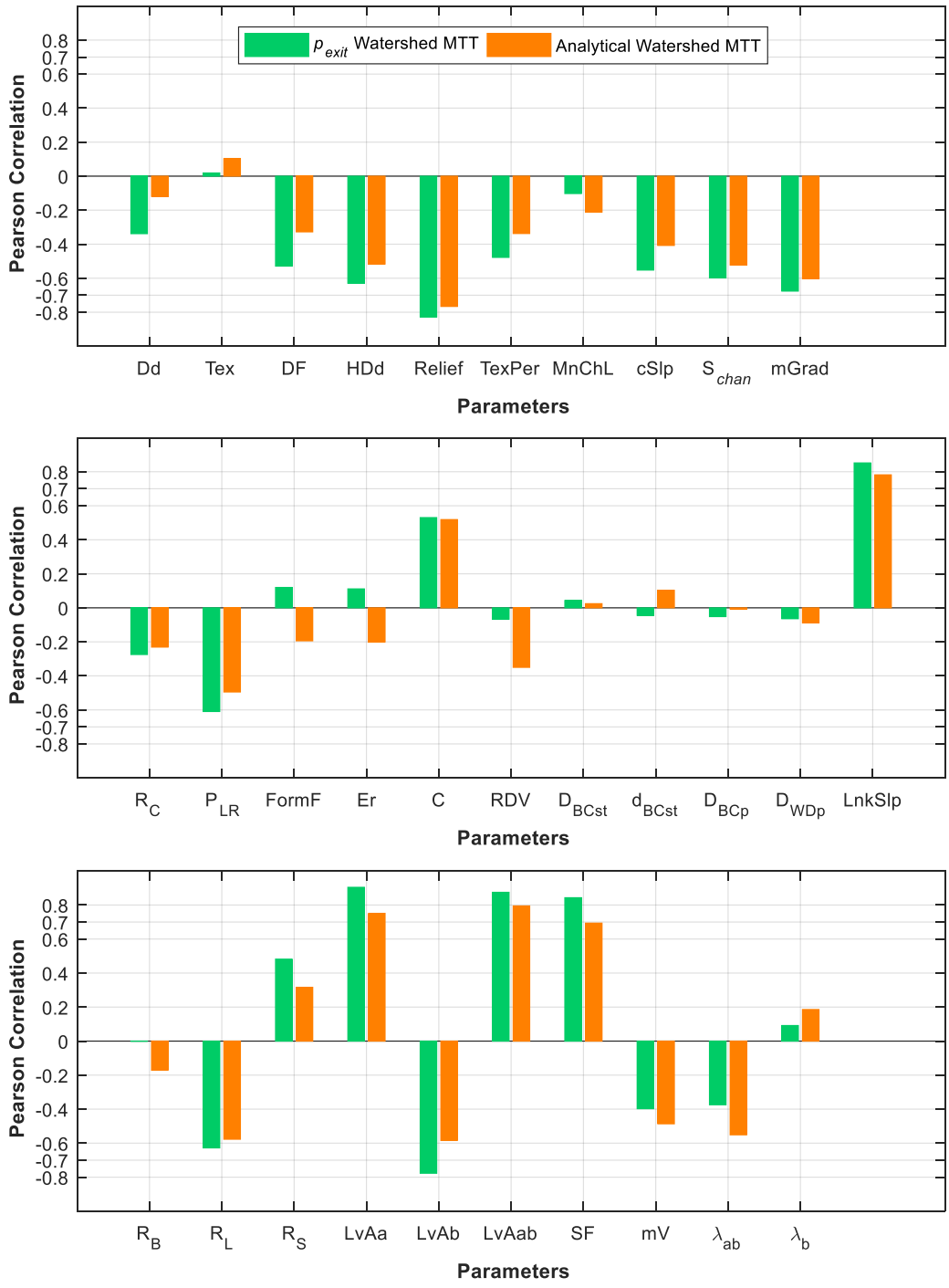


Figure B10. Pearson correlations between watershed MTTs and geomorphological indices.

Table B3. MLR models to predict wMTT presented together with their respective goodness of fit measures. Models 4 and 5 were created without considering analytical model parameters as predictors. Initial [I] and final [F] models are presented.

| Model | Expression | $R^2$ | RMSE | AIC | BIC | Condition Index |
|---|---|---|---|---|---|---|
| 1 | wMTT = **76.2** - 0.36·HDd + 8.7e-3·**Relief** + 8.2·$D_{BCp}$ - 14.9·**$\lambda_L$ab** [I] | 1.0 | 0.01 | -39 | -40 | 345 |
| | wMTT = **83** – 288.5·HDd – 14.45·**$\lambda_L$ab** [F] | 1.0 | 0.82 | 16 | 16 | 62 |
| | [p=1e-6; 6e-5; 6e-5] | | | | | |
| 2 | wMTT = **84.5** – 0.4·DF - 0.27·HDd – 18.3·Uo - 14 ·**$\lambda_L$ab** [1] [I] | 1.0 | 0.01 | -38 | -39 | 109 |
| | wMTT = **93.6** – 6.8·DF – 17.1·**$\lambda_L$ab** [F] | 0.94 | 4.54 | 37 | 36 | 55 |
| | [p=3e-4; 1.1e-2; 8e-3] | | | | | |
| 3 | wMTT = **65.9** – 3.4·**Schan** + 25·LnkSlp + 4.2e-2·**SF** – 11.3·**λab** [I] | 1.0 | 3e-3 | -52 | -53 | 232 |
| | wMTT = **84.2** – 4.33·Schan – 13.6·**$\lambda_L$ab** [F] | 0.95 | 4.2 | 36 | 35 | 56 |
| | [p=1e-4; 9e-3; 8e-2] | | | | | |
| 4 | wMTT = **-11.3** + 259 **LnkSlp** + 7.8 **$R_B$** – 32.5 LvAa – 31.9 **LnkSlp*$R_B$** [I] | 1.0 | 3e-2 | -26 | -27 | 224 |
| | wMTT = **41.3** + 109.7 LnkSlp – 10.7 **$R_B$** [F] | 0.99 | 2.1 | 28 | 27 | 10 |
| | [p=2.2e-3; 6.7e-4; 2.6e-3] | | | | | |
| 5 | wMTT = **81.2** – 1.2e-3·**MnChL** – 86.3·**$R_C$** + 28.7·LnkSlp + 1.6e-3·**MnChL·LnkSlp** [I] | 1.0 | 0.06 | -17 | -18 | 55 |
| | wMTT = **166.1** – 1.058e-3·MnChL – 151.6·$R_C$ - 6.9e-3·**MnChL·$R_C$** [F] | 0.95 | 4.96 | 37 | 37 | 21 |
| | [p=1.2e-2; 4e-2; 4.1e-2; 0.18] | | | | | |

[1]Model terms highlighted in bold font are terms involved in dependency identified by the respective condition index.

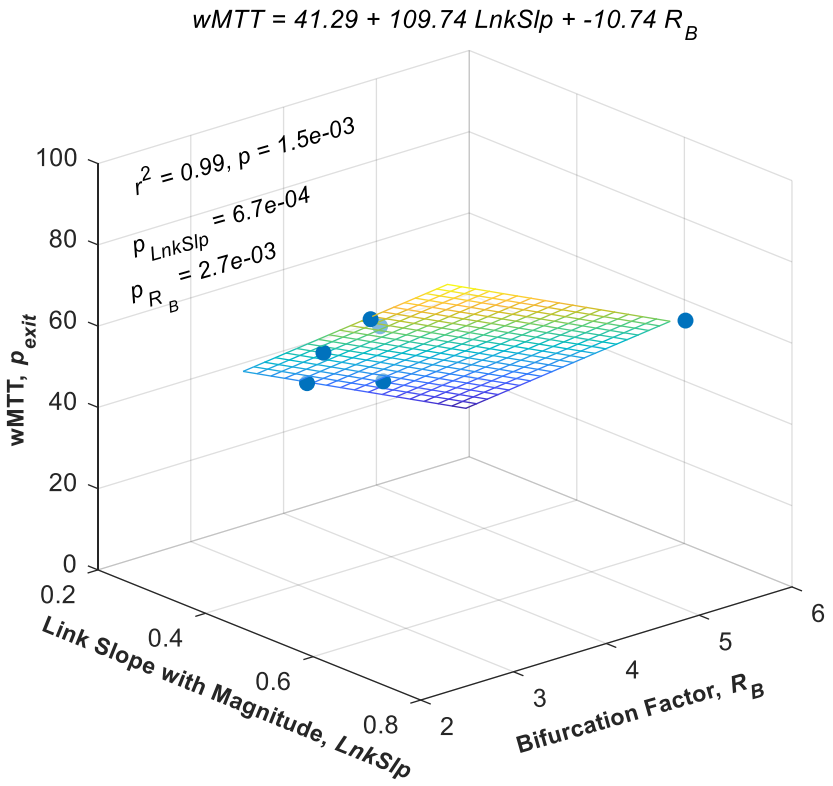


Figure B11. Selected MLR model to predict wMTT using $\lambda_L ab$ and DF as predictors. The p-value for each predictor is also shown with the $r^2$ value of the function.

### Predictive Models Applied to Verification Watersheds

Using the tools developed to select watersheds where the analytical model could potentially perform well, three verification watersheds were selected (Figure B12). The selection process followed the ranges of values specified for Tier 1 and Tier 2 indexes (Table 3-3). A numerical model for each of these sites was also build, following similar specifications used for previous watersheds evaluated in this study.

An analytical model was applied to each watershed employing the predicted parameter values for *SF*, *Uo*, and $\lambda_L$ (from *a*, and *a·b*, for the power function of $\lambda_L$) from both SLR and MLR models (Table B4). Some of the initially proposed models did not work properly and alternative models were used that did not score high initially. See main text for details.

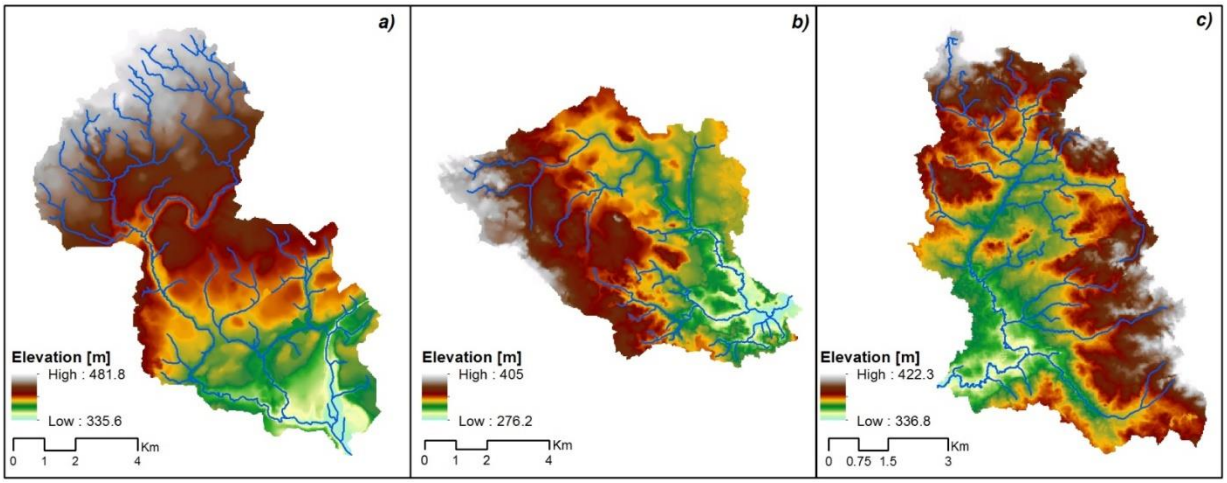


Figure B12. Verification study sites selected by using predictive tools based on geomorphological indexes for applying the analytical model. a) Carroll Creek, b) Schneider Creek, and c) Nith River.

The pMTT estimated from the analytical model were compared with its numerical counterpart. Both the spatially-bound comparison (Figure 3-14) and the comparison of the distribution of these estimates (Figure B13) yielded similar results to those from which the predictive tools were developed. When predicting wMTT from their geomorphological

indexes, not all the proposed models delivered comparable estimates against the numerical model estimates (i.e., indexes *LvAab* and *LnkSlp* in SLR model). Different MLR models generated similar wMTT predictions, but all seemed insensitive to the geomorphological changes in the watershed. However, the implemented analytical model predictions fell within 3.2%, 9.8%, and 74%, for Carroll Creek, Nith River, and Schneider Creek, respectively (Table B5).

Table B4. Predicted analytical model parameters (*SF*, *Uo*, $\lambda Lb$, and $\lambda Lab$) using SLR and MLR models developed in previous sections. Expressions for secondary models that performed better than originals are also provided.

| Predicted | Indexes | Carroll Creek | Schneider Creek | Nith River |
|---|---|---|---|---|
| *Single Linear Regressions (SLRs)* | | | | |
| ***SF*** | *Relief* | 146 | 129 | 86 |
| | ***SF*** | ***17*** | ***20*** | ***31*** |
| | *LvAab* | $L = 1.24*A^{0.565}$ | $L = 0.504*A^{1.01}$ | $L = 0.504*A^{0.715}$ |
| | ***SF*** | ***29*** | ***0*** | ***0*** |
| ***Uo*** | $d_{BCst}$ | 1.059 | 1.043 | 1.064 |
| | ***Uo*** | ***0.077*** | ***0.110*** | ***0.069*** |
| | *DF*[1] | Using, $Uo = 8.9e\text{-}2*DF^{-0.35}$ | | |
| | ***Uo*** | ***0.067*** | ***0.076*** | ***0.065*** |
| ***λLb*** | *TexPer* | 0.432 | 0.379 | 0.483 |
| | ***λLb*** | ***0.61*** | ***0.59*** | ***0.64*** |
| ***λLab*** | *Dd* | 1.63 | 1.05 | 1.63 |
| | ***λLab*** | ***0.48*** | ***1.01*** | ***0.48*** |
| | *DF*[1] | Using, $\lambda Lab = 1.08*DF^{-1.10}$ | | |
| | ***λLab*** | ***0.44*** | ***0.66*** | ***0.40*** |
| *Multiple Linear Regressions (MLRs)* | | | | |
| ***SF*** | *Relief & LvAab* | Using, $SF = -1647.7\text{-}2.4*Relief+2298.3*LvAab+4.4*Relief*LvAab$ | | |
| | ***SF*** | ***62*** | ***-498*** | ***-890*** |
| ***Uo*** | *DF and Dd* | Using, $Uo = 0.23 - 0.19*Dd + 0.05*DF$ | | |
| | ***Uo*** | ***0.032*** | ***0.109*** | ***0.044*** |
| ***λLb*** | *C* | 6.18 | 5.91 | 6.41 |
| | *Tex* | 0.44 | 0.54 | 0.79 |
| | ***λLb*** | ***0.33*** | ***0.28*** | ***0.55*** |
| ***λLab*** | *Tex & HDd* | Using, $\lambda Lab = 3.66 - 2.3 \cdot Tex - 0.1 \cdot HDd + 0.05\ Tex \cdot HDd$ | | |
| | *HDd* | 0.014 | 0.007 | 0.009 |
| | ***λLab*** | ***2.65*** | ***2.41*** | ***1.84*** |

[1]: Recommended models instead of those presented in Figure 12b and 12c. These are secondary models that provided better estimates in verification watersheds of analytical model parameters.

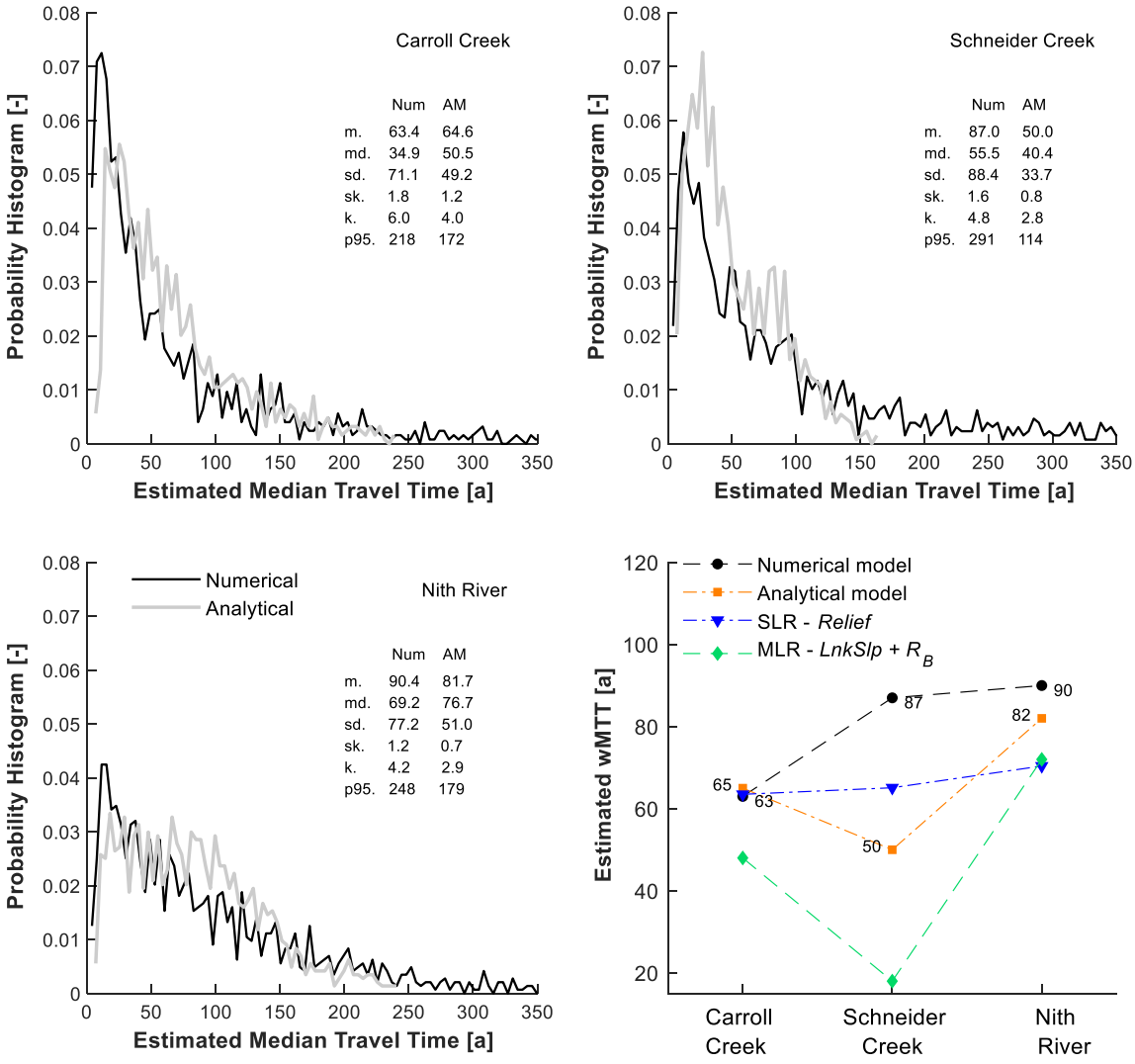


Figure B13. Verification study sites selected by using predictive tools based on geomorphological indexes for applying the analytical model. a) Carroll Creek, b) Schneider Creek, and c) Nith River.

Table B5. SLR and MLR models predicting watershed MTT from geomorphological indexes for verification study sites. Estimates of watershed MTT from numerical and analytical models are also presented.

| ***Indexes*** | ***Carroll Creek*** | ***Schneider Creek*** | ***Nith River*** |
|---|---|---|---|
| *Single Linear Regressions (SLRs)* | | | |
| *Relief [m]* | 146.2 | 128.8 | 85.5 |
| $wMTT = 163.8*Relief^{0.19}$ | | | |
| **wMTT (a)** | **63.5** | **65.1** | **70.4** |
| *LnkSlp* | 0.56 | 0.34 | 0.39 |
| $wMTT = 94.4*LnkSlp^{0.65}$ | | | |
| **wMTT(a)** | **65.1** | **47.0** | **50.8** |
| *LvAa* | 1.24 | 0.50 | 0.50 |
| *LvAb* | 0.56 | 1.01 | 0.71 |
| *LvAab* | 0.70 | 0.51 | 0.36 |
| $wMTT = 204.4*LvAab^{3.0}$ | | | |
| **wMTT (a)** | **70.3** | **27.0** | **9.6** |
| *Multiple Linear Regressions (MLRs)* | | | |
| $wMTT = 41.3 + 109.7\ LnkSlp - 10.7\ R_B$ *[Model 4]* | | | |
| *LnkSlp* | 0.41 | 0.35 | 0.60 |
| $R_B$ | 3.62 | 5.77 | 3.31 |
| **wMTT (a)** | **48** | **18** | **72** |
| $wMTT = 93.6 - 6.8\ DF - 17.1*\lambda Lab$ *[Model 2]* | | | |
| *DF* | 2.24 | 1.56 | 2.47 |
| *λLab* | 0.44 | 0.66 | 0.40 |
| **wMTT (a)** | **71** | **72** | **70** |
| $wMTT = 84.2 - 4.33\ Schan - 13.6\ \lambda Lab$ *[Model 3]* | | | |
| *Schan* | 2.06 | 1.37 | 0.94 |
| *λLab* | 0.44 | 0.66 | 0.40 |
| **wMTT (a)** | **69** | **69** | **75** |
| **Analytical model** | **65** | **50** | **82** |
| **Numerical model** | **63** | **87** | **90** |

### Comparison to Haitjema's Approach

A brief description of this approach is included in section 1.3.1. In Haitjema (*1995*)'s approach, the TTD is a function of porosity ($\theta$=0.35), recharge rate ($r$=6.5e-4 m/d) and saturated thickness (H) of the aquifer. In order to compare this method to the modeling conditions for this study, both porosity and recharge rate were kept constant for the study watersheds. For the estimation of the saturated thickness for each study site, the water table was approximated by the hydraulic head in FEFLOW to calculate an average H value for the watershed. Considering that the ratio $r$[7.3x10$^{-9}$ m/s]/$K_{avg}$ [6.09 x 10$^{-5}$ m/s] = 1.2x10$^{-4}$ is similar to the plotted output of residence time in his Figure 7 for $r/K_{avg}$ = 1.0x10$^{-4}$, a corrected expression for unconfined aquifers was not necessary to be applied as the difference with the original equation is minimum for this range of $r/K_{avg}$ values. Using equation 1.1, the TTD was estimated for each study site (Figure B14), as well as the value of T, which corresponds to the wMTT given by the centroid above the CDF exponentially-based curve. These CDF curves are not directly comparable with the gamma-like distribution curves generated by the Soltani & Cvetkovic (*2013*)'s equation nor the breakthrough curve of travel time output by FEFLOW, only the derived wMTT can be compared (Figure B15). The Haitjema-based wMTT exhibited some correlation ($r^2$=0.50) with the numerical model when including the entire set of watersheds, which was reduced to nil ($r^2$=0.0) after excluding the RPT watersheds where the numerical model did not provide reliable results. While the analytical method explained 71 and 89 % of the target wMTT, in both instances, respectively.

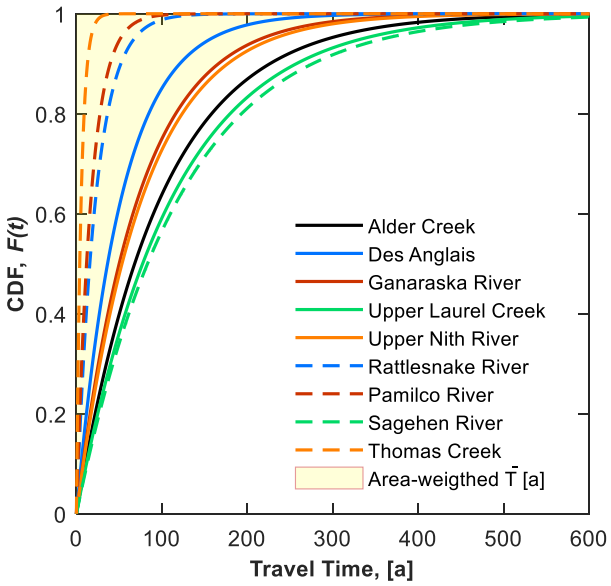


Figure B14. Watershed-scale travel time distributions estimated using the Haitjema (*1995*) method. The centroid of the highlighted area corresponds to $\overline{T}(\theta H/r)$ or wMTT.

# Appendix C

# Supplementary Material: Chapter 4

## Estimation of N Requirement for Corn

Corn is part of a common row cropping practice in the Grand River basin together with soybeans and winter wheat (*Liu et al., 2016*). According to OMAFRA (*2017*), the recommended annual N requirement for corn depends on: the type of cultivated soil (Table C1), crop yield, crop heat exposure, and previous crop cultivated on land (i.e., soybeans). The areas of the soil types overlying the row crop land use category was used to estimate a mean value for annual N requirement for corn.

Table C1. Area-weighted estimation of N requirement for corn as per soil type overlying the row crop land use category in Carroll Creek (*OMAFRA, 2017*).

| Soil Type | Area [ha] | Base N Requirement [kg/ha][1] |
|---|---|---|
| Clay loam till | 696.3 | 40 |
| Fine sand and silt | 19.9 | 38 |
| Fine sand over grave | 7.6 | 52 |
| Gravel | 118.6 | 52 |
| Loam till | 497.4 | 36 |
| Medium sand | 85.5 | 52 |
| Organic | 526.9 | 53 |
| **Row Crops –Land Use** | 1952.2 | **43.8** |

[1] Recommended N requirement for corn as per soil type. Taken from OMAFRA (*2017*) for southwest and central Ontario.

Using values provided by OMAFRA (*2017*), the determination of the total N requirement for corn is given by the following adjustments:

| | | |
|---|---|---|
| Base mean N requirement based on soil type: | 43.8 | kg/ha |
| Assuming a mid-range Yield: | 10.5 | t/ha |
| Yield adjustment: | 142.8 | kg/ha |
| Guelph Crop Heat Unit [CHU-M1]: | 2828 | |

| | |
|---|---|
| Heat Unit adjustment: | 1.148 kg/ha |
| Previous crop adjustment [Soybeans]: | 30 kg/ha |
| Price ratio adjustment for mid-range N ($1.50) relative to mid-range Corn Price ($170/t): | 26 kg/ha |

**Suggested Total N requirement for Corn = 142 kg/ha**

## Litterfall and Crop Residue Production

Representative litterfall rates data for septentrional forests were sought in the literature (Table C2), as well as crop residue rates for row crops in the Carroll Creek watershed. In the study site, coniferous, deciduous, and mixed forests are found mostly as extensions of the riparian zone. The thesis work by Raimbault (2011) identified a litterfall rate that is twice as high as that of deciduous forest stands in New Hampshire (Yang et al., 2017). These rates can be used as a range for this N flux.

Table C2. Total litterfall density and N litterfall density in deciduous, riparian, and mixed forests.

| Reference for Forested Land Use | Site Description | Litter Density [g/m$^2$] | Litter Density [kg/ha] | Litter N Density [kg N/ha] |
|---|---|---|---|---|
| Yang et al. (*2017*) | Mean annual litterfall mass [New Hampshire] | 299.4 | 2994 | 26.3 |
| Vogt et al. (*1986*) | Cold temperate broadleaf deciduous [World forests] | 385.4 | 3854 | 33.9 |
| Vogt et al. (*1986*) | Cold temperate needle leaf deciduous [World forests] | 359.0 | 3590 | 31.6 |
| Raimbault (*2011*) | Natural forest, riparian zone South Ontario | -- | -- | 53.0 |
| Jerabkova et al. (*2006*) | Conif, Decid, Mixed forest in North Alberta | 170.2 | 1702 | 15.0 |

Table C3. Annual rate of crop residue for corn, soybeans, and winter wheat.

| References for Agricultural Land Use | Corn | Soybean | Winter Wheat |
|---|---|---|---|
| ***Crop Residues*** | | | |
| OMAFRA and University of Guelph (*2012*) [kg N/ha] | 28.33 | 16.63 | 15.53 |
| Smil (*1999*) [US crops, kg N/ha] | 50 | -- | 25 |
| ***N concentration*** | | | |
| OMAFRA and University of Guelph (*2012*) [% N] | 0.74 | 1.05 | 0.63 |

## Variation of $\delta^{15}N$ in Liquid and Solid Manure with Temperature

Karr et al. (*2003*) measured the change of $\delta^{15}N$ in liquid manure from a secondary slurry manure lagoon in North Carolina. It varied from +10‰, at the peak of winter (9th of February), to +30.8‰ in early summer (4th of June), period during which the mean daily temperatures oscillated from -1 to 31 °C. While mean daily temperatures in the area of Waterloo, Ontario changed from -10 to 25 °C (Figure C1). Considering that similar isotopic compositions are unavailable locally, Karr et al. (*2003*)'s values were used unaltered for liquid manure. For solid manure the range of $\delta^{15}N$ was modified to follow instead: +3.4 to +20.4 ‰, obtained from Bateman & Kelly (*2007*). These data allowed the development of a relationship of δ15N with rising and declining limbs whose rate of change with time for liquid and solid manure are presented in Table C4.

Table C4. Rising and declining limbs of the relationship between $\delta^{15}N$ and mean daily temperature.

| Manure | Rising Limb | Declining Limb |
|---|---|---|
| Liquid | 0.171*Days + 10 | -0.069*Days + 39 |
| Solid | 0.149*Days + 3.4 | -0.067*Days + 28 |

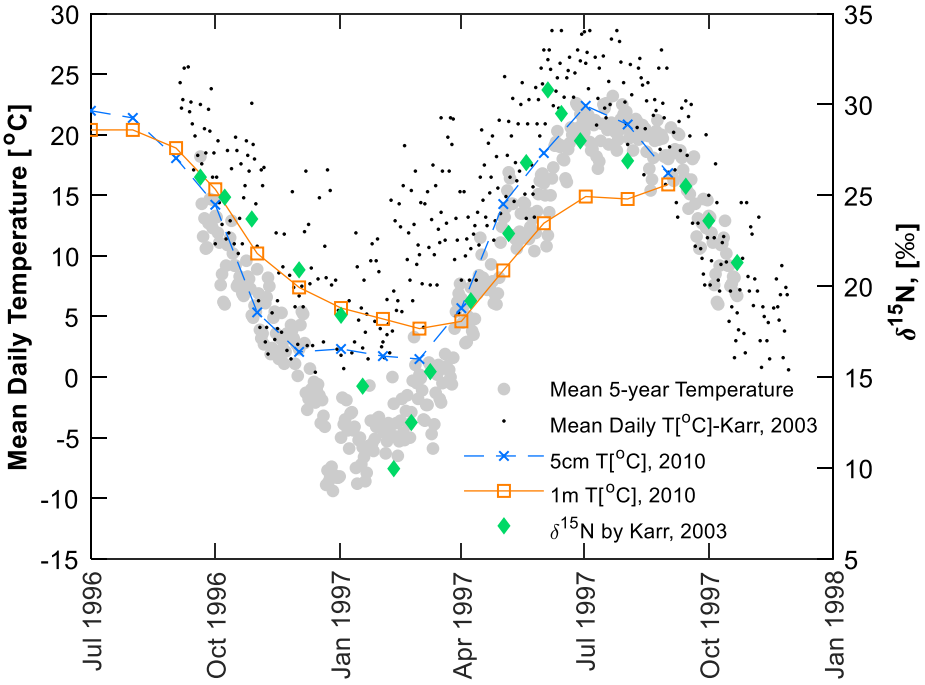


Figure C1. $\delta^{15}N$ and temperature data measured by Karr et al. (*2003*) in liquid manure from a slurry lagoon in North Carolina. Mean daily temperature in Waterloo, Ontario (gray circles) and temperature from a concrete manure storage near Drayton, Ontario at 5 cm (blue x) and at 1m (orange squares) from the surface (*Johannesson et al., 2017*).